Anisotropic and Hierarchical Porosity in Multifunctional Ceramics

Aaron Zev Lichtner

A dissertation
submitted in partial fulfillment of the
requirements for the degree of

Doctor of Philosophy

University of Washington
2015

Reading Committee:
Rajendra Bordia, Chair
Eric Stuve
Christophe Martin
Lucien Brush
Guozhong Cao
Qifeng Zhang

Program Authorized to Offer Degree:
Materials Science and Engineering

University of Washington

Abstract

Anisotropic and Hierarchical Porosity in Multifunctional Ceramics

Aaron Zev Lichtner

Chair of the Supervisory Committee:
Professor Rajendra Bordia
Materials Science and Engineering

The performance of multifunctional porous ceramics is often hindered by the seemingly contradictory effects of porosity on both mechanical and non-structural properties and yet a sufficient body of knowledge linking microstructure to these properties does not exist. Using a combination of tailored anisotropic and hierarchical materials, these disparate effects may be reconciled.

In this project, a systematic investigation of the processing, characterization and properties of anisotropic and isotropic hierarchically porous ceramics was conducted. The system chosen was a composite ceramic intended as the cathode for a solid oxide fuel cell (SOFC). Comprehensive processing investigations led to the development of approaches to make hierarchical, anisotropic porous microstructures using directional freeze-casting of well dispersed slurries. The effect of all the important processing parameters was investigated. This resulted in an ability to tailor and control the important microstructural features including the scale of the microstructure, the macropore size and total porosity. Comparable isotropic porous ceramics were also processed using fugitive pore formers. A suite of characterization techniques including x-ray tomography and 3-D sectional scanning electron micrographs (FIB-SEM) was used to characterize and quantify the green and partially

sintered microstructures. The effect of sintering temperature on the microstructure was quantified and discrete element simulations (DEM) were used to explain the experimental observations. Finally, the comprehensive mechanical properties, at room temperature, were investigated, experimentally and using DEM, for the different microstructures.

Acknowledgments

"Saint-like. I'm holy. HOLE-y."

– J.K. Rowling, *Harry Potter and the Deathly Hallows*

It's been a long journey getting to this point. This dissertation spans 4+ years and two continents of work. Over 10 months of time were spent living and working in Grenoble, France and I can truly say that without the help of my French counterparts, this would be a very different document. I'd like to thank my French co-advisor Prof. Christophe Martin for the time and effort that he spent working with me, Dr. David Jauffrès for his unflinching insight and critiques and most of all the *now* Dr. Denis Roussel[1] for his hard-work, friendship and generally massive contribution to this effort. I would also like to thank a few other members of the lab in France for their willingness to aid this lost American: Dr. Èdouard Biguereau, Dr. Jéremy Croquesel, Dr. Jaroslaw Sar, Maya Cherif, and Ozden Celikbilek. A quick thank you must also be given to Dr. Daniel Röhrens at the Forschungszentrum in Jülich, Germany for his aid using their optical dilatometer.

Back here in the states, I of course have to thank my family, friends and colleagues for their continuing support of me. Thanks especially goes to my Mom, Dad and Sister for their guidance and understanding of my generally grumpy mood during the past six months. Throughout my tenure here at UW I had multiple undergrad students and high school interns working with me. They all deserve credit for the help that they gave but in particular I'd like to acknowledge the work of Madie Melcer who was tireless in her efforts and genuine pleasure to work with. I'd like to acknowledge Tuesday Kuykendall who was always there with her help, advice and support. A debt of gratitude goes out to Eli Seward who was with me essentially from day one in Seattle.

Finally I'd like to thank my advisor Prof. Raj Bordia for his advice and the aid that he gave me during my time here.

Fun Fact: I used more than **1100 liters of LN2** in 4 years. Don't avoid the voids!

---

[1] He beat me to the punch

Contents

1

Project Overview

Chapter Contents

1.1 Motivation

Porosity in technical ceramics has traditionally been considered problematic due to its deleterious effect on mechanical properties. Recently however, porous ceramics have begun to draw considerable attention for their impressive non-structural characteristics and wide-ranging potential uses like filtration, catalysis, energy storage, energy conversion, insulation and bone regeneration [1]. As technologies utilizing these materials become more prevalent however, the engineering challenges of using porous ceramics become more apparent. Typically, non-structural performance properties such as permeability and electrochemical activity, both sought after characteristics of porous ceramics, increase with porosity while thermal stability, transport properties and mechanical integrity decrease with porosity [1].

The strong dependence of porous ceramic microstructure on functional properties at fixed chemical compositions is well known [2–4]. Similarly, there is good understanding of the mechanical properties and stability of porous ceramics [5–7]. There is however, a lack in understanding of the combination of these two bodies of knowledge. Each newly proposed porous ceramic system must be individually optimized for both targeted performance and mechanical stability making advancements in the field slow and costly. By recognizing some commonalities across the field of porous ceramics, new systems can be more efficiently developed. Studies have shown that by using anisotropic and/or hierarchically porous ceramics, it becomes feasible to enhance functional performance while simultaneously maintaining, or even improving mechanical integrity [8–11]. It is no longer sufficient to simply increase porosity in a random fashion; new technologies require deliberate, designed "smart" porosity, that is, porosity which is placed only where it is needed. Currently, there is no established process for systematically optimizing a porous multi-functional ceramic system, especially one with a designed and architectured porous microstructure.

1.2 Planned Project Approach

The goal of this thesis is to develop an overarching methodology for designing and optimizing multi-functional porous ceramic structures, and in doing so, better understand the link between porosity, non-structural properties and mechanical performance. To accomplish this task, we will develop a closely integrated experimental and meso-scale simulation approach for the design of electrochemical ceramics with multi-functional design requirements (Fig. 1.1). Architectured porous ceramics with various microstructural geometries will be synthesized and their properties correlated with microstructure and processing. Specifically, we will focus on the role that anisotropic and/or hierarchial porosity plays on performance. The techniques to process and control anisotropic and hierarchical porous structures will be developed at the University of Washington, as will mechanical testing and microstructural characterization. Our collaborators in SiMaP Lab at the University of Grenoble in France will perform electrochemical testing and concurrently develop discrete-element method (DEM) simulations to further study the performance and characteristics of our porous ceramics. Focused-ion beam tomography (FIB) and X-Ray Synchrotron Radiation Tomography (X-ray Tomo) will be used to create digital reconstructions of our physical specimens. These reconstructions will allow us to closely tie realistic experimental structures directly into our theoretical simulations. Experimental results will be used to validate and fine tune the simulation results and the simulations will in turn be used to design optimal microstructures for targeted applications. This process will be iteratively repeated to optimize and better understand our porous ceramic system and in doing so, establish some general methods for future porous architecture development.

Because of the fundamental nature of these investigations, the research will be applicable to a wide range of materials and applications. In order to validate the research however, we

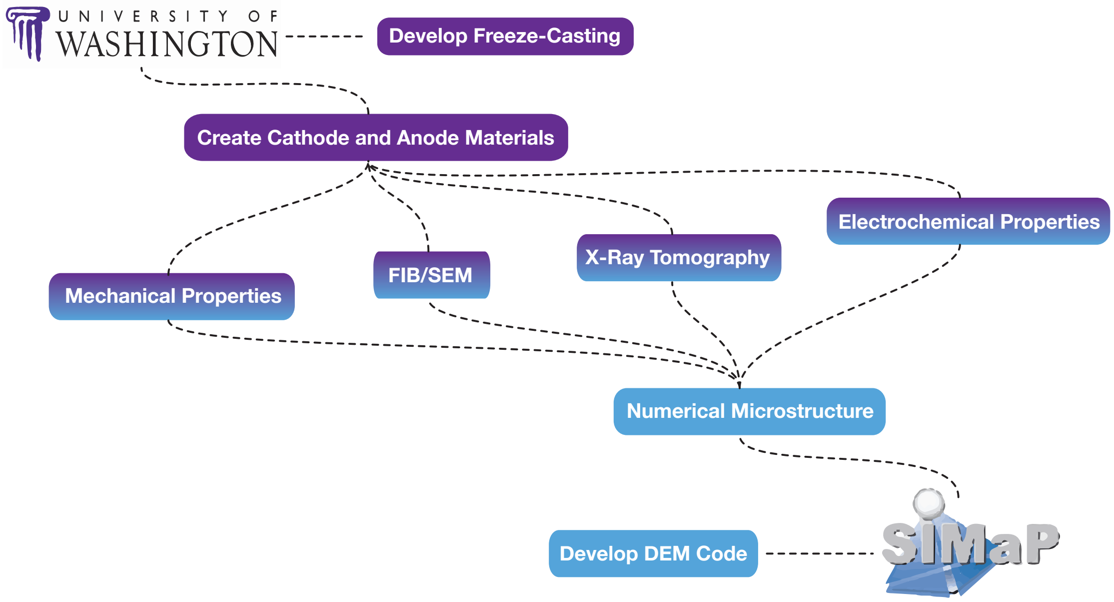

Figure 1.1: Basic breakdown of core work for the collaborative project.

will narrow our focus primarily to investigating the electrodes of Solid Oxide Fuel Cells (SOFCs). These electrochemically active ceramics require mechanical and thermal property optimization without sacrificing chemical or electrochemical performance [12, 13]. The complicated nature of the electrode function requires the simultaneous optimization of the microstructure for multiple fundamental properties and therefore the methods that we develop should be applicable to other complex porous ceramic systems [12, 14].

Throughout the project, we will be comparing the contribution of the anisotropic natures of our ceramics on performance. To do this, we will often create two general types of samples; anisotropically porous hierarchical ceramics and isotropically porous hierarchical ceramics (Fig. 1.2). As much as possible, characteristics like material, total porosity, pore size and sintering temperature will be kept consistent across all samples types so that only the deliberate, tailored differences between the materials can be investigated. Additionally, the effects of porous hierarchy will be characterized by altering sintering temperature and testing relevant properties.

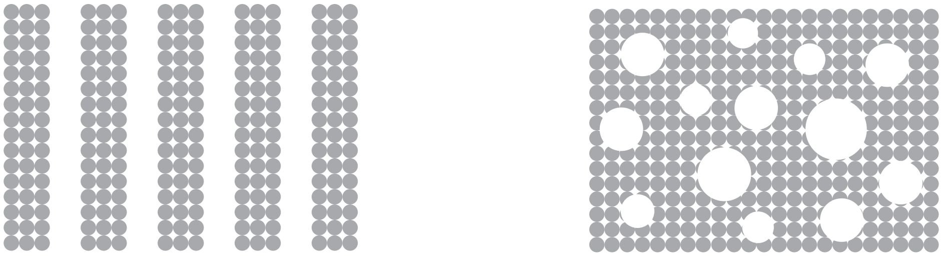

(a) Anisotropic / Hierarchical **(b)** Isotropic / Hierarchical

Figure 1.2: Cross-sectional schema for the porous materials tested during this thesis.

1.3 Resources and Collaboration

This project is being conducted jointly with funding from the National Science Foundation (NSF) under Grant No. 1008600 (PI: Prof. Bordia) and the French research agency ANR under Grant No. 2010 BLAM 093101 (PI: Prof. Martin) as a Materials World Network project. We are directly collaborating with Prof. Christophe Martin from the GPM2 lab within SiMaP at the University of Grenoble in France. Under the supervision of Prof. Martin are one post-doc (David Jauffrès) and one graduate student (Denis Roussel). The research presented within this thesis represents a culmination of our collaborative efforts thus far. At the University of Washington, we were able to access resources at the Nanotech User Facility (NTUF) and while in Europe, we were able to use the equipment and expertise at le Commissariat á l' ènergie atomique (CEA), the European Synchrotron Radiation Facility (ESRF) (both in Grenoble, France) and the Forschungszentrum in Jülich, Germany.

2

Literature Review

Chapter Contents

As previously mentioned, the overarching goal of this thesis is to develop a more thorough understanding of the role that porosity, and specifically designed porosity, plays on the properties of multi-functional porous ceramics. Using this knowledge, we can then develop models and procedures which can be extended to other multi-functional ceramic systems, streamlining the research and development process. To that end, the literature review is laid out to first discuss general porosity in ceramics, its manifestations, effects and applications. Then our specific multi-functional model ceramic system (Solid Oxide Fuel Cells) will be explored in detail including current processing methods, performance and areas in need of improvement. The various methods used to create designed porosity will be discussed with a heavy focus on freeze-casting, our method of choice. Finally, some properties of multi-functional porous ceramics and the simulation methods which were used to model our ceramic system will be discussed.

2.1 Porous Ceramics

The word “pore” derives from the Greek word “póros” meaning “passageway”. The Greek word also refers to a specific type of coarse limestone found in the Peloponnesus peninsula which was used extensively as a building material by the ancient Greeks. The Greeks highly valued this material for its strength and lightness and recognized even then that it was these “passageways” within the material that lent the “póros” it’s unique properties.

For much of the modern scientific age, researchers have sought out ways to avoid porosity. Cracks, voids, pores and holes were believed to invite early failure and less-than-optimal properties in already brittle ceramics. Indeed, porosity is still often referred to as a “flaw” whose very definition is that of an imperfection. As new technologies however begin to exploit porosity, some once ingrained notions must be reevaluated. Porosity, it turns out, can be a powerful ally if properly taken advantage of. Systems like filters, catalytic membranes, insulators and bio-active scaffolds not only benefit from porosity but rely on it for their core functions [15]. Porous ceramics can be designed to combine several advantages inherent to their architecture [1]. They are lightweight, can withstand high temperatures and possess high specific strength, particularly in compression [16]. Subtle distinctions in the type, amount or distribution of porosity can have dramatic effects on the function and behavior of porous ceramics. To begin to draw meaningful insight into the role of porosity in multifunctional ceramics it is important to first understand what porosity is, in what forms it may manifest and how it is classified.

2.1.1 Classifying and Quantifying Porosity

The simplest and possibly most influential, measure of porosity is the *total porosity*. That is, the volume fraction of an object that is occupied (or not occupied depending on your preference) by void space. The total porosity is a gross measurement of how dense a sample is relative to its theoretical density (density without any pores). Properties like heat capacity and dielectric constant can be directly related to total porosity without knowing anything further about the ceramic [17]. Other properties like mechanical and permeability characteristics can be indirectly related to the total porosity but for an accurate picture, further microstructural characterization is required. It becomes necessary to determine where pores are located, how many there are, as well as their size, shape and orientation.

Each pore can individually be further described as either open or closed (Fig. 2.1). *Open porosity* is made from pores that are accessible from the outside of the material, i.e. if the sample were dropped in water, the water could feasibly penetrate into these pores. *Closed porosity* is made from pores that are entirely encapsulated by the matrix material and therefore inaccessible [17]. As one might imagine, a water filter made from a completely closed pore ceramic would be highly inefficient since no water could penetrate the ceramic. Similarly, a hot-air insulating ceramic made using an open-pore architecture would be less than ideal since hot air could merely pass through.

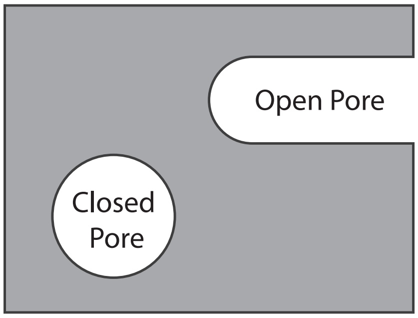

Figure 2.1: Open versus closed porosity.

An additional classification of porosity is whether or not a pore is *intrinsic* or *extrinsic*. Intrinsic pores are those that are inherent in a ceramic such as interstitial voids left between packed ceramic particles. By their very nature, these pores are smaller than the constituent parts of the surrounding matrix. Extrinsic pores on the other hand are those that are externally introduced into the system; usually by the addition and subsequent removal of pore-formers, graphite flakes, air bubbles or other additives (Fig. 2.2). Extrinsic pores are typically, although not necessarily, larger than the matrix constituents. Distinctions such as these can prove important as was shown by Shang et al. [18] who demonstrated that intrinsic and extrinsic pores behave differently under identical conditions. Under uniaxial compressive loading, intrinsic pores will actually align their long axes parallel with the axis of loading while extrinsic pores (above a certain threshold size) tend to align perpendicular to the axis of loading.

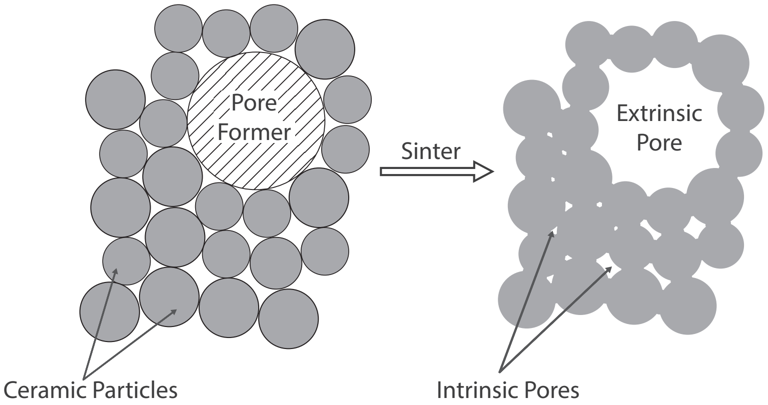

Figure 2.2: Intrinsic and extrinsic porosity in ceramics. The extrinsic pore evolves from the addition and burnout of some sort of pore-former. The intrinsic pores are simply the remaining interstitial spaces between packed particles.

Two more classifications which will be used extensively throughout this thesis are *anistropic porosity* and *hierarchical porosity*. Anistropic porosity means that some aspect of the pores (shape, location, size) is directionally dependent. Finally, hierarchical porosity occurs in materials where there are at least two distinct pore populations based on size. Often, the median pore size must be at least an order of magnitude different between the two for the microstructure to be considered hierarchical.

Beyond these basic classifications however, describing the porous microstructure of a ceramic becomes a complex exercise. There are infinite morphologies of porous ceramics. Pores can be rough and tortuous or smooth and straight. Pores can be spherical in shape or prismatic. Different pore morphologies have been shown to have a significant effect on both mechanical and non-mechanical properties so it is of the utmost importance to carefully classify porosity as objectively, and in as much detail as possible [19, 20]. Herein lies a core issue with porous ceramics. Apart from principal values like total, open and closed porosity, how does one quantitatively define a porous microstructure? Measurements as seemingly innocuous as pore size will vary from lab to lab and person to person because the metrology in the area of microstructure classification can be so subjective and ill-defined.

A method developed by Roy Rice [21] attempts to bypass the complexities of pore descriptions by essentially ignoring the pores and defining only the non-porous area. This method, called the minimum-solid-area (MSA) method [21] defines a geometric parameter equal to the minimum area fraction of solid normal to a given direction. Rice states that the properties of a ceramic (i.e. strength, permeability, resistance...) will be proportion to the MSA [22–24]. Unfortunately, methods such as the MSA method typically have a stringent set of assumptions meaning that they really only function well for ideal systems, something that porous ceramics are often not.

2.1.2 Effects of Porosity

It is difficult to summarize concisely the effect that porosity can have on various functions and properties, indeed that is the goal of this entire thesis, however there are some general trends which may be discussed. As porosity increases, there is typically an increase in surface area that may be used to enhance reactions [16], filter various physical/chemical products or in the case of a battery, increase the storage capacity [25]. Often accompanying an increase in porosity however is a decrease in mechanical and thermal stability [26].

In terms of the effect of porosity on material properties we can define three general categories (Table 2.1):

Table 2.1: Porosity Dependence of Properties [27]

	Dependence	**Effected Properties**
(I)	No dependence	lattice parameter, thermal expansion coefficient
(II)	<u>Amount</u> of porosity	density, heat capacity/volume, dielectric constant
(III)	<u>Amount</u> and <u>character</u> of porosity	mechanical, electrical and thermal properties, surface area, tortuosity...

There are properties which have no dependence at all on the porosity (I); lattice parameter, or thermal expansion coefficient for example. These are inherent to the material itself. Often times, for properties which fall into category (II), one can predict their value using a rule of mixtures:

$$X = X_s(1-P) + X_p P \tag{2.1}$$

where X is the property of the porous body given as a function of that same property for the solid phase X_s, the porous phase X_p and the total porosity of the system P. Using this expression, properties like heat capacity and density can be calculated without knowing anything further about the microstructure other than the total level of porosity. However, in most cases we are interested in properties which fall into category (III) which is where things become complicated and interesting. Take for example the property of permeability [17]. It is absolutely crucial that the character of the porosity be known, otherwise you could have a ceramic composed exclusively of closed pores or highly tortuous ones where fluids would be unable to penetrate or the flow rate would be insufficient. It becomes necessary therefore to include descriptions of spatial pore distribution, pore sizes as well as factors describing pore shape and to provide these in a quantitative manner [28].

2.1.3 Applications of Porosity

Porous ceramics are used in a wide range of multifunctional systems in fields ranging from electrochemical, thermal, structural, biological and others [29].

Ceramic waters filters for example are a commonly found application of porous ceramics. These systems can be inexpensive, highly effective and have excellent portability. A good example of such a filter can be found in the Lifesaver Systems line of water filters [Fig. 2.3 (a)]. Spurred into action by the tragic humanitarian crises following the Asian-Pacific Tsunami in 2004 and Hurricane Katrina in 2005, Michael Pritchard developed the Lifesaver bottle which uses a series of nanoporous ceramic filters to remove bacteria and turbidity from what was previously undrinkable water [30]. The London School of Hygiene and Tropical Medicine found that these inexpensive, lightweight water bottles could filter out nearly 100 % of bacteria and turbidity from water contaminated to levels far beyond those that would ever be naturally occurring [31]. This invention is potentially game-changing for disaster response, where access to water is often the most difficult and expensive human need to satisfy.

Bio-medical engineering has been a major driving force for technological development. This discipline has managed to bring together a number of disparate fields to perform scientifically impressive achievements. In 2003 for example, materials science researchers at the University of Illinois at Urbana-Champaign, along with surgeons, computer-designers and 3D artists were able to fabricate a porous ceramic jaw bone and successfully implant it into the mandible of an ailing 73-year-old woman. The porous ceramic was fabricated by 3D-printing hydroxyapatite, a material chemically identical to human bone [32]. The implant was specifically designed for the woman to fit her exact jaw bone, contour around nerves and provide the necessary porosity for bone ingrowth [Fig. 2.3 (b)]. The traditional process for such a procedure would have been to surgically carve a piece of bone out of the patient's hip, a dangerous and costly procedure.

The use of porous ceramics as thermal insulators is well known and has led to impressive technological advancements like the reusable space vehicle (ex. the space shuttle) [33]. This insulative capability can be taken to the extreme in a class of materials known as aerogels [Fig. 2.3 (c)]. Commonly made from silica, the porosity of these materials typically falls between 90 and 99.8+ %. Aerogels are prized for their impressive thermal insulating capabilities, specific strength and optical properties. They are made by taking a gel of silica, carbon or even alumina and putting it through a process known as supercritical drying. This removes the solvent without collapsing the gelled network [34].

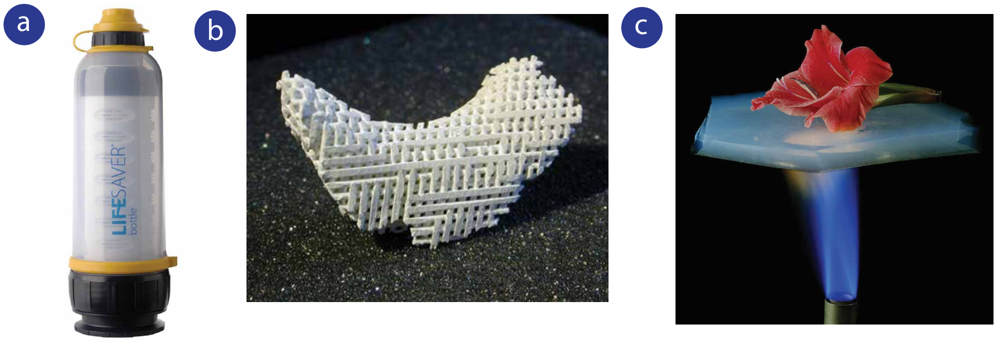

Figure 2.3: (a) Lifesaver systems^{TM} bottle [30]. (b) Porous ceramic jaw-bone implant made from 3D-printed hydroxyapatite [32] (c) Flower sitting atop a piece of aerogel suspended over an open flame. The superb insulative power of the aerogel protects the flower from burning up. Credit: NASA and JovanCormac.

Other notable uses for porous ceramics include high temperature gas separation membranes, electrodes in batteries, catalysis systems, solid oxide electrolysis cells and the electrodes of solid oxide fuel cells (SOFCs) [29].

2.2 Solid Oxide Fuel Cells (SOFCs)

2.2.1 Historical Background

In 1839, W. R. Grove, a well-known Welsh scientist, reported the first fuel cell or so-called *gas battery* (Fig. 2.4). The battery consisted of several pairs of separated gas containers, one for oxygen and one for hydrogen that were open on one end to the inside of a dilute sulfuric acid bath. Platinum electrodes connected alternating pairs in series and the entire system was then connected to two platinum electrodes submerged in an enclosed, water-filled gas vessel. Grove noted a constant current flowing through the system but of greater interest was that the water level decreased in the water vessel while the liquid level increased in each of the battery's cells. What Grove witnessed was the electrolysis of water caused by the recombination of hydrogen and oxygen gas itself inside the battery itself [35].

At the time, these observations sparked intense debate about the mechanisms behind such a reaction. Two distinct schools of thought arose to explain Grove's observations. The first, and more prevalent theory of the age, known as *Contact Theory* championed that the mere contact between two specific, dissimilar materials would give rise to a sort of electromotive force which would in turn drive the reaction. The second theory, *Chemical Theory*, maintained that it was chemical changes and affinities between materials which led to the observed electrical currents [36]. Interestingly enough, each theory contained a partial truth. Chemical reactions within the gas battery take place in the "contact" zone where the three phases: reactant, electrolyte and electrocatalyst meet [35]. This "contact" zone, or as Grove called it "notable surface of action" [13] turns out is the key to fuel cell function and has been the focus of intense research ever since (see section 2.2.4).

In the years following Grove's initial discovery, many scientists jumped on the proverbial "gas battery bandwagon" searching for that elusive design which would yield a highly efficient conversion ratio. It wasn't until the 1880s however that workable prototypes for gas batteries began to emerge from US and European laboratories. At this point in time though, fuel cells were a solution seemingly without a problem. Energy was cheap and readily available in coal [35]. This was the case at least until WWII when coal reserves dwindled and fears for energy security were high. Wartime brought with it a surge in fuel cell research. Sir Francis Thomas Bacon of Britain is noted for developing fuel cell technolo-

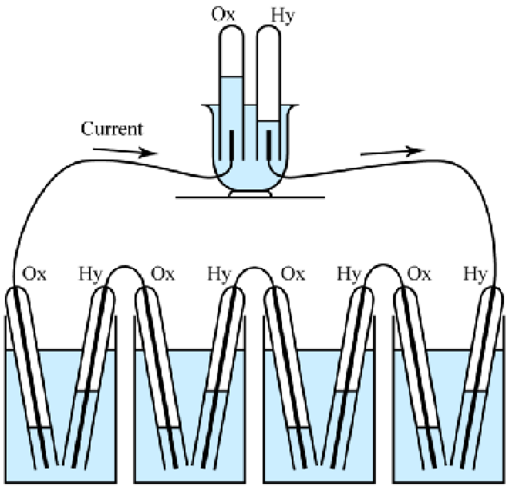

Figure 2.4: Grove's Gas Battery. The apparatus contained several beakers of dilute-sulfuric acid each one containing a tube of oxygen and hydrogen gas. Platinum electrodes in the tubes were connected in series and finally into a "voltameter" that was essentially a water-filled gas vessel with submerged platinum electrodes. Credit: mycoolelectric-car.com.

gies to replace the dangerous and highly volatile batteries used in Royal Navy submarines. Although Bacon's work was never fully implemented, the rights were purchased by Pratt & Whitney and later used for the Apollo space missions [37].

Since Grove's initial discovery in 1839, a number of fuel cell technologies have come to maturity:

- Polymer Electrolyte Membrane Fuel Cell (PEMFC)
- Alkaline Fuel Cell (AFC)
- Phosphoric Acid Fuel Cell (PAFC)
- Molten Carbonate Fuel Cell (MCFC)
- Solid Oxide Fuel Cell (SOFC)

Details concerning these five types of fuel cells are listed in table 2.2 [3]

The operating principles behind each of these fuel cell technologies is the same, essentially they physically separate the combustion of a fuel into separate oxidation and reduction reactions channeling ions across a selective electrolyte while electrons flow through an external circuit [3]. The defining difference between the cells is the type of electrolyte used

Table 2.2: Types of Fuel Cells

Type	Electrolyte	Temperature °C	Fuel	Applications
PEMFC	Sulfonated Polymer	70 - 110	H_2, CH_3OH	Mobile, Vehicles
AFC	Aqueous KOH	100 - 250	H_2	Air and Space
PAFC	H_3PO_4	150 - 250	H_2	Stationary Applications
MCFC	$(Na, K)_2CO_3$	500 - 700	Hydrocarbons, CO	Stationary Applications
SOFC	$(Zr, Y)O_{(2-\delta)}$	700 - 1000	Hydrocarbons, CO	Stationary Applications

and their respective operating temperatures. Low temperature fuel cells like PEMFC, AFC and PAFC are often used for low power or mobile applications such as powering a car or running a laptop since they are lightweight and highly scalable. Their low operating temperature however typically requires the inclusion of expensive catalysts to reduce the activation energy of the combustion reaction. Additionally, either highly pure hydrogen or methanol must be used so as to not poison the cells with impurities [13]. Due to their high operating temperatures MCFCs and SOFCs do not require the addition of expensive catalysts and they are able to reform many hydrocarbons into usable fuels without the need for external reforming systems. Their high operating temperatures however come with their own list of complex engineering challenges.

Solid Oxide Fuel Cells, which are the model system specifically targeted in this thesis, have their historic roots in 1899 following the discovery by Nernst of solid oxide electrolytes [13]. He quickly patented a mixture of zirconia doped with 15 mol. % yttria, a material quite similar to the one still in use today. In 1905, Haber filed the first patent on a fuel cell made with a solid oxide electrolyte, one using glass and porcelain. By the late 1930s, after many unsuccessful attempts, a Swiss scientist named Emil Baur and his colleague H. Preis demonstrated a yttria-stabilized zirconia fuel cell which successfully operated at 1000 °C. The high operating temperature and highly reducing atmosphere however led to serious material problems and despite a thorough search by Baur and other researchers [38], no suitable material replacements were found [13].

By the 1950s, solid oxide technology had begun to accelerate in places like the Central Technical Institute in the Hague, Netherlands, the Consolidation Coal Company in Pennsylvania and at GE in Schenectady, New York. These groups developed strong solid oxide programs but were thwarted by high internal resistance and short-circuiting due to semiconductivity of the electrolyte. Many scientists generally agreed that there were fundamental limitations to the conductivity of solid oxide electrolytes and agreed that molten carbonate cells had more short-term likelihood for success. Nevertheless, research in the

SOFC field continued and eventually, in 1962, researchers at Westinghouse demonstrated good cell performance based off a zirconium oxide and calcium oxide cell [38]. Continuing into the 1990s, Westinghouse furthered its research in SOFCs and in 1997 demonstrated a test cell that ran for nearly six months (4035 hours). Following testing, the cell was refurbished and operation resumed until an accumulated total of 16,612 hours (almost two years) was achieved. Indeed, testing was not stopped due to failure but rather because the program came to its end date. At the point of shutdown, the cell was providing 100 kW into the local grid with an overall efficiency of 46 %. Even after two years of operation, this efficiency was still higher than the average efficiency of a combustion generator (36 %) [13] and in addition, the fuel cell stack was concurrently providing 65 kWh worth of hot water into the local district's heating system [39].

As research has continued in this area, many engineering hurdles have been overcome and efficiencies are higher than ever. Commercial SOFCs represent a burgeoning field and companies like Bloom Energy and Mitsubishi Heavy Industries are pushing hard to make SOFC technology more competitive [40]. A rapidly developing market for SOFCs have been those which require "high-quality" uninterrupted power supplies like hospitals, airports and data centers where companies are willing to pay the high capital costs for the energy security that SOFCs provide [13].

Fuel cells offer a number of advantages compared with more conventional power sources. They are more efficient than thermo-mechanical energy conversion systems (ex. internal combustion engines and turbines) and they are especially attractive options in urban areas where localized pollution is problematic. SOFCs in particular are highly fuel flexible meaning that they can run off anything from hydrogen to biogas and landfill gases. They are also well suited for remote applications because they are reliable and low-maintenance and can be scaled to meet user needs ($<$ 10 Watts to $>$ 100 MW) [13]. Still, SOFCs are a niche market, and there are a number of issues to resolve before this technology becomes a more viable alternative to the status quo. However, with the increasing cost of energy, depleting fossil fuel reserves, as well as political and socio-economic instabilities worldwide it is more important than ever to restructure our current energy landscape. SOFC technology could be an important piece of that very complex puzzle.

2.2.2 The SOFC Principle

A Solid Oxide Fuel Cell (SOFC) is a solid-state electrochemical device that operates at elevated temperatures (700 - 1000 °C), converting fuel into electricity at efficiencies greater than 80 % when coupled with heat reforming systems [12, 13, 41]. This technology is highly desirable for its clean-burning operation, excellent fuel flexibility, reliability, quiet operation and high power outputs. Typically because of the numerous coupled auxiliary systems, SOFCs can be quite large and heavy. They are therefore more commonly designed for stationary, standalone, high-power applications such as office blocks, industrial factories or hospitals.

An SOFC system (stack) is composed of multiple cells and each cell is comprised of a dense ion-conducting electrolyte sandwiched between two highly porous electrodes (Fig. 2.5) [12, 42]. These porous electrodes facilitate the transfer of gases into and out of the electrode while at the same time providing the necessary surface area for electrochemical reactions to take place. Additionally, each electrode must conduct both electrons and oxygen ions often along separate pathways while maintaining mechanical and chemical stability at a range of temperatures and atmospheric conditions.

The elevated temperatures of an SOFC allow it to be self-reforming. This means that when a fuel, be it natural gas (CH_4), methanol (CH_3OH) or even heavier fuels like diesel ($C_{12}H_{28}$), are injected into the cell, they will be broken down into H_2 + CO, known as *syngas*, prior to reaching the anode. This self-reforming capability is a huge advantage of SOFCs over other fuel cells since it negates the need for complex and expensive reformation systems allowing the cell to be highly fuel flexible [13].

During operation, the fuel is electrochemically converted at high temperatures in the presence of oxygen. If hydrogen is used as the fuel, the overall reaction is (Eq. 2.2):

$$H_{2(g)} + \frac{1}{2}O_{2(g)} \rightarrow H_2O_{(g)} \tag{2.2}$$

In a typical gas turbine engine, this process runs at an efficiency of approximately 36 % with much of the energy losses due to the evolution of heat and sound [13]. A fuel cell separates the oxidation and reduction reactions from one another to maximize efficiency. Air is injected into a porous cathode where molecular oxygen is reduced to oxygen anions that are then transported through the dense oxygen-ion-conducting electrolyte to the

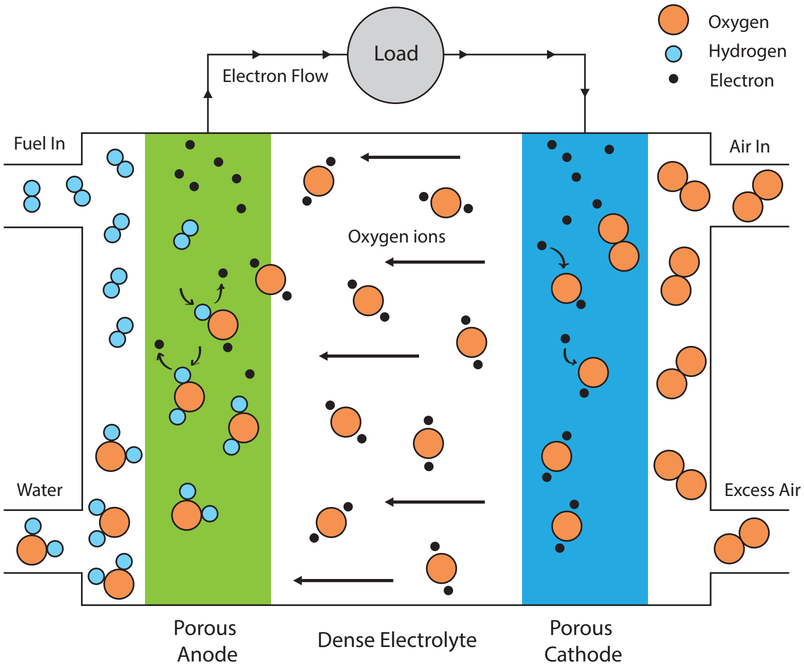

Figure 2.5: From right to left, diatomic oxygen is pumped into the cell where it is reduced to O^{2-} ions by the incoming electrons. The ions travel through the dense electrolyte towards the anode where they then oxidize hydrogen, creating water and releasing electrons back into the external circuit to perform work.

anode interface (Eq. 2.3) [14]:

$$\frac{1}{2}O_{2(g)} + 2e^- \rightarrow O^{2-} \tag{2.3}$$

Concurrently, fuel is injected into the anode side of the cell where it is oxidized by the following reaction (Eq. 2.4):

$$H_{2(g)} + O^{2-} \rightarrow H_2O_{(g)} + 2e^- \tag{2.4}$$

The electrons produced on the anode side of the cell are at a different potential than those consumed on the cathode side, creating a voltage potential available to perform work [12, 14]. By combining a number of these cells in either series or parallel, an SOFC stack capable of high power output is created.

2.2.3 Electrochemical Performance

The potential difference between those electrons produced on the anode side and those consumed on the cathode side of the cell is equal to the Nernst Potential (E):

$$E = E^o - \frac{RT}{zF} ln Q_r \tag{2.5}$$

where E^o is the standard cell potential calculated according to Eq. (2.6) as the difference in Gibbs free energy between the products and reactants of the fuel cell at standard temperature and pressure, z is the number of electrons consumed per mole reacted and Q_r is the reaction quotient. For the case of a H_2/O_2 fuel cell, $z = 2$ and $Q_r = \frac{p_{H_2} p_{O_2}^{0.5}}{p_{H_2O}}$:

$$E^o = \frac{-\Delta G^\circ}{nF} \tag{2.6}$$

Unfortunately, the potential actually available to perform work (V) is not equal to the Nernst potential, but the Nernst potential (E) minus all associated polarization losses across the cell (Eq. 2.7):

$$V = E - \overbrace{\eta_{act} - \eta_{ohm} - \eta_{conc}}^{\text{Polarization Losses}} \tag{2.7}$$

where η_{act} is the activation polarization, η_{ohm} is the ohmic polarization and η_{conc} is the concentration polarization [43].

- Activation (η_{act}) polarization represents all the necessary chemical reactions which occur in the cell and the various energy penalties (activation barriers) that must be paid [43].
- Ohmic (η_{ohm}) polarization accounts for resistances throughout the cell but is particularly effected by the ionic resistances within the electrolyte. If the ionic conductivity is enhanced, this loss will go down [3].
- Concentration (η_{conc}) polarization losses evolve from the practical limitations of mass transport of gases within the cell. The voltage losses are due to spatial variation in reactant and product concentration within the electrode possibly due to poor gas flow or uneven chemical conversion across the electrode. This loss is particularly rampant

in the anode where the anodic reaction produces steam, diluting the incoming fuel and causing inhomogeneities [43].

Because the maximum theoretical power at a given set of conditions is fixed by the Nernst potential, improvements in efficiency must by achieved by reducing these polarization losses. This has meant a great deal of research into cell/stack configuration, material enhancements, processing techniques and microstructural design. The porous electrodes in particular have been found to be highly sensitive to microstructural changes [14].

A key indicator of performance for an SOFC is the voltage output as a function of current density drawn [3]. This is also known as a polarization curve (Fig. 2.6). From the polarization curve, one can see that peak power is produced at relatively high levels of drawn current, before the effects of concentration polarization become significant [3]. The relationship between current and potential is nearly linear over a large range of current [2]. This region of the polarization curve is predominantly affected by η_{ohm} and it is here that SOFC operation is primarily targeted.

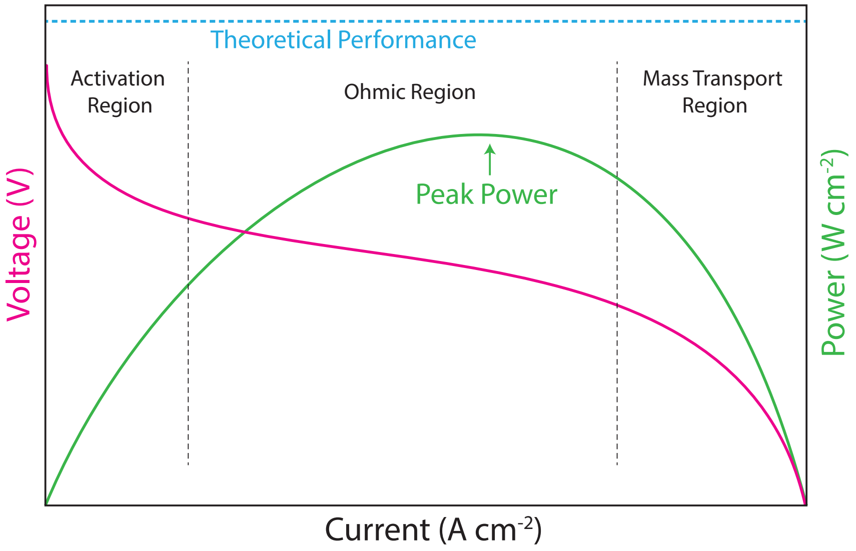

Figure 2.6: Model polarization curve showing approximate regions of activation, ohmic and mass transport (concentration) polarization.

Briefly, there are a few things which should be kept in mind to enhance electrochemical performance by reducing losses within the cell:

1. Design the cell so that gases easily diffuse in and out, reducing η_{conc} by preventing any buildup of reactant or product gases.

2. Reduce η_{ohm} by ensuring that the materials used have high conductivity, are as thin as possible, and relatively defect-free.
3. Ensure that necessary chemical reactions can happen easily and efficiently, lowering η_{act} as much as possible.

This third point is primarily accomplished through microstructure optimization and will be the focus of the following section.

2.2.4 Microstructural Requirements and SOFC Components

Microstructures of the individual SOFC components are complex and play a pivotal role in SOFC performance (as well as the performance of any type of fuel cell). The primary goal of the electrolyte is to form a selective barrier between the anode and cathode, allowing only oxygen ions to flow through. The primary objective of the electrodes is to facilitate the reaction of gases with ions and electrons.

All materials used within the fuel cell must be chemically and physically stable in their respective environments (high-temperature/oxidizing/reducing) but also be chemically and physically stable with materials that they are in contact with. They must possess appropriate conductivity, have similar thermal expansion coefficients, be low-cost, durable and easy to fabricate reproducibly. As one can imagine, the list of workable material combinations is a short one.

The most firmly established materials system for SOFCs is 8 mol. % yttria-stabilized zirconia (YSZ) as the electrolyte and the oxygen ion-conducting phase in both the cathode and anode, lanthanum strontium manganite (LSM) as the electron-conducting phase in the cathode and nickel-metal (Ni) as the electron-conducting phase in the anode. Lanthanum Strontium Chromite ($LaCrO_3$) is often used as the interconnect. These materials are chosen because they are stable at the temperatures necessary for SOFC operation, chemically compatible and their thermal expansion coefficients are close to one another decreasing the likelihood of delamination or cracking during thermal cycling [12, 14].

The Three-Phase Boundary and Percolation

It was W.C. Grove himself who very succinctly put into words a primary obstacle for achieving high-performance fuel cells.

> *"As the chemical or catalytic action...could only be supposed to take place...at the line or watermark where the liquid, gas, and platina met, the chief difficulty was to obtain anything like a notable surface of action."*
> *— W. R. Grove, 1842 [44]*

Grove of course was referring to his gas battery where he observed a reaction occurring at the convergence point of the platinum electrode with the dilute sulfuric acid and reaction gases. The reaction took place at the line where the three phases met [45]. In a three-dimensional system, when three-phases meet, they will always do so as a line. It becomes complex therefore to achieve high reaction densities because we are unable to create "surfaces of action" only "lines of action" which scale linearly as opposed to parabolically.

Today, these "lines of action" are termed *Triple Phase Boundaries* or TPBs. These are the locations where the porous gas-conducting phase meets the electrolyte (ion-conducting) and electrocatalyst (electron-conducting) phases (Fig. 2.7). To enhance performance, it is imperative to maximize the number of these junctures; however, it is equally crucial that there be continuous networks, known as percolation paths, from each TPB to both the electrolyte and current collectors of each electrode [12, 46]. An isolated TPB, that is, one that is unconnected to one or more percolation paths, will reduce the overall efficiency of the SOFC since the evolved electronic and/or ionic species will be unable to migrate through the electrode [46, 47].

An easy metric for defining the number of TPBs is known as the TPB density d_{TPB}:

$$d_{TPB} = \frac{\sum^{TPB} l_{TPB}}{V} \tag{2.8}$$

where d_{TPB} is equal to the cumulative length of all each TPB (l_{TPB}) over the sampled volume (V) of material. One must take caution however when citing TPB densities since often times this number is a gross calculation that does not take into account the fact that some TPBs are inactive due to incomplete percolation pathways or inadequate gas access. For this reason, the number should be scrutinized carefully.

The microstructural requirements of SOFC electrodes pose a unique challenge for researchers who must always attempt to maximize the number of junctures while maintaining complete percolation of the three separate phases in the electrode. In the middle of the 19th century, scientists realized that to maximize efficiency of their fuel cells, the best way was to use a large pore size distribution [44] and very often, this is still the methodology employed for many fuel cell electrodes.

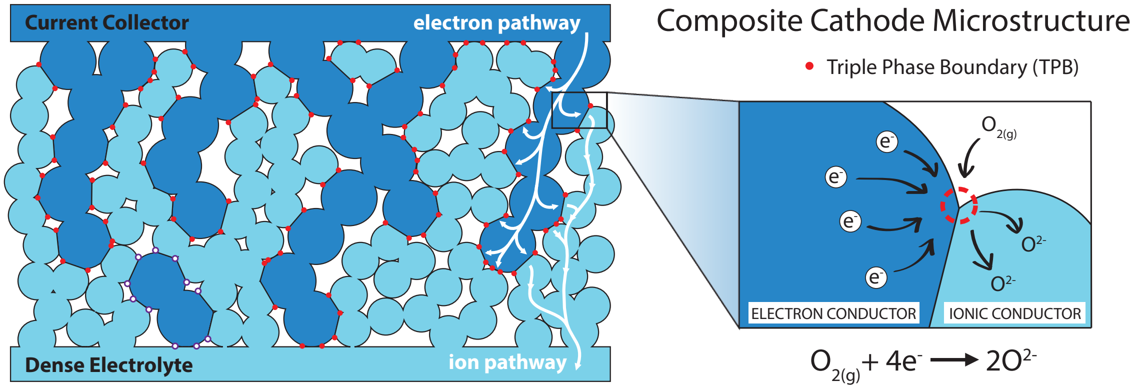

Figure 2.7: Schematic composite cathode microstructure showing both the electron conducting phase (dark blue) and the ion-conducting phase (light blue). An inset (right) demonstrates the triple phase boundary concept. White lines depict potential percolation paths from the current collector and electrolyte to the TPBs.

Electrolyte

Although the focus of this thesis is on modifications to the porous electrodes, it is prudent to start with the solid oxide electrolyte since it lends its characteristics to both electrodes. Additionally, the operating temperature of the cell is governed by the electrolyte whose oxygen ion conductivity is nearly always limiting [13]. SOFC electrolytes, like all SOFC components, have multiple functions. Firstly, it is responsible for conducting ions (and blocking electrons) from the cathode to the anode. Secondly, the electrolyte must prevent any leakages of gas from one side of the cell to the other. Any leaks, of gas or electrons would short-circuit the cell, drastically reducing efficiency. Often times, the electrolyte is also used as a mechanical-support for the cathode and anode layers. Since the electrolyte bridges the cell, it is exposed to both oxidizing and reducing atmospheres and must be compliant with whatever material is used on the cathode and anode sides. The most common SOFC electrolyte is yttria-doped zirconia, not so different from the composition used by Haber et al. in 1905. This material has sufficient ionic conductivity, is electrically-insulating, abundant, low-cost, easy to fabricate, stable at a variety of temperatures and atmospheric conditions and relatively non-reactive with the materials typically used in an SOFC [13].

Pure zirconia (ZrO_2) is monoclinic at room temperature, transitioning to tetragonal above 1170 $^\circ C$ and then to a cubic structure above 2370 $^\circ C$ with an associated 3 - 5 % volume change going from monoclinic to tetragonal [48]. Doping the zirconia with yttria, or another aliovalent oxide ($Sc_2O_3, CaO, MgO...$) stabilizes the zirconia into a cubic fluorite structure that remains stable from ambient conditions up to 2680 $^\circ C$ (Fig. 2.8). Doping has the additional benefit of increasing the oxygen ion vacancies (Eq. 2.9), significantly increasing ionic conductivity by the following reaction:

$$Y_2O_3 \overset{ZrO_2}{\Longleftrightarrow} 2Y'_{Zr} + 3O^x_O + V^{\cdot\cdot}_O \tag{2.9}$$

Here, Y_2O_3 is doped into a ZrO_2 matrix resulting in trivalent Y^{3+} substituting into a Zr^{4+} site with an apparent negative charge Y'_{Zr}, leaving three oxygen lattice ions O^x_O and one vacancy at an oxygen site with a double positive charge $V^{\cdot\cdot}_O$. It is the existence of these oxygen lattice vacancies which enhances the ionic conductivity of YSZ. Oxygen ions are transported through the structure by "hopping" from vacancy site to vacancy site (vacancy diffusion). The concentration of these vacancies, and therefore the oxygen ion conductivity is given by the dopant level. Studies have been performed to determine the optimal level of doping for YSZ [48]. If too low, the zirconia is only partially stabilized and still able to phase transition, if too high, the ionic conductivity significantly drops due to defect ordering and vacancy clustering [13]. The maximum oxygen ion conductivity occurs at the minimum dopant level necessary to stabilize the cubic fluorite phase [48]. Typical values used will be between 6 and 10 mol. % yttria with 8 mol. % (8YSZ) being the most common. 8YSZ is fully stabilized, has good ionic conductivity and negligible electronic conductivity.

As mentioned early, it is possible to stabilize ZrO_2 with a number of potential dopants. In 1992, Badwal et al. [48] demonstrated the effect of various dopants on the conductivity of pure zirconia. They found that dopants whose cations were closest to the size of zirconia

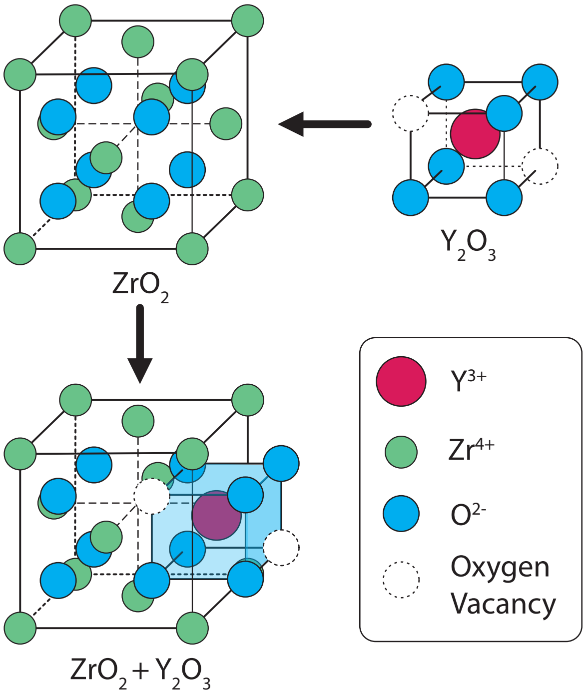

Figure 2.8: Stabilization of ZrO_2 with Y_2O_3 into the stabilized cubic fluorite structure.

achieved the highest conductivity. This can be explained by steric blocking effects. Conductivity tests showed that both Sc^{3+} and Yb^{3+} performed better than Y^{3+} but due to cost constraints, yttria has become the dopant of choice.

Advanced zirconia powders with small size distributions are now readily available. These powders pack sufficiently well to allow full densification at low sintering temperatures allowing research labs more flexibility when sintering their cells [13]. There is a trade-off however involved with using very fine powders as ionic conductivity tends to decrease with decreasing grain size [48].

Because of the high temperatures needed to achieve adequate ionic conductivity of YSZ, there is a concerted effort to find new materials to be used for the SOFC electrolyte. Some of the more promising candidates include gadolinia-doped ceria (CGO), lanthanum-gallate based oxides (LSGM) and scandia-doped zirconia. These new materials possess increased ionic conductivity compared with YSZ but typically are more reactive and less stable in operation. LSGM for example, when used with nickel oxide (NiO), a commonly used anode material, can react to form La-Ni-O insulating phases which gather at the electrolyte/electrode boundary and lead to decreases in conductivity and deterioration of the interface [2].

Cathode

The cathode is responsible for reducing the incoming oxygen into ions by enabling electron flow from the current collector to the TPBs. The cathode must possess high electronic conductivity (> 100 S cm^{-1}) to prevent ohmic losses [14]. Because of the highly oxidizing atmosphere and high operating temperatures, the material choices are limited to conducting oxides and noble metals. For economic reasons therefore, the cathode material is nearly always a conducting oxide and the most common ones are lanthanum manganites doped with a divalent ion like strontium (LSM) as shown in figure 2.9.

$$La_{(1-x)}Sr_{(x)}MnO_3 \tag{2.10}$$

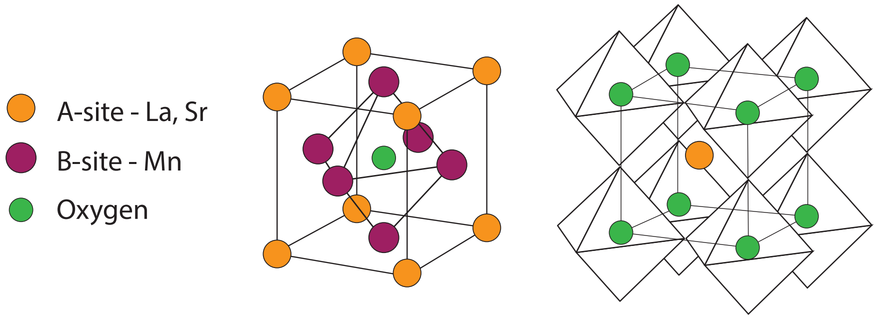

Figure 2.9: Perovskite crystal structure of LSM.

LSM is a perovskite material with intrinsic p-type conductivity that derives from cation vacancies in the perovskite structure [13]. This materials has the standard ABO_3 formula with the large cation (La, Sr, Ba, Ca) occupying the A-site and the small cation (Mn, Co, Fe, Ti, Zr) occupying the B-site. LSM shows excellent electronic conductivity and negligible ionic conductivity at high temperatures. Additionally, LSM has a suitable thermal expansion coefficient for use with YSZ electrolytes. The conductivity of LSM can be altered by doping the A or B sites with divalent cations (i.e. calcium, strontium, barium...). Conduction within LSM works by a small polaron-hopping mechanism [13].

During cell operation the reaction within the cathode is [49]:

$$O_2(g) + 4e^{'} + 2V_O^{\cdot\cdot} \xrightarrow{TPB} 2O_O^x \tag{2.11}$$

Oxygen in the form of air is pumped into the cathode. The oxygen is reduced at the TPBs by incoming electrons traveling through the LSM network. The oxygen ions are then incorporated into the electrolyte phase (typically YSZ) and travel by vacancy diffusion towards the anode side of the cell.

SOFC cathodes are often made by mixing the electrolyte (YSZ) and electrocatalyst (LSM) phases together. The idea being that by creating a composite, you are essentially extending the electrolyte/cathode interface, increasing the number of TPBs. To achieve percolation of the ionic and electronic conducting materials within the cathode, the electrolyte and electrocatalyst phases must be properly dispersed throughout the porous microstructure. If both the ionic and electronic conductors had the same particle size and conductivity, the ideal volume ratio for maximum electrochemical performance would be 50:50 since there would be an even distribution of both phases. Since however, the conductivity of YSZ is more than 100 times slower than that of LSM, a 40:60 volume ratio of LSM:YSZ has been shown to increase cell performance by decreasing ohmic losses while still maintaining percolation of both the electron- and ion-conducting networks [47, 50].

In practice, there are typically two cathode layers employed in an SOFC cell. The first one is the previously mentioned composite LSM/YSZ composite which is applied and fired so as to remain highly porous. It is in this region of the electrode that the physical cathodic reaction occurs, therefore surface area and porosity must be high. The second cathode layer is typically pure LSM and functions essentially as a current collector. An additional benefit from this setup is that by having a composite layer sandwiched between the pure, dense electrolyte and current collector, there will be a more gradual step-down in thermal-expansion mismatch than if pure LSM was used for the entire cathode [13].

Although, LSM does satisfy a number of the criteria required for a good SOFC cathode material, it does have its downsides. At high temperatures ($>$ 1250 °C) LSM is prone to forming undesirable phases such as $La_2Zr_2O_7$ and $SrZrO_3$ at the boundaries between the LSM and electrolyte phases [2]. These phases are highly insulative, decreasing electrochemical performance. Additionally, although the high-temperatures used during SOFC operation ensure sufficient conductivity, it can result in coarsening of the LSM grains, reducing surface area and therefore TPB density.

Another material which has been highly researched is doped lanthanum cobaltites. Like lanthanum manganites, $LaCoO_3$-based materials possess high levels of intrinsic p-type conductivity. The conductivity can be enhanced with the addition of divalent ions on the lanthanum site (Sr is often used) and even further enhanced by substituting iron (Fe) in the cobalt site $La_{(1-x)}Sr_xCo_{(1-y)}Fe_yO_3$ to make LSCF. This material has superior conductivity compared with LSM however it also has a higher chemical reactivity with zirconia-based electrolytes and is more susceptible to reduction at high temperatures. It is most commonly used as the cathode material in Intermediate-Temperature SOFCs (IT-SOFCs) [51].

Anode

The anodic reaction in an SOFC, regardless of the fuel used, occurs when oxygen ions traveling across the solid oxide electrolyte oxidize the incoming fuel producing water vapor, electrons and heat. As in the cathode, these reactions take place at the TPBs where the electrolyte, electrocatalyst and gases all meet. All three phases must have adequate conductivity and phase percolation for the electrode to function.

The fuel used is often reducing in nature so metals are typically adopted as the anodic material [13]. Still, the metal must be resistant to oxidation and corrosion under operating conditions ($> 700\ ^{\circ}C$) essentially limiting the choices to nickel, cobalt or the noble metals. For cost-cutting measures, the majority of SOFC anodes are made from nickel. Commonly this is done by creating a cermet from powders of yttria-stabilized zirconia (electrolyte) and nickel oxide. The powders are then partially sintered together and the nickel is reduced to nickel-metal creating interconnected and interpenetrating networks of YSZ and nickel [52].

The anode must maintain a high level of porosity to facilitate gas flow into and out of the cell and additionally provide significant active surface area for the anodic reaction to occur. Normally however this requirement proves trivial to satisfy. If using a nearly dense composite mixture of 66 wt. % NiO with 34 wt. % YSZ, reduction from NiO to Ni-metal results in a microstructure with approximately 50:50 vol. % Ni-metal and YSZ with 35 vol. % porosity due to the non-negligible volume change which occurs during reduction.

The nickel metal particles form a network around the YSZ skeleton so even though there is a significant volume change from the reduction of NiO to nickel, macroscopically there is little shrinkage since the YSZ skeleton remains intact. This structure achieves percolation of each phase but is however highly susceptible to re-oxidation.

RedOx Cycling of SOFC Anodes

Reduction-oxidation cycling (RedOx) poses a significant bottleneck to the advancement of SOFC technology [52, 53]. The reason being that during operation, Ni particles can re-oxidize, expanding in volume by up to 66 %, severely damaging the brittle ceramic microstructure [54] (Fig. 2.10).

Ideally, once the anode is in its reduced state, it will never see any oxidation. In reality, there are a number of potential causes for reoxidation of the anode [52]:

1. Under high currents, the local oxygen partial pressure in the anode can increase up to a critical value if reaction kinetics are slow enough at the TPBs to allow for a build-up of oxygen or water vapor.
2. Oxygen partial pressure can increase near the compressive seals of the cell eventually causing micro-leaks into the anode.
3. There is an interruption in the fuel supply producing a build-up of unreacted oxygen anions at the anode.
4. The fuel cell is shutdown without first filling the anode with a protective gas.

Using SOFC-wide safety systems, many of these more accidental causes of redox cycling can be avoided. The fact remains however that redox cycling is still a risk since even a single or partial cycle can produce irreversible damage to the entire system [52]. A significant amount of effort has therefore been spent trying to understand the conditions when and how redox cycling occurs.

In 1996, Cassidy et al. [54] reported the first data on shrinkage and expansion of Ni-YSZ anode-supported cells. In addition, they measured open circuit voltages and determined how cycling affected electrochemical performance of SOFC half-cells. They found that during the initial reduction of NiO to Ni-metal that there was a 40 % reduction in volume whereas the first reoxidation resulted in a 66 % volume expansion of the nickel phase [54]. Later works by Tikekar et al. [55] helped to establish some of the oxidation kinetics for the Ni-YSZ system. The oxidation of Ni is a thermally-activated process which generally follows an Arrhenius relationship. It turns out however that nickel oxidizes by different mechanisms depending on the temperature and partial pressure of oxygen present. At intermediate temperatures ($\sim$ 600 °C), *homogeneous oxidation* occurs throughout the anode and the reaction follows a parabolic curve with time, indicating a diffusion-controlled process, proportional to $exp(-E_a/RT)$ [55]. Under these conditions, oxidation is limited by solid-state oxygen diffusion through the oxidized layer with an effective diffusion coefficient of $10^{-7} cm^2\ s^{-1}$ [55]. At higher temperatures (800 - 950 °C), oxidation appears to be a gas-diffusion controlled process where the diffusion coefficient is proportional to $T^{-3/2}$ [56]. This heterogeneous oxidation process manifests itself as surface oxide layers which form and then move inwards through the anode.

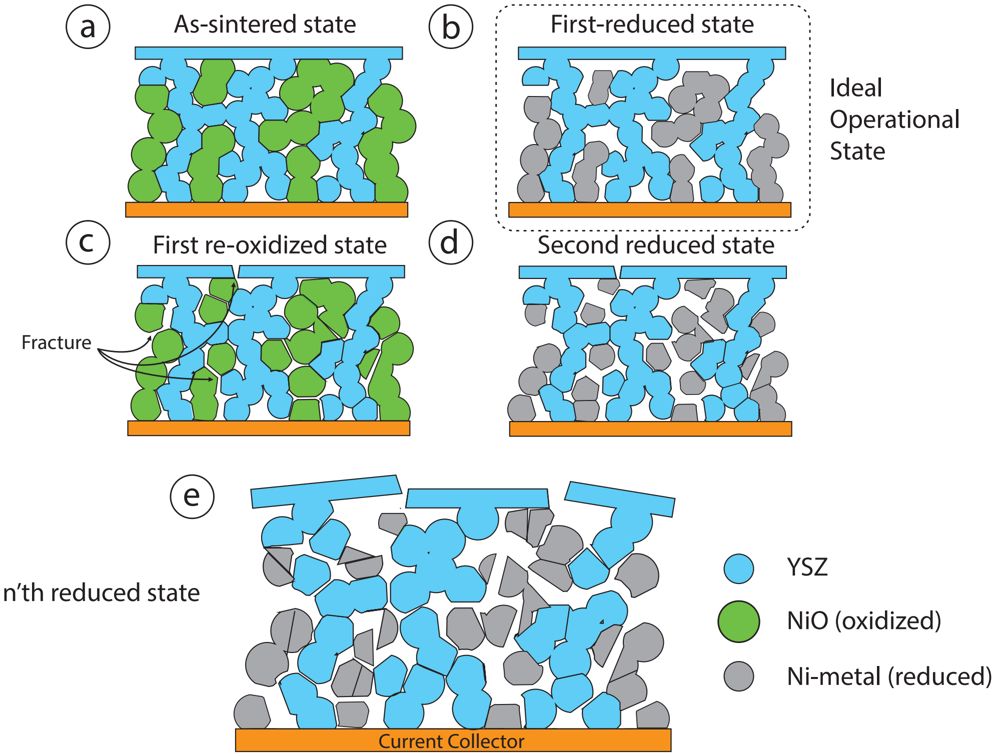

Figure 2.10: Schematic of RedOx cycling for a Ni-YSZ anode.

Whether an anode oxidizes homogeneously (low-temp) or heterogeneously (high-temp) turns out has serious implications on its properties. Homogeneous oxidation is typically a slower process producing even volume changes within the cell. Heterogeneous oxidation leads to warping or bending of the composite sample at the border between oxidized and reduced regions. Using half-cell configurations, Ettler et al. concluded that heterogeneous oxidation will result in a cell bent towards the anode while homogeneous oxidation results in curvature in the opposite direction, towards the electrolyte. Both processes however are detrimental to the cell [57].

Multiple redox cycles eventually lead to rapid deterioration of the anode structure due to the opening of further porosity (allowing greater diffusion) and microcracking of the ceramic support (Fig. 2.10). Interestingly enough, it has been shown that during the initial few redox cycles, it is possible to actually gain mechanical and electrochemical performance due to stiffening of the structure and opening of the nickel phase which initially increases TPB length. Once residual stresses become too high however, cracks in the electrolyte will cause gas leaks and the cell will fail (Fig. 2.11). It has been shown that in an anode-supported cell, an expansion of only 0.2 % will lead to cracks through the electrolyte [52]. Because, most SOFCs are currently anode-supported (allowing the use of the thinnest possible electrolyte [2]), they are especially sensitive to redox cycling [52].

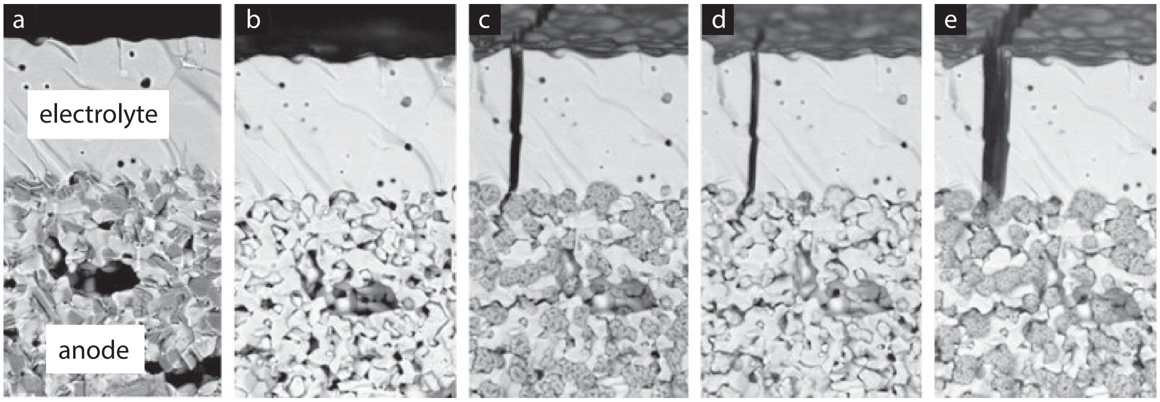

Figure 2.11: scanning electron microscope (SEM) images of microstructural changes on an anode and substrate due to reduction/reoxidation cycles: (a) initial co-fired state, (b) reduced, (c) reoxidized, (d) re-reduced, (e) re-reoxidized [57]

.

2.2.5 SOFC Architectures

To get the high current and/or voltage outputs required for SOFC applications, cells are combined into stacks which are connected in parallel (increased voltage), series (increased current) or a combination of the two. Numerous SOFC configurations have been developed including planar, tubular, monolithic, single-chamber and bell-and-spitgot [58]. The different architectures have advantages over one another for various applications. The main difference between the various configurations is the current path, gas flow and connections between cells (interconnections). Often times, the chosen stack configuration is dictated by performance criteria and cost constraints. The most common stack architectures used are tubular and planar [58]. Tubular SOFCs typically consist of a number of individual cells connected to a fixed support (Fig. 2.12). The tubes are closed on one end and open at the other. Oxidizing gases flow within each tube while fuel circulates around the outside of each tubular cell. The advantage of tubular SOFCs is that their small radius reduces the impacts of thermal gradients compared with large planar cells [12, 59]. Planar cells are often used in research because they are easily processed and scalable (Fig. 2.13). Additionally, the tools needed to process planar fuel cells can be readily procured for small-scale lab output. These cells can be electrolyte-, anode-, or cathode-supported making them highly flexible.

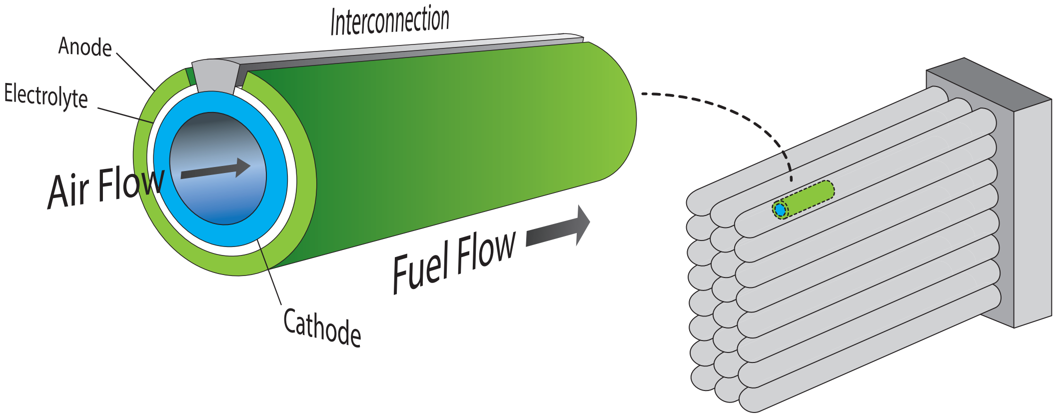

Figure 2.12: Schematic of a tubular SOFC stack. Groups of tubular SOFC cells are connected to a central support providing both the oxidizing gas and fuel as well as electrical connections. Each cell is electrically connected through their interconnections.

2.2.6 SOFC Cell Processing and Issues

The most common processing techniques for fabricating SOFC electrodes are screen-printing, tape-casting, dip-coating and spin-coating [2, 51, 59, 60]. In screen-printing, a ceramic slurry is loaded into a hopper and then dragged across a stencil using a squeegee or doctor blade. Using this method, thin layers are formed which are typically fired individually before the application of the next layer. Tape-casting is a well-known colloidal-shaping technique used to make thin-layers ranging from 20 μm to a few millimeters in thickness [61]. Using a doctor blade, the mixture containing the ceramic powder, solvent and binder is drawn over a carrier film. Subsequent drying and shaping is then performed if required. Many layers can be built up upon the same tape. This method produces high outputs needed on the industrial scale [61]. Dip-coating involves taking a substrate, often the thin, dense electrolyte and dipping this into a solution containing the cathodic or anodic mate-

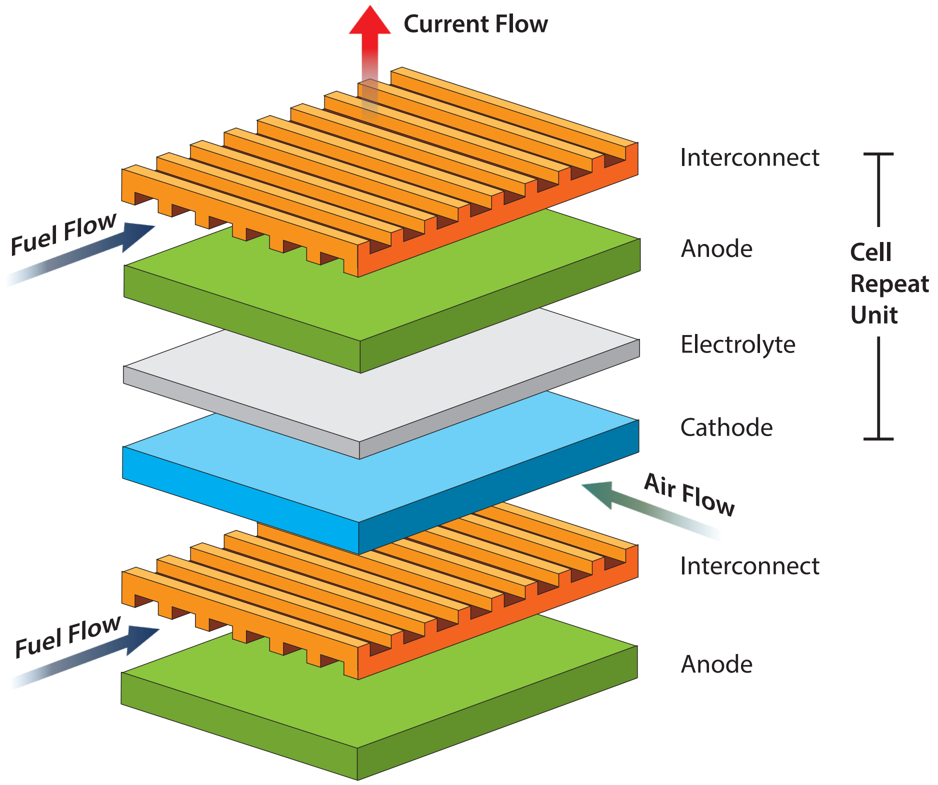

Figure 2.13: Schematic of a planar SOFC stack. Many cell repeat units (Cathode, Electrolyte, Anode, Interconnect) are stacked together to form an SOFC system.

rials and then slowly withdrawing the electrolyte back out with the clinging electrode film now attached [62]. Depending on the surface tension of the liquid and the rate of withdrawal, the thickness of the produced electrode can be controlled. Finally, spin-coating involves dropping the desired ceramic suspension onto a spinning substrate. The suspension spreads outwards and depending on the viscosity and surface tension of the slurry along with the RPMs of the substrate, the thickness of the deposited layer can be controlled [2].

The main issue with the aforementioned methods is that the produced SOFC electrodes suffer from a lack of microstructural control at different length scales [2, 42]. Each method typically uses fugitive pore formers to add the required porosity for gas percolation [59] and the isotropic microstructures which result tend to have highly tortuous gas and percolation pathways which hinder gas flow and lead to reduced electrochemical efficiencies [47]. In addition, the resulting structures, though highly porous, have isotropic mechanical and thermal properties and possess no preferential directionality for gas flow. In contrast, both gas flow requirements and mechanical stresses experienced within an SOFC electrode are normally anisotropic in nature [12]. For example, in a typical anode-supported planar SOFC, both the stresses and gas flow requirements are perpendicular to the SOFC face [63].

Thermal expansion mismatch and unequal sintering are both concerns that must be addressed when developing SOFC systems. If the thermal expansion of any layer is significantly different than another, stresses can develop during sintering, cooling or operation that lead to cracking and delamination of the layers. This is a material problem and usually is addressed either through material selection or by grading a composite so that the thermal expansion coefficient gradually changes instead of an abrupt shift [13]. Unequal sintering can also cause delamination of the layers when one layer, the cathode for example, shrinks to a greater extent than the anode or electrolyte. Curvature of the cell after sintering is a tell-tale sign of sintering mismatch.

A chief concern for today's SOFC is to lower the operating temperatures (600 - 700 °C), thereby decreasing some of the complications and high-costs incurred when operating at high temperatures. Lower-temperature operation would help to slow some of the microstructural degradation which is seen at elevated temperatures [42] and in addition lower the material costs associated with high-temperature seals and interconnects. Other than finding better materials, the only way to reduce operating temperatures is to reduce the three polarizations losses. This can be most effectively accomplished through microstructural optimization.

Various novel electrode processing techniques have been attempted for SOFC electrodes and some have shown great promise as potential replacements for isotropically processed materials [42, 63–66]. These attempt to enhance performance by increasing TPB density and gas flow while providing enhanced stability to the cell [8, 63]. One particularly flexible technique for tailoring microstructures is called the sacrificial-template method which was used by Ruiz-Morales et al. [42] to make SOFC cells. Using a hexagonal polymer mesh (NOMEX), researchers created a dense YSZ-backbone by dip-coating the mesh in a ceramic slurry and allowing it to dry. The coated template was then heated to burn out the polymer template and densify the remaining ceramic. Researchers subsequently infiltrated cathodic and anodic materials on either side of the honeycomb electrolyte. The honeycomb YSZ-backbone enhanced mechanical strength of the cell and because of its unique shape researchers were able to reduce the amount of required anodic and cathodic active materials by 70 % [42].

Although there has been considerable progress in the SOFC field within the last few decades, significant challenges remain before this technology can be adopted on a large scale. SOFCs remain expensive to build and operate. Their operation must become more reliable, a factor which has been shown to be correlate directly with electrode microstructure performance [66–68].

2.3 Creating Architectured Porous Microstructures

An architectured microstructure is one that is specifically designed, controlled and tailored for its particular application and whose properties are enhanced when compared to an unarchitectured microstructure. A plethora of examples exist in nature where materials which have the same chemical make-up exist as drastically different structures, each suited to a specific climate and task (Fig. 2.14). Humans frequently attempt to mimic these structures with limited success but in doing so, we have gained significant insight into how nature builds smarter materials. Often, it seems that these architectured microstructures benefit from an inherently hierarchical nature. That is, they are patterned on multiple length scales. A gecko's ability to adhere itself to surfaces for example is often attributed to the hierarchical and fibrillar structure on its foot pads [Fig. 2.14 (c)]. The hierarchical nature provides the necessary compliance and high-surface area required for attachment [69]. The predominant material found in these pads is a hard protein called $\beta - keratin$ which coincidentally is the same material found in the shafts of feathers, cat claws, and porcupine quills all of which have significantly different properties that can be tied to their individual microstructural architectures. Nature also has created a number of architectured porous materials such as bone, wood and sea sponges among others.

2.3.1 Porosity Control

There are seven general categories in terms of porous ceramics [74]: (1) foam, (2) interconnected, (3-5) pores between particles, plates or fibers, respectively, (6) large-pore networks and (7) small-pore networks. Within these categories, ceramics with interconnected pores,

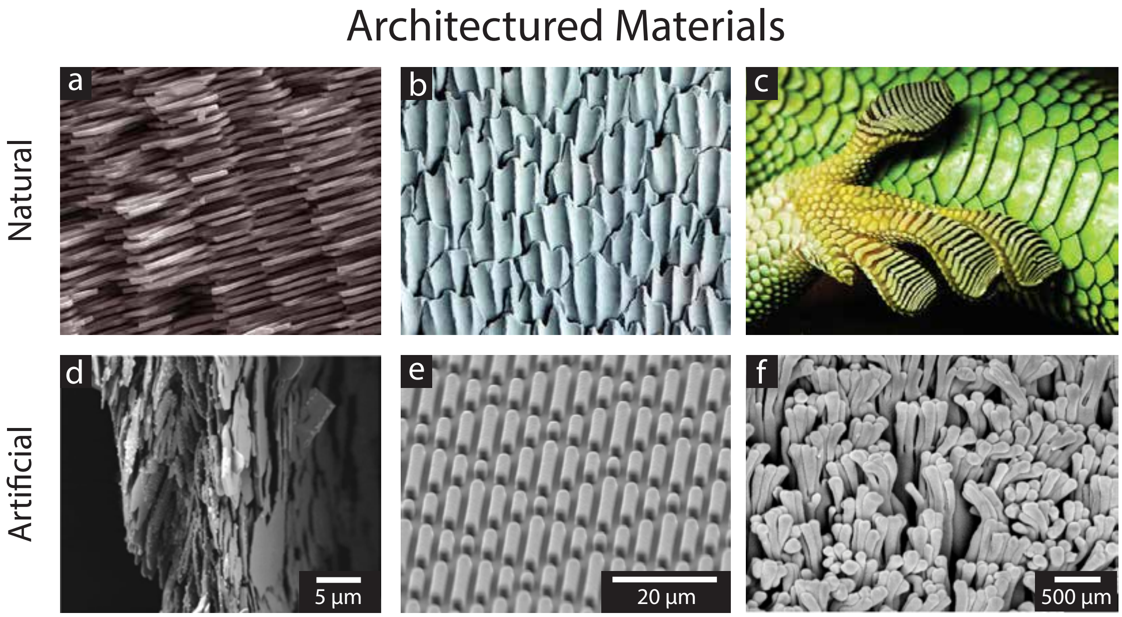

Figure 2.14: Architectured materials found in nature and their artificial biomimetic equivalents (a) Brick-and-Mortar structure of an Abalone shell (Photo by Sylvain Deville on Flickr) (b) Thresher-shark skin [70] (c) Gecko foot [71] (d) Nacre-like structure formed by ice-templating ceramic platelets [72] (e) Sharklet^{TM} textured coating made from silicon etching [73] (f) Nanofibril "gecko-feet" created by the nanoimprinting of a polymer substrate [69].

particularly those where the porosity is aligned into channels are recently attracting a good deal of attention because of their high fluid permeability and mechanical strength making them ideal for applications such as bone-scaffolds [75, 76], gas-membranes [9, 74] and potentially SOFC electrodes [8, 63]. Numerous different techniques have been developed for tailoring the porosity within a ceramic. These can for the most part be classified into six general processing methodologies which are used to create architectured porosity. These have been schematically depicted in figure 2.15. Briefly they are:

1. **Bottom-Up Techniques** - Begin with small building blocks, (ceramic particles or polymer spheres) and structure these into a larger monolith. Often times structure-directing agents like surfactants are used to order the packing of the bottom-up building blocks [77].
2. **Top-Down Techniques** - One can also start with a bulk material and use it to build an architectured porous structure by removing material from where porosity is desired [78].

3. **Phase Segregation** - Using some sort of suspension or solution, phase segregation is induced resulting in two or more distinct phases dispersed throughout the system. Often times, one of the phases will be subsequently removed, producing porosity [79].

4. **3D Printing** - Similar to a bottom-up technique, 3D printing is normally accomplished by taking a polymer or ceramic slurry and literally printing it in a layer-by-layer fashion. This relatively new technique has exploded in popularity in recent years and the new technologies allow for hithertofore unthinkable precision and control of microstructure [80].

5. **Emulsion Techniques** - A mixture is foamed through the evolution or addition of various gases. Owing to the surface tension of the bubbles, these systems can retain their foamed structure after calcination producing very high levels of porosity [15].

6. **Sacrificial Templating** - Often times, a natural or artificial material already exists that has a desirable architecture. These can be used as negative or positive scaffolds to generate architectured porous monoliths (ex. wood, bone, sponges) [64].

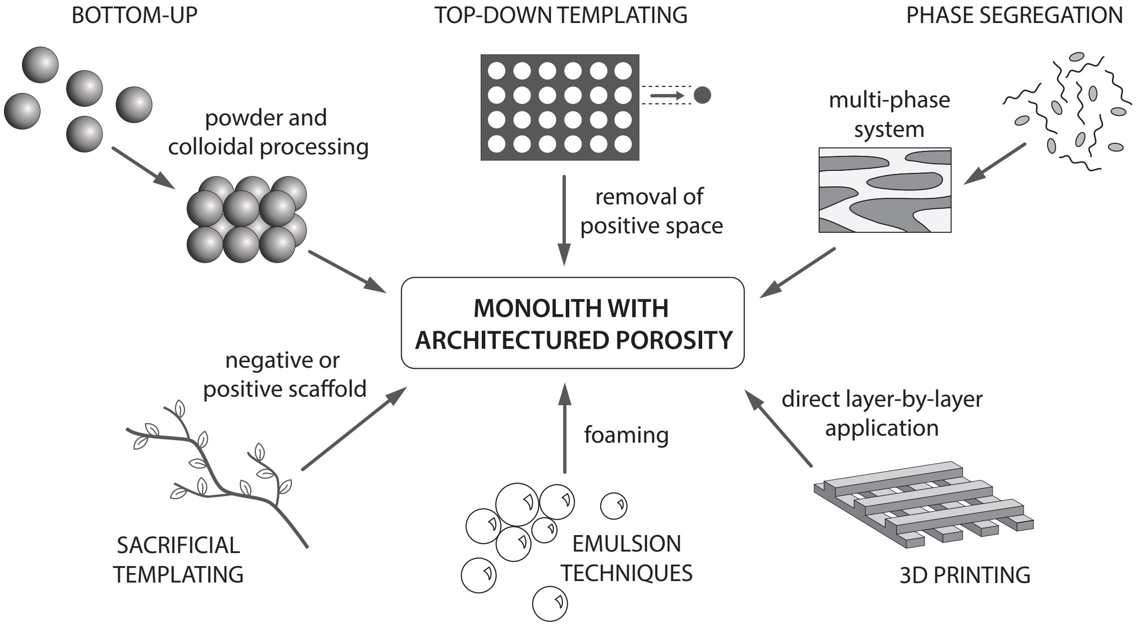

Figure 2.15: Generalized methods for architecturing porosity within ceramics. Adapted from Colombo et al. [16]

Fabrication processes based on these methods can be used individually or in combination with one another to generate architectured porous microstructures. Some example porous structures are shown in figure 2.16. Each of the shown microstructures is made using one of the six general categories discussed to show the broad range of structures possible.

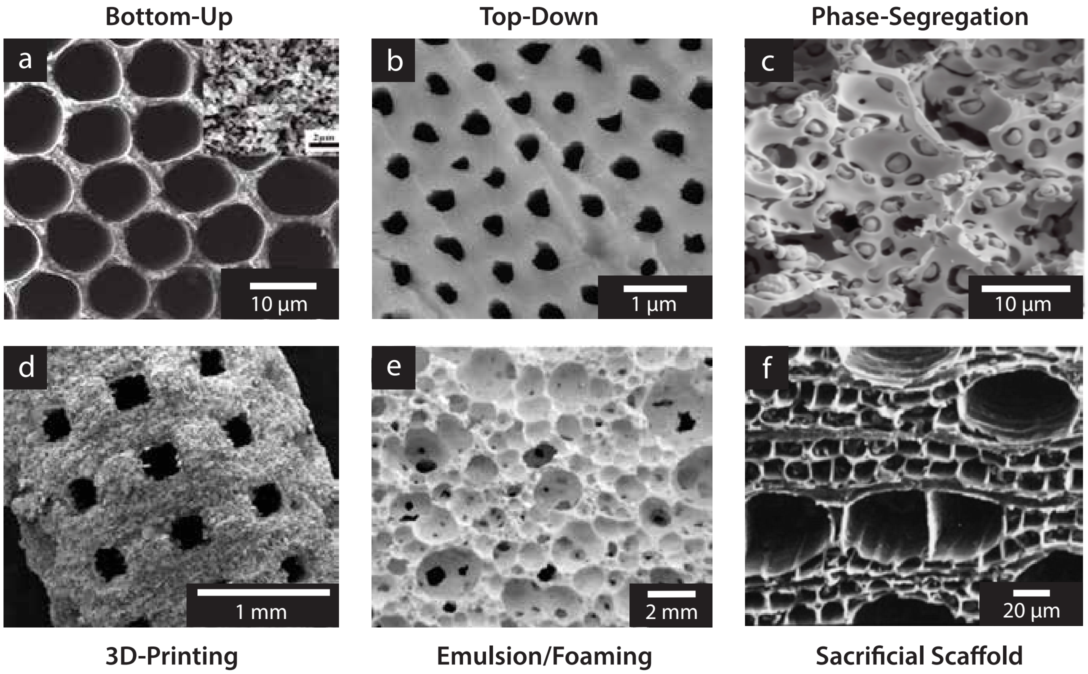

Figure 2.16: Architectured porous ceramics (a) Self-organized porous alumina [77] (b) Unidirectionally porous ZrO_2 prepared by selective etching [78] (c) Hierarchical ceramic from sol-gel process [79] (d) 3D-printed bone scaffold [80] (e) Particle-stabilized ceramic foam [11] (f) Porous ceramic from silicified wood [81].

The method most commonly used to fabricate SOFC electrodes is to incorporate a fugitive phase, or pore formers into a ceramic slurry before sintering[1] [82]. These pore formers, which are typically polymer beads or carbon particles, burn off during sintering leaving behind extrinsic porosity. By partially sintering the ceramic powder a hierarchical ceramic can be created with large pores left by the pore formers and small inter-particle (intrinsic) porosity left by partial sintering. This structure, though hierarchical, is isotropic, limiting the degree of microstructural control available to engineers. As has been discussed previously, it would be beneficial to have anisotropically porous electrodes to guide gases into and out of the cell, provide enhanced TPB density and provide mechanical stability [8, 63].

---

[1] This is a bottom-up technique in combination with sacrificial templating.

Techniques to evolve anisotropic porosity include filter pressing, where pressure is applied to a slurry containing fugitive pore formers thereby aligning the pore formers along an axis or by using alginate chemistry to develop tube-like pores [83, 84]. The technique that we have chosen to focus on to generate anisotropic, hierarchical ceramics is known as directional freeze-casting [85–87]. Also called unidirectional templating and freeze-gelation, freeze-casting is a combination of a bottom-up technique combined with phase segregation.

2.3.2 Freeze-Casting: The Basics

The first observation of cellular structures resulting from the freezing of water goes back over a century [88] but the first reported instance of freeze-casting in the modern sense was in 1954 when Maxwell et al. [89] attempted to fabricate turbosupercharger blades out of refractory powders. They froze extremely thick slips of titanium carbide, producing near net-shape castings that were easy to sinter and machine. The goal of this work however was to make dense ceramics. It wasn't until 2001, when Fukasawa et al. [90] created directionally porous alumina castings, that the idea for using freeze-casting as a means of creating novel porous structures really took hold. Since that time, research has grown considerably with 100s of papers coming out within the last decade [91].

Freeze-casting is the exploitation of the highly anisotropic solidification behavior of a solvent (generally water) in a well-dispersed slurry to controllably template a directionally porous ceramic [1, 43]. By subjecting an aqueous slurry to a directional temperature gradient, ice crystals will nucleate on one side of the slurry and grow along the temperature gradient. The ice crystals will redistribute the suspended ceramic particles as they grow within the slurry, effectively templating the ceramic. Once solidification has ended, the frozen, templated ceramic is placed into a freeze-dryer to remove the ice crystals. The resulting green body contains anisotropic macropores (extrinsic) in an exact replica of the sublimated ice crystals and micropores (intrinsic) found between the ceramic particles in the walls (Fig. 2.17). This structure is often sintered to consolidate the particulate walls and provide strength to the porous material.

Because freeze-casting is a physical process, the techniques developed for one material system can be applied to a wide range of materials [86]. Additionally, due to the inordinate amount of control and broad range of possible porous microstructures that freeze-casting can produce, the technique has found its niche in a number of disparate fields such as

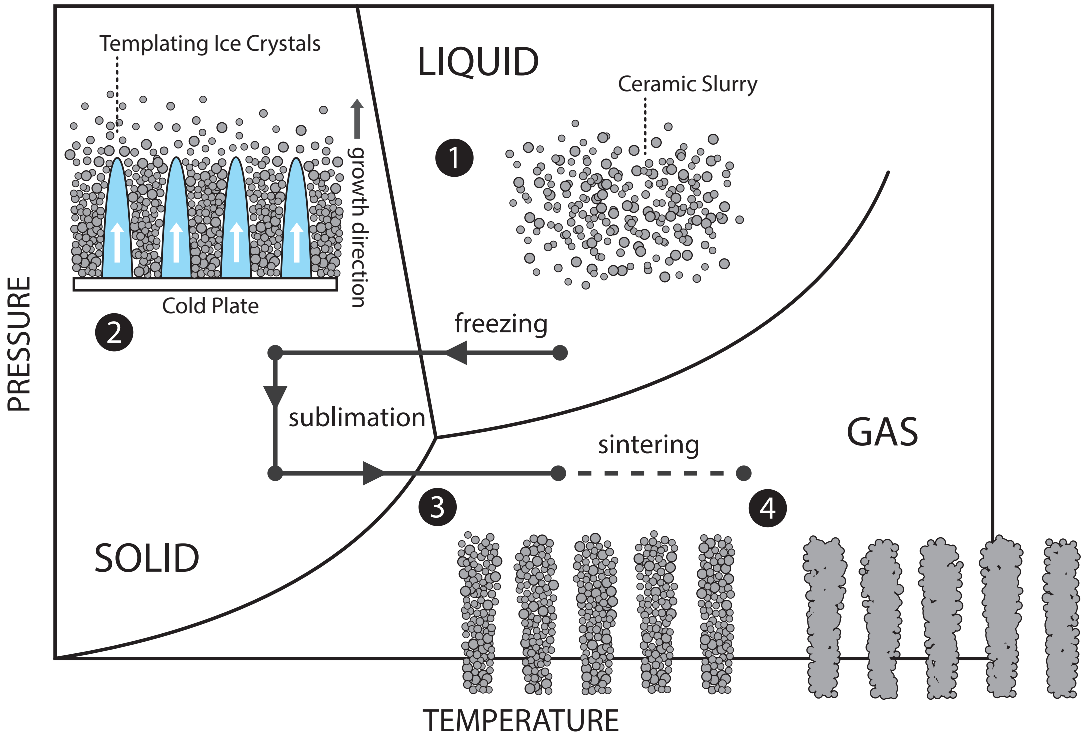

Figure 2.17: Steps in the freeze-casting process, adapted from Deville et al. [1].

tissue scaffolds [75, 76], photonic structures [92], metal-matrix composites [93], dentistry [94], materials science [72], and even food science [95].

Work within the field of directional freeze-casting primarily began with capability studies. A variety of materials and differing setups were used to explore the range of structures possible with this technique. Freeze-casting was able to achieve an impressive range of solid loadings and pore morphologies, but little was done to explain the phenomenological basis for the directional-templating method itself. Initial explanations were based on either single-phase solidification of alloys or analytical models based on the interactions of planar surfaces with single particles [87]. Both methods were limited in their scope and applicability to the multi-particle, multi-phase colloidal segregation seen in freeze-casting. Recently, X-ray tomography has provided researchers with an unparalleled ability to probe the 3D structure during directional solidification both in-situ and post-mortem. Even so, a number of fundamental questions remain concerning the freeze-casting process. Currently, the majority of models are based on experimental data that are specific to a set of material and experimental conditions, making the them only incrementally useful.

2.3.3 Freeze-Casting: In-Depth

Disclaimer: *Freeze-casting is a highly dynamic phenomenon involving the simultaneous coordination of a number of complex processes many of which are as of now incompletely understood. It is difficult therefore to satisfactorily explain everything involved in freeze-casting and the broad range of controls available when directionally templating. Therefore the approach of this in-depth review is to explore the current state-of-affairs when it comes to this exciting process. Often times, the explanations of certain authors can be at odds with one another. This is not to say that one explanation is fundamentally wrong while another is right. More often than not, each explanation contains kernels of truth and it is the task of future researchers to string together the most accurate explanations.*

There are three possible end results to uni-directionally freezing a suspension of particles (Fig. 2.18). First, the ice-growth proceeds as a planar front, pushing particles in front like a bulldozer pushes a pile of rocks. This scenario usually occurs at very low solidification velocities ($< 1\ \mu\text{m s}^{-1}$) or with extremely fine particles because they are able to move by Brownian motion away from the front. The resultant structure contains no macroporosity. If you were to moderately increase the solidification speed, size of the particles or solid loading, the particles begin to interact in a meaningful way with the approaching ice front. The result is typically a lamellar or cellular templated structure whose exact morphology depends on the specific conditions of the system. It is in this category that we'd ideally like to fall when fabricating directionally porous ceramics. The third possibility for a freeze-cast structure occurs when particles are given insufficient time to segregate from the suspension, resulting in complete encapsulation of the particles within the ice front. This occurs when the freezing rates are rapid, particle size becomes sufficiently large or when the solids loading is high enough to hinder particle motion [1].

Assuming we want to remain in the templating regime [Fig. 2.18 (b)], we must ensure that the particles are ejected from the oncoming front. Energetically speaking, this will occur if there is an overall increase in free energy if the particle were to be engulfed ($\Delta\,\sigma > 0$: Eq. 2.12) [76].

$$\Delta\sigma = \sigma_{ps} - (\sigma_{pl} + \sigma_{sl}) \tag{2.12}$$

where $\Delta\sigma$ is the change in free energy of the particle, σ_{ps} is the surface potential between

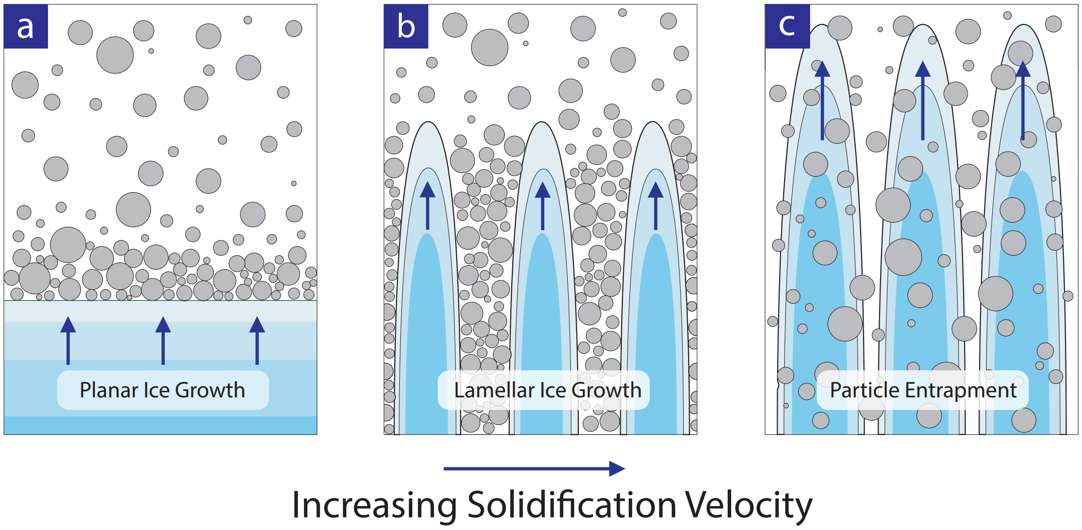

Figure 2.18: Depending on the speed of the freezing front, particle size and solids loading there are three possible morphological outcomes: (a) planar front where all particles are pushed ahead of the ice, (b) lamellar/cellular front where ice crystals template particles or (c) particles are engulfed producing no ordering.

the particle and interface, σ_{pl} is the potential between the particle and the liquid phase and σ_{sl} is the surface potential between the solid and liquid phases. This expression is valid at low solidification velocities, when the system is shifted only slightly from equilibrium. At high solidification velocities, kinetics must also be taken into consideration.

As seen in figure 2.19, there will be a liquid film between the front and particle to maintain constant transport of the molecules which are incorporated into the growing crystal. When the front velocity increases, this film thickness (d) will decrease due to increasing drag forces. A critical velocity (v_c) occurs when the film is no longer thick enough to supply the needed molecular supply. At this speed the particle will be engulfed. Most authors express v_c as a function of particle size where $v_c \propto \frac{1}{R}$ [86]. The transition from a porous (lamellar) morphology to one where the majority of particles are entrapped occurs at v_c, which was defined by Deville et al. [76, 86] to be:

$$v_c = \frac{\Delta\sigma d}{3\eta R}\left(\frac{a_0}{d}\right)^z \tag{2.13}$$

where a_0 is the average intermolecular distance of the molecule that is freezing within the liquid, d is the overall thickness of the liquid film, η is the solution viscosity, R is the particle radius and z is an exponent that can vary from 1 to 5 [86, 96]. As expected, we see that v_c decreases as particle radius R goes up.

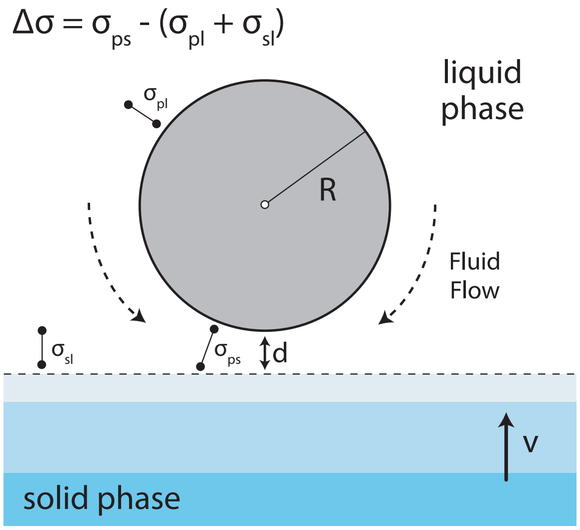

Figure 2.19: Schematic of a particle within the liquid phase interacting with an oncoming solidification front.

Waschkies et al. [97] studied the structure of dilute to concentrated freeze-casts from low ($< 1\ \mu m\ s^{-1}$) to extremely high ($> 700\ \mu m\ s^{-1}$) solidification velocities. From this study they were able to generate morphological maps for freeze-cast structures made under various conditions (Fig. 2.20).

Maps such as these are excellent for showing general trends but they are quite specific to the materials system from which they were derived. In this case, monomodal alumina was freeze-cast without any binders or additives. For most applications where freeze-casts will be used after freezing, binders are needed to supply strength in the green-state. The addition of binder can significantly alter the chemistry within the freezing environment, depressing the freezing point and hampering particle motion leading to particle entrapment at speeds far below the predicted v_c [97].

Assuming however that we are operating at speeds below v_c and above those which produce a planar front, we will achieve some sort of cellular structure with both ice-crystals and walls composed of packed ceramic particles. The morphology of this structure is tied to a number of variables but the most influential is the temperature gradient as a function of time and distance along the freezing direction.

Looking at the cross-section of a freeze-cast, there are at least three apparent morphological regions (Fig. 2.21) [98]. At the side where freezing initiates is a nearly isotropic region with

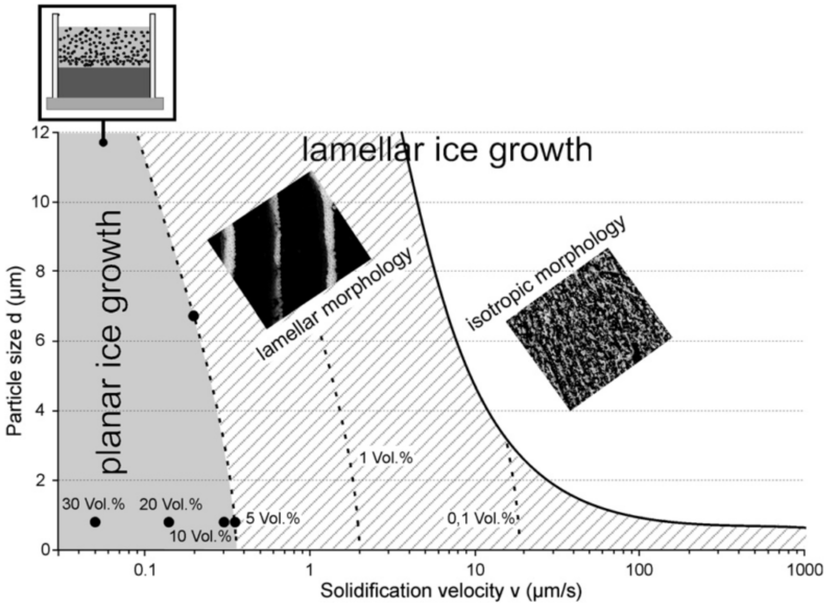

Figure 2.20: Phase map for various freeze-casting morphologies using different particle sizes and solidification velocities [97]. Dark points and lines represent measured values and dashed lines are the predicted values.

no visible macropores dubbed the *Initial Zone (IZ)*. Directly after the IZ is the *Transition Zone (TZ)*, where macropores begin to form and align with one another. The pores in this region may appear randomly oriented. The third zone is called the *Steady-State Zone (SSZ)*, macropores in this region are aligned with one another and grow in a regular fashion. Within the SSZ, the structure is defined by a value λ that is the average thickness of a ceramic wall and its adjacent macropore (Fig. 2.22) [87].

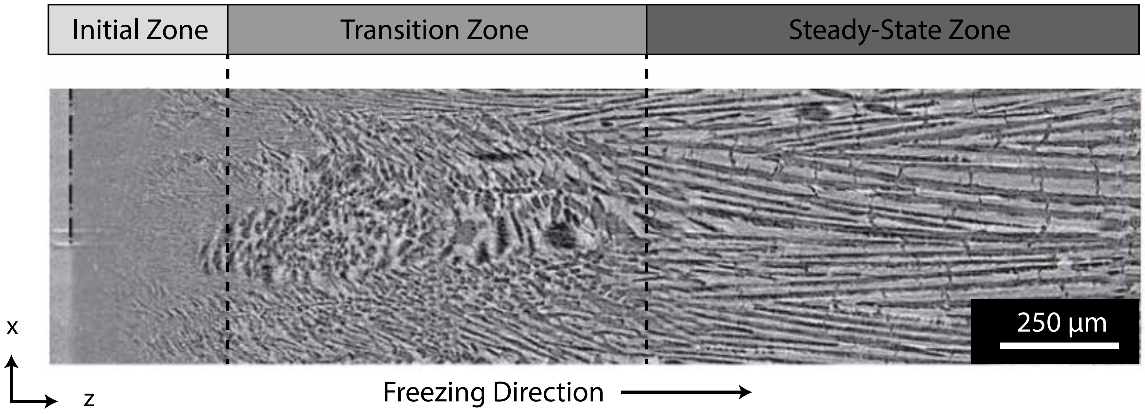

Figure 2.21: Morphological Zones within a freeze-cast. Adapted from [84].

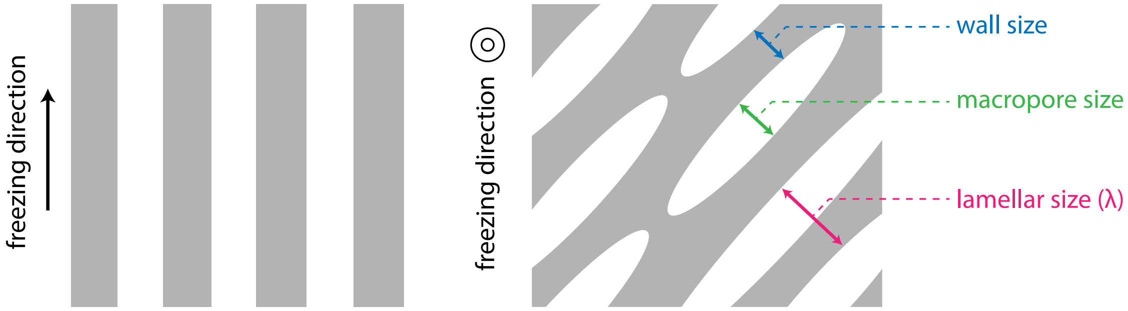

Figure 2.22: General schematic of freeze-cast features showing (left) the structure within the SSZ parallel to the freezing direction and (right) a cross-section with wall, macropore and λ depicted.

Initial Zone: Nucleation and Growth Mechanisms

Although the ability of ice to exclude suspended particles has long been known, the mechanism is still being debated. It was initially believed that during the moments immediately following the nucleation of the ice crystals, particles were ejected from the growing planar ice front, leading to the formation of a constitutionally super-cooled zone directly ahead of the growing ice. This unstable zone eventually led to perturbations, breaking down the planar front into a columnar ice front, a phenomenon better known as a Mullins-Serkerka instability [99–102]. After the breakdown, the ice crystals grow along the temperature gradient, pushing ceramic particles from the liquid phase aside so that they accumulate between the growing ice crystals. Recent in-situ X-ray radiography of directionally frozen alumina suspensions however reveal a different mechanism [84].

In-situ testing reveals that freeze-casting is a competitive growth process. In the moments immediately prior to nucleation, the suspension is in an unstable super-cooled state. Homogeneous (spatially speaking) nucleation of ice crystals occurs followed by explosive crystal growth in every spatial and crystallographic direction. The initial nucleation and growth steps are so rapid (approaching 800 μm s^{-1}) that all suspended particles are completely engulfed by the oncoming ice front because not enough time is given for particle redistribution, resulting in a structure with an isotropic particle distribution [Fig. 2.18 (c)]. This step is what gives us our initial zone structure [84, 97].

Transition Zone: A changing microstructure

As solidification slows and growth kinetics become rate-limiting, the ice crystals begin to exclude the particles, redistributing them within the suspension. A competitive growth process develops between two crystal populations, those with their basal planes aligned with the thermal gradient (z-crystals) and those that are randomly oriented (r-crystals) giving rise to the start of the TZ (Fig. 2.23) [98, 103, 104].

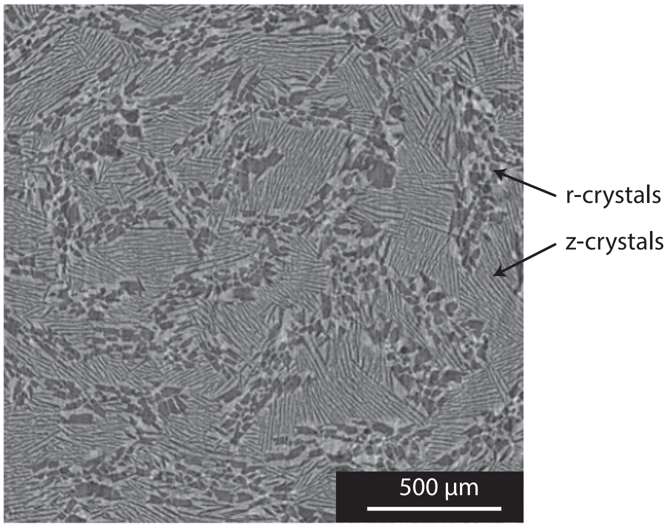

Figure 2.23: z- and r-crystals found within the transition zone of a freeze-cast. Image taken normal to the freezing direction [84].

As the image in figure 2.23 shows, there appear to be colonies of similarly aligned ice crystals growing throughout the suspension. There are fine lamallae of aligned z-crystals growing with their basal planes aligned with ΔT (out of the page). The r-crystals appear in this cross-section as platelets but in actuality they are most similar to columnar dendritic crystals cut along a bias.

Within the transition zone, the r-crystals either stop growing or turn into z-crystals which eventually become the predominant orientation and lead to steady-state growth. There are a number of reasons as to why this occurs. For one, during freezing, the growing crystals tend to align with the temperature gradient, as this is the lowest energy configuration and thermodynamically preferential. Aligned growth however can mean two different things. Assuming the temperature gradient is vertical, the growing crystal will either be parallel (z-crystal) or perpendicular (r-crystal) to this gradient. A crystal that lays horizontally can still grow in line with the temperature gradient but it will mean growing along its face rather than its edge. Since the thermal conductivity of ice is so low (1.6 - 2.4 W mK^{-1}) compared with most every other ceramic (ex. Al_2O_3 = 40 W mK^{-1}), the growing ice will have a significant insulative effect on the localized thermal conditions within the slurry. This can be illustrated using simple resistor elements (Fig. 2.24) [87, 98].

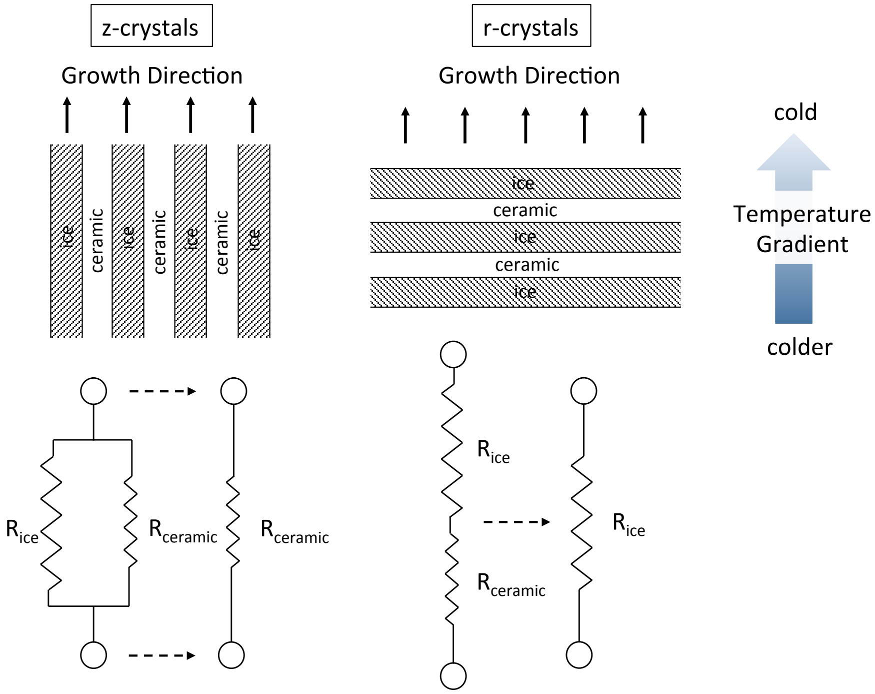

Figure 2.24: z- and r-crystal resistor element representations.

When ice crystals are aligned with their basal planes parallel to the temperature gradient (z-crystals), they can be represented as two resistors in parallel. The thermal resistance of the ceramic is significantly smaller than that of the ice however so the apparent resistance can be represented as the smaller $R_{ceramic}$. If the ice crystals are aligned perpendicular to the temperature gradient (r-crystals), they can be approximated as two resistor elements in series. For this case, the R_{ice} is limiting and will dictate the localized thermal conditions. The lower thermal resistance for the z-crystal case leads to lower temperatures and greater heat flux at the growing crystals tips, driving further growth in this direction while at the same time, the large R_{ice} value hinders growth of the r-crystals. Each ice crystal growing within the slurry will be some combination of these two scenarios. Thermodynamics dictate that all crystals will tend to align with the preferential temperature gradient causing r-crystals to eventually give way to z-crystals, which can be seen from the following radiographs taken within the TZ (Fig. 2.25) [84, 102].

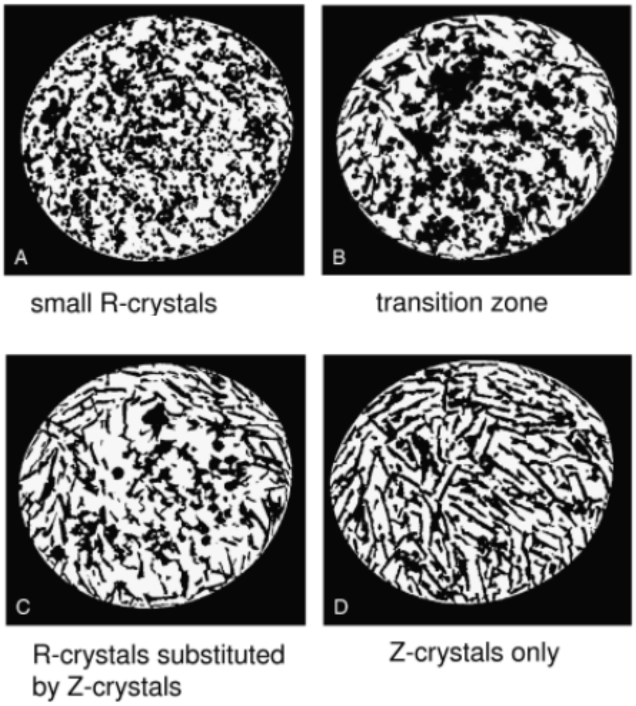

Figure 2.25: X-ray radiographs taken at different heights in a freeze-cast showing the transition from r-crystals to z-crystals. Taken from [102].

When z-crystals become the only significant crystal orientation present, the ice-front grows in a steady-state manner excepting there are no major changes to the system conditions.

It was observed in 2012 that in the initial moments of freezing there are dendritic r-crystals which grow 5 - 15 times faster than the solidifying front. These shoot up into the suspension ahead of the main ice front and partially melt back [105]. Interestingly, these crystals actually stop growing at the point where the TZ will eventually fully transition to the SSZ. Researchers determined that this specific point marks the position where the suspension is in an equilibrium state (i.e. freezing temperature and suspension temperature are equal) [105]. We can say then that the size of the initial and transition zones are controlled by the extent of supercooling beyond the already depressed freezing temperature. If the freeze-casting setup is controlled so that nucleation is favored at only small supercoolings, then the TZ will give way to the SSZ sooner [105].

Steady-state growth zone (SSZ)

The structure in this final region contains long, aligned lamellae that alternate between ice crystals and ceramic walls [1, 87, 98]. The faster a sample is frozen, the finer its solvent crystals (and its eventual macroporosity) will be. Within the SSZ, the normal speeds which are usable for colloidal templating are 10 - 100 μm s^{-1} [103] leading to solvent crystals typically between 2 μm and 200 μm. Subsequent sublimation of the ice within the SSZ yields a green ceramic preform with porosity in a nearly exact replica of these ice crystals [43].

The microstructure of a freeze-cast within the SSZ is defined by its wavelength (λ) which is the average thickness of a single ceramic wall plus its adjacent macropore [86]. Several publications have reported the effects of solidification kinetics on the microstructures of freeze-cast materials [1, 43, 60, 106–108]. It has been shown that λ follows an empirical power-law relationship with solidification velocity (ν) (Eq. 2.14) [60]:

$$\lambda = A\nu^{-n} \tag{2.14}$$

Both A and n are used as fitting parameters as currently there is no way of calculating them from first principles, although it is generally believed that A is related to slurry parameters like viscosity and solid loading [86, 97] while n is influenced by particle characteristics [109].

2.3.4 Controlling the Porous Structure

Firstly, in order to design porous structures using freeze-casting it is beneficial to understand the tools which are available. There are two general categories of tools for architecturing a freeze-cast:

1. *Chemistry of the System* - freezing medium and chosen particulate material(s), any additional binders, dispersants or additives.
2. *Operational Conditions* - temperature profile, atmosphere, mold material, freezing surface etc.

Initially, the materials system is chosen based on what sort of final structure is needed. This review has focused on water as the vehicle for freezing but there are a number of other solvents which may be used. Notably, camphene, which is an organic solvent that is waxy at room-temperature. Freezing of this solvent produces highly branched dendritic crystals [110]. Once the materials system is settled on however the majority of microstructural control comes from external operational conditions such as mold material and temperature gradient.

The following table gives a brief overview of some of the structural parameters that can be controlled when freeze-casting (Table 2.3). In addition, the specific control is listed, as well as its length scale and relevant study from literature.

Table 2.3: Structural Features of Freeze-Cast Materials and their Controls [111]

Structural Feature	Control	Length Scale	Reference
Orientation and alignment of lamella	Patterning, temperature gradient, applied electric field	100 µm cm^{-1}	[111, 112]
Pore shape	Additives, solid content, solvent, solidification velocity	5 - 200 µm	[111, 113, 114]
Lamellae and pore size	Solidification velocity, particle size, solid loading	2 - 200 µm	[86, 97]
Surface roughness of lamellae	Additives, solidification velocity, particle size	50 nm - 10 µm	[111]
Ceramic bridges	Additives	2 - 50 µm	[96, 111, 115]
Pore interconnectivity	Solids Content	µm	[86]

Controlling Pore Size

The microstructural wavelength (average pore + wall thickness) can be described as a function of the solidification velocity v ($\lambda = Av^{-n}$) where A is dependent on solids loading [83]. There are two ways then that the pore size can be controlled. The first is to change the solidification speed which then alters the microstructural wavelength, or the solids loading can be changed. In doing so, the ratio of pore size to wall size is changed [116].

It is often more prudent to alter the solidification velocity seeing as how a minimum solid loading is usually desired. Since microstructural size (λ) is inversely related to the velocity of the freezing front, faster speeds lead to finer structures while slower speeds produce a coarse microstructure. Controlling the solidification velocity is therefore crucial to being able to control the microstructure [83, 97].

Static vs. Dynamic Freezing Profiles

If a freeze casting setup with a constant temperature on either side of the freezing system is used, (static freeze-casting) the solidification front velocity in the SSZ will decrease over time due to the increasing thermal buffer caused by the growing ice front [87, 98]. When this occurs, more time is given for the anisotropic ice crystals to grow perpendicularly to the freezing direction (c-axis) resulting in a structure with ice lamellae that increase in thickness along the length of the sample (Fig. 2.26).

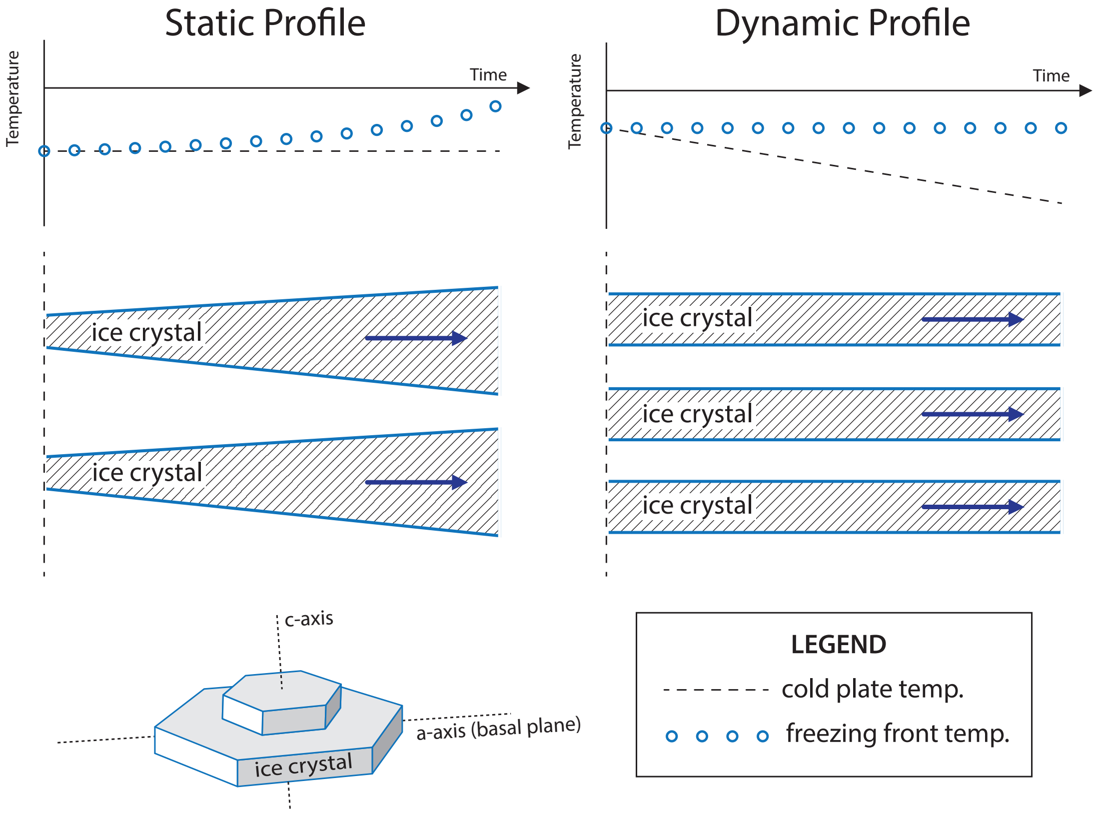

Figure 2.26: Static and dynamic freezing profiles in the steady-state freezing regime.

To ensure highly anisotropic, yet predictable solidification behavior within the SSZ, dynamic freezing profiles are preferred [87, 99]. Using dynamic freezing, the velocity of the solidification front, and therefore the ice crystal size, can be controlled with a changing temperature gradient. The increasing thermal gradient counters the effect of the increasing thermal buffer imposed by the growing ice front [87, 98]. It has been shown that a linearly decreasing temperature on one side of a freeze-cast will result in near constant solidification velocity, yielding ice crystals with almost constant thickness along the SSZ of an entire sample [87]. As pointed out by Waschkies et al. however, even with constant solidification velocity, the thickness of the ice crystals does increase slightly over the course of freezing [83].

Controlling Pore Shape

A number of researchers have shown that additives can prove highly effective and versatile in changing the morphology of pores. These work by affecting the growth kinetics and microstructure of the ice in addition to the topology of the ice-water interface [111]. Some additives work by altering the phase diagram of the solvent. For example, water and $NaCl$ have a eutectic phase diagram. When $NaCl$ is added into a freeze-casting suspension, the solid ice phase and liquid regions are separated by a zone where both solids and liquids can coexist. This briny region is removed during sublimation but its existence has a strong effect on the microstructure of the porous ceramic [111]. Other additives work by either altering the interfacial surface energies between the solid/liquid and particle/liquid, changing the viscosity of the suspension or the degree of undercooling in the system. Studies have been done with glycerol [114], sucrose [111], ethanol [111], coca-cola [111], acetic acid [117] and more.

Anisotropy of the Interface Kinetics

Even if the temperature gradient within the slurry is perfectly vertical, it is common to see tilting or curvature of the lamellae as they grow through the suspension. To explain this, it is possible to define two distinct growth directions for each ice crystal [86]. There is the direction defined by the temperature gradient and the one defined by the preferred growth direction crystallographically speaking. These angles are often at odds with one another and their balance will describe the tilt of the crystal (Fig. 2.27).

The non-overlapping growth directions also help to explain why dendritic textures are often seen in freeze-casts. This texturing is usually found only on side of each lamellae; the direction of the imposed temperature gradient. The ceramic structure left behind shows the negative image of these dendrites. In 2013, Deville et al. [118] made the interesting observation that the periodicity of these dendrites (tip-to-tip distance) actually seems to be related to the main crystal thickness.

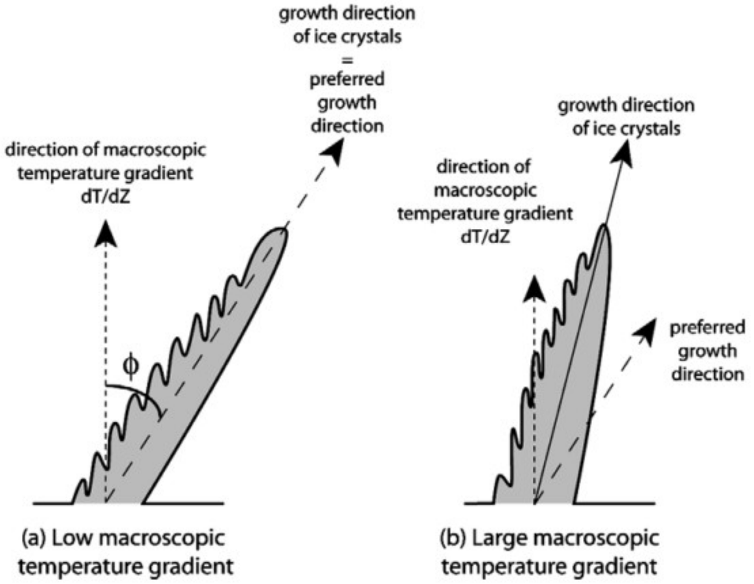

Figure 2.27: Growth direction of ice crystals with imposed macroscopic temperature gradient and preferred growth direction [86].

Particle Packing Effects

Up till now, the focus has mostly been on the structure of the ice itself, the particles are almost an afterthought to the templating process but in fact the particles can and do play a significant role during freeze-casting. It turns out that particle arrangement also changes as a function of the freezing conditions. For example, researchers have shown that freezing velocity has a marked effect on wall roughness. Faster freezing rates produce rougher walls since particles are given insufficient time to rearrange [96, 115]. This could be of use when developing permeable gas transfer membranes where tortuosity and roughness could impede gas flow.

It also turns out that z- and r-crystals do not interact with ceramic particles in the same way. The z-crystals pack particles in the x-y plane while r-crystals pack particles primarily in the z-direction. R-crystals actually pack particles more efficiently than z-crystals and because of this, the area fraction of the particle-rich phase (1 - area fraction of ice crystals) changes as the crystal population shifts from a mixture of z- and r- crystals to only z-crystals [84].

Starting from where ice crystals first begin to exclude particles, marking the beginning of the transition zone, we have a majority of r-crystals and a high value for the particle-rich phase fraction. We can assume that because the solidification speed is still rapid that

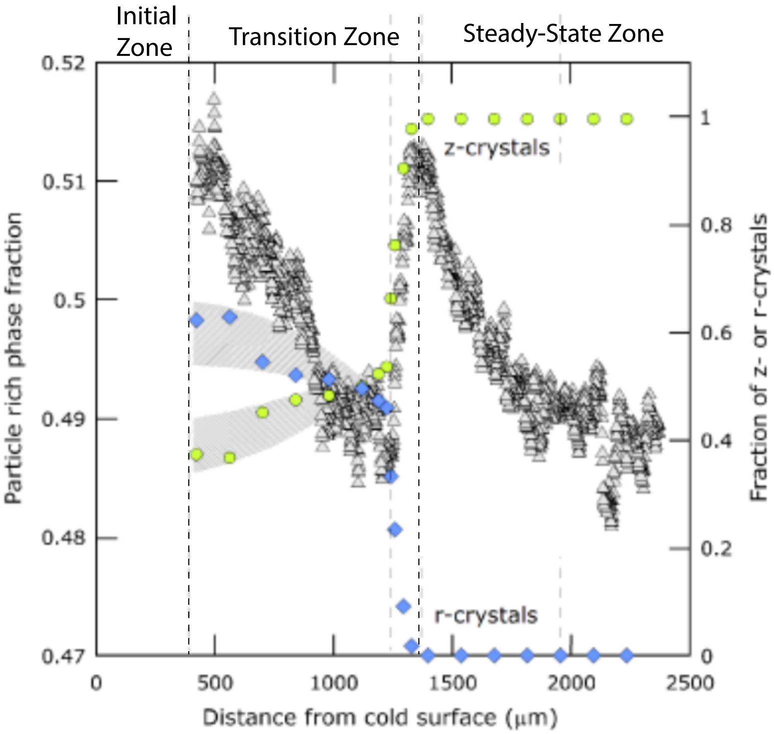

Figure 2.28: Area fraction of the particle rich phase as a function of distance from the freezing surface. The relative amount of z- and r-crystals are superimposed on top [84].

the particles will not be packed efficiently. As the solidification speed slows down however, the area fraction of the particle-rich phase drops indicating an increase in packing efficiency. At the same time, the competitive growth process is taking place, replacing r-crystals with z-crystals. At a certain point nearing the end of the transition zone, the particle-rich phase fraction rises sharply since z-crystals are less efficient at packing particles than r-crystals. The apex of this curve marks the point where only z-crystals are present (SSZ). During steady-state growth, after the maximum particle-rich phase fraction is reached, the efficiency of packing increases as steady-state is achieved [84].

In 2011, researchers at Yale University set out to probe the actual spatial packing of particles within the walls. Using small-angle X-ray scattering (SAXS) they characterized the particle size, shape and interparticle spacing of nominally 32 nm silica suspensions that had been freeze-cast at different speeds [119]. Computer simulations indicated that for this system, the particles within the walls should not be touching but rather separated from one another by thin films of ice. Testing however revealed that the particles were in fact touching and more than that, they attained a packed morphology that cannot be explained by typical equilibrium densification processes [119].

Morphological Instabilities

In an ideal world, the spatial concentration of particles within the SSZ would remain constant throughout solidification. As it happens though, the concentration of particles does change during solidification and this process is highly sensitive to solidification speed. At low freezing speeds, Brownian motion takes place, allowing particles to easily move away from the solid-liquid interface and maintain a homogeneous suspension. In this situation, the suspension is always warmer than the solidified portion. At fast solidification speeds, approaching v_c, the concentration and concentration gradient at the solid-liquid interface increases because particles cannot redistribute fast enough. When it has built up enough, the freezing point of the suspension is below the temperature gradient in the solution and morphological instabilities can occur (Fig. 2.29) [75].

For situations where the particle concentration bleeds into the diffusion layer, both the actual and freezing temperature dip below the equilibrium freezing temperature creating an unstable system [103]. Often times, these situations lead to the formation of what are known as ice lenses (Fig. 2.29).

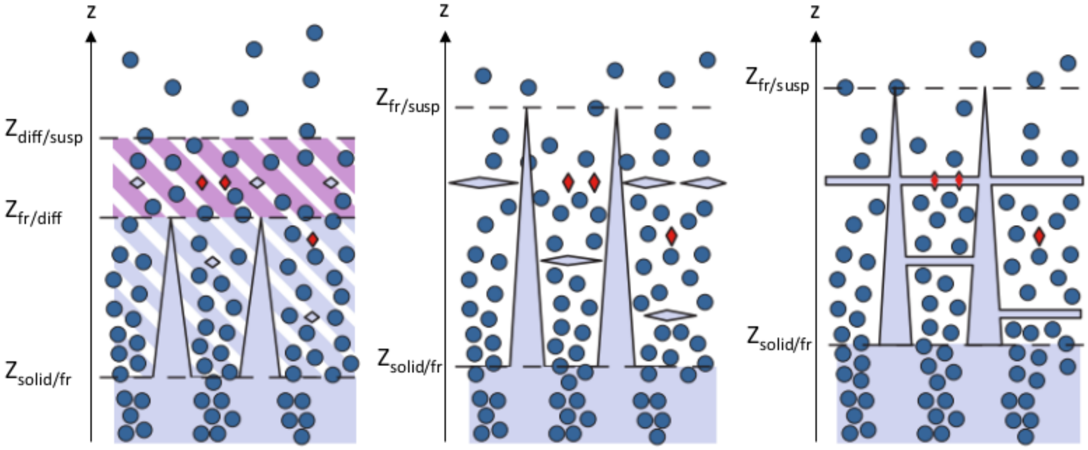

Figure 2.29: Ice lenses resulting from morphological instabilities [101].

These morphological instabilities can trap particles, preventing full redistribution and resulting in inhomogeneous distribution of solids along the freezing direction as well as discontinuities in the ceramic walls, creating voids larger than intrinsic pores within the walls of the porous ceramic [120].

2.3.5 Novel Freeze-Casting Techniques

Freeze-casting can be applied to numerous materials systems including ceramics, polymers [121] and metals [122]. As long as there are particles which may be excluded when the solvent changes phase, a templated structure is possible.

Using various novel processing techniques, some authors have demonstrated even greater levels of architecturing made available with freeze-casting (Fig. 2.30). Munch et al. [111] showed that it is possible to control the long-range arrangement and orientation of crystals normal to the growth direction by templating the nucleation surface. This technique works by providing lower energy nucleation sites to control the initial crystal growth and arrangement. The orientation of ice-crystals can also be affected by applied electromagnetic fields as was demonstrated in 2010 by Tang et al. [123]. Using specialized setups, researchers have been able to create radially aligned freeze-casts tailored for filtration or gas-separation applications [66]. Inspired by nature, scientists have also been able to use coordinating chemicals and cryopreservers to create remarkably distinctive microstructural architectures [114, 117].

2.3.6 Freeze-Casting for SOFCs

There have been some attempts to use freeze-casting for SOFC electrodes [8, 63, 65, 66, 124]. The results from these studies are quite preliminary and for the most part focus on the development of freeze-cast anodes. Researchers at NASA attempted a novel cell architecture which they dubbed the bi-electrode cell or BSC. It consisted of two green parts cut from the same freeze-cast YSZ tape that were laminated together with their freezing directions opposing one another and then sintered (Fig. 2.31). The active electrode materials were then infiltrated inside the scaffold and calcined. The advantage of this cell is that because you are starting with an entirely YSZ structure you can fully sinter it without worrying about thermal expansion mismatch or the evolution of undesirable phases [65].

In 2012, Chen et al. presented electrochemical data for freeze-tape-cast anodes with high performance. Using a conventional NiO-YSZ powder system, they freeze-tape-cast thick SOFC anodes then screen-printed a thin electrolyte and cathode on top. The thick anode allowed them to reduce the thickness of the dense electrolyte making reduced operating temperatures possible. Their cells achieved power densities of 1.28 W cm^{-2} and a low polarization resistance of only 0.166 $\Omega\ \mathrm{cm}^{-2}$. They saw nearly double the performance com-

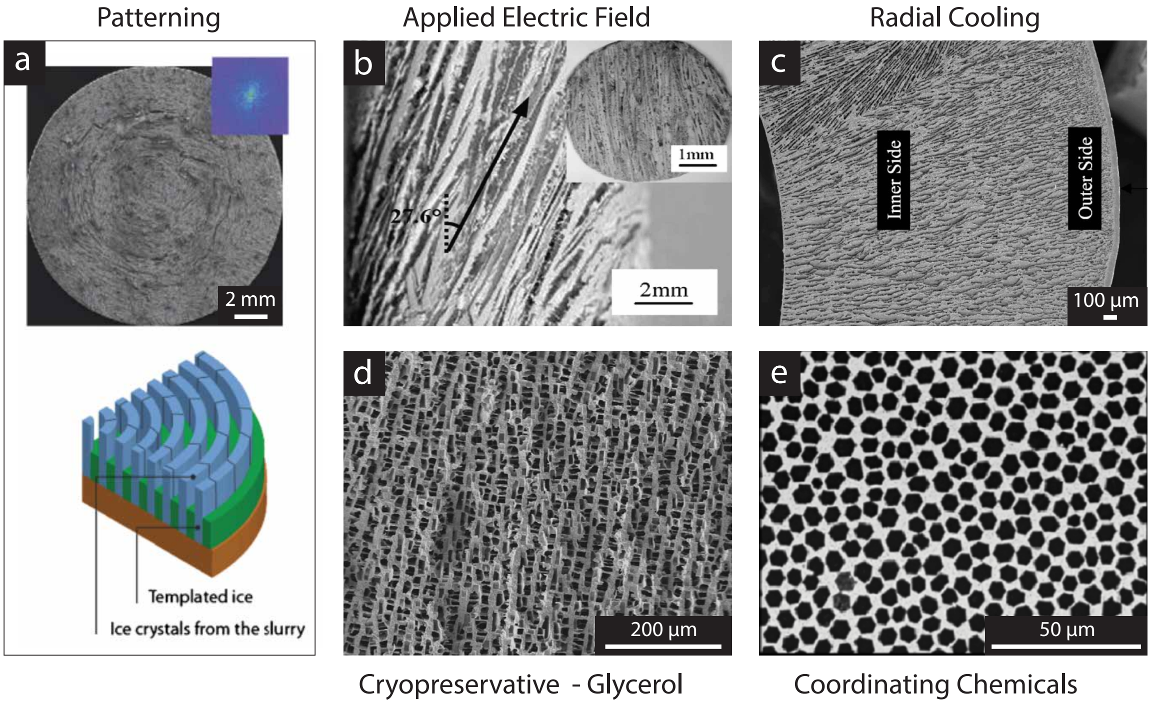

Figure 2.30: Novel freeze-casts: (a) A complex circular pattern is imposed onto the growing crystals by templating the freezing surface [111] (b) 40 kV m^{-1} electrostatic gradient is applied to an alumina scaffold, tilting the growing crystals [123] (c) radial pores are created by freezing in a special cylindrical mold [66] (d) glycerol is added, altering the water/ice phase diagram [114] (e) zirconium acetate powder is used to coordinate with the growing ice crystals , inhibiting certain growth directions [117]. Freezing direction is normal-to-the-page for a,d-e and parallel for b and c.

pared with a standard dry-pressed cell. They attributed their enhanced performance to both the reduced electrolyte thickness (η_{ohm}) and easier gas access (η_{conc}) from the aligned macroporosity.

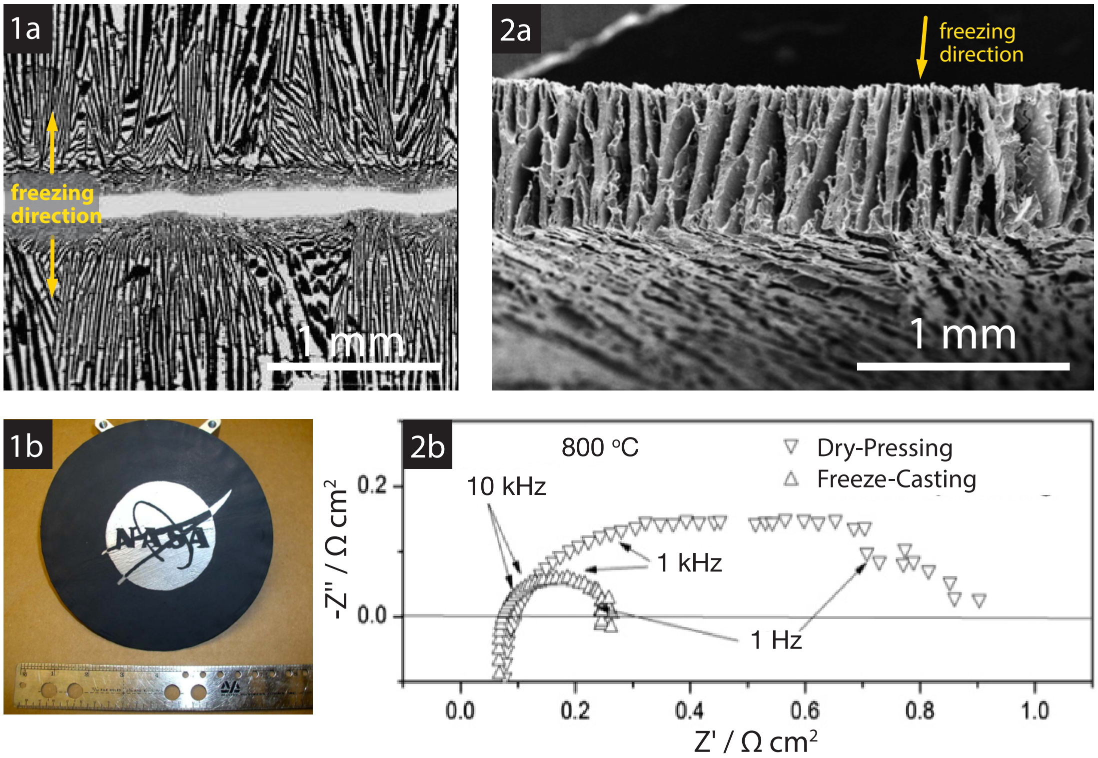

Figure 2.31: (1a) (1b) NASA's BSC fuel cell [65] (2a) Freeze-tape-cast NiO-YSZ scaffold before the addition of the electrolyte and cathode (2b) Nyquist plot for the freeze-tape-cast cell and standard dry-pressed cell [8].

2.4 Ceramic Particle Dispersion + Surface Chemistry

Ceramic powder processing techniques (freeze-casting included) often require a homogeneous suspension (colloid) of ceramic particles dispersed in a solvent [125]. Depending on the material system and desired loading (ratio of solid to liquid) however, this can be a non-trivial task. Most materials are inherently attracted to one another due to Van Der Waals forces. Left to their own devices, Brownian motion will cause particles to come into contact and if there are no opposing repulsive forces, particles will flocculate creating clusters of material known as *flocs*, destabilizing the colloid. To homogeneously suspend particles requires careful balancing of the attractive and repulsive forces of the suspended material with both itself and the solvent it is suspended in [26].

There are three mechanisms which may be used to attain colloid stability:

- Electrostatic Stabilization

- Steric Stabilization
- Electrosteric Stabilization

Electrostatic Stabilization

In a solvent, dispersed particles often become charged. Whether it's from ionization of surface groups, differential disassociation of crystal lattice ions into solution, or adsorption of chemical species in the solvent to the particle [126]. In all cases, to balance out the charge, ions within the dispersion medium will form what is known as an *electric double layer* surrounding each particle (Fig. 2.32). Immediately at the particle surface will be a layer of charged ions in what is known as the *Stern plane*. Outside of the Stern plane is a layer containing free ions known as the *Diffuse Layer*. When colloidal particles move about the dispersion medium, these layers travel with the particle. The boundary of the layer that travels with each particle is called the slipping plane or shear plane and it is here that the electric potential known as the *Zeta-potential* is defined. This particular value is easily measured and is a good indicator of the suspension state of the colloid. Typically values less than $-30\ mV$ or greater than $+30\ mV$ are considered necessary for colloid stability [127].

In the 1940s, Deryagin, Landau, Vewey and Overbeek developed a theory to determine the stability of colloids based on electrostatic forces (DLVO theory). Their theory essentially states that colloid stability is determined by the potential energy between two particles which is found by summing their attractive Van der Waals forces V_A and their repulsive couloumbic forces V_R [126]:

$$V_T = V_R - V_A \tag{2.15}$$

For spherical particles with radius r:

$$V_T = \overbrace{2\pi r \varepsilon \varepsilon_0 \zeta^2 e^{-kD}}^{\text{Repulsion}} - \overbrace{\frac{A}{12\pi D^2}}^{\text{Attraction}} \tag{2.16}$$

where r is the particle radius, ε is the dielectric constant of the dispersion medium, ε_0 is permittivity in a vacuum, ζ is the zeta-potential, k is a function of the ionic concentration,

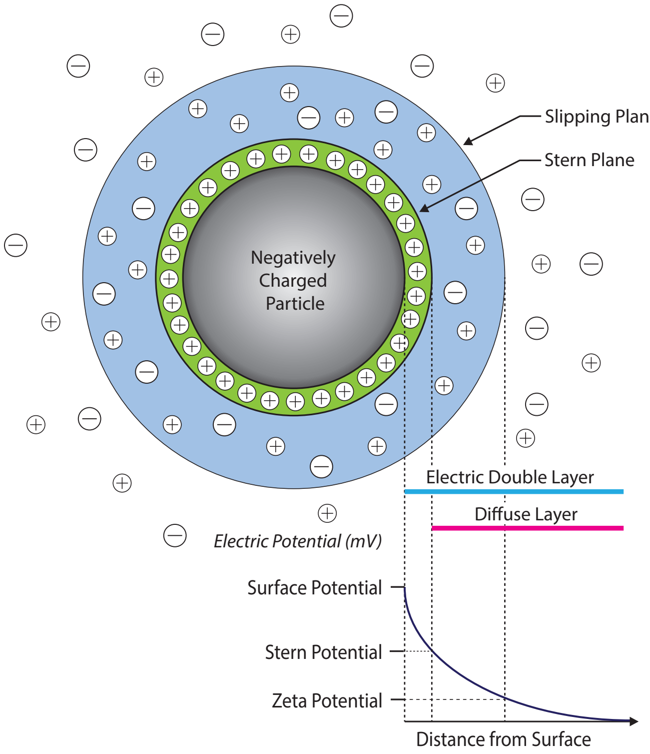

Figure 2.32: Electric double layer of a ceramic particle in solution.

A is the Hamaker constant for spherical particles, and D represents the distance between particles.

Depending on the shape of the summed curve $[V_T(D)]$, we can determine the equilibrium position of two charged particles (Fig. 2.33). There will always be a deep energy well at small values of D indicating that if any two particles get too close they will become trapped and dispersal will be impossible. That being said, if there is a high enough energy barrier in front of this well, the particles will remain in the repulsive regime. As a good rule of thumb, the energy barrier must be greater than $k_B T$[2], otherwise, the collisions from normal Brownian motion will contain enough energy to cause the system to irreversibly coagulate [127].

It is possible to alter the coulombic forces between particles by controlling the pH and types of ions in the dispersion medium. In this way, the interparticle potential can be

---

[2] At room temperature (25 °C) this is approximately 4.11 x 10^{-21} J

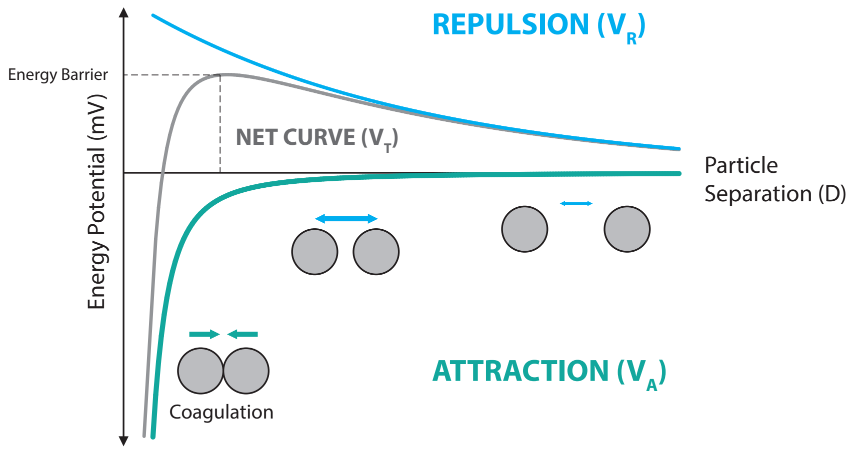

Figure 2.33: Energy potential diagram for two spherical particles as a function of particle distance.

changed to favor stability. When attempting to determine optimal dispersion conditions, zeta-potential is measured as a function of pH since zeta-potential is highly sensitive to ions in solution [127]. For oxides at low pH (acidic conditions), zeta-potential is high, as pH increases from the addition of negative alkali ions into solution, zeta-potential will decrease. Often times, there is a point when the zeta-potential curve will cross the x-axis (0 mV). This is the point at which the colloid is least stable and is known as the iso-electric point (IEP).

The ionic concentration in solution also plays a role in colloid stability. At low salt concentrations for example, the interparticle electrostatic repulsion is often high. Once additional salt ions are added into solution the effects of the electrostatic repulsion become shielded by the charged ions in solution leading to a lowering of the energy barrier, making flocculation easier [127].

Steric Stabilization

The second method for dispersing particles is known as steric stabilization or steric repulsion. Small organic molecules are added into solution that adsorb, chemically or physically, to the ceramic particles, encasing them in an organic layer. When successful, this organic layer acts like a coating of springs, repelling the steric layers of other particles through a process known as steric hindrance [Fig. 2.34 (a)] [127].

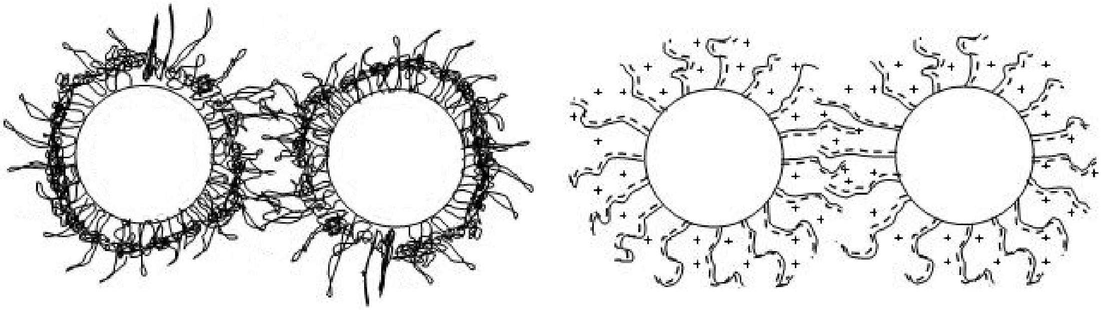

Figure 2.34: (a) Steric stabilization of two particle and (b) electrosteric stabilization [128].

This simple act prevents particles from being able to flocculate, producing stable suspensions.

Electrosteric Stabilization

The third method is simply a combination of the first two known as electrosteric stabilization or repulsion [Fig. 2.34 (b)]. Charged short chain polymer molecules (ex. Ammonium polymethacrylate)[3] are added into solution where they adsorb to the ceramic particles. The combination of electrostatic repulsion along with steric stabilization can produce highly stable colloidal systems capable of handling high ceramic loadings.

Hetero-Codispersion

Often times, it is complicated enough to stabilize a single material. Dispersing multiple particle types in solution can produce a variety of new complications. Every material when placed in aqueous conditions will have either a positive, negative or neutral surface charge. The charge depends on the surface characteristics of the material as well as the pH of the water. The pH at which the charges on the surface neutralize is known as the iso-electric point or IEP. At pH values above the IEP, the predominant surface species is $M - O^{-}$ while at pH values lower than the IEP, the predominant species is $M - OH^{2+}$. At all pH values other than the IEP, ions with opposite charges to the surface charges (counterions) will form a cloud around each particle (electric double layer). When two particles approach, their respective counterion clouds overlap, increasing the counterion concentration between the particles and resulting in a repulsive force [129].

---

[3] This was the dispersant most often used during the course of this thesis

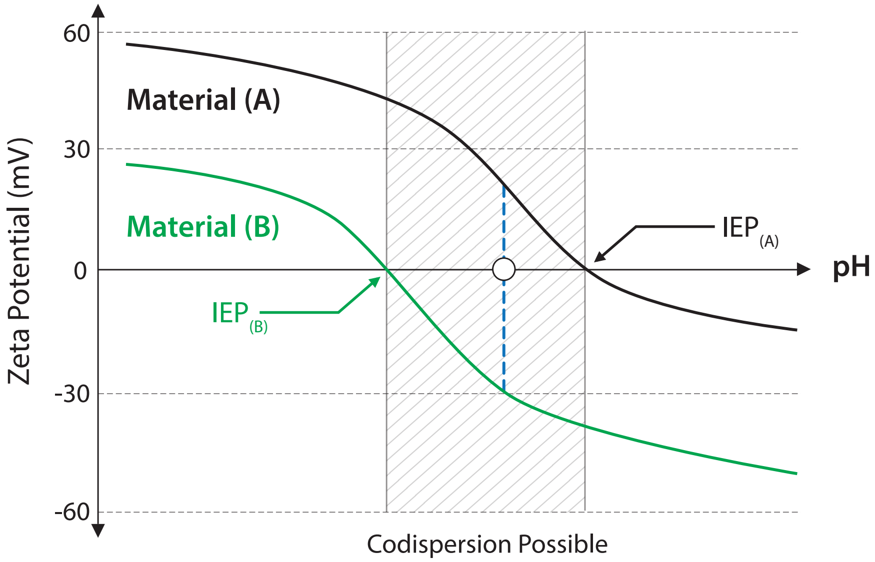

Figure 2.35: Schematic of the zeta-potential for materials A and B during hetero-codispersion.

Using two different materials, with significantly different IEP values, a process known as *hetero-codispersion* can be used to evenly distribute the materials in a stable suspension. By changing the pH of the suspension to a value in between the IEPs for the two particles A and B, particle A will become charged positively while particle B will gain a negative charge (Fig. 2.35). Particle A and B will become attracted towards one another while at the same time A will repel A and B will repel B. The result is a suspension that remains stable, homogeneous and fully dispersed [129, 130]. All things being equal, if the combined absolute value of their two zeta-potentials is greater than 30 mV then the slurry will be stable.

2.5 Mechanical Properties of Cellular Materials

Enhancements to functional performance (gas flow, reactionary area, filtration...) of porous materials are often realized by indiscriminately increasing porosity, typically resulting in decreased mechanical performance [26]. No matter the end use however, every ceramic, structural or not, must maintain a minimum level of structural integrity. Studies have shown however that by optimizing porous architecture, both functional and mechanical performance may be simultaneously improved [131]. It is important therefore to recognize the role that shape, location and size distribution of pores play on mechanical performance

[23, 132]. Unfortunately, research into the mechanical performance of porous materials has been primarily empirical in nature. Characterization of a particular material or processing method is used to interpret performance data. Although methods such as these have intrinsic value, adequate attention hasn't been paid towards the prediction of performance [133].

Predictive modeling of cellular ceramic mechanical properties has predominantly been driven by the refractory and structural ceramics industries. Effective methodologies for predicting bulk mechanical behavior was needed for their large-scale output [22]. There are two schools of thought when it comes to porous ceramic modeling:

1. *Mechanics Community* - tends to consider a specific pore shape and develop analytical solutions for the mechanical properties using porous volume fraction as the independent variable.
2. *Materials Community* - experimental results are obtained and "best-fit" curves relating porous volume and mechanical properties are correlated with observed microstructures.

Results from these two methodologies often produce differing and even conflicting results. The models from both schools of thought however can be grouped into three general categories (Linear, Power and Exponential) [133]:

Linear Relationships

One way of describing a porous ceramic is to use a special case of the rule of mixtures (Eq. 2.1) where one assumes the porous ceramic is a bi-phasic material: the solid and the pores. Using this approach, for example, for elastic modulus, the porous phase will have zero stiffness. These relations are really only valid for so-called "dilute-limit suspensions" where pores are isolated and do not interact with each other. The original relation is credited to Dewey et al. [134] who in 1947 developed dilute-limit expressions for the elastic properties of materials containing non-rigid, spherical fillers:

$$E_p = E_0(1 - aP) \tag{2.17}$$

In this expression, E_p is the elastic modulus of the porous material, E_0 is the bulk modulus,

a is dependent on pore-geometry as well as Poisson's ratio and P is the total porosity. The assumptions required for use of linear methods (i.e. low-porosity, non-overlapping stress fields) tend to make linear models rather restrictive for anything but low-porosity idealized microstructures.

Power Relationships

Predictive models based on power-laws have proved more robust when it comes to modeling mechanical performance. Most models are validated up to 40 or 50 vol. % porosity [133]. For reference, the most useful range of porosity for multifunctional ceramics is between 20 and 50 vol. % [133]. The various power-law models available all contain fitting parameters which researchers tend to relate to microstructural characteristics in an offhand way. Explanations concerning these equations are often cursory at best. The general form for power-law relationships follows the equation originally developed in 1949 by Bal'Shin et al. [133]:

$$E_p = E_0(1 - jP)^i \tag{2.18}$$

where both i and j represent fitting parameters which can loosely be tied to microstructure and all other variables are as defined previously. These models were the basis for works by Gibson and Ashby and still today prove to be some of the more robust methods for determination of ceramic foam properties [10, 135, 136].

Exponential Relationships

Back in 1953, Ryshkewitch [137] showed that strength varies logarithmically with porosity in sintered alumina. These results were later generalized by Duckworth [138] as:

$$S_p = S_0\, e^{-kP} \tag{2.19}$$

where S_p is the strength of the porous material, S_0 is the bulk strength and k is a material-dependent constant. Analyses by Knudsen showed that the ratio of S_p/S_0 would be proportional to the contact or load-bearing area [139]. His works later became the basis for the minimum-solid-area or MSA theories developed by Roy Rice in the 1970s [133]. The

MSA method operates on the “weakest link” concept. It says that for an applied load, the stresses will be most concentrated, and therefore limiting, at the plane normal to the applied load with the minimum amount of solid area. According to Rice, this model is appropriate for any flux-related phenomena: strength, elasticity, conductivity, gas flow, etc. [21]. From this work, Spriggs [140] developed an analogous model for elastic properties and validated the model for alumina with porosities as high as 37 vol. %:

$$E_p = E_0\, e^{-bP} \tag{2.20}$$

where b represents the packing and shape of particles and all other values are as defined previously. Critics cited the fact that these empirically developed relations are valid only for a limited porosity range since as $P \rightarrow 1$, mechanical properties do not converge to 0. Rice acknowledged this limitation but noted that in practice, mechanical integrity goes to null far before porosity ever reaches 100 %. For a simple cubic stacking of identical spheres for example, the critical porosity occurs when P = 0.52.

For porosity levels beyond those of the Sprigg’s relation seen in Eq. 2.20, (i.e. porosity $>$ 40 vol. %), Rice realized that the role of the pores and matrix material could be exchanged (Fig. 2.36) leading to the following relation which is valid at high porosities:

$$E_p = E_0[1 - e^{-b'(1-P)}] \tag{2.21}$$

where b' represents the packing and shape of pores rather than the matrix material. The power of the MSA method is that these relations, Eqs. (2.20) and (2.21), are shown to be directly proportional to the ratio of the minimum solid area under load divided by the total cross-sectional area normal to the applied stress:

$$\frac{A^\star}{A_0} = MSA = \frac{E_p}{E_0} = e^{-bP} \tag{2.22}$$

where $A^\star$ is the minimum solid area under load and A_0 is the total cross-sectional area. The ratio of these is defined as the MSA which is directly proportional to the normalized performance metric (elastic modulus, strength, conductivity, and so on).

Theoretically, using the MSA method, one could predict mechanical properties using purely geometric reasoning provided the structure is understood and regular. In practice it has

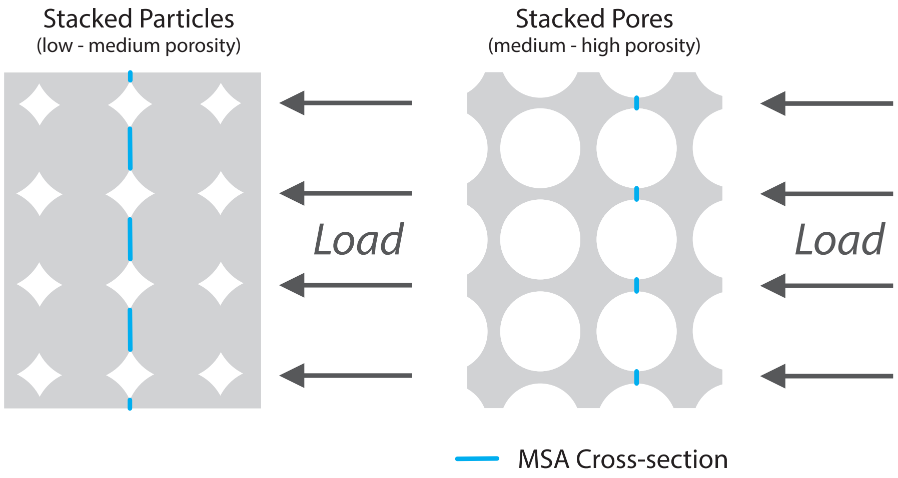

Figure 2.36: Representations of the MSA for a packing of particles (low to medium porosity) and stackings of pores (medium to high porosity) under load.

been shown to be effective only in a limited number of cases and often times fitting parameters from empirical data are still needed [133].

The fact remains that most models are simply best-fit curves from experimentally produced data. Often times authors provide little more than average porosity in their results. This is especially problematic as it has been shown by multiple groups that pore shape and distribution play a significant role on mechanical performance [133]. As it is, there remains a definitive lack of correlation between porous microstructures and associated mechanical properties.

Hierarchically Porous Materials

As was demonstrated by Pecqueux et al. [135], there are a number of models describing the effects of macropores (extrinsic) and similarly those which attempt to model the behavior of ceramics with microporosity (intrinsic). There are however, few that attempt to describe the behavior of a bimodal ceramic, with both micro- and macroporosity. Those which are available typically present only empirical data and associated regression curves [135].

To describe the behavior of a hierarchical ceramic, such as those used in this thesis, there are a few simplifications which can be considered. If the size of the micro- and macropores are significantly different enough (i.e. at least 1 or 2 orders of magnitude) the material can be considered as a quasi-continuous microporous "matrix" containing isolated macropores. Then the effects of the two porosity populations on Young's modulus can be separated as follows [135]:

$$E_p = E_0 \cdot f_1(P_{macro}) \cdot f_2(P_{micro}) \tag{2.23}$$

where E_p is the Young's modulus for the porous material and E_0 is the Young's modulus for the fully dense body. The functions f_1 and f_2 represent the macroporosity and microporosity, respectively, within the hierarchical structure. Depending then on the specific micro and macroporous morphologies, it is possible to select two distinct models to describe the overall behavior. For the sake of completeness, let's assume that we have a ceramic composed of submicron size, partially sintered spherical grains with randomly distributed, large voids (> 10 μm) spaced throughout the structure. For the macroporosity we could use the model by Wagh et al. [141] to describe these isolated macropores. This power model uses the relative density of the ceramic (P) along with a fitting parameter (m):

$$E_p = E_0 \cdot (1 - P_{total})^m \tag{2.24}$$

and because our "matrix" material is itself microporous, the Young's modulus is reduced as compared to the bulk value ($E_0 \rightarrow E_{micro}$) resulting in the expression:

$$E_p = E_{micro} \cdot (1 - P_{macro})^m \tag{2.25}$$

where E_{micro} is the Young's modulus of a partially sintered ceramic without macropores and the porosity variable now refers only to the contribution from the macropores. The function f_2 can be described by Jernot et al. [142] which is well suited to describe such a structure as it applies to partially sintered packings of spherical grains:

$$E_{micro} = E_0 \cdot [N_C \cdot (1 - P_{micro}) - (N_C - 1) \cdot (1 - P_{micro})^{2/3}] \tag{2.26}$$

where N_C is the mean coordination number of particles within the packing. The inclusion of this parameter takes into consideration the morphology of the micropores in the cellular matrix. These two equations can be combined to describe the elastic modulus of the hierarchical structure:

$$E = E_0 \cdot [N_C \cdot (1 - P_{micro}) - (N_C - 1) \cdot (1 - P_{micro})^{2/3}] \cdot (1 - P_{macro})^m \qquad (2.27)$$

going further, it is possible even to extend these concepts and models to fracture toughness and even compressive strength [135].

2.5.1 Mechanical Properties of Freeze-Casts

The alignment of ceramic walls which occurs in freeze-casts makes them obvious candidates for porous structural ceramics. One would think therefore that there would be a significant number of studies concerning the mechanical properties of these materials but in reality only a limited number have been published. Studies that report mechanical properties of freeze-cast materials tend to focus solely on properties in the direction of freezing [111, 115, 131] and of the few that report on properties perpendicular to the freezing direction, even fewer study the structural stiffness in both directions [121]. These freeze-casts, in addition, are typically tested with all three of their microstructural regions (IZ, TZ, and SSZ) intact. The effects of the IZ and TZ regions on mechanical properties are unknown, and they may potentially skew the results of mechanical testing.

In general, it has been shown that like all materials, as porosity increases, the mechanical properties will deteriorate [9]. Various studies have also reported that increased cooling rates have been shown to increase the compressive strength of a freeze-cast up to a certain point. It is believed that as pore size decreases, strength increases because the defects (pores) become smaller [9].

Hunger et al. [131] also noted that higher freezing rates (smaller lamellar spacing and wall thicknesses) result in higher Young's modulus and strength. In addition however, they reported that increased solidification velocity tends to reduce the aspect ratio of the macropores normal to the freezing direction and it is this structural change which is primarily responsible for the impressive mechanical characteristics of freeze-casts made using fast cooling rates. The freeze-casts which they fabricated using an alumina-gelatin-chitosan system had a distinctly honey-comb microstructure at higher freezing rates. Further characterization of their structures revealed a number of stiffening and strengthening bridges which were hypothesized to stabilize the lamellae through rib stiffening and reduce failures attributed to interlamellar shearing. The authors cite the fact that these bridges hinder lateral motion, strengthening the overall structure. Such stiffening bridges have been spotted in other studies [96, 115, 131, 143] and seem to be a key component to the impressive mechanical performance attainable by freeze-casts.

2.6 Discrete Element Simulations (DEM)

2.6.1 DEM Principle

The discrete-element method or DEM is a meso-scale simulation tool that models systems of individual elements as opposed to the finite-element method (FEM) which models systems as meshes of points and geometric units (Fig. 2.37) [47]. Since our ceramics consist of partially sintered powders, we benefit from DEM by modeling on an appropriate scale; each discrete unit can represent a single particle. Additionally, DEM reduces the computing requirements that would be necessary for FEM simulations of similar scale, allowing researchers to more quickly model their systems [144, 145]. The particular DEM code used during the course of this thesis is called discrete-powder 3D (dp3D). It was developed in the SiMaP lab at Grenoble-INP specifically to study particulate material microstructures. The software is powerful, flexible, and results show that dp3D simulations have excellent agreement with experimental data of real-life phenomenon [26, 125, 146].

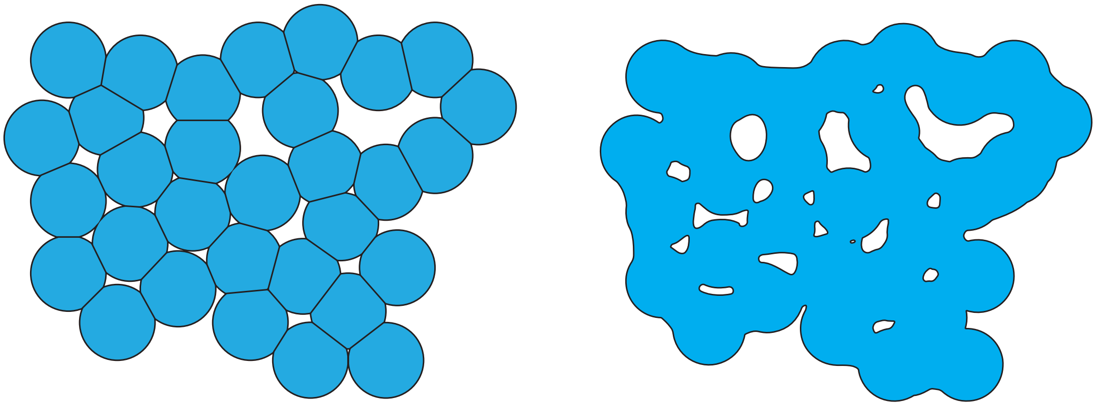

(a) Discrete-Element Model (DEM) **(b)** Finite-Element Model (FEM)

Figure 2.37: DEM and FEM models of a similar packing of particles. This example highlights how the particulate nature of the sample is lost with FEM.

2.6.2 Creating a Numerical Microstructure

There are three distinct steps involved when creating a DEM microstructure from particles (Fig. 2.38) [26]:

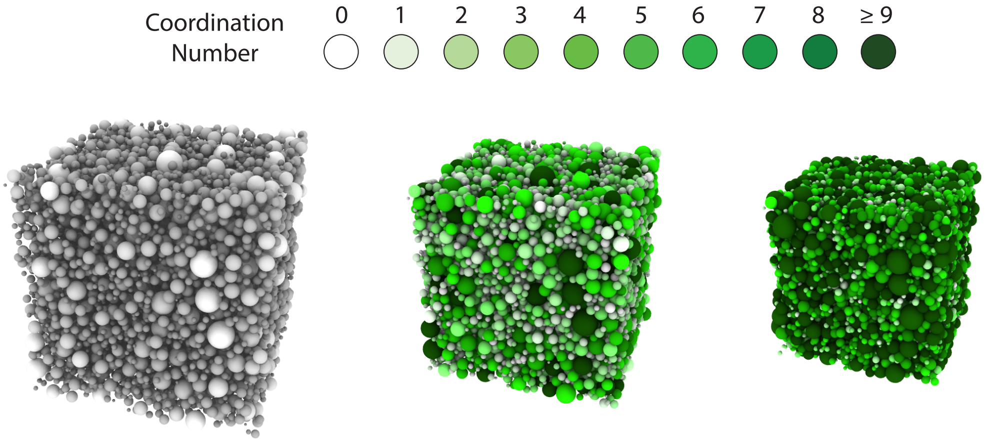

(a) Gas of Particles **(b)** Packed green-body **(c)** Sintered

Figure 2.38: Initially, (a) particles begin with a coordination number of 0 (density = 0.3). As packing (b) and subsequent sintering (c) take place however, this number increases until a final desired density (ex. 0.75) is reached or the simulation is stopped.

Gas Particle Generation

First, a random "gas" of particles in a box of predetermined size is generated [Fig. 2.38 (a)]. The system is constrained so that no particles may touch one another. There are no gravity effects at this stage [147]. The particle size distribution and material properties can be input by the user during initialization to mimic experimental conditions. Additionally, multiple material types may be used simultaneously to represent composite microstructures (i.e. LSM-YSZ composite cathodes).

At this stage in the process, it is also possible to incorporate "pore-formers" which are discrete shapes, often spheres, that are significantly larger than the average particle size. These can be used to create hierarchical structures where the final material has a distinctly non-monomodal pore size distribution, such as would be seen in isotropically porous SOFC electrodes made using pore formers. These DEM pore-formers can be incorporated in a random or non-random fashion into the microstructure and then are removed at some point during the sintering process, exactly as would happen if one were to physically sinter a ceramic with incorporated fugitive pore-formers. Often times, pore formers such as these are used to determine the effects of large flaws [26, 148].

Obtaining a Green Body

Once a "gas" of particles is populated, the size of the box is reduced, packing the particles together until they are unable to move (generating the green structure) as shown in figure 2.38 (b). This process is done until the density (d) of the microstructure reaches a desired value in accordance with:

$$d = \frac{V_{part}}{V_{tot}} \tag{2.28}$$

where V_{part} is the cumulative volume of all the particles and V_{tot} is the volume of the simulation box. As the simulation box size is reduced the particles interact with one another as they become compacted. These interactions are limited to purely elastic behavior. This stipulation ensures that there are no inherent stresses or plastic deformations prior to the sintering step [146].

Numerical Sintering

To achieve a realistic consolidated structure with bonds between particles, DEM is able to numerically sinter the green body to a desired final density [Fig. 2.38 (c)]. Appropriate physical contact laws are followed during the sintering step in order to generate realistic microstructures [145, 149]. The sintered DEM structure can then be imported into a variety of different software packages that can compute properties such as electrical/ionic conductivity, gas permeability and mechanical properties.

The sintering model used is based off the one proposed by Bouvard and McMeeking [146, 150, 151] which considers grain boundary and surface diffusion to be the main drivers of mass transport in the system [147]. Normal contact forces between particles are introduced to account for the diffusion phenomena that takes place between particles at elevated temperatures. Using these laws means that the resultant structure is not random but actually sinters realistically to reduce the overall surface energy of the system [148]. In the model, the authors denote γ_s as the surface energy and Δ_b as the diffusion parameter for the system:

$$\Delta_b = \frac{\Omega}{kT}\delta_b D_b \tag{2.29}$$

where $D_b = D_{0_b} exp(-Q_b/RT)$ is the diffusion coefficient for vacancy transport in a grain boundary with thickness equal to δ_b, activation energy of Q_b, and atomic volume of Ω. For two spherical particles with radii R_1 and R_2, a contact radius of a_b and an overlap of h_b (Fig. 2.39), the normal force N_s acting on a contact is given by:

$$N_s = \overbrace{\frac{\pi r_c^4}{8\Delta_b}\frac{dh_b}{dt}}^{\text{Diffusion Term}} - \overbrace{\frac{9}{4}\pi R^\star \gamma_s}^{\text{Surface Energy}} \tag{2.30}$$

where $R^\star = R_1 R_2/(R_1 + R_2)$. Additionally, there is a tangential force component at each contact that is defined by:

$$T_s = -\eta \frac{\pi a_b^2 R^{\star 2}}{2\Delta_b}\frac{du}{dt} \tag{2.31}$$

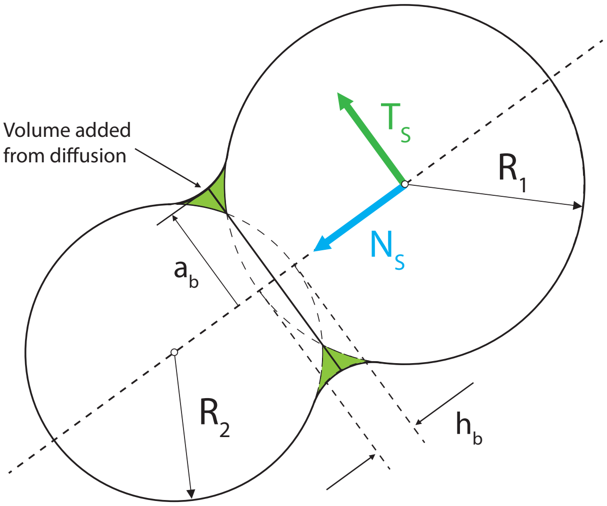

Figure 2.39: Schematic of two particles sintering during DEM. The normal (N_s) and tangential force vectors (T_s) are indicated as arrows on particle 1. Adapted from [151].

where η is a dimensionless parameter characterized by the viscosity which acts depending on the rate of approach between two particles (dh_b/dt). It is assumed that contacts are large enough to inhibit any rotational movement. During sintering, particles overlap and their contact size is given by Coble's model [152] to be:

$$a_b^2 = 4R^\star h_b \tag{2.32}$$

The contact size is important to note as it has a dominant effect on the mechanical response of the simulated microstructure [148]. The contact size, as determined by Eq. 2.32 is larger by a factor of $\sqrt{2}$ compared with the simple geometric intersection of spheres since the Coble model takes into account conservation of volume, adding the volume from the intersection of the two spheres to the outer contact radius.

Diffusion and the reduction in surface energy drive the sintering reaction, and from the constitutive sintering equations, the forces acting on each particle are determined for a particular timestep. A system of linear equations are populated describing particle velocity and position that account for the applied forces from sintering. These are solved and the system is updated with a new set of positions and particle contact sizes. The process then repeats for the new timestep [151]. During sintering, new contacts form, but they may also break given the right circumstances, leading to realistic packings of what are essentially truncated spheres with flat, perfectly elastic contacts between particles [146]. Using time-temperature dependent rate laws, the simulation tool is even robust enough to account for differing sintering rates of small versus large particles and the varying sintering temperatures for different materials. Unfortunately, the model still relies on certain experimental parameters (diffusion coefficients, surface energies...), some of which are hard to find in literature or difficult to measure depending on the system [148]. Another limitation is that the current version of DEM has only been implemented for spherical particles.

Studies have shown, that these DEM structures can realistically duplicate many particle systems covering a wide range of porosities, material types, particle distributions and microstructures [125, 146, 151, 153]. The model used does not consider grain growth however making it applicable only to partially sintered systems.

2.6.3 Mechanical Contact Laws

Because it is important to be able to realistically simulate performance of our architectured ceramics, it is necessary that the DEM representations achieve natural behaviors. Therefore, the generated DEM structures must possess appropriate physical contact laws so as to be able to simulate mechanical properties. Early models for the linear-elastic response of discrete-element materials were unsatisfactory as they didn't account for the finite contact size and multi-particle interactions between neighboring particles [154]. Models such as those produced by Walton in 1987 [155] and Norris and Johnson in 1997 [156] used uniform strains and assumed small-contact sizes between particles. Later models, like those developed by Misra and Chang in 1993 [157], didn't account for elastic coupling.

SOFCs are often left partially sintered, retaining their particulate nature, for this reason DEM is well-suited to model their behavior. The theory being that these meso-scale simulations are built to model the length-scale of the particle [148]. The model which is used to describe the mechanical behavior of the particulate system is a simplified version of the one developed by Jefferson et al. [154].

As seen in figure 2.39, a flat, cylindrical contact forms between two sintered contacts which is defined by an overlap h_b. This contact represents an elastic junction between two particles whose properties may be defined by user input. Each particle is modeled as a sphere which may mechanically interact with other particles. Two types of contacts are considered: (i) contacts between bonded particles and (ii) contacts between particles whose bonds have broken and are now back in contact (Fig. 2.40) [26]. At each timestep in the mechanical simulation, the total force applied to each particle is used to compute its displacement by imposing mechanical equilibrium, conservation of mass and quasi-static conditions. For two particles (1) and (2) with elastic constants (Young's Modulus and Poisson's ratio) given by E_1, E_2, ν_1, ν_2 and radii R_1 and R_2 we can define an equivalent modulus and radius as [26]:

$$E^\star = 2\left(\frac{1-\nu_1^2}{E_1} + \frac{1-\nu_2^2}{E_2}\right)^{-1} \tag{2.33}$$

$$R^\star = \frac{R_1 R_2}{R_1 + R_2} \tag{2.34}$$

The normal contact force between these two particles (1) and (2) would be given by:

$$N_b = E^\star f_N a_b u_N \tag{2.35}$$

where u_N is the normal displacement and f_N is a function that accounts for the interaction between neighboring particles:

$$f_N = \frac{1 + a^\star[\frac{\pi}{6}(1-\nu^2)(1+2a^\star) - a^\star]}{\sqrt{1-a^{\star 2}} - \psi(a^\star + a^{\star 2}[\frac{\pi}{6}(1-\nu^2)(1+2a^\star) - a^\star])} \tag{2.36}$$

$a^\star = a_b/2R^\star$ is the bond normalized radius and ψ is a material independent factor that allows bond interactions to be taken into account. In this model, ψ is used as a fitting parameter.

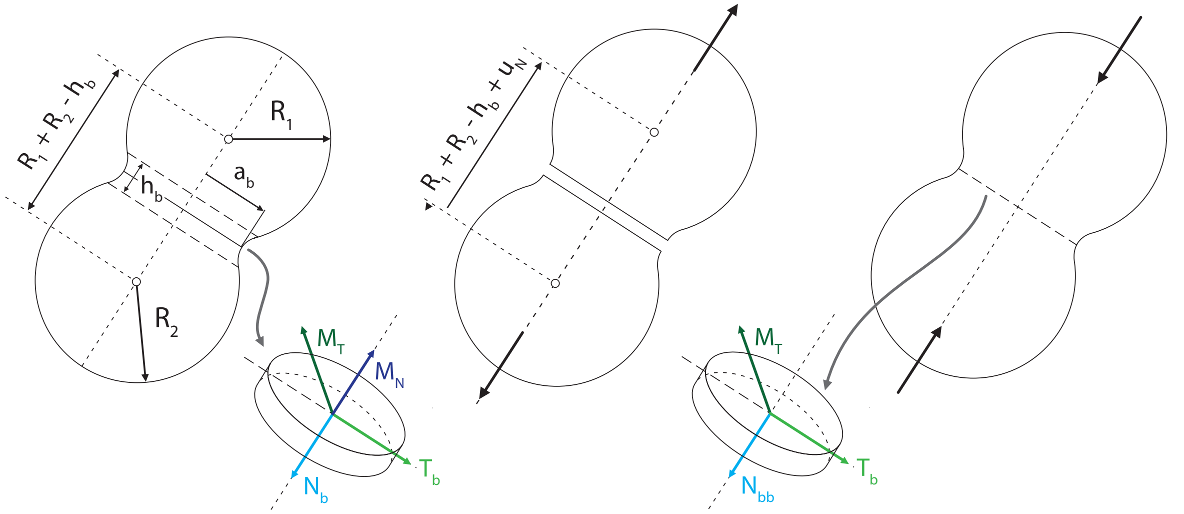

(a) Bonded contact (b) Broken contact (c) Contact after fracture

Figure 2.40: Model of the forces considered with dp3D for (a) bonded, (b) ruptured, and (c) contacting free surfaces after fracture [26].

Similarly, the tangential forces on each particle can be calculated based on the tangential displacement u_T and on the bond radius a_b:

$$T_b = E^{\star\star} f_T a_b u_T \tag{2.37}$$

where

$$E^{\star\star} = 4\left[\frac{(2-\nu_1)(1+\nu_1)}{E_1} + \frac{(2-\nu_2)(1+\nu_2)}{E_2}\right]^{-1} \tag{2.38}$$

and f_T is equal to:

$$f_T = \frac{1 + a^{\star 2}[\frac{\pi}{6}(1-\nu^2)(1+2a^\star) - a^\star]}{\sqrt{1-a^{\star 2}}} \tag{2.39}$$

Additionally, this model accounts for the moments transmitted either normally or tangentially through the elastic contact. These are respectively:

$$M_N = 4E^{\star\star}R^{\star 3}f_T a^{\star 3}\theta_N, \qquad M_T = 2E^\star R^{\star 3} f_N a^{\star 3}\theta_T \tag{2.40}$$

where θ_N and θ_T are the relative rotations for each direction. The fracture strength of a contact is limited by a critical strength σ_c that is determined based on an elastic stress intensity factor related to the contact size a_b and contact toughness Γ [148]:

$$\sigma_c = \sqrt{\frac{E}{1-\nu^2}\frac{\Gamma}{\pi a_b}} \tag{2.41}$$

It was determined from experiments and simulations that this fracture strength at contact-length scale may be approximated by the energy required to create two new surfaces (ideal brittle fracture) [148]. For most materials, this is on the order of a few $J\ m^{-2}$.

Once a contact has broken, the particles may resume contact but the adhesive forces of the two free surfaces must be taken into account. In compression, this is a non-issue as the contact will behave as a bonded contact would, in tension however the new normal force is denoted:

$$N_{bb} = N_b - 2\pi w R^\star \tag{2.42}$$

where $2\pi w R^\star$ represents the additional force necessary to separate the two surfaces from one another due to surface adhesion ($w \approx 2\gamma_s$). The broken contact will transfer a moment in the tangential direction (T_b) but no longer in the normal direction [26].

DEM has proved a powerful tool for modeling particulate systems with realistic results. Data shows that these models agree well with experimental data (Fig. 2.41). The dp3D software is constantly being updated to expand its capabilities and better reproduce realistic results [125, 158].

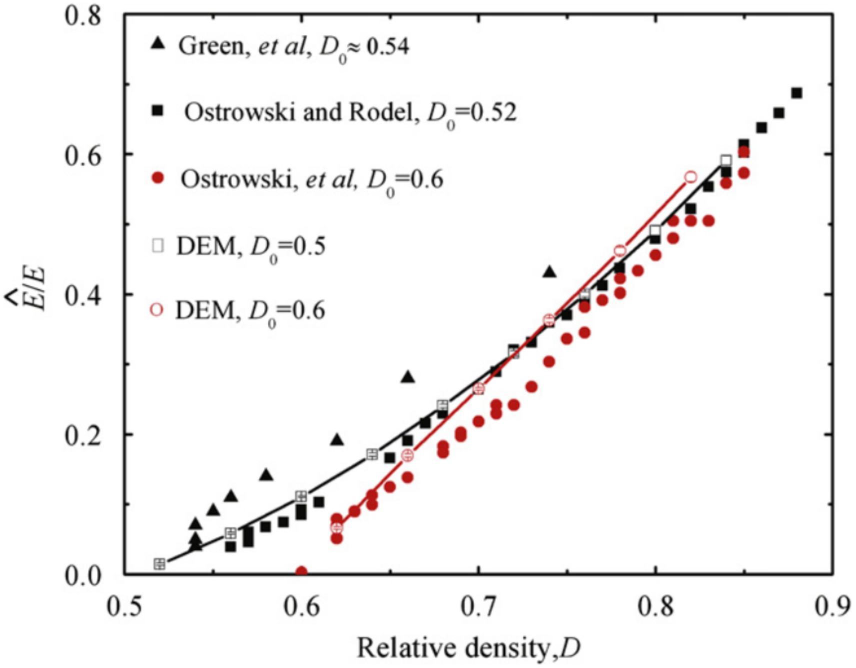

Figure 2.41: Normalized elastic modulus as a function of the relative density D for two values of the initial green relative density (D_0 = 0.5 and 0.6) [26]. Comparison with experimental data from Green et al. (1990); Ostrowski et al. (1998); Ostroski and Rodel (1999). Error bars (barely visible) are calculated from five DEM simulations.

2.7 Summary and Motivation

The sheer volume of knowledge concerning porous materials is overwhelming. There is an equally vast amount of information concerning solid oxide fuel cells, simulations and ceramic processing. Making meaningful connections between the bodies of knowledge is however difficult and relatively uncharted territory. We attempt to bridge some of the gaps in understanding by applying the process of freeze-casting to SOFC microstructures and trying, from a broad perspective, to reach some general conclusions concerning the characteristics of porous architectures.

Future improvements to SOFC technology will require higher degrees of both designed porosity and strength, and these two seemingly contradictory properties may be resolved by creating an engineered ceramic with an anisotropic and/or hierarchical porous microstructure [1, 43, 60, 106]. Using an anisotropically porous microstructure, an electrode could be designed to efficiently guide gas flow along short direct pathways to the TPBs where electrochemical reactions take place, thus improving conversion efficiency. Additionally, anisotropic microstructures can provide direct percolation pathways for ionic and electronic species between the cathode, anode, electrolyte and current collectors, which would represent a significant improvement over conventional SOFCs [60, 107, 108, 159]. Anisotropic structures could also be designed to provide increased strength in the direction of mechanical loading i.e. in-plane of the cell. Therefore, a tailored microstructure should allow for optimization of pore sizes; improved gas flow, maximization of the triple phase boundaries, increased strength and an overall increase in cell lifetime [14, 51, 107, 108].

Freeze-casting as a method to create porous ceramics is little over a decade old but has received a significant amount of recognition for its flexibility and impressive capabilities. There is a large volume of knowledge concerning its capabilities and properties of resultant structures. Still, a number of unresolved questions exist including exactly what parameters control microstructure and the phenomena that occur within the slurry during freeze-casting. Rather than treating freeze-casting merely as a means to an end, we attempt to expand and document further capabilities of freeze-casting and study the method itself.

3

Methods and Materials

"A watched freeze-cast never freezes."

– Aaron Lichtner, *Everyday of my life...*

Chapter Contents

The Methods and Materials chapter is laid out as follows. The first section will discuss the various methods used to physically process porous ceramics. These include procedures for processing isotropic and anisotropic microstructures and will discuss both the successes and failures. Section 3.2 deals with the techniques used to characterize and analyze these porous ceramics. Finally, section 3.3 briefly describes the digitization of the porous ceramics and their analysis using discrete-element methods.

3.1 Specimen Processing

Porous ceramics were made by either slip-casting[1] or freeze-casting slurries composed of either LSM-YSZ, NiO-YSZ, alumina, zirconia, hydroxyapatite (HAP) or silica. For the most part, total porosity ranged from a low of approximately 20 vol. % up to 70 vol. % porosity. The micro to macroporosity ratio was controlled using the sintering temperature, the volume fraction of pore formers (for isotropic samples) and the solid particle volume fraction (for anisotropic samples).

3.1.1 Aqueous Slurry Dispersion

Irregardless of whether or not the final sample was to be slip-cast or freeze-cast, all samples started from an aqueous dispersion. Depending on the characteristics of the dispersed media used, this could be a complicated process (see section 2.4). Typically, a slurry contains the solvent, ceramic powder(s), a dispersant and often times a binder to provide strength in the green-state. The specific make-up for the different slurries used are given below. All slurries were stabilized using electrosteric dispersion methods.

LSM - YSZ (Cathodes)

Ceramic suspensions were prepared by mixing deionized water (DI) with 1.6 - 2.4 wt. % (of the solids) of an ammonium polymethacrylate dispersant (Darvan C-N, R.T. Vanderbilt Co., Norwalk, CT) at neutral pH after which, 3 - 5 wt. % (of the solids) of polyethylene glycol (PEG) binder (Polyethylene Glycol 400 MW, Carbowax PEG 400 NF, FCC Grade,

---

[1] Slip-casts included Poly(methyl) methacrylate (PMMA) pore formers to create macropores.

Union Carbide Inc., Danbury, CT) was added into solution [86][2]. The solution was stirred for 20 minutes to ensure complete homogenization of the dispersant and binder. The pH of the solution was adjusted back to neutral using nitric acid and then YSZ powder (d_{50} = 0.3 um, TZ-8Y, Tosoh, Japan) was slowly added while mixing. The pH was again readjusted to between pH 7 - 8 with nitric acid and LSM powder (d_{50} = 0.8 um, LSM20-P, NexTech Materials, Lewis Center, OH) was slowly added under continued mixing and heavy sonication (S-450A, Branson Ultrasonics, Danbury, CT). The ratio of LSM to YSZ was kept at a constant 40:60 vol. % as per [160]. This suspension was used for both anisotropic (freeze-cast) ceramics and for isotropic (slip-cast) samples by the addition of PMMA polymer bead pore-formers.

Table 3.1: Standard LSM-YSZ Slurries 20 - 40 vol. % Solids Content

Component	20 % solids	30 % solids	40 % solids
YSZ	39.8 g	39.8 g	39.8 g
LSM	29.6 g	29.6 g	29.6 g
DI-Water*	43.5 mL	23.85 mL	13.9 mL
Darvan C-N*	1.0 mL	1.3 mL	1.64 mL
PEG	1.845 mL	1.845 mL	1.845 mL

* Only the water and dispersant ratio were changed to produce different slurries

NiO-YSZ (Anodes)

NiO-YSZ slurries were made using a pre-mixed powder composed of 34 wt. % YSZ and 66 wt. % NiO (NexTech Materials, Lewis Center, OH). Unlike the LSM-YSZ slurry, no specific conditions were required for a satisfactory suspension to be created (Table 3.2). Approximately 2 wt. % (of the powder) of Darvan C-N was mixed into deionzed water. A PEG binder (4 wt. % of the powder) was then incorporated to provide strength in the green-state. The solution was mixed for 20 minutes to ensure complete dissolution of the dispersant and binder. NiO-YSZ pre-mixed powder was then slowly incorporated while mixing.

---

[2] Please note that both the dispersant and binder were received pre-diluted in solution. The reported amounts used refer to the solutionized dispersant and binder. Density of PEG and Darvan solutions = 1.1 g mL^{-1}

Table 3.2: NiO-YSZ Slurry

Component	**Amount**
NiO-YSZ	80.1 g
DI	33.1 mL
Darvan C-N	1.45 mL
PEG	2.90 mL

Other Materials

Because of ice's ability to exclude particles indiscriminately, multiple ceramics (polymers and metallic powders can also be used) can easily be made using freeze-casting. In addition to LSM-YSZ and NiO-YSZ, alumina, zirconia, silica and hydroxyapatite were all freeze-cast for various applications, see table 3.3. The general dispersion procedure is as follows:

> **General Dispersion Procedure:** Darvan C-N and a PEG binder are dissolved in deionized water for a minimum of 20 minutes. The desired particles are then slowly added under continued mixing, applying sonication as necessary. The slurry can then be used directly or stored in an airtight container.

3.1.2 Slip-Casting of Isotropic, Hierarchical Porous Ceramics

For the isotropically porous samples, it was important to match the total porosity values and the average size ranges of the microstructural features (micro and macropores) achieved during freeze-casting. This allowed us to decouple the effect of the pore anisotropy itself. For the slip-casts, the macroporosity was controlled not by the ratio of water to ceramic but by the ratio of the volume of the fugitive polymer particles to the ceramic $\left(Solid\ Loading = \frac{V_{Ceramic}}{V_{Pore\ Formers}+V_{Ceramic}}\right)$. PMMA beads with diameters ranging from 10 - 50 microns, were added to the same aqueous slurries used to make freeze-casts (see section 3.1.1). The slurries were then de-aired in a vacuum dessicator to remove any air and pipetted into cylindrical Teflon molds sitting atop a flat porous gypsum plate (Fig. 3.1). The gypsum slowly drew the water out of the slurry allowing the suspended particles to settle into a pellet. Once completely dry, these green-bodies were removed from their molds. They were then partially sintered to replicate the intrinsic microporosity found within the freeze-cast samples.

Table 3.3: Slurries made throughout this thesis

Slurry	**Material Make-up**	**Supplier**	**Solids vol. %**	**Dispersant (Darvan wt. %)**	**Binder (PEG wt.%)**	**Applications + Notes**
LSM-YSZ	60 vol. % Lanthanum-Strontium Manganite 40 vol. % 8 mol. % Yttria-Stabilized Zirconia	FuelCellMaterials, Lewis Center, OH Tosoh USA Inc. Grove City, OH	15 - 40	1.6 - 2.4	3 - 5	SOFC Cathodes, pH must be held between 7 - 8
NiO-YSZ	66 wt. % Nickel-Oxide 34 wt. % 8 mol. % Yttria-Stabilized Zirconia	FuelCellMaterials, Lewis Center, OH	20 - 25	2	4	SOFC Anodes
Alumina	Alumina	Praxair Chemicals	9 - 46	1.5 - 2.2	2.2 - 4.4	Process Characterization, Water Filtration
YSZ	8 mol. % Yttria-Stabilized Zirconia	Tosoh USA INc. Grove City, OH	30 - 45	2.4	3	Dense Electrolytes, Ablative Coating Substrate
HAP	Hydroxyapatite	Transtech Inc., Adamstown, MD	25	1 - 3	3	Bone-Scaffolds
Silica	Silicon Dioxide	Sigma-Aldrich	10 - 20	1 - 5	3	Only low solid loadings were possible

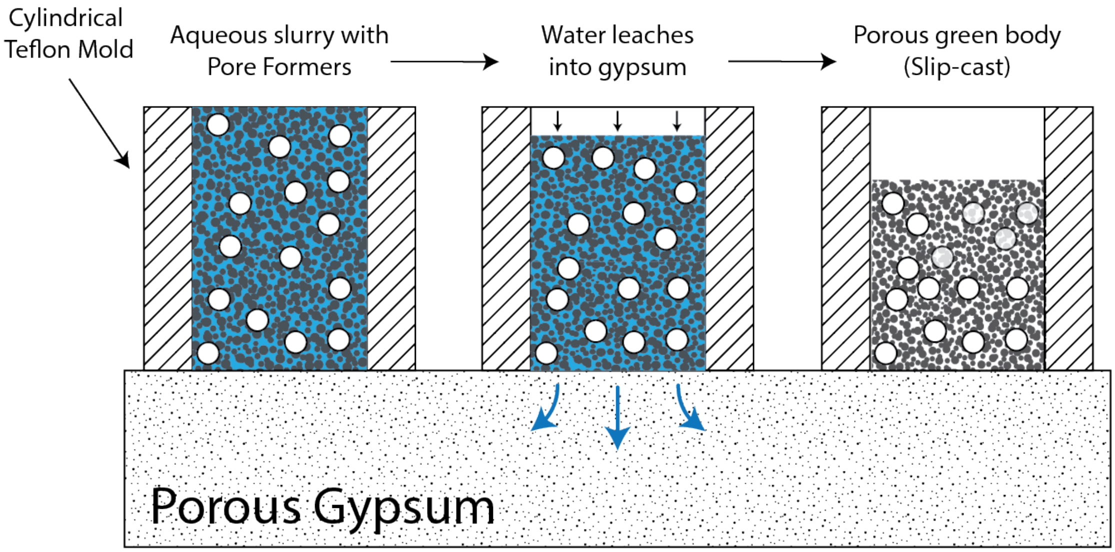

Figure 3.1: A slurry containing PMMA pore-formers is poured into teflon molds sitting on a porous gypsum platen. As the water is drawn into the gypsum, the particles and pore formers settle to form a green-body.

Unfortunately, the slip-casts did not always consolidate evenly. Often times, during the slip-casting process the top of the sample shrunk unevenly compared with the base. Mechanical grinding after sintering was often necessary to correct these discrepencies to make as perfect a cylinder as possible.

3.1.3 Freeze-Casting of Anisotropic, Hierarchical Porous Ceramics

Freeze-Casting Equipment

At the University of Washington, we have two custom built freeze-casters, each capable of producing different thermal conditions (Fig. 3.2).

Each freeze-caster is controlled by the manual addition of liquid nitrogen into the reservoirs surrounding the copper cooling fingers. The temperature at the freezing surface is monitored using K-type thermocouples. The low-speed freeze-caster however includes a proportional-integral-derivative (PID) controlled heating sleeve near the freezing surface making it capable of high precision thermal profiles from approximately 1 - 5 °C min^{-1}. Additionally, temperatures can be kept constant over long periods of time between a range of -100 °C and 60 °C using the thermal feedback loop. The high-speed freeze-caster has high surface area copper fins which when submerged in liquid nitrogen can create con-

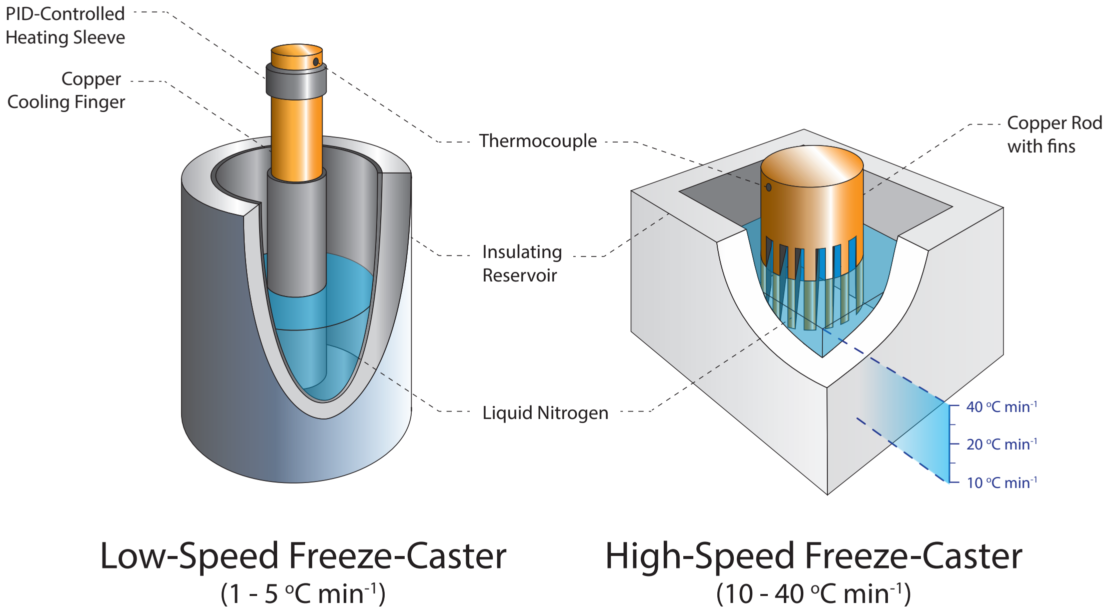

Figure 3.2: Freeze-casting equipment used during this thesis.

trolled freezing rates from 10 to 40 °C $\min^{-1}$. The rate is controlled by holding the nitrogen level at pre-calibrated heights along the copper fins. Additionally, the high-speed freeze-caster has a larger freezing surface allowing for the creation of multiple small samples at the same time or single large diameter samples up to 76 mm in diameter. The standard molds used for freeze-casting are thick-walled acrylic or Teflon cylinders that have been carefully machined and polished on their interior surfaces to be as smooth as possible (Fig. 3.3).

The molds were attached to either the low or high-speed freeze-caster with a thin layer of vacuum grease that served the additional purpose of making the mold water-tight. Slurries were always de-aired in a vacuum dessicator prior to being carefully poured into their molds. A small amount of room was left at the top of the mold to allow for expansion of water to ice during freeze-casting.

Two-sided freeze-casting

The low-speed freeze-caster is actually capable of controlling the temperature on both sides of the slurry since there is an opposing copper cooling finger, nitrogen reservoir and PID-controlled heating sleeve setup suspended opposite the one shown in figure 3.2.

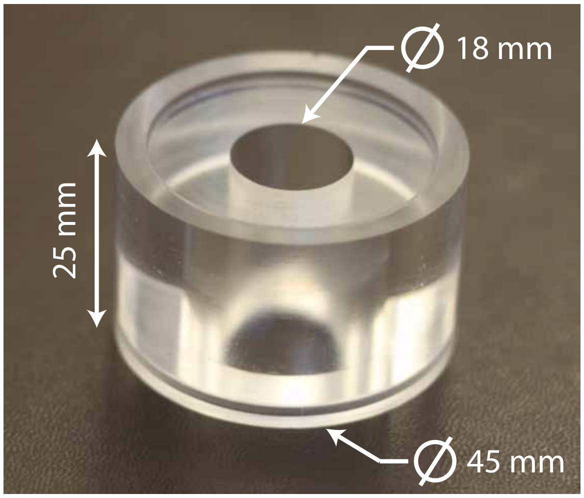

Figure 3.3: Typical acrylic mold used for freeze-casting. The teflon molds (not pictured here) do not have the lip on the top and bottom making them easier to attach to the high-speed freeze-caster.

Research had indicated that controlling the temperature on both sides of the suspension would allow greater control of the microstructure [83, 97] however our preliminary findings indicated that not only was controlling the temperature on both sides of a freeze-cast unnecessary for the types of microstructures we desired (long linear pores), but often it led to logistical problems with the experiment. For example, in order for the top cooling finger to be in contact with the suspension, it was necessary to slightly overfill the mold and press the top down onto it. If this step wasn't performed, there was a layer of insulative air between the copper finger and slurry. If the freezing surface was in contact with the slurry, there were issues which stemmed from the non-negligible expansion of water as it turns to ice. For example, if the top setup remained fixed in place, significant residual stresses built up in the freeze-cast resulting in a poor microstructure. If the top freezing surface was able to freely move as the ice expanded, often times it lost full contact with the freezing suspension. For these reasons one-sided cooling was the primary method used in this investigation.

Initial Conditions: Quenching vs. Homogenous Cooling

There are two general initial conditions used for freeze-casting. The first is known as *quenching*. This is when a slurry at room temperature is poured into a freeze-casting setup that has already been pre-cooled to some degree. Quenching was used when rapid, initial nucleation was desired. The second initial condition is dubbed *homogenous cooling*[3]. Here, every part of the setup begins at ambient temperature then the temperature of the freeze-casting setup is slowly reduced in accordance with some desired thermal profile. This established a strong thermal gradient within the slurry before the nucleation temperature was reached, resulting in a quick transition to steady-state growth and better-aligned crystals within the steady-state zone SSZ of the microstructure (Fig. 3.4).

Freezing Profile: Dynamic vs. Static Freezing

Related to the initial conditions is the freezing profile as a function of time. The simplest thermal profile is a single, unchanging *static* temperature from $t = 0$ until the sample is completely frozen. A static profile often goes hand-in-hand with initially quenching a slurry. When a slurry-filled mold is placed in contact with such a setup the resulting microstructure is erratic and ill-defined due to the fast nucleation and weakly-defined temperature gradient. This type of structure is characterized by long initial (IZ) and transition zones (TZ). Additionally, because the thermal gradient is static, as the freezing front grows forward, the drive for growth decreases and so the ice crystals increase in thickness within the steady-state zone (Fig. 3.4). Our setups allow for what is called *dynamic freezing* where we can start from any temperature and then change the temperature at will (Fig. 3.4). The most common profile used begins with the entire system, slurry and mold included, starting at ambient conditions. The temperature of the copper-cooling finger is cooled at a linear or parabolic temperature rate by the addition of liquid nitrogen. This creates a strongly oriented temperature gradient in the slurry far before nucleation begins. After nucleation, the crystals will quickly align along the thermal gradient in the slurry through a process of competitive growth. The resulting structure is highly oriented and reaches steady-state growth soon after the initial nucleation step.

It is also possible to pre-cool (quench) the freeze-casting setup to a desired temperature, introduce the mold and slurry (which may or may not be pre-cooled) and begin dynamically changing the temperature profile at this point. The resulting structure will include a large IZ and TZ region because freezing starts quickly before a substantial temperature gradient has established itself. Once the thermal conditions within the slurry "equilibriate" the SSZ region grows much the same as it would if the entire freeze-casting set-up had started from ambient conditions (Fig. 3.4).

---

[3] This was the primary method used in this thesis

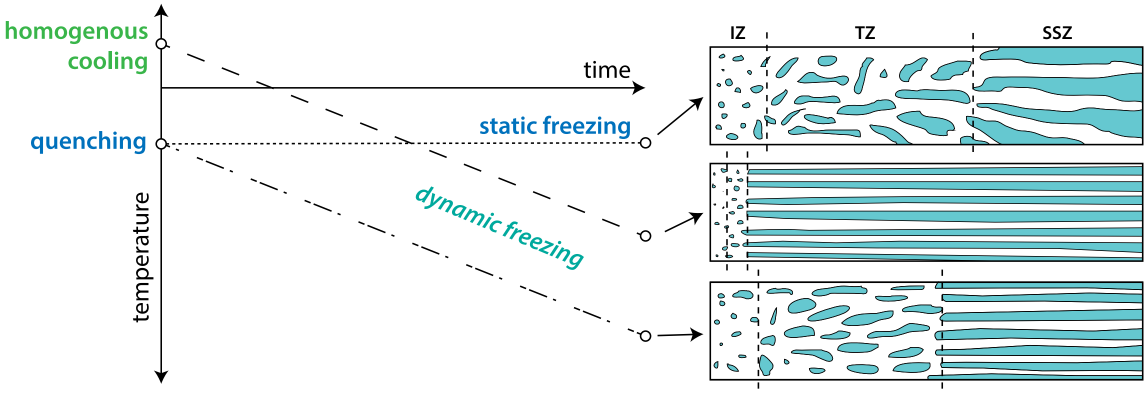

Figure 3.4: Representative thermal profiles which can be used during freeze-casting and schematic of their associated microstructures.

During freezing, the temperature of the copper cooling finger is recorded at regular intervals and the height of the freezing front can also be recorded using timed photos of the freezing mold. These can later be used to establish the temperature profile and associated solidification front velocity. It should be noted that certain slurries are significantly easier to track than others. For example, the front in an LSM-YSZ slurry shows up as significantly darker than the unfrozen slurry. For alumina, silica and pure-YSZ slurries, the tracking of the freezing front was a challenge (due to the lack in contrast between the slurry and frozen solid).

Typical Freeze-casting Procedure:

1. Secure mold to freezing surface with vacuum grease
2. De-air slurry using a vacuum dessicator
3. Establish desired initial conditions (quench or homogenous cooling)
4. Fill mold leaving some space at the top for expansion
5. Control freezing profile by adding liquid nitrogen
6. Once frozen, place in freeze-dryer (to sublimate ice) or freezer for storage

Freeze-Drying and De-molding

After complete solidification, the castings were freeze-dried while still in their molds (FreeZone 1L; Labconco, Kansas City, MO) for a minimum of 12 hours to ensure complete removal of the solvent crystals. At this point the structure is held together only by the organic binder and weak particle-particle attractions. Therefore, the samples must be handled gently. De-molding is usually accomplished using a small, smoothly polished metal or plastic cylinder whose diameter is slightly smaller than that of the mold itself. The green-body is gently worked out of the mold using light pressure. It was sometimes beneficial to press on the sample from either side alternatively until it came out freely. If the structure is difficult to remove, often there is a small amount of vacuum grease preventing easy sliding. This should be removed. If once the freeze-cast is removed it turns to powder there is a good chance that more binder is required. Samples made with low solid loadings or slow freezing rates are typically the most difficult to remove successfully.

3.1.4 Sintering

Samples were sintered in air by heating at 2 °C min^{-1} to 450 °C and holding until all organic compounds were burned out (approximately 2 - 4 hours) and then heated at 5 °C min^{-1} to the final sintering temperature where they were held for 2 hours (CM Rapid Temp Furnace, Bloomfield, NJ). The majority of samples, unless otherwise specified were sintered to 1200 °C. This temperature was chosen because it left a significant amount of residual interparticle porosity, maintained adequate strength and did not result in the formation of insulative phases at the grain bondaries between LSM and YSZ. Samples were cooled to room temperature at 10 °C min^{-1}. Figure 3.5 shows the complete thermal profile.

3.1.5 One-Pot Isotropic, Hierarchical Zirconium Monoliths

At the beginning of the project, a method detailed by Drisko et al. [79] to make zirconium monoliths with isotropic hierarchical porosity was attempted. This method was highly attractive because of its ease-of-use and versatility.

1. Dissolve pluronic in ethanol at 35 °C with the $ZrCl_4$ in a vial
2. Add furfuryl alcohol and close the vial
3. Gently agitate for 15 minutes until there is a noticable color change (clear → dark brown). During this time, the furfuryl alcohol is polymerizing into poly(furfuryl) alcohol (PFA)

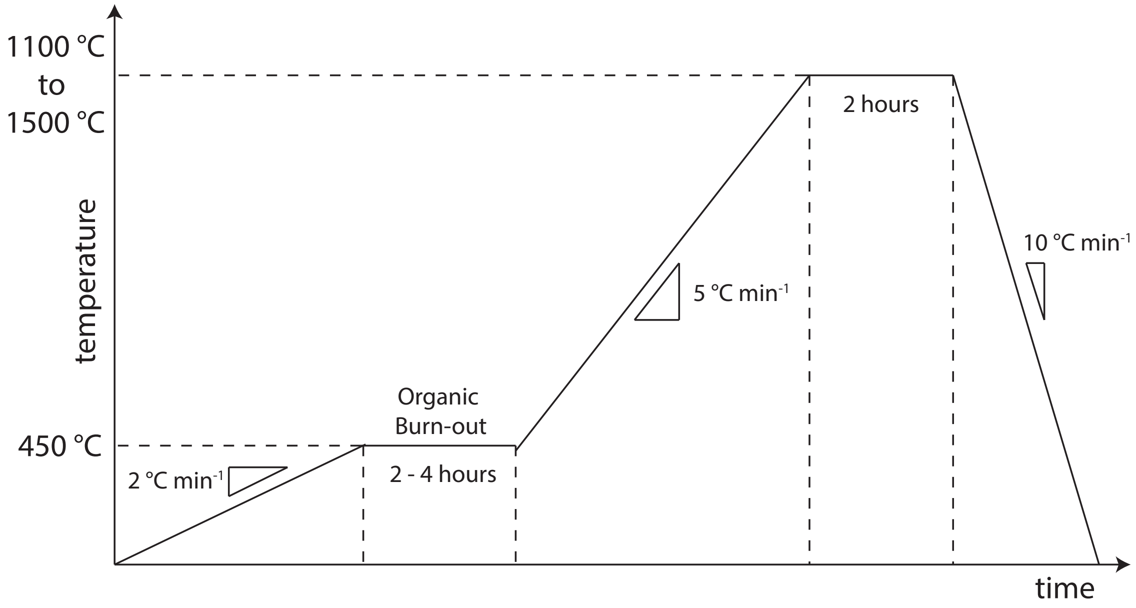

Figure 3.5: Standard sintering profile used throughout the thesis, the top temperature is chosen based on the material and the degree of partial sintering desired.

4. Remove lid and put punctured parafilm over it
5. Allow to dry under ambient conditions for 24 hours
6. Dry for several more days between 60 - 135 $^\circ C$
7. Calcine under low air flow at 450 $^\circ C$ for 2 hours

The reagents are shown in table 3.4.

Table 3.4: Formulation for One-Pot Synthesis of Porous Zirconia

Reagent	Amount
$ZrCl_4$	0.38 g
Pluronic Acid	0.125 g
Furfuryl Alcohol	0.35 mL
Ethanol	3.81 mL

The generalized methodology behind this sol-gelation process is depicted in figure 3.6.

A visiting student, Ms. Maya Cherif, worked on adopting this approach to make LSM-YSZ composite ceramics using appropriate sols. The results are detailed in her report. This approach has potential but needs to be investigated further.

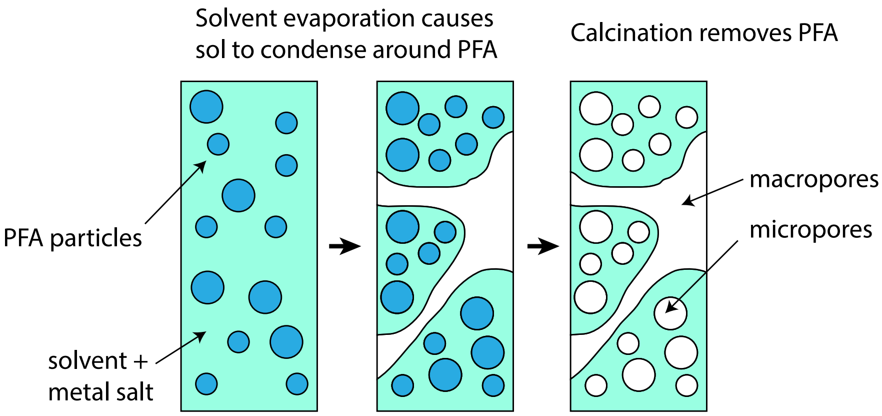

Figure 3.6: Basic schematic explaining how the sol-gel produces a hierarchical structure.

3.1.6 Processing of Half-Cells

One of the desired goals of this project was to fabricate and test working SOFC half-cells (cathode and electrolyte) and determine the effect of various anisotropic and hierarchical microstructures on electrochemical behavior. Numerous techniques were developed to fabricate freeze-cast half-cells all with the ultimate goal of securing a highly porous cathode to a dense YSZ electrolyte. Because it was our desire to maintain the microporosity within the walls (hierarchical nature), we were constrained in sintering temperature (maximum 1200 °C). Additionally, due to the nature of freeze-casting, the region of interest (aligned macropores) is often located in the center of the freeze-cast, meaning that methods had to be developed to remove the center of a freeze-cast and then attach that to a dense YSZ electrolyte without sustaining damage to the internal structure of the cathode.

Preliminary Methods

Many different procedures were developed and tested to create SOFC cathode half-cells. They are outlined below.

"Cut and Sinter" Starting with a full LSM-YSZ freeze-cast, sinter it to 1100 °C (100 °C below the final desired sintering temperature) then infiltrate it with resin. Remove a slice (~1 - 2 mm thick) transverse to the freezing direction somewhere within the SSZ. Sinter this to either a fully-dense YSZ pellet or an unsintered YSZ tape. This can be done with or without pressure. It was often beneficial to apply a thin layer of YSZ slurry as a sort of "glue" between the layers.

"YSZ sol-gel" A sol-gel was created and dip-coated onto the YSZ electrolytes and cut rounds of LSM-YSZ freeze-cast. The two pieces were then pressed together and pyrolyzed. Although the sol was created successfully, unfortunately the sol-gel did not provide a significant amount of attachment between the layers. The formulation of the YSZ sol is given below.

Compound	**Amount**
Zirconium isopropoxide (70 wt. % in 1-propanol)	2.24 mL
Yttrium (III) Nitrate * H_2O	0.306 g
1-propanol	6.18 mL
Acetylacetone	0.417 mL

To do this, zirconium and yttrium solutions were prepared under an inert N_2 atmosphere then mixed together to form a sol-gel. For the Zr-solution, Zr-isopropoxide was diluted with 1-propanol then chelated with acetylacetone. For the Y-solution, the yttrium salt was slowly dissolved in 1-propanol. The two solutions were combined while stirring vigorously. After homogenization the electrolyte and electrode were dip-coated in the solution, still under inert atmosphere. The solvent was then evaporated off at 60 $^\circ C$ for 20 minutes, consolidating the YSZ film. The half-cells were removed from the glove box and pyrolyzed at 1000 $^\circ C$ for 2 hours in air.

"Freeze and Attach" Attempts were made to freeze the composite cathode slurry directly onto either a YSZ pellet or tape. Because we desired to test the effect of the anisotropic SSZ region, the electrolyte (YSZ) had to be placed at the top of the mold during freeze-casting rather than at the freezing surface. Attachment between the two layers was rare and difficult to achieve. It was found to greatly depend on the surface roughness of the electrolyte.

"ESD Coating" Pure YSZ was applied using Electro-Spray Deposition (ESD) to thin, sintered and uninfiltrated freeze-cast cathodes. Varying solution flow rates, application temperatures and times were used to create as dense a layer as possible [161]. Two different formulations were attempted:

	Suspension		Solution	
Formulations	Ethanol	25 mL	Ethanol	13.3 mL
	Acetlyacetone	12.5 mL	Butyl Carbitol	26.6 mL
	YSZ	1.0 g	Zr Acetate	915.6 mg
	–	–	YCl_3	62.5 mg
Target Temp.	$75\ ^{\circ}C$		$350\ ^{\circ}C$	
Deposition Time	55 min		1 hour 50 min	
Flow Rate	0.4 mL hr^{-1}		0.4 mL hr^{-1}	
Voltage	5.7 keV		5.7 keV	
Thermal Treatment	1200 °C		800 °C	

Both the suspension and solution were agitated for an hour then stirred overnight before being used for ESD.

To perform ESD the desired formulation, either the suspension or solution, was drawn into a syringe and placed in a servo-controller pump. The solution was slowly pumped through a fine gauged needle and converted into an aerosol by applying a voltage potential between the needle tip and sample target. Because the sample target was heated, the aerosol evaporated on impact leaving a thin film.

ESD samples made with either the suspension or solution were subsequently sintered (or pyrolyzed in the case of the solution), sectioned and imaged for examination.

In short, many different methods were attempted to make freeze-cast SOFC cathode half-cells with only minimal success. Different sintering profiles, surface preparation techniques were used but they mostly resulted in half-cells with only marginal strength. The most effective of the preliminary methods was “cut and attach” using a YSZ slurry as a glue between the two layers. It was discovered late in the project that two slurries could be made and freeze-cast simultaneously into one ceramic.

The working solution we present here is not optimal but it shows the greatest promise to date for fabricating working SOFC button half-cell cathodes by freeze-casting.

Suggested Procedure for Further Investigation

Rather than fight the typical freeze-cast morphology (ie. IZ, TZ, SSZ), we were able to use it to our advantage. We exploited the fact that the isotropic IZ region of our freeze-cast is dense by actually freezing a pure YSZ layer within this layer effectively creating our YSZ electrolyte in-situ. Two slurries were placed one on top of the other so that the pure-YSZ layer was closest to the freezing surface (Fig. 3.7). The viscosity of the YSZ slurry was high enough so that (1) it held its shape without the mold walls and (2) it prevented mixing with the more dilute LSM-YSZ cathode layer.

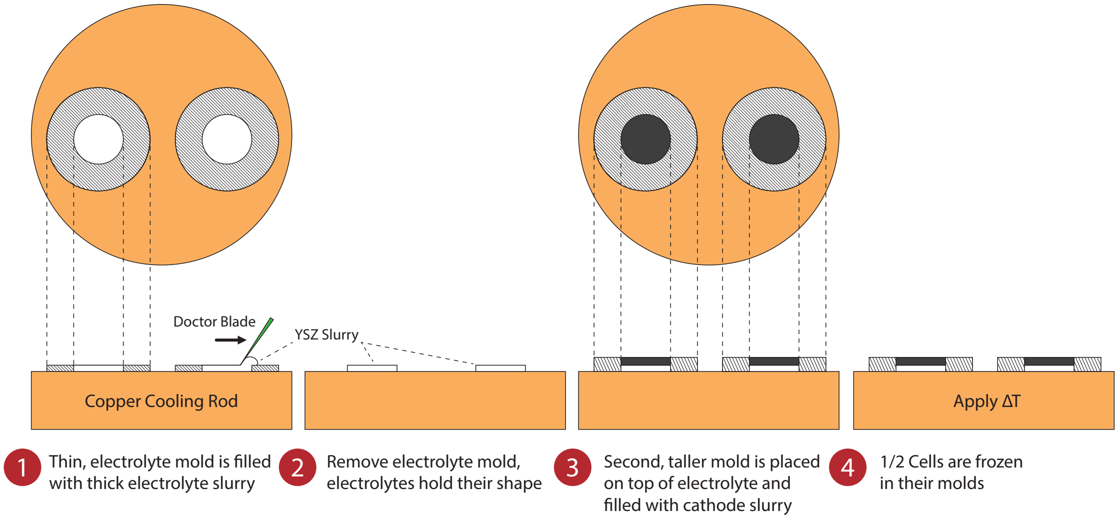

Figure 3.7: Suggested half-cell fabrication procedure.

Initially, a paper mold with cut out circles approximately 23 mm in diameter was attached with vacuum grease to the freeze-casting surface. A thick, high solid content YSZ-slurry was spread evenly across this mold making sure to create a layer of uniform thickness. The fact that the mold was paper helped prevent self-wetting of the slurry. The paper template was removed and a thin plastic mold 2.1 mm tall with a 23 mm inner diameter was placed on top of the YSZ layer. The LSM-YSZ slurry was carefully poured in until the mold was full. The differing viscosities of the slurries prevented them from mixing significantly. The samples were then frozen and freeze-dried in their molds. Finally they were de-molded, sintered[4] and prepared for electrochemical testing. Different ratios of electrolyte thickness to electrode thickness were tested.

---

[4] Weights were often applied during sintering to reduce curvature of the half-cells.

3.2 Characterization and Analysis Techniques

3.2.1 Rheological Measurements

The rheological properties of the various slurries were evaluated using a Haake VT550 Rotational Viscometer (Thermo Fisher Scientific, Inc., Waltham, MA, USA) with an SV-2P type sensor and concentric cylinder (SVP) geometry. The viscosities were measured at ambient temperature using a controlled step-wise shear rate from 20 - 200 s^{-1} to investigate the shear rate dependent viscosity.

3.2.2 Archimedes Density Measurement

The weight of the porous ceramics were recorded dry (m_{dry}). They were then allowed to soak in deionized water until all the open pores had filled with water (minimum of 30 minutes). The ceramic was then weighed twice on an Archimedes apparatus, once wet (m_{wet}) and then once submerged underwater on a spring ($m_{submerged}$). Using the theoretical density of a 100 % dense material (d_{mat}), the apparent density, total porosity, open and closed porosities can be calculated from these three weights. The process is repeated a minimum of three times and the reported numbers are the average of these measurements. Using the Archimedes principle we calculate the mass of water displaced and the total porosity of the submerged sample:

$$m_{water} = \overbrace{m_{dry} \frac{d_{water}}{d_{mat}} \frac{1}{1 - P_{total}}}^{\text{Weight of displaced water}} = m_{dry} - m_{submerged} \tag{3.1}$$

where P_{total} is the total pore fraction of the system. The mass of water imbibed (taken up) is then:

$$m_{imbibed} = m_{water} - m_{dry} \tag{3.2}$$

The mass of imbibed water can immediately give the value of open porosity P_{open} simply by dividing $m_{imbibed}$ by the density of water d_{water}. The value of closed porosity is found by subtracting P_{open} from P_{total}.

Below is a table of the non-porous densities used for various tested materials. These were also used when calculating solid loadings of suspensions.

Table 3.5: Densities of used materials (g cm^{-3})

LSM	**YSZ**	**NiO**	**Alumina**	**HAP**	**Silica**	**PMMA**
6.10	5.90	6.67	3.95	3.16	2.65	1.18

3.2.3 XRD Analysis for Phase Composition

In the literature, it has been observed that LSM and YSZ may react together under appropriate conditions to form the $La_2Zr_2O_7$ phase which is detrimental to electrode performance due to its low conductivity [162, 163]. To establish whether or not this phase was present within the composite material, X-ray diffraction (XRD) patterns were taken of sintered LSM-YSZ freeze-casts that had been crushed into a fine powder after sintering. Diffractograms were taken with an X'Pert Pro MPD diffractometer (PANalytical Company) using Bragg-Brentano Geometry and a Copper $K\alpha$ wavelength of 1.5418 Å. The patterns were indexed using the EVA software database.

3.2.4 2D Image Analysis Techniques

Freezing Front Tracking

Instantaneous freezing velocity values were attained by taking photographs of the freezing front (Canon Rebel Ti1, 50mm f1.8 fixed lens) at regular intervals as it progressed through the slurry (Fig. 3.8). Additionally, an image analyis batch method was created (ImageMagick[5]) to locate and track the freezing front within the image thereby allowing precise measurements to be taken. As a note, it is far easier to locate the freezing front in a non-white slurry (i.e. LSM-YSZ or NiO-YSZ).

Thermal Imaging

Thermal image scans were taken using a FLIR i7 Compact Thermal InfraRed Imaging Camera. These were taken at regular intervals and then fed into a computer for image

---

[5] **ImageMagick** - Image stack processing in UNIX-based systems `http://www.imagemagick.org/`

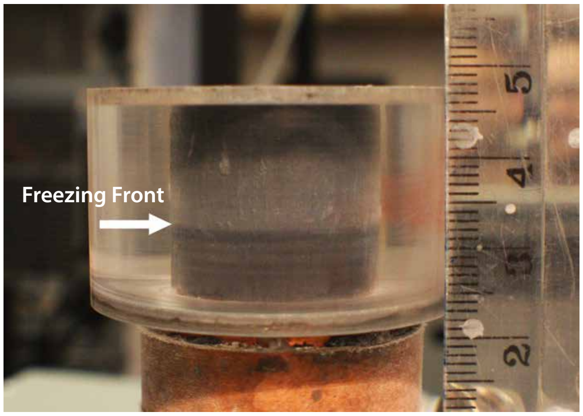

Figure 3.8: Solidification of a 23 wt. % solids slurry freezing at 5 °C min^{-1}. This image was taken 10 minutes into the solidification process. The darker region below the arrow on the lower third of the sample is the frozen slurry.

analysis [6]. A range of temperatures from -40 °C to 15 °C was selected as the range of interest. The thermal camera was accurate to within 1 - 2 °C. Using this setup, we were able to track specific isotherms as they moved through the casting mold.

Sample Preparation

Quite often because samples were only partially sintered, they required additional strength during preparation, handling and characterization. The following is the typical sample preparation that was done for most samples, both anisotropic and isotropic (Fig. 3.9).

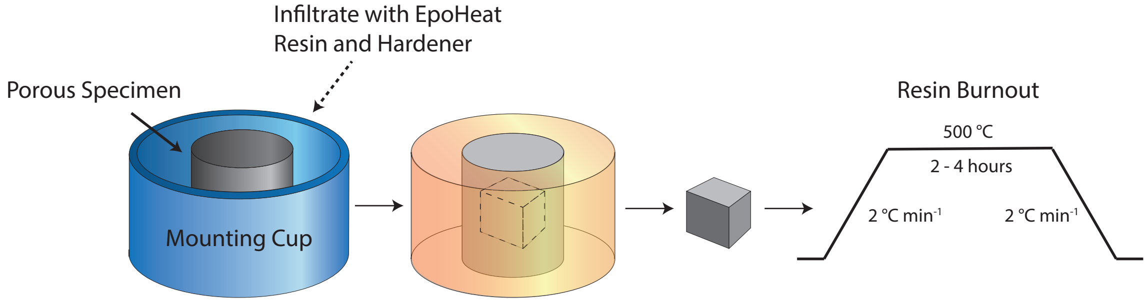

Figure 3.9: General sample preparation method. The pre-sintered porous ceramic is infiltrated with a low-viscosity resin then sectioned and polished as needed. The sample can be imaged in this state or the resin can be removed without causing significant damage to the internal structure by heating it slowly to 500 °C in air.

The porous ceramic, no matter the preparation or material, was allowed to dry in air or a

---

[6] **ImageJ** - Image Analysis software `http://imagej.nih.gov/ij/`

drying oven (often after Archimedes density measurement) and then placed into a specimen mounting cup. A low-viscosity polymer resin (EpoHeat, Buehler, Irvine, CA) was poured around the sample and allowed to infiltrate the pores. By heating the sample and resin to approximately 55 °C in a warming oven, the viscosity reduced to nearly that of water, driving the resin into even the smallest open porosity. Once cured, the ceramic was easily handled since the pores were now supported from collapse by the resin. Sections could then be cut out using a low-speed diamond saw. These were polished for imaging and further characterization. Often, once the sample was fully shaped and polished, the resin was burned-out so that only the freeze-cast structure was visible. This was accomplished by heating at 2 °C min^{-1} to 500 °C in air and then cooling at 2 °C min^{-1} to room temperature.

Optical Microscopy

Optical microscopy was used throughout the project for a number of studies including characterizing freeze-cast porous structures. An Olympus AX70 optical microscope along with AnalySiS 3.1 software was used for the majority of optical microscopy.

Scanning Electron Microscopy (SEM)

Various SEMs were used throughout the course of this thesis. For general imaging purposes, the freeze-casts and slip-casts were imaged without resin [Fig. 3.10 (a)]. For quantitative structural characterization, samples were generally infiltrated with resin before imaging [Fig. 3.10 (b)]. This made it easier to achieve representative flat cross-sections that could be easily analyzed using image analysis. All samples were sputtered using a Au/Pd target for a minimum of 50 seconds and secured to an SEM stub using carbon tape prior to imaging. The majority of samples were imaged at low voltages (5 - 10 keV).

Electron Dispersive Spectroscopy (EDS)

Electron dispersive spectroscopy (EDS) was used to examine spatial distributions of certain elements within our microstuctures. An FEI Sirion SEM coupled with an EDAX system allowed for high-resolution element detection. A 10 keV accelerating voltage and spot size of 6 was used for the majority of elemental mapping. The EDAX system was primarily

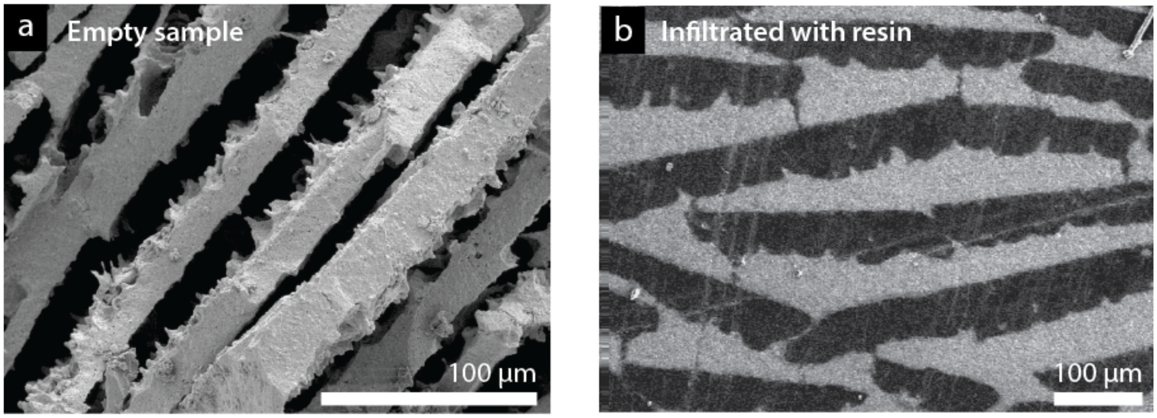

Figure 3.10: Images of freeze-casts (a) as-sintered or (b) after infiltration and subsequent polishing.

calibrated to search for zirconium and lanthanum to discern for YSZ and LSM. Zr and La have Lα X-ray band edges at 2.0 and 4.6 keV, respectively. Images were processed using the AzTeK EDS program available at the Nanotech User Facility (NTUF) at the University of Washington.

Dilation-Erosion Analysis

Using a set of high-contrast images gathered from either SEM or optical microscopy (Fig. 3.10), we performed thresholding operations to isolate macropores from the walls creating a binary image. A plug-in was developed for ImageJ which took this binary image and performed subsequent dilation and erosions operations with a larger number of pixels each dilation/erosion cycle. The plug-in counts the number of pores/walls that have closed during each cycle of the dilation/erosion step until all pores/walls have been filled. The plugin can be calibrated using the number of microns per pixel from the images to give a physical measurement [164]. A Gaussian curve is then fit to the raw data providing the mean pore/wall size and standard deviation. Often, we were actually interested in λ which is sum of the average wall and macropore thicknesses (see figure 2.22).

3.2.5 3D Imaging Methods (Tomography)

Advancements in image capture, image analysis and computational abilities have made 3D-imaging (or tomography) a powerful and indespensible tool for materials scientists.

The technologies used however are still relatively young and we are still limited in what can be imaged and reconstructed. The sample volume being tested is often restricted by the radiation source as well as the properties of the tested material itself [165]. Additionally, there is always a trade off between image size and image resolution which must be considered. For example, if you want to capture a large volume of a sample the resolution must be reduced so as to keep the file sizes (which are often > 1 GB) manageable. Due to the hierarchical nature of our samples it was necessary to perform two types of 3D imaging, one at the microscale using high-resolutions and a small sample volume and the other tomography on the mesoscale using lower resolution but a larger overall imaged volume. These two tomographies were used together to represent our structures without losing a significant amount of information.

We began by reconstructing the mesoscale structure composed of macropores and walls using X-ray synchrotron tomography. Sample sizes were on the order of 100 x 100 x 100 µm and included on average about 5 - 10 walls and macropores. Then to characterize the microstructure within the walls of our materials we performed focused-ion beam tomography (FIB) which allows for high-resolution imaging of the composite LSM-YSZ structure. Sample sizes were on the order of 20 x 20 x 20 µm.

X-ray Synchrotron Tomography

X-ray synchrotron samples are limited in size by the X-ray absorbance of the material being imaged and the energy of the beam being used. The beamline at the ESRF in Grenoble is capable of 29.6 keV of beam energy. The 40:60 vol. % mixture of LSM:YSZ which we used has a maximum acceptable thickness of 200 µm at 29.6 keV[7]. For this reason, the samples which we tested had to have a maximum depth in two of their dimensions of less than 200 µm. A procedure was developed to create freeze-cast samples with these dimensions without altering the original freeze-cast structure (Fig. 3.11).

(a) A freeze-cast sample was infiltrated with a low-viscosity resin (EpoHeat, Buehler, Irvine, CA) then a slice less than 1 mm in thickness was taken parallel to the freezing direction using a slow speed saw with a diamond blade.

---

[7] Calculated so as to have a minimum of 40 % beam transmission using the resource at The Center for X-ray Optics `http://henke.lbl.gov/optical_constants/`

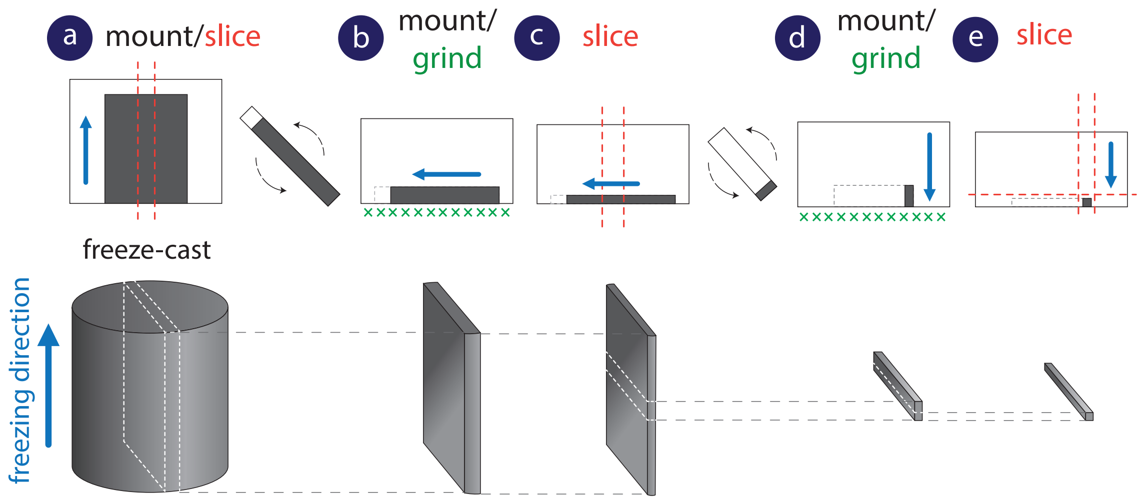

Figure 3.11: Method used to make "matchstick" samples for synchrotron radiation. The blue arrows indicate the freezing direction.

(b) This slice was then placed flat in the bottom of a mounting cup and a quick-set resin (QuickSet, Buehler, Irvine, CA) was poured around the piece of EpoHeat resin containing the slice of freeze-cast. Once cured, the now encapsulated slice of freeze-casting was gently polished to decrease its overall thickness.

(c) When the cross-sectional thickness was less than 200 μm (this can be determined by looking at the side of the sample using an optical microscope) a slice less than 1 mm in thickness was taken transverse to the freezing direction near to the desired imaging location. The freeze-cast sample now resembled a matchstick, but only one of its dimensions was less than 200 μm.

(d) This new slice was placed with the non-polished side face-down in a mounting cup and once again filled with quick-cure resin. Once completely cured, this new mount was polished until it was below 200 μm in thickness in the direction normal to the polishing face. The freeze-cast is now less then 200 μm in two dimensions.

(e) A "matchstick" of resin approximately 1 x 1 x 15 mm containing the freeze-cast specimen was carefully cut out with the slow-speed diamond saw and stored until use (Fig. 3.12).

The imaging process required mounting this "matchstick" to a metal mount and then placing it within the beampath. Four anisotropic freeze-casts and two isotropic slip-cast tomographies were created. For each tomography, 1999 images were collected for 360° of rota-

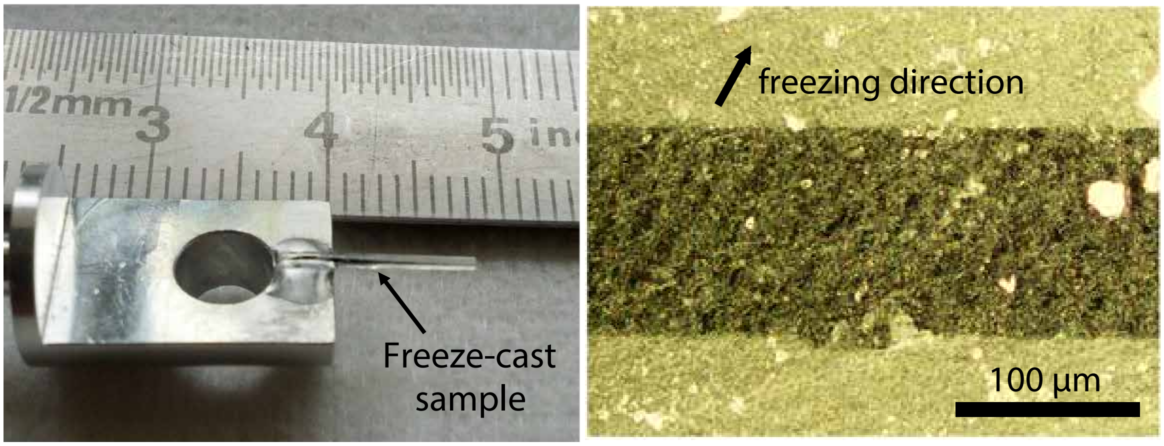

(a) Sample on Mount **(b)** Matchstick in resin

Figure 3.12: "Matchstick" freeze-cast sample prepared for irradiation in the synchrotron. Sample is attached to a metal holder which rotates during image aquisition. The freezing direction is more-or-less aligned with the impinging beam.

tion with an aquisition time of 1 s per radiograph. Using image analysis software (ImageJ), the images were segmented to reveal macropores and ceramic walls. 3D visualization was performed using either the *volume viewer* plugin built into ImageJ or a freeware MRI software known as OsiriX[8].

X-ray Tomo experiments were performed at the nano-imaging end station (ID22NI) of the ESRF ID22 beamline in Grenoble, France under the direction of Dr. Julie Villanova using a process known as nano-holo-tomography [165]. With X-ray Tomo we were able to see multiple walls and macropores, giving excellent insight into the macrostructure of our anisotropic and isotropic porosity ceramics. The spatial resolution however was not small enough to distinguish the structure found within the ceramic walls. Full three-dimensional representations of our structures therefore require a composite model combining X-ray Tomo results with high resolution FIB-nanotomography.

FIB-Nanotomography

FIB-nanotomography allows for three-dimensional reconstructions of microstructures with high resolution. It works by slicing into a microstructure and taking an image of the revealed face. A new slice and image are taken and the process repeated until a stack of images representing the desired volume is generated. These images can then be digitally reconstructed to build a 3D-model. The reconstructions created were on the order of 20 x

---

[8] **OsiriX** - 3D Raw Image Visualization `http://www.osirix-viewer.com/`

20 x 20 μm with approximate voxel sizes of 20 nm. At this resolution, individual grains can be distinguished.

In our case, a dual column FIB (Ga-ion)-field-emission gun scanning electron microscope (FEG-SEM NVISION 40, Carl ZEISS) with a 54° angle between the columns was used for FIB-SEM tomography. Before imaging, samples were infiltrated with a low viscosity resin (EpoHeat, Buehler, Irvine, CA) and mechanically polished to a "mirror" finish. This improved contrast between the pore, LSM and YSZ phases. The volume surrounding the region of interest was milled away using the FIB gun so that a planar cross-section of the ceramic wall was presented. Two types of images were then taken simultaneously: secondary electron (SE) images were used to reveal any pores which were possibly unfilled by resin and backscatter electron (BSE) images were recorded to differentiate LSM from YSZ (Fig. 3.13). After both images were acquired, a 20 nm slice was taken off the sample and a set of images was recorded of this newly exposed surface. This procedure was repeated until stacks of SE and BSE images of the desired sample volume were acquired.

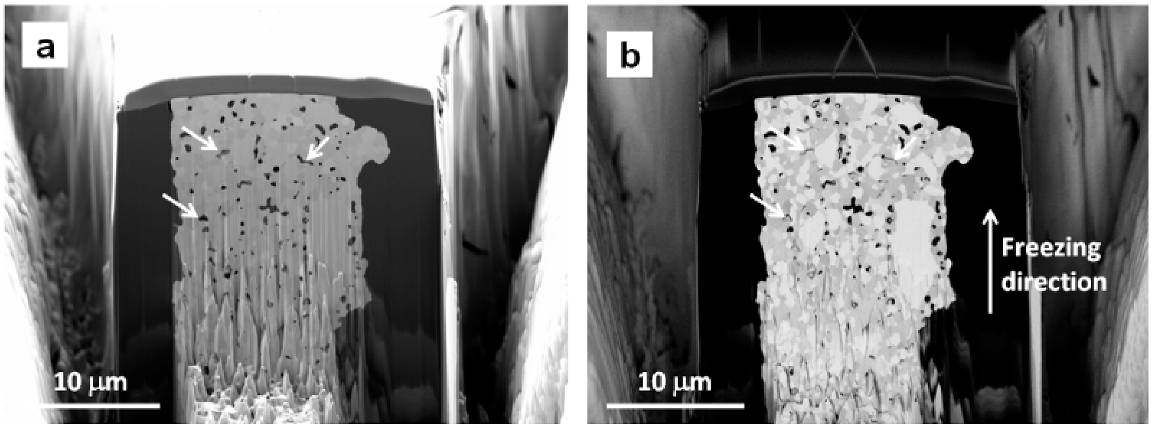

Figure 3.13: (a) Secondary (SE) and (b) backscatter (BSE) electron images of a single wall within an LSM-YSZ freeze-cast sintered at 1300 °C. In the BSE image, infiltrated resin appears black, YSZ in medium gray and LSM in light gray. Pores appear black in the SE image even if unfilled by resin (arrows).

Both stacks of raw grayscale images were first aligned using the *Stackreg* ImageJ plugin to correct for a slight thermal drift. A median filter was applied to reduce noise and improve subsequent segmentation of the selected region of interest. Each phase was first segmented independently using a single threshold value and then several morphological operations (erosion and/or dilation) were applied to eliminate artifacts caused by the thresholding operation so that a good visual match was obtained with the initial grayscale image. For certain samples, there was a non-negligible fraction of closed porosity which was unfilled by resin. The contrast between the unfilled pores and LSM or YSZ was not sufficient on the BSE images for good segmentation [Fig. 3.14 (a)]. To overcome this issue, the SE images were used to segment the pore phase on this sample [Fig. 3.14 (b)]. The three segmented images were then combined into a single image with three levels of gray corresponding to the three different phases [Fig. 3.14 (c)].

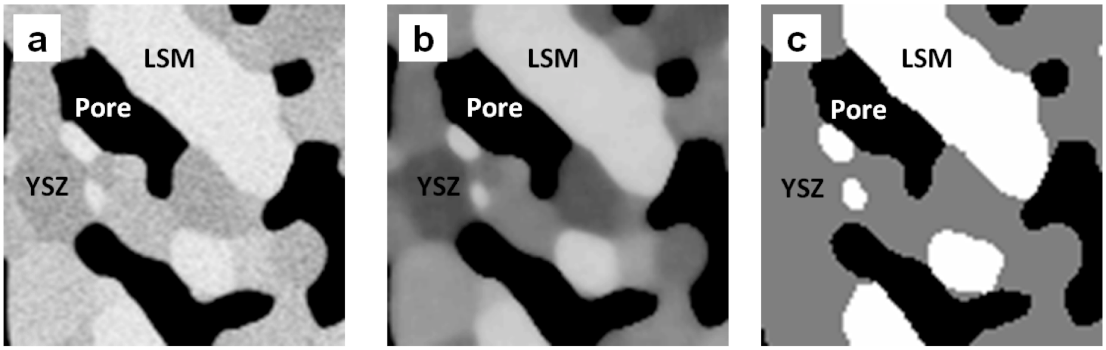

Figure 3.14: Image processing. (a) Raw gray-scale BSE image (b) Image after median filtering (c) Final segmented image.

Table 3.6: FIB-Tomography Samples

Sample	Name	Type	Sintering Temperature
1	LSM-YSZ	Freeze-Cast	1300 °C
2	LSM-YSZ	Freeze-Cast	1200 °C
4	LSM-YSZ	Slip-Cast	1200 °C

– Samples (1) and (2) were imaged at CEA-Grenoble, the slip-cast sample was imaged at Clemson University.

3D Morphological Analysis

Once stacks of phase-segmented images were created from the FIB tomographs, each phase was geometrically analyzed in terms of size distribution, connectivity and TPB density using image analysis. A classical granulometry analysis with successive morphological erosions allows the size distribution of each phase to be obtained [46, 47]. The LSM:YSZ ratios extracted from the 3D segmented images were compared with the expected value of 40:60 to validate the segmentation process.

To ascertain TPB density, first the LSM, YSZ and pore phases have to be examined for connectivity. A connectivity value (connected, unconnected or unknown) was assigned to each voxel depending on its connection to the overall percolating networks. As the full electrode structure could not be imaged, assumptions were made for the connectivity of the faces from the 3D volume (Fig. 3.15).

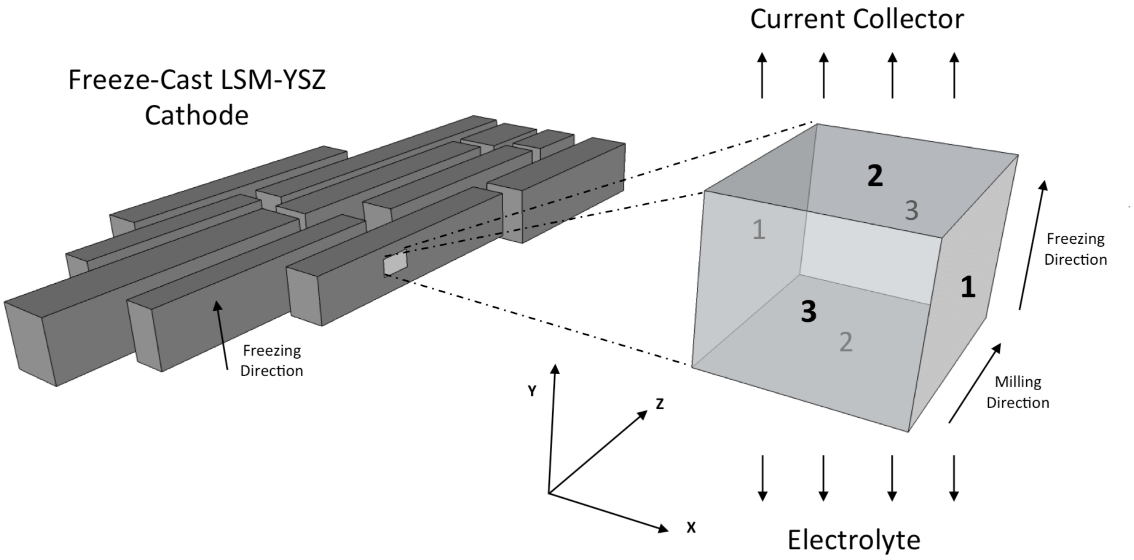

Figure 3.15: Schematic of FIB-SEM sample and orientation of faces relative to the greater microstructure. The 1-1 faces are parallel to macropore gas channels. The 2-2 faces are perpendicular to the freezing direction and therefore connected to the entire LSM-YSZ conduction network and the 3-3 faces are assumed to have unknown connectivity. Both the electrolyte and current collector would presumably be applied normal to the freezing direction.

The 1-1 faces of the sample are assumed to be connected to gas channels on both sides and therefore unconnected to the ionic and electronic conductor networks. The 2-2 faces are assumed connected for ions and electrons but unknown for gas since there may be unconnected pores above and/or below the sampled volume. The connectivity of the 3-3 faces is assumed unknown for the porous, electronic and ionic phases since the sampled volume's location along the z-axis is unknown relative to the ends of the ceramic walls.

In order to be electrochemically active, a TPB line should be connected to the three percolating networks for gas conduction (open porosity), ionic conduction (YSZ) and electronic conduction (LSM). TPBs were located using a custom-made voxel edge detection algorithm [61, 63, 166] that searched through the stacks of images for locations where the three SOFC cathode phases met. The values reported were corrected by a factor of 1.455 to account for the steps due to the voxel discretization, as proposed by Wilson et al. [63]. TPBs were counted as active if all three phases (pore, LSM and YSZ) were connected.

Calculation of Tortuosity

In addition to determining phase connectivity and TPB density, simulations were performed to obtain tortuosity factors for each phase (electronic/ionic conducting and pores). The effective diffusivity was calculated for the segmented 3D images by solving the Laplace equation (Eq. 3.3) with the GeoDict software package [167].

$$\Delta C_i = 0 \tag{3.3}$$

where C_i is the concentration of the species i which can be either an ion, electron or gas molecule. Periodic conditions were used assuming mirror symmetry along the three orthogonal directions in the microstructure. The tortuosity τ in a direction k (either x, y, or z) is then calculated as:

$$\tau_k = \frac{\varphi D_{int}^0}{D_{k^{eff}}} \tag{3.4}$$

where D_{int}^0 is the intrinsic diffusivity of a species in its correspondent phase and φ represents the volume fraction of the considered phase. This intrinsic diffusivity is normalized by the effective diffusivity $D_{k^{eff}}$ in the tested tortuous porous structure [168, 169].

3.2.6 Optical Dilatometry

An optical dilatometer is a high-temperature furnace equipped with two aligned quartz windows on either side of where a sample sits (Fig. 3.16). At one quartz window is a high-powered light source and at the other is a high-speed camera equipped with a telecentric lens[9]. The light source throws the sample in the furnace into silhouette which is then captured by the camera. During sintering, software integrated into the system tracks the edges of the silhouetted sample as it expands or contracts. Since an entire face of the sintering sample can be seen, the strains in multiple directions can be tracked making this technique ideal for anisotropic or irregular samples.

Prior to dilatometry, freeze-cast and slip-cast samples were heated to 1000 °C to form necks

---

[9] Two optical dilatometers were used, the first at SiMaP in Grenoble, France and the second at the Forschuzentrum Institute for Energy and Climate Research in Jülich, Germany with the help of Dr. Daniel Röhrens

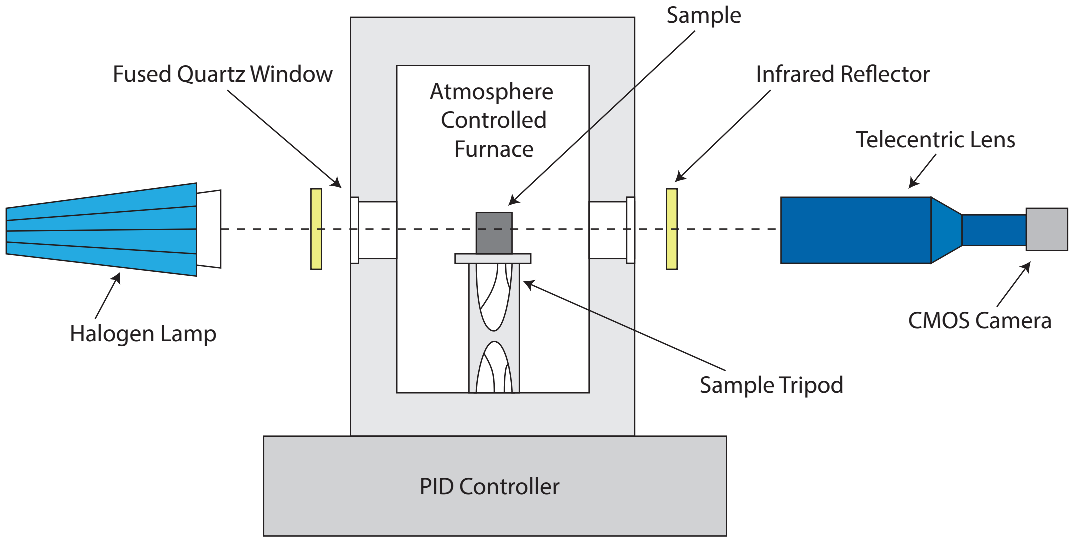

Figure 3.16: Schematic of the inner-workings of an optical dilatometer.

between particles, increasing the green body strength without causing significant densification. Additionally, this step removed all organics within the ceramics which may have been damaging to the internal workings of the dilatometer furance had they off-gased inside. The samples were embedded in EpoHeat resin and then cut into cuboidal specimens approximately 5 x 5 x 5 mm in size. Care was taken to ensure that both the IZ and TZ portions of the freeze-casts were excluded. Once cut and ground flat on each side, the resin was carefully burned out of the samples by heating at 2 °C min^{-1} to 500 °C and holding for 2 hours. The fragile, green samples were then placed into the optical dilatometer (TOMMIplus, Fraunhofer ISC, Wertheim, Germany) taking care to note the relative freezing direction for anisotropic samples. During testing, the samples were sintered to 1500 °C at a rate of 10 °C min^{-1} in air. The optical dilatometer camera captured an image each minute by averaging together a total of 10 images to reduce noise. The stock optical dilatometer software was used to compute linear shrinkages both parallel and transverse to the freezing direction. It does this by tracking the edges of the specimen as a function of time and temperature.

Data Analysis

Unfortunately, the built-in software available for tracking the edges of samples during sintering was found to be highly unstable, often giving nonsensical readings. A plugin was developed for ImageJ which has the ability to count pixels in vertical and horizontal directions at predetermined locations giving both the shrinkages parallel and transverse to the freezing direction.

3.2.7 BET Nitrogen Adsorption

Brunauer-Emmett-Teller theory (BET) nitrogen adsorption tests were run on a number of samples to determine whether or not information concerning surface area or pore size could be gathered. Freeze-cast and slip-cast LSM-YSZ samples made using differing sintering temperatures were cut into small pieces approximately 4 x 4 x 6 mm in size. These were heated to remove any adsorbed water vapor and then weighed precisely. The pieces were then placed into clean BET adsorption tubes which were subsequently filled with nitrogen gas (Tristar 3000, Micromeritics). The samples were allowed to equilibriate for 24 hours at elevated temperatures and then they were once again precisely weighed. A computer program that had been calibrated to the specific setup was used to calculate data concerning surface area and pore size distribution.

3.2.8 Mechanical Testing

Sample Preparation

Two types of hierarchically porous LSM-YSZ samples (slip-cast and freeze-cast) were made using the same initial green-state porosities and similarly sized micro- and macropores (Table 3.7). The isotropic samples contained macropores that were created using spherical PMMA pore formers while the anisotropic macropores in the freeze-casts formed due to the lyophilization of directionally frozen ice crystals within a particulate slurry. The freeze-cast samples were tested both parallel and perpendicular to their freezing direction. Green-state porosities of either 70 (low porosity) or 80 vol. % (high porosity) were targeted for all ceramics. In addition to their macropores, all ceramics contained isotropic micropores derived from a partial sintering step at 1200 °C. For each sample treatment, a minimum of five samples were tested.

To prepare samples for mechanical characterization, isotropic and anisotropic samples were infiltrated with EpoHeat and cut into cuboidal shapes. The freeze-cast samples were cut at 2 mm and 16 mm along the freezing direction to remove the IZ and TZ and ensure

Table 3.7: Mechanical Testing Sample Treatments

Process	**Designation**	**Green Porosity**	**Macro-Pore Control**			**Sinter**
Slip-Cast	Isotropic	70, 80 (vol. %)	Pore Formers	→	20, 30, 40 μm	1200 °C
Freeze-Cast	Parallel	70, 80 (vol. %)	Freezing Rate	→	1, 5, 10, 20, 40 °C min^{-1}	1200 °C
	Transverse	70, 80 (vol. %)	Freezing Rate	→	1, 5, 10, 20, 40 °C min^{-1}	1200 °C

that all the samples were approximately the same height (Fig. 3.17). The edges of every sample were rounded with sandpaper to remove any potential sources of stress concentration. After shaping, the top, bottom and sides of each sample were coated in ink and stamped onto a piece of paper. This was later used to calculate the exact surface area of the mechanical testing samples since each sample differed slightly in size and shape. Before testing, the resin in the samples was burned out by heating at 2 °C min^{-1} to 500 °C and holding for at least two hours.

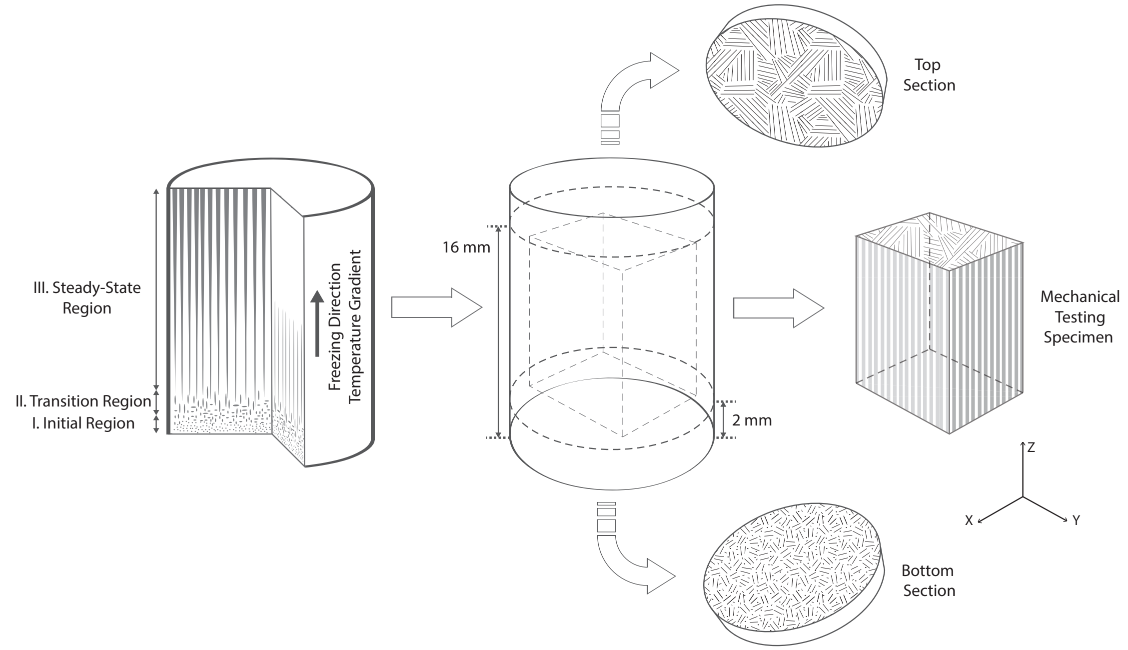

Figure 3.17: Schematic of anisotropic freeze-cast specimen preparation. The bottom section containing the isotropic and cellular regions was cut at 2 mm along the freezing direction while the top section was cut at 16 mm along the freezing direction. The z-direction is aligned with the freezing-direction while the x-y plane is normal to it.

Testing Conditions and Data Analysis

Isotropic, slip-cast samples were tested only in one direction while freeze-casts were tested both parallel (z-direction) and perpendicular (in the x-y plane) to their freezing-direction to determine the effects of their microstructural anisotropy. Compression testing was performed using an Instron 5585H Electro-Mechanical Test Frame with a 2 kN load cell at a constant strain rate of 0.01 mm s^{-1}. To account for imperfectly flat compression surfaces and asperities, a cyclic compression method with successively increasing peak loads from 100 - 2000 N was used (Fig. 3.18). By testing in this manner, imperfections can be removed from the sample surfaces during the preliminary loading sequence without causing significant damage to the inner structure [170]. Additionally, stiffness values can be more accurately determined by taking the slope of the unloading portion from a load/unload cycle. Compressive strength values were taken as the peak stress before a significant (> 10 %) drop in stress was seen. Reported stiffness values were taken from the load/unload cycle prior to reaching the compressive strength. Note that the term stiffness was used rather than elasticity since the question arises as to whether or not a reversible domain exists for these porous materials. High-definition video (Canon Rebel Ti1 with Canon EF100 Macro Lens) was taken of each sample using a macro lens so that we were able to correlate stress-strain behavior with physical crushing of the sample.

Using image analysis, the appropriate surface areas of each sample was calculated from the surface area stamps and used to convert load vs. displacement data into stress vs. strain. Using a macro, we were able to quickly find the slopes of the unloading portions of the curves that represent the stiffness of the sample.

3.2.9 Impedance Spectroscopy

Impedance spectroscopy shows the response of an electrochemical system to an applied sinusoidal potential or current. This response can tell a great deal about the electrochemical behavior of the system. Many processes within SOFCs occur at different frequencies (charge transfer, ion and electron transport, gas diffusion...) so by changing the frequency of the applied potential or current we can selectively characterize these different processes. In general, the current response will be the same frequency as the applied one but it will have shifted in phase and reduced in amplitude because of the sample's resistance.

Impedance itself is a measure of a system's ability to resist the flow of electrical current.

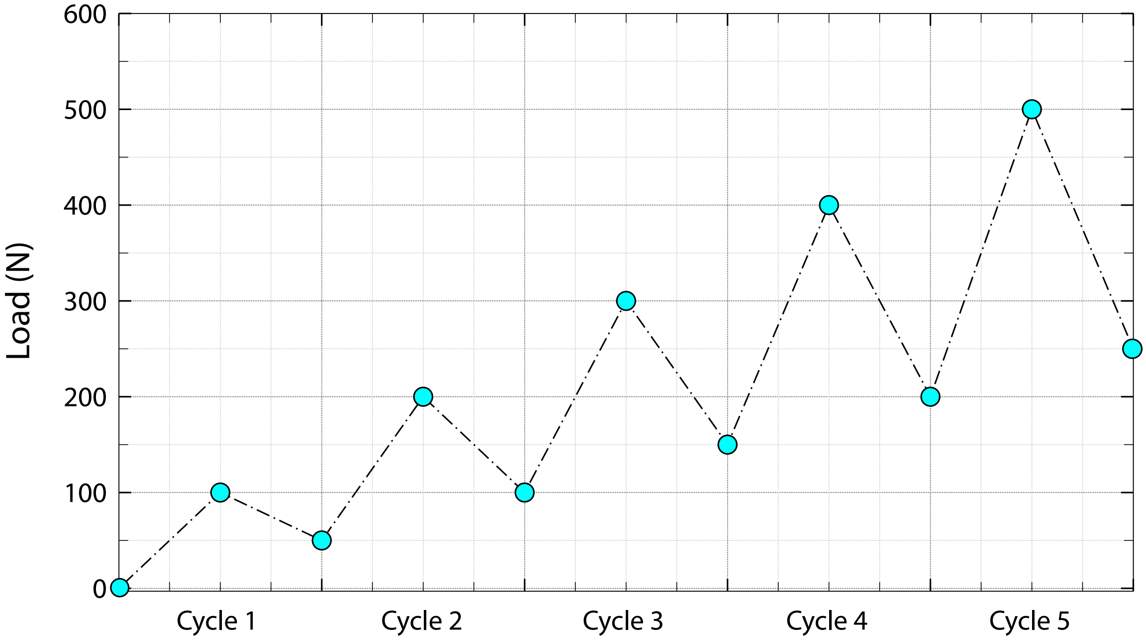

Figure 3.18: Representative loading scheme used for compressive testing of porous ceramics. This loading pattern was used up to 2000 N or until the sample failed completely.

Unlike a perfect resistor however, impedance is composed of both real and imaginary elements. It is defined by Ohm's law as:

$$Z(\omega) = \frac{V(t)}{I(t)} = \frac{V_0 e^{j\omega t}}{I_0 e^{j\omega t - \varphi}} = Z' + jZ'' \tag{3.5}$$

where:

ω - radial frequency as a function of frequency (f), $\omega = 2\pi f$

$Z(\omega)$ - complex impedance as a function of radial frequency (ω)

$V(t), I(t)$ - potential signal and current signal as a function of time (t)

V_0, I_0 - amplitudes of the potential and current

φ - phase shift between potential signal and current response

j - imaginary number $j^2 = -1$

Z', Z'' - real (resistance) and imaginary (reactance) part of impedance

The results from impedance spectroscopy are often plotted on a Nyquist plot where the real impedance (Z'), which is equivalent to resistance, is on the x-axis and the imaginary component (Z'') is plotted on the y-axis. Often times it is beneficial to constuct model circuits to represent the impedance plots. These are however only useful if they have some physical basis. The four primary circuit elements used to represent SOFC cells are shown in Table 3.8.

Table 3.8: Equivalent Circuit Elements

Element	**Impedance**	**Schematic**
Resistor	$Z_R = R$	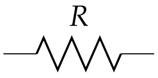
Capacitor	$Z_C = \frac{1}{j\omega C}$	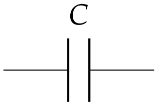
Inductor	$Z_L = j\omega L$	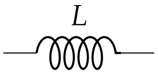
Constant Phase Element	$Z_{CPE} = \frac{1}{C_0(j\omega)^p}$	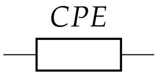

Very few electrochemical systems can be modeled with a single circuit element. Therefore multiple elements connected in some combination of series and parallel must be best-fit to represent the system. Generally, bulk effects (diffusion, grain resistance etc.) correspond to high frequencies and more overall electrode responses correspond to lower frequencies.

Sample Preparation and Testing Conditions

Three different electrodes are used during impedance testing, the working-electrode (WE), counter-electrode (CE) and reference-electrode (RE). These are placed at specific locations relative to each other and to the half-cell. Two different electrode configurations were used for our half-cells depending on whether the electrolyte was thick (> 1 mm) or thin (Fig. 3.19).

The working electrode was always a platinum wire mesh pressed down onto the cathode surface. For the counter electrode, typically a platinum paint was applied directly to the YSZ electrolyte opposite the WE. The reference electrode was either painted on (for thin electrolytes) or a thin platinum wire was wrapped around the half-cell (for thick electrolytes), halfway up the electrolyte thickness.

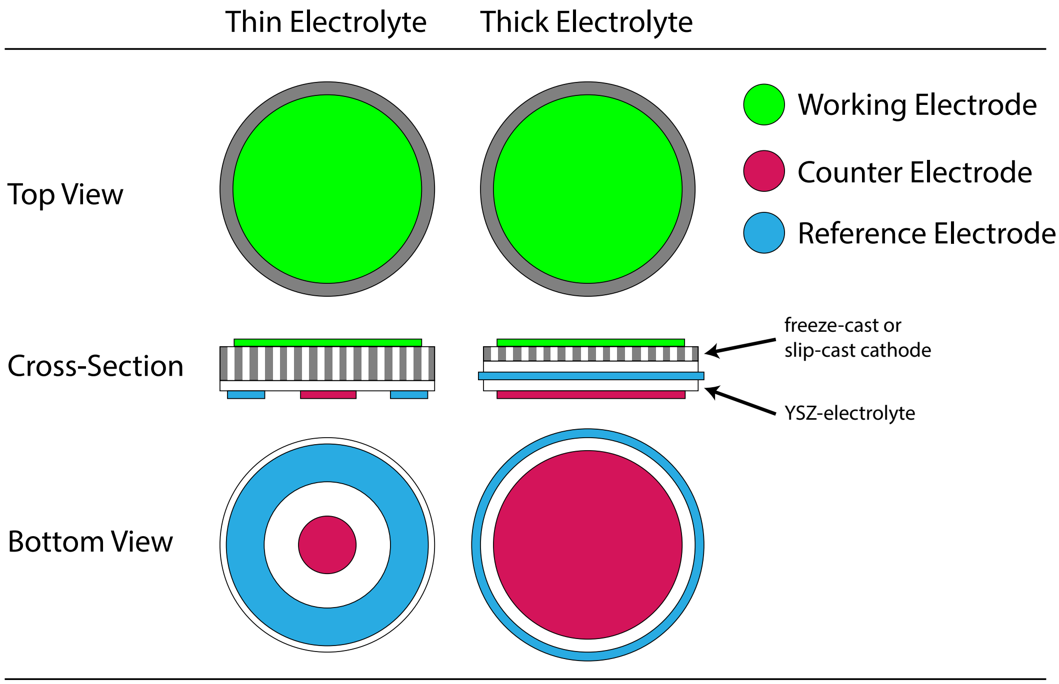

Figure 3.19: Electrode placement for 3-point impedance testing of thin and thick-electrolyte SOFC half-cells.

The platinum paint was cured under a heat lamp and then fired in a furnace at 800 °C overnight. After cooling, the half-cell was carefully hooked into the impedance spectroscopy setup. It was then brought up to the desired testing temperature and held there for a minimum of 4 hours to ensure that the system was isothermal (even small fluctuations in temperature can result in unstable data readings).

A sinusoidal potential sweep was applied to the half-cell and the current response recorded using the three-point setup. The voltage used was typically 0.2 or 0.3 V with a frequency range from 0.025 Hz to 100 kHz. Multiple readings were taken at the same temperature to check for consistency. The temperature was then changed and the system allowed to equilibriate before another set of potential sweeps was performed.

Data Analysis

Results from impedance spectroscopy were analyzed using NOVA 1.9 software. Using this software, model circuits could be built to represent our electrochemical behavior.

3.2.10 RedOx Testing

NiO-YSZ freeze-casts were prepared as outlined in section 3.1.1 then sintered under oxidizing conditions. The structure was infiltrated with EpoHeat resin and then small cuboidal samples, approximately 5 x 5 x 5 mm, were removed from the middle of the freeze-cast. These were carefully honed and polished until their sides were as parallel and flat as possible.

Immediately prior to testing, precise dimensions were taken for the redox specimens and the resin was removed by heating the samples to 600 °C at approximately 2 °C min^{-1}. After cooling to room temperature, the sample was placed into a standard dilatometer, taking care to ensure that the freezing direction was in the desired orientation for testing. The sample was heated at 5 °C min^{-1} to a temperature of 800 °C under reducing conditions (gettered Argon or a hydrogen-rich gas). This step initially reduces the $NiO \rightarrow Ni$. The system remains at elevated temperatures until the length change stabilizes. Once it is certain that the specimen is entirely reduced, the atmosphere is changed to air which re-oxidizes the freeze-cast. Linear expansion measurements are recorded. When the sample's size no longer changes it is safe to assume that no further oxidation is taking place. The atmosphere can now be once again changed back to either gettered Argon or a Hydrogen-rich mixture to re-reduce the sample. The cycle is repeated multiple times to ascertain the red-ox cycling behavior.

3.3 DEM Simulations

Mesoscale DEM structures were built representing the six LSM-YSZ X-ray tomography samples. The microstructures within the walls of these simulated porous materials were modeled after our FIB reconstructions. The hierarchical digital representations were used to simulate the mechanical behavior of the porous ceramics under load.

3.3.1 Creating Representative Structures

Two sets of DEM structures were created for simulations. The first set was composed of 50,000 particles and was used initially to test the simulation parameters without using a signifcant amount of computational resources. The second set of experiments was performed using approximately 4 million particles which is representative of the number of real particles in our own samples. The process is laid out in Table 3.9.

3.3.2 Simulation Parameters

Once the representative structures were built, mechanical simulations were run using a master file containing all desired simulation parameters and conditions such as material properties, step size, strain rate etc. (Table 3.10). While running, dp3D produces a set of coordinate files with locations for each particle at every time step. In addition it tracks internal stresses and broken bonds which can be subsequently visualized.

Mechanical simulation parameters were chosen to closely mimic the real compressive testing performed at the University of Washington. A strain rate of 0.01 mm s^{-1} was used. Each sample whether anisotropic or isotropic was tested in each of the three ordinal directions (x, y, z) to see any effects of anisotropy. In order to produce realistic mechanical behavior, dp3D uses the energy to create new surfaces as the metric for whether or not a bond will fracture (bond toughness). This value is known with relative precision for YSZ ($\Gamma_{YSZ/YSZ} = 1\ J\ m^{-2}$) it is however unknown for LSM or for an LSM/YSZ bonded couplet. Since the surface energy for a ceramic however is ~ 0.5 J m^{-2}, it seemed reasonable to set $\Gamma_{YSZ/YSZ}$ and $\Gamma_{LSM/YSZ}$ also to 1 J m^{-2}.

3.3.3 Visualization and Post-Treatment

An open-source software named Ovito[10] was used to visualize and further analyze the generated xyz files from dp3D. Ovito reads in files which contain information concerning position, particle size, particle type, broken bonds etc.. It is then possible to color or hide particles based on boolean expressions meaning that for example, only particles with more than two broken bonds can be displayed. This was used extensively to better understand where fractures originated within the structure and how stresses were transferred throughout the DEM model.

---

[10] **Ovito** - DEM visualization and analysis `http://www.ovito.org/`

Table 3.9: Hierarchically Porous DEM Generation Procedure

(1)	Generate a cubic sintered green body with the desired particle types (LSM-YSZ), size distributions and density. Pore formers may be incorporated if desired.	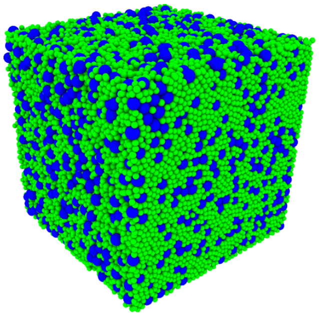	*DEM Greenbody*
(2)	Prepare a cubic high-resolution 3D, binary raw file from X-ray synchrotron tomography representing the macroporous ceramic structure to be replicated. Black should be set to pores and white to solids.		*Tomography*
(3)	Merge the DEM green body with the raw file. Depending on whether a DEM particle falls in the white or black boundary of the raw file will label it as part of the ceramic wall (cream) or as a macropore (purple), respectively.	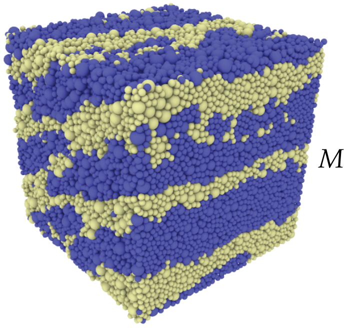	*Merged DEM*
(4)	Remove any particles which are now labeled as macropores. Redefine proper particle distribution (i.e. Walls → LSM + YSZ). Generate elastic bonds between overlapping particles using the Coble model, this ensures realistic depiction of the bond size.	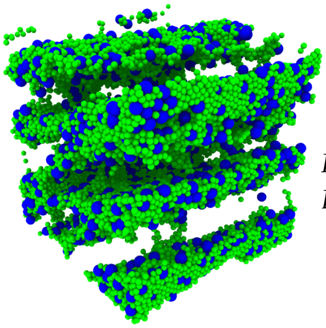	*Finished DEM*
(5)	Establish boundary conditions normal to the desired direction of loading tangent to the outermost particle ($d = 0$). The boundaries of the two non-loading directions should be made sufficiently far from the structure ($d = 50 \cdot R_{particle}$) so as to ensure no unwanted interactions.	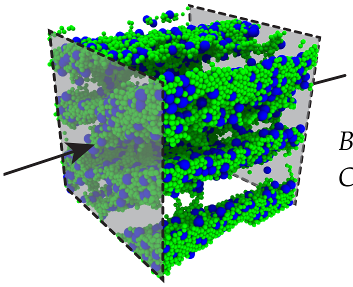	*Boundary Conditions*

Table 3.10: Simulation Parameters

Property	**LSM**	**YSZ**	**Reference**
Particle Size	1 μm ± 5 %	0.5 μm ± 5 %	
E	122 GPa	220 GPa	[171]
Poisson	0.377	0.316	[171]
Bond Toughness $\Gamma_{/YSZ}$	$1.0\ J\ m^{-2}$	$1.0\ J\ m^{-2}$	[172]
Bond Toughness $\Gamma_{/LSM}$	$1.0\ J\ m^{-2}$	$1.0\ J\ m^{-2}$	
Density	$6.1\ g\ cm^{-3}$	$5.7\ g\ cm^{-3}$	
System Variables			
Friction	0.5		
Adhesion	0.0		
Boundary Toughness*	4.0		

⋆ ensures that the boundary planes are significantly tougher than the particles themselves

4

Results

Chapter Contents

4.1 Processing of Anisotropic and Hierarchical Materials

One of the goals of this thesis was to develop and test a series of procedures for fabricating controlled porosity ceramics with anisotropic and/or hierarchical porosity. By far, the most commonly used approaches were freeze-casting or slip-casting using pore-formers followed by partial sintering. Some preliminary success however was seen with sol-gel based ceramics.

4.1.1 Sol-Gel Based Monoliths

Using the methods detailed in section 3.1.5, Zr-monoliths with two distinct levels of porosity were attempted. The sol-gelation process appeared to proceed smoothly. The color changes during the reaction were similar to those originally specified by Drisko et al. [79]. When pyrolyzed however it was clear that zirconia had not been produced. The monoliths shrunk between 15 and 40 % during the calcination step yet they remained black and a strong organic smell lingered on them.

These sol-gels hadn't properly pyrolyzed into zirconia; still, even in this imperfect state they presented an attractive, hierarchical microstructure. As an offshoot of this project, the method initially laid out in [79] was utilized in conjunction with a method based on work by Gaudon et al. [173] to form LSMx-YSZ based powders and thin films. This work was performed by a visiting student (Maya Cherif) who was able to successfully fabricate hierarchically porous LSM-YSZ monoliths using zirconium, lanthanum, manganese, strontium and yttrium salts (Fig. 4.1). The structures produced exhibited two distinct levels of porosity which were independently controllable. They were however extremely fragile due to their low solids content.

4.1.2 Freeze-Cast Processing

Equipment Capabilities

For freeze-casting, preliminary studies were undertaken to determine our capabilities and to compare our setups with those discussed in the literature. It was important that we had good control over the freezing conditions. In order to validate the ability of our equipment

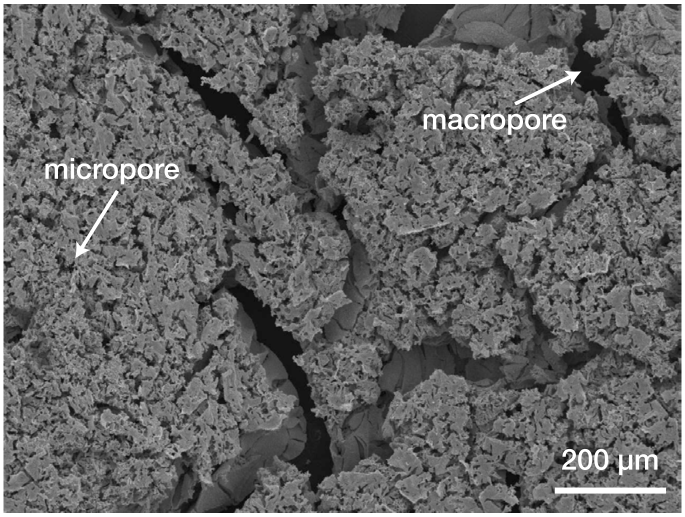

Figure 4.1: LSMx-YSZ derived sol-gel showing two distinct levels of porosity.

to control cooling rate, multiple freeze-cast runs[1] using either 1, 3, 5, 10, or 40 °C min^{-1} nominal freezing rates were conducted. The actual temperature along with the target profiles are shown in figure 4.2.

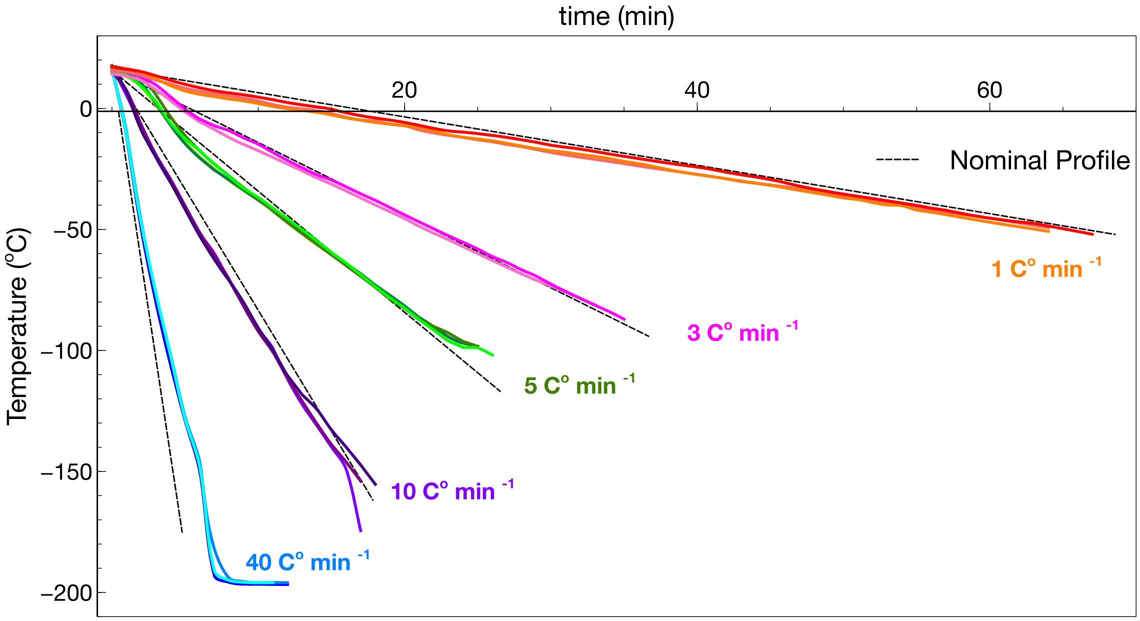

Figure 4.2: Temperature profiles from multiple freezing runs using dynamic (linear) cooling rates and homogeneous initial conditions.

---

[1] Low-speed freeze-caster was used for 1, 3, and 5 °C min^{-1} rates and the high-speed freeze-caster was used for the 10, and 40 °C min^{-1} profiles. The details of the two different freeze-casters are presented in section 3.1.3

Freeze-casts from this study were approximately 22 mm high and temperature readings stopped when the sample had completely frozen. One can see that samples cooled at 1 °C min^{-1} took over an hour to freeze whereas those frozen at 40 °C min^{-1} froze in ten minutes or less. Even though temperature is controlled manually by the addition of liquid nitrogen, we found that with some practice, one can maintain the predetermined temperature profiles within 1 - 2 °C min^{-1} of the nominal profile. More importantly however is the fact that the profiles are repeatable meaning that samples made at different times but under the same conditions should be comparable.

It should be noted that for the 40 °C min^{-1} freezing rates, the temperature profiles reach their minimum (-196 °C[2]) before the samples have fully frozen. As can be seen in figure 4.2, the temperature readings from these freezing runs level out for the final minutes of freezing. This change can be thought of essentially as going from a dynamic to a static temperature gradient in-situ. It is believed that since the solidification front should already have progressed into the steady-state regime, that the brief change to a static profile shouldn't have a significant effect on the resultant microstructure. This was later confirmed by microstructural measurements at various heights within 40 °C min^{-1} freeze-casts (figure 4.15)[3].

As a note for controlling the freezing profile, there is typically a sharp drop in the measured temperature (seen as a slope shift at -150 °C for the -40 °C min^{-1} profiles) which occurs in the range of -140 to -160 °C. At this point the measured temperature drops to approximately -180 °C accompanied by a decrease in visible gases and an audible hissing sound. It is due to the condensation of oxygen to a liquid.

Solidification Front Tracking

It was possible to track the freezing front in two ways, using photographs and using a thermal imaging infra-red (IR) camera. Since microstructural wavelength (λ) is controlled in part by the solidification velocity, we often times would track the freezing front to estimate this velocity and cross-reference this with microstructural data. Shown here is an example of freezing water[4] at -20 °C min^{-1} (Fig. 4.3).

---

[2] Boiling temperature of liquid nitrogen = -196.4 °C

[3] Comparing samples frozen at 10, 20 and 40 °C min^{-1} within this figure, we see essentially no difference in microstructural feature size, even though the sample frozen at 40 °C min^{-1} goes through a period of static temperature towards the end of the freezing process.

[4] Food-coloring was added to enhance contrast

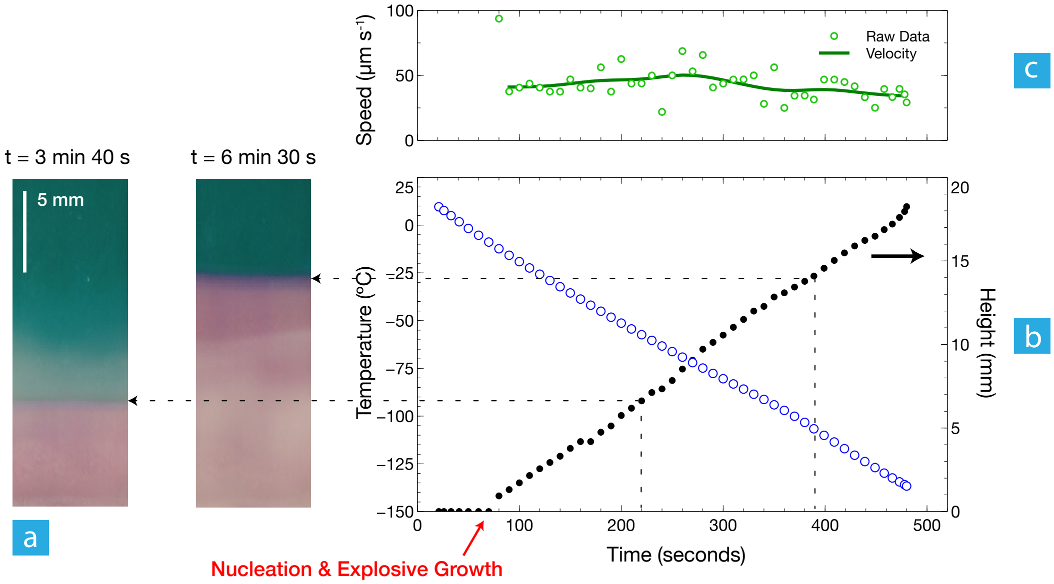

Figure 4.3: (a) Images of the freezing front were used to determine (b) solidification height as a function of temperature and time and then (c) solidification speed. These data are from the freezing of water at 20 °C min^{-1}. Images were taken every 10 seconds.

The nucleation and initial growth process of a freeze-cast initial zone (IZ) and transition zone (TZ) occurs so rapidly that it is impossible to estimate the velocity using our stop-motion photography setup. Indeed, it has been postulated by Deville et al. that the initial freezing speeds can be upwards of 750 μm s^{-1} [84]. This is why typically our velocity curves show a null velocity and then jump to the stabilized value (Fig. 4.3 (c)). In general, in order to template a particulate system (non-planar front, and no particle entrapment) solidification speeds ranging from $\sim$ 1 - 100 μm s^{-1} should be used (see figures 2.18 and 2.20). Using 20 °C min^{-1} rates, we see average solidification velocities ranging between 40 - 50 μm s^{-1}, well within the usable range of templating velocities.

In an effort to better visualize and understand the solidification front moving through the slurry, a basic thermal imaging IR camera was procured. The idea was to track thermal isotherms as they moved through the slurry and see whether or not these agreed with results from optical imaging of the front. The camera had a thermal sensitivity of ± 2 °C and could detect temperatures in the range of -40 to +250 °C. Multiple experiments were run using different cooling rates and then comparing the temperatures determined by the thermal imaging camera with thermocouples placed at the base and top of the casting as well as optical images showing the front moving through solution. The issue that we ran into was that the insulative plastic mold itself and the cold air flowing around the freeze-cast obfuscated the readings, producing thermal images that were not reflective of the actual temperature *inside* the freezing vessel. We were however able to see isotherms which appeared to more or less follow the ice front as it progressed through the mold. For these reasons, we came to the conclusion that thermal imaging should be used more for basic visualization of the freezing process rather than for quantitative temperature determination (Fig. 4.4).

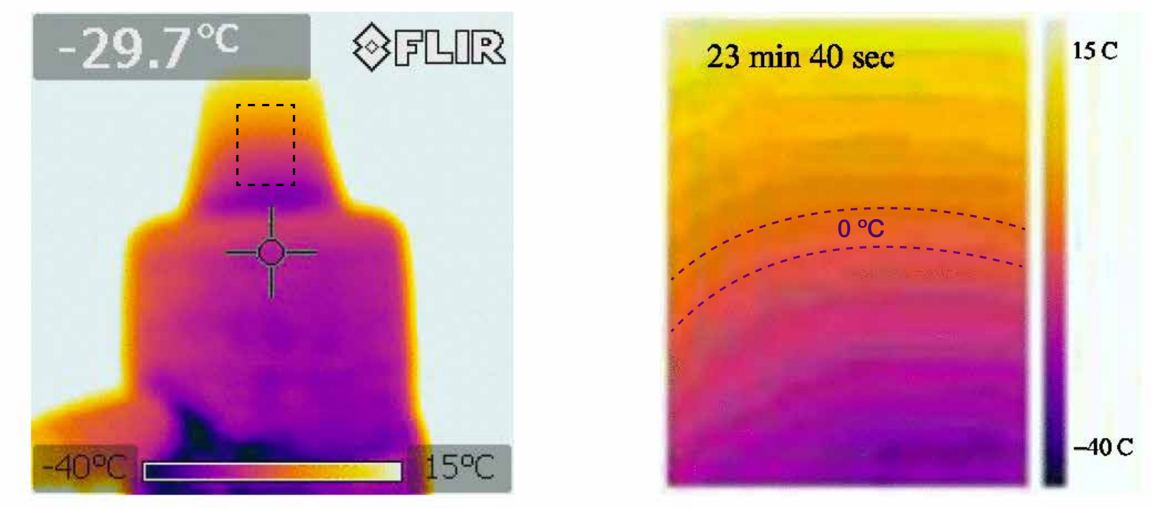

Figure 4.4: Thermal imaging scans 23 min and 40 sec into freezing an alumina slurry.

Using the lessons learned from thermal imaging, an alternative setup was devised and preliminary testing performed (Fig. 4.5). This thermal imaging setup could be used to gather significantly more quantitative data to better understand heat transfer during the freezing process. Essentially, the freeze-cast is turned on its side and takes place within a thin 2D-mold which is open on top. In this way, the thermal imaging camera is actually taking the measurement of the solution rather than the mold. Isopropyl alcohol and dry ice is used in conjunction with a computer fan which continually blows the evaporated CO_2 away from where imaging is taking place. Figure 4.5 shows our prototype mock-up using water with blue food coloring to enhance contrast in the optical photos.

It should be noted that we were using a thermal imaging camera made for spotting missing insulation in walls[5]. If thermal imaging were to be performed for R&D purposes, a research level IR camera with higher precision and greater dynamic range should be used (i.e. the Flir A6700sc IR camera).

---

[5] Rented from Home Depot

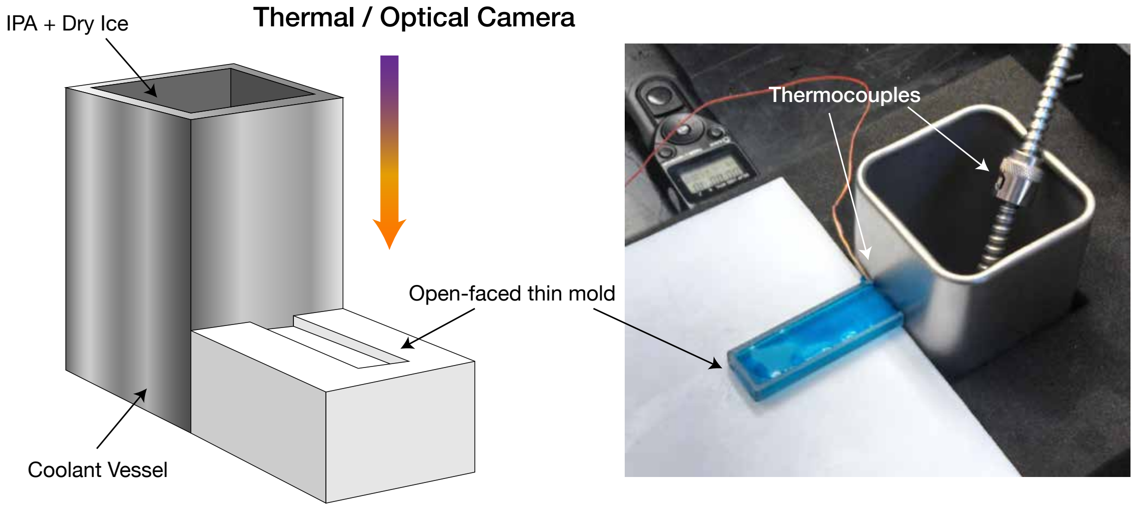

Figure 4.5: Prototype mock-up of a thermal imaging system for analyzing thermal gradients in freeze-casts with high precision and accuracy.

Preliminary Results on Freeze-Casting

Freeze-cast experiments began with static temperature profiles as these were by far the simplest to perform in practice. A room temperature slurry was poured into the freeze-casting setup (mold and cooling finger) which were already pre-cooled. We found that the greater the ΔT between the slurry and copper cold finger (more significant quenching), the longer the IZ and TZ regions were within the produced structures. Once steady-state was achieved, the macropores obviously increased in thickness over the course of freezing due to the decreasing thermal drive for growth in the freezing direction. Ideally, we wanted to see a structure with as small an IZ and TZ as possible followed by fine, linear, and continuous pores.

The next natural step was to use the double-sided temperature profiles discussed in literature [83, 97] which provide greater control over the temporal temperature gradient. These types of freezing profiles are logistically more difficult to perform considering that temperature is controlled manually at both the top and bottom cooling rods. Structures produced using these methods were also found to be weak and damaged, no doubt due to the inherent stresses which built up within the templated structure since the freeze-cast could not expand vertically to relieve pressure. Microscopy revealed that these structures did transition to the SSZ sooner than quenched structures and had a significantly more favorable structure (aligned pores with constant spacing) than static profiles but we found that they were no better than those produced by single-sided dynamic freezing profiles.

The motivation lauded in the literature behind double-sided freeze-casting is that by controlling the temperature on both sides of the slurry, a constant ΔT is kept between the solidification front and the non-frozen suspension. Waschkies et al. [83] show this being performed by keeping a constant temperature on one side of the slurry while the other side decreases in temperature linearly or parabolically. When we performed single-sided dynamic freezing profiles the top of the slurry was left open to ambient conditions. The room itself acts as a sufficient heat sink to keep the top of the slurry near a constant temperature driving growth forward at more or less a constant rate controlled by the cooling rate of the cold finger.

Initial conditions were found to also have a significant impact on growth dynamics. Using single-sided linear, dynamic profiles a short study was undertaken wherein the initial temperature of the entire setup was altered. For example, the suspension, mold and cooling finger were all held at 5 °C and then at $t = 0$, the temperature of the cooling finger was lowered linearly. We found it was absolutely critical that sufficient time be given *before* nucleation of the ice in the slurry to establish a strong temperature gradient within the slurry, otherwise macropores tend to grow in multiple directions due to the non-ideal nucleation conditions. In a practical sense this means that the starting temperature of the freeze-casting setup and slurry (T_o) should be greater than 10 °C. As mentioned previously, this is coined homogeneous cooling.

Even though using homogeneous cooling and dynamic profiles, nearly constant freezing velocities were achieved, the lamellar size did still increase over the course of freezing. The increase in size was less drastic than when using static temperature profiles but it was nevertheless apparent. Similar results were seen from Waschkies et al. who despite using very controlled temperature setups with precision temperature profiles, still saw a statistically significant increase in lamellar size over the course of freezing [83].

These preliminary trials were performed with alumina for which there is significant reported results [86, 111]. Other particle types were attempted to extend the breadth of our capabilities and eventually lead to more complicated SOFC material systems. We saw that even though freeze-casting is essentially thought to be non-material-specific, there were clearly microstructural differences between freeze-casts made using different ceramic particles. Alumina for example [Fig. 4.37 (a)] produced highly cellular pores whereas hydroxyapatite particles [Fig. 4.37 (b)] resulted in longer more geometric pores. Silica particles

[Fig. 4.37 (c)] seemed to form a biphasic structure with regions of agglomerated silica and regions of lamellar silica probably attributable to the highly viscous nature of the nano-silica slurry.

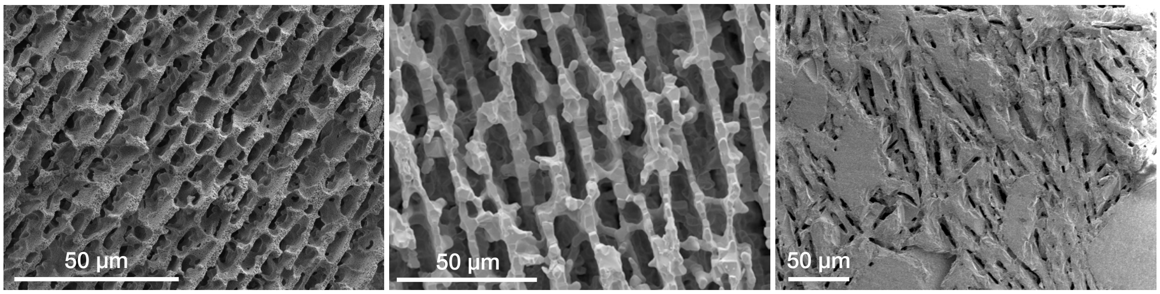

(a) Alumina **(b)** Hydroxyapatite **(c)** Nano-silica

Figure 4.6: Freeze-casts made using various materials.

It was clear from freeze-casting these different materials that the phenomenon of ice-templating does involve some sorts of interactions with the material itself. Researchers from other labs have subsequently confirmed that material properties can significantly effect ice crystal growth [117]. Our primary concern however was the effects of porosity on more advanced, multifunctional ceramics systems (i.e. SOFCs). There are few examples of freeze-casting composite powder mixtures [63] and at the time of this work, no literature at all on even producing aqueous mixtures of LSM and YSZ.

Bimodal Freeze-Casting

Within the literature review it was discussed that during freeze-casting ice crystals can template particles or engulf them (see figure 2.18). Our studies show that these two scenarios can actually occur simultaneously. The following micrographs were taken of freeze-casts made using a bimodal slurry of alumina composed of 0.1 μm alumina particles and alumina agglomerates approximately 50 - 100 μm in diameter (Fig. 4.7).

In figure 4.7 (a) there is horizontal line visible slightly less than halfway up the figure above which the majority of the larger agglomerates are located. We can infer that up until this point, the large agglomerates were pushed upwards through the slurry until some critical concentration was reached where the agglomerates were engulfed. From figures 4.7 (b - d) however we see that even though the large agglomerates were engulfed, the smaller particles continued to be templated producing the unique microstructure seen here. This is an excellent example of a morphological shift in the ice-templating process.

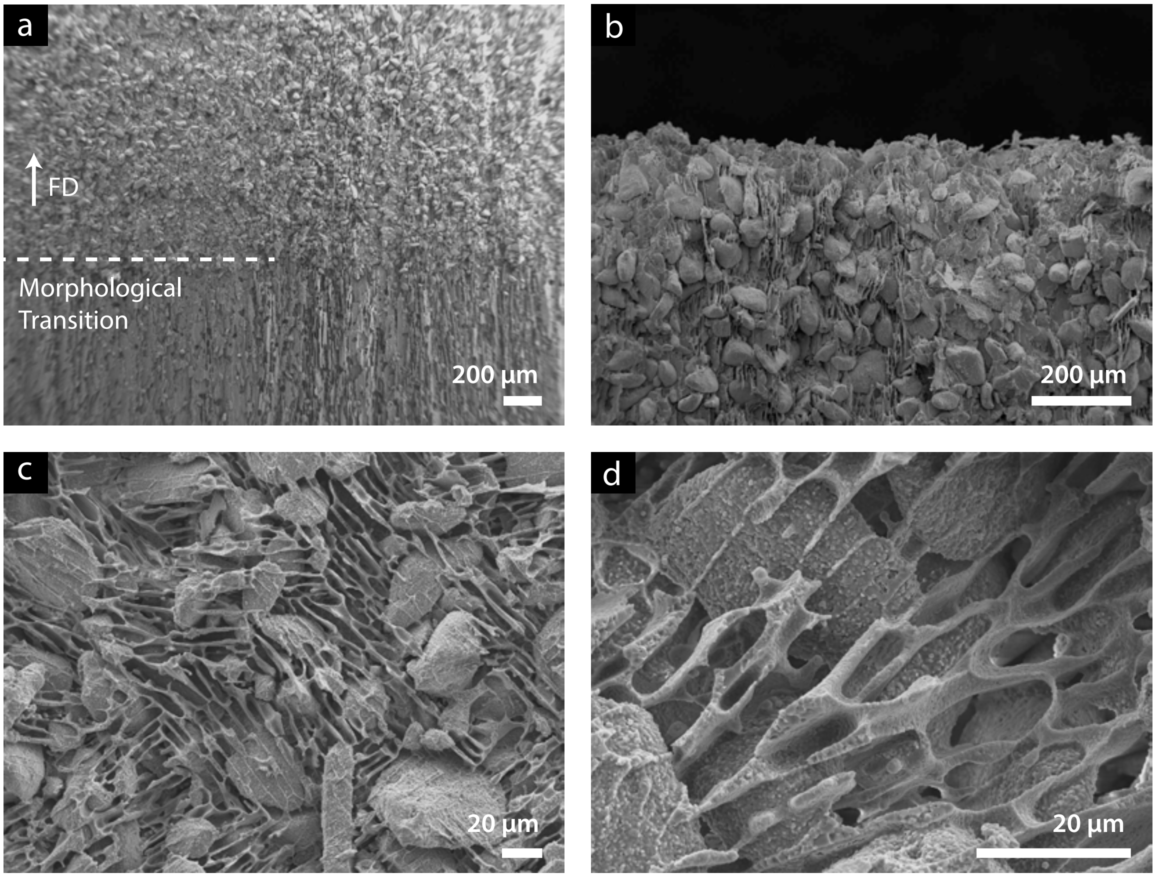

Figure 4.7: Microstructure of freeze-cast alumina with bimodal size distribution showing (a) the morphological transition which occurred in the freezing-direction triggered by the building concentration of large agglomerates. (b) The top of the bimodal freeze-cast showing the structure parallel to the freezing direction. (c) Cross-section of the bimodal freeze-cast and (d) magnified image of the cross-section showing how the small, templated particles seem to nucleate from the larger agglomerates themselves.

4.1.3 Aqueous Co-Dispersion of LSM-YSZ

Initial attempts at slurry dispersion and freeze-casting of LSM and YSZ were based on previously successful methods for co-dispersing SOFC anode materials [63]. The LSM and YSZ powders were first ball-milled dry to form a homogeneous powder. This mixture was slowly added into deionized (DI) water containing Darvan C-N until approximately 25 vol. % solids was reached. The pH was not controlled during these initial attempts. The slurries produced using this method were highly viscous and impossible to freeze-cast no matter the level of dispersant used.

More advanced, methods for the co-dispersion of two materials typically rely on exploiting the isoelectric points of the individual materials [166]. These methods alone proved inadequate however and the suspensions which were initially created were unstable and resulted in the immediate segregation of LSM from YSZ. Indeed, no matter the experimental parameters (18 - 25 vol. % solids, 1.5 - 5 wt. % dispersant, 3 - 5 wt. % binder, pH = 6 - 10), the slurry conditions proved inadequate and resulted in the formation of spherical YSZ agglomerates, which sintered into dense spheres 10 - 50 µm in size, which would embed themselves within the larger freeze-cast matrix (Fig. 4.8). EDS spectra showed that these spheres were composed almost exclusively of YSZ. The spheres reduced the active volume fraction of YSZ within the freeze-cast matrix inhibiting the percolation of the ion-conducting phase.

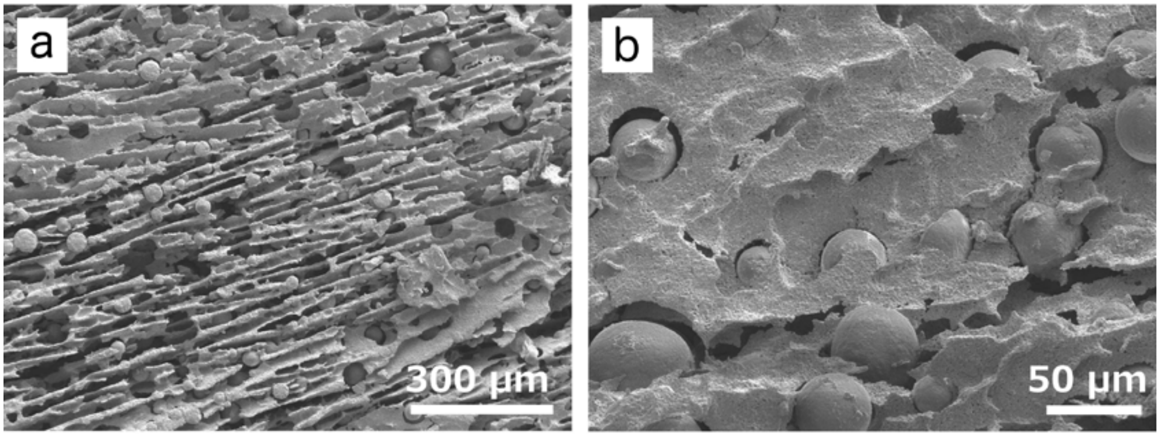

Figure 4.8: Overview (a) and magnified (b) SEM micrographs of the LSM-YSZ structure containing dense, embedded YSZ-spheres that formed spontaneously in response to non-ideal dispersion conditions. Samples were partially sintered to 1200 °C before being sectioned and imaged.

Three steps were required to produce a stable, aqueous co-dispersion suitable for freeze-casting. First, YSZ had to be fully dispersed on its own, prior to the addition of the LSM, thereby allowing full coverage of the dispersant on the YSZ particles. Second, the pH of the solution during co-dispersion had to be carefully controlled. Acidic pH values can potentially lead to the leaching of yttrium ions out of solution while values too close to the isoelectric points of the materials (6 and 8.4 for LSM and YSZ, respectively) will result in particle sedimentation [61, 174, 175]. For these reasons, the pH of the slurry was kept between 7 and 8 (see section 2.4). Lastly, the viscosity of the slurry had to remain high enough to partially coagulate the suspension, hindering the majority of particle segregation, while at the same time be low enough to still allow the slurry to be easily freeze-cast

[149]. For the LSM-YSZ system, the range of usable dispersants was found to be between 1.4 - 2.6 wt. % of the solids for slurries ranging from 17 to 40 vol.% solids, and though these values appear high, they were found to be the necessary levels of dispersant for this particular system. Once formed, these slurries were highly stable, often lasting many days without appreciable degradation.

Rheological Testing

Rheological testing was used to better understand the necessary slurry viscosity for freeze-casting LSM-YSZ in an aqueous environment. Two variables were targeted for their effect on slurry viscosity: solid content and the amount of dispersant. All tested slurries exhibited a clear shear-thinning behavior with viscosity decreasing with increasing shear rate.

Solid loading, within a range of 17 to 27 vol. % solids, was found to have a small effect on slurry viscosity [Fig. 4.9 (a)]. At high shear rates the 27 vol.% slurry was only 3.5 times more viscous than the least viscous (17 vol.%) slurry. The amount of dispersant however was found to have a marked effect on the rheological properties of the suspension. There was a significant decrease in viscosity when the level of dispersant was increased from 1.4 to 2.6 wt.% [Fig. 4.9 (b)] in a 23 vol. % solids slurry. From the viscometry curves, it was found that at high shear rates, the 1.4 wt.% dispersant slurry was 51 times more viscous than the 2.6 wt.% dispersant slurry. At low shear rates the 1.4 wt.% dispersant slurry was 230 times more viscous than the 2.6 wt.% slurry.

Using 23 vol. % solids, only slurries made using dispersant levels between 1.6 and 2.0 wt. % Darvan C-N were found to be viable. Images of slurry droplets made with various levels of dispersant are included as references to how workable slurries should look. The topmost image [Fig. 4.9 (c)] shows what an over-coagulated slurry looks like. This slurry remains dispersed but is unworkable for freeze-casting because it will not settle and fill its container. Large voids will remain if such a slurry is freeze-cast. Figure 4.9 (d) shows the behavior of a slurry appropriate for freeze-casting. It will flow easily to fill its mold but is partially coagulated enough so that the LSM and YSZ are prevented from segregating (at least on the time-scale of an experiment). The final image, figure 4.9 (e) shows what an overly dispersed LSM-YSZ suspension looks like. This slurry is too thin and because of this, the two particle types will separate due to density difference. There will be a visually obvious color change in the freeze-cast, with the lighter YSZ particles at the top while the dense LSM particles will settle to the bottom.

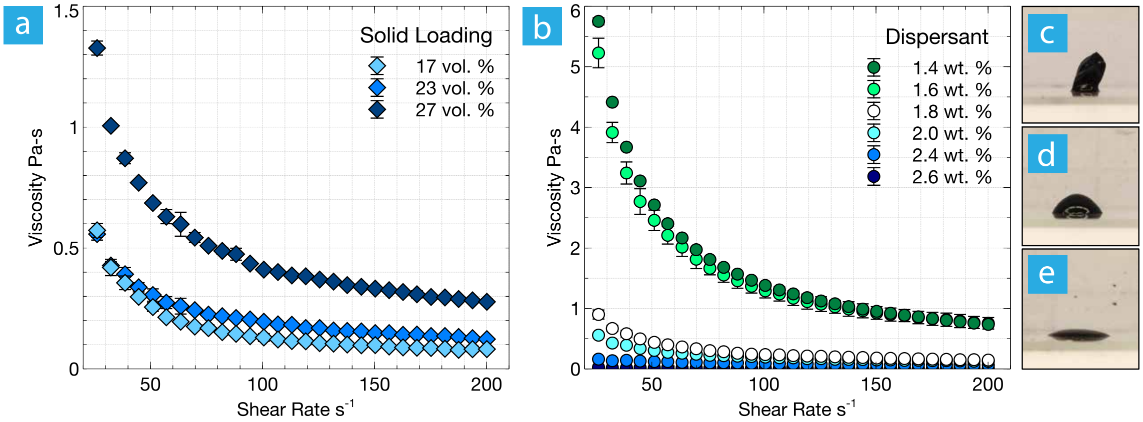

Figure 4.9: (a) Viscosity curves for various solid loadings using 2.0 wt. % dispersant. (b) Viscosity curves for 23 vol. % solid slurries with various amounts of dispersant. Images of slurry droplets which are (c) underdispersed, (d) properly dispersed and (e) overdispersed. Each viscosity curve represents 3 measurements.

Using experience from making over 80 different LSM-YSZ slurries, a processing map was created to give future researchers a general idea of how to properly disperse their slurry (Fig. 4.10).

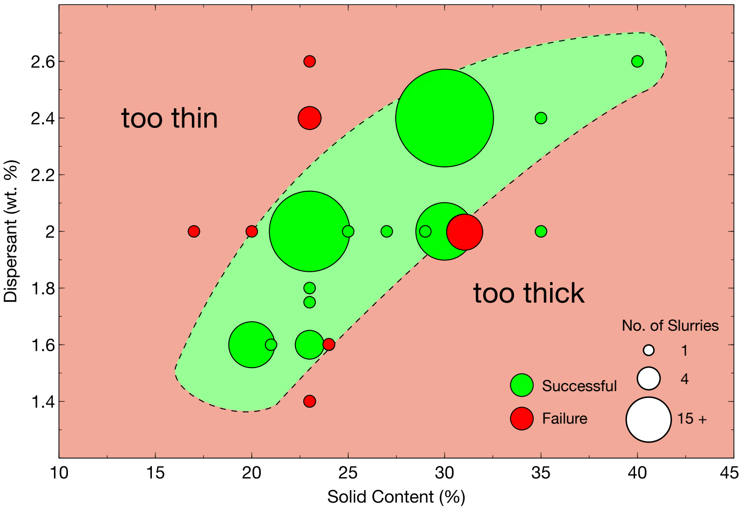

Figure 4.10: Processing map for LSM-YSZ slurries made using the proper aqueous co-dispersion procedure. No datapoints are included for slurries made using additional PMMA pore-formers.

EDS Phase Dispersion

Looking at the microstructure itself, the procedure developed for co-dispersing and subsequently freeze-casting LSM-YSZ results in visually homogeneous distributions of the LSM and YSZ particles (Fig. 4.11). Elemental mapping shows no significant segregation of the phases within the microstructure indicating good percolation of the electron and ion-conducting phases.

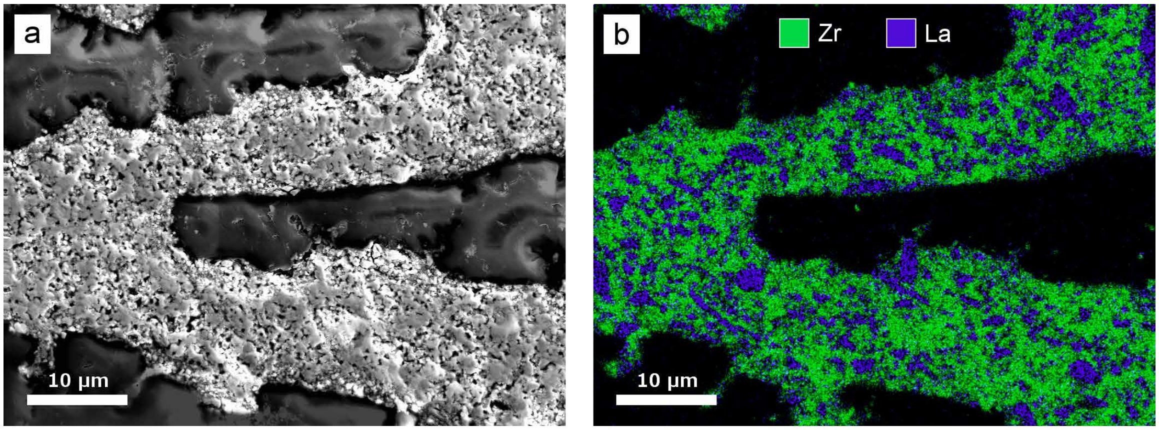

Figure 4.11: (a) SEM image of freeze-cast walls and macropores sintered at 1200 °C. (b) EDS map of zirconia (green) and lanthanum (blue) showing the spatial distribution of LSM and YSZ particles across two freeze-cast walls. The macropores of the sample have been infiltrated with an epoxy resin (black regions) for sample preparation. The freezing direction is normal to the image.

XRD Phase Analysis

XRD of LSM-YSZ samples sintered at 1300 °C in air and then ground into powder can be indexed by only two phases, YSZ ($Y_{0.19}Zr_{0.81}O_{1.91}$) and LSM ($La_{0.8}Sr_{0.2}MnO_3$) (Fig. 4.12). There is no indication of the detrimental $La_2Zr_2O_7$ phase. Since there was no appreciable reactivity between LSM and YSZ at a high sintering temperature (1300 °C), it is safe to assume that all samples sintered at that temperature or below are free of the $La_2Zr_2O_7$ phase.

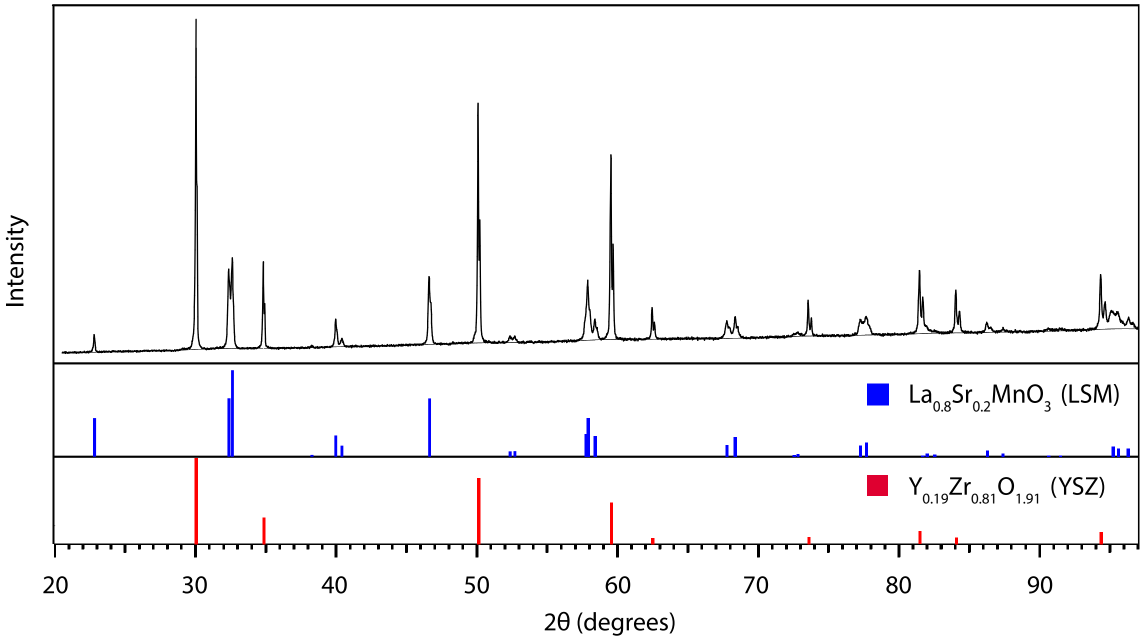

Figure 4.12: XRD diffractogram of LSM-YSZ sintered to 1300 °C with overlayed diffraction peaks.

4.1.4 Processing Control of LSM-YSZ Freeze-Casts

Solidification Velocity and Microstructural Wavelength

Once the protocol for properly dispersing and freeze-casting LSM-YSZ was established, it was necessary to determine the range of microstructures that we could make. The following design-of-experiment (DOE) (Table 4.1) was used to determine the effects of freezing rate, slurry viscosity and solid loading on solidification velocity and λ for the LSM-YSZ system. λ once again is the microstructural wavelength of a freeze-cast, found by averaging together the width of a ceramic wall and its adjacent macropore.

Table 4.1: LSM-YSZ Processing DOE

	Test	**Solid Loading (vol. %)**	**Dispersant (wt. % of solids)**	**Freezing Rate (°C min^{-1})**
I	Effect of freezing rate	23	2.0	1, 3, 5
II	Effect of slurry viscosity	23	1.6, 2.0, 2.4	5
III	Effect of solid loading	17, 23, 27	2.0	5

Solidification images taken during freeze-casting were used to calculate instantaneous solidification velocities for each sample during the entire freeze-casting study. Just like with alumina freeze-casts (see section 4.1.2), we found that although we achieved constant solidification velocities, lamellar size increased over the sample height (Fig. 4.13).

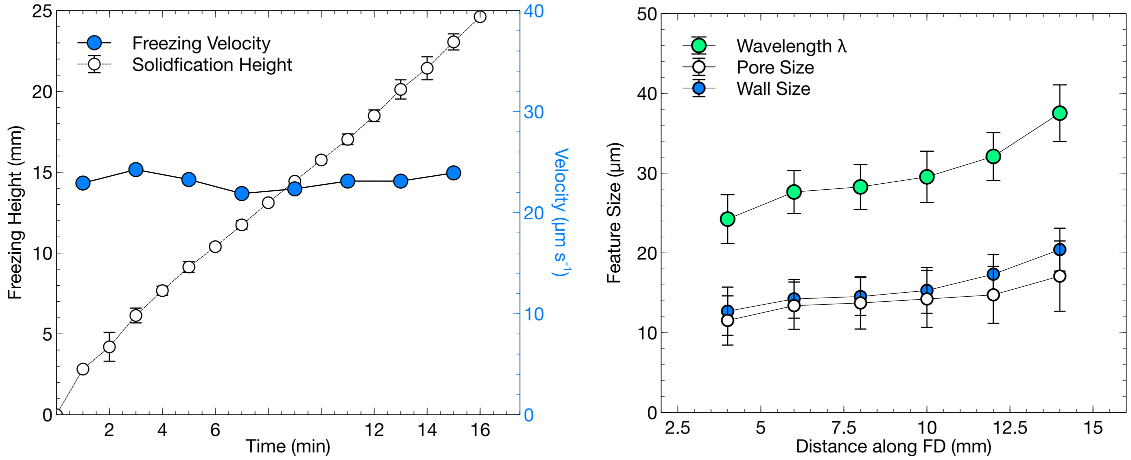

(a) Solidification velocity and height **(b)** Corresponding microstructural size

Figure 4.13: (a) Derived solidification velocity from solidification height measurements for multiple samples frozen at 5 °C min^{-1}. (b) Averaged measurements of macropores, walls and λ as a function of freezing height for samples frozen at 5 °C min^{-1}.

Interestingly enough, there was a region in all freeze-casts where the lamellar size increase was minimized. In our case, this was from 6 to 12 mm along the freezing direction. The freezing velocities measured from these constant solidification regions were averaged and compared across each experimental treatment to see which factors, if any, affected the average solidification velocity of composite LSM-YSZ freeze-casts (Fig. 4.14). Average λ values (from 6 - 12 mm along the freezing direction) as a function of each experimental variable have been plotted directly below the solidification velocity plots to better understand the interrelationships between experimental processing, freezing velocity, and resultant microstructure.

As solid loading was found to have little influence on slurry viscosity within this solid loading range (see section 4.1.3) we were able to assume that the amount of dispersant and solid loading would act as independent variables and their contributions to the resultant freeze-cast properties would be distinguishable from one another.

From the freezing velocity plots [Fig. 4.14 (a - c)] it was found that the only variable that had a significant effect on the freezing velocity was freezing rate. Increasing the freezing rate from 1 to 5 °C min^{-1} increased the average solidification velocity from 12 to 23 µm s^{-1} which corresponded to a decrease in average λ from 82 to 31 µm [Fig. 4.14 (d)]. Altering solid loading and viscosity had no significant effect on the freezing velocity indicating that

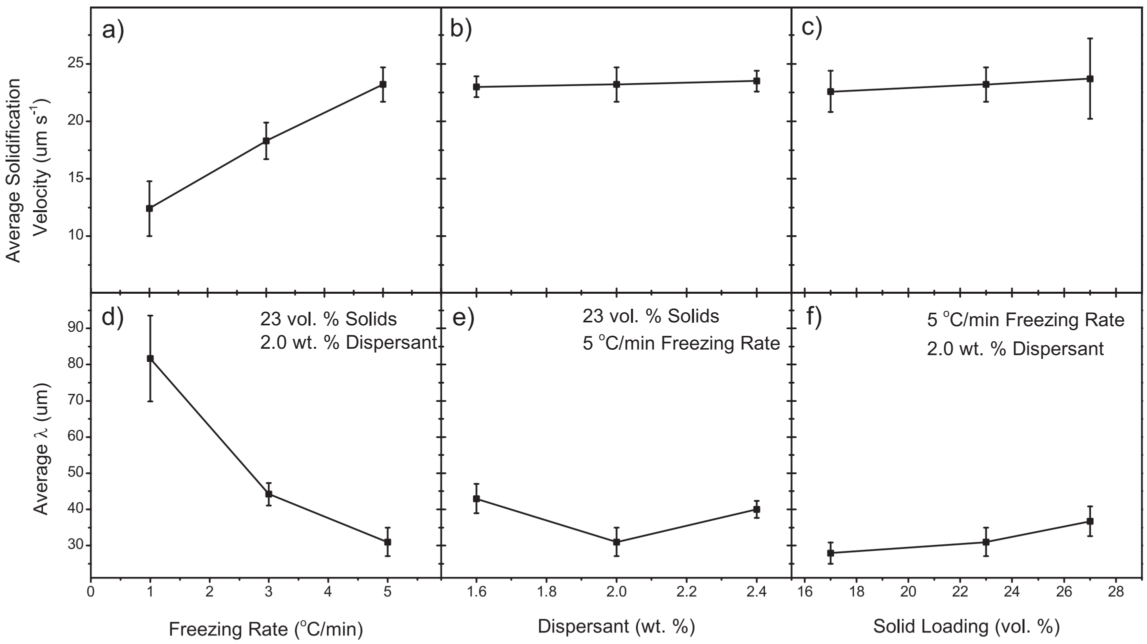

Figure 4.14: Plots of average constant solidification velocity as functions of (a) freezing rate; (b) amount of dispersant; and (c) solid loading. Error bars represent the range from a minimum of 18 measurements. Average λ size as a function of (d) freezing rate; (e) amount of dispersant; and (f) solid loading. Error bars represent the range for a minimum of 500 measurements.

solidification velocity is mainly dictated by the thermal profile and the solvent being used. The effect of the amount of dispersant (slurry viscosity) on λ is complex. It appears that at intermediate levels of dispersant (2.0 wt.%) the average microstructural wavelength of a freeze-cast will be approximately 10 ± 2 μm smaller than those of freeze-casts made with either low or high levels of dispersant [Fig. 4.14 (e)]. It is believed that the behavior exhibited by these samples could be attributed to the competing effects of supercooling and particle mobility. Increased levels of dispersant will decrease slurry viscosity (Fig. 4.9) and enhance the effect of freezing point depression and supercooling of the slurry before it freezes, altering the nucleation regime and subsequent growth; while decreasing dispersant levels (increasing viscosity) hinders ice growth by introducing resistances to particle mobility. It is however unknown what the exact extent of these competing factors is for the LSM-YSZ system.

Interestingly, although solidification velocity did not change with different solid loadings, average λ increased from 28 to 36 μm with an increase in solid loading from 17 to 27 vol. % [Fig. 4.14 (f)], with the most noticeable effect occurring at the highest solid loading. It can be assumed from this observation that an increase in wall thickness (from increased solid loading) does not lead to an equivalent decrease in macropore size and vice versa. There is clearly an additional contribution to λ apart from solidification velocity. Both the dispersant amount and solid loading have a minor but measurable effect on λ in addition to the dominant effect of solidification velocity (controlled by the freezing rate).

Using the high speed freeze-caster, we were able to attain even higher solidification rates. Shown in figure 4.15 we can see the average macropore size for freeze-casts made with freezing rates up to 40 °C min^{-1}. Measurements were taken from 2 mm (bottom) and 16 mm (top) along the freezing direction. As previously shown, although linear temperature profiles were used, macropore size does not remain constant along sample height. The trend is strongest for slower freezing rates which showed the greatest increase in average pore size over sample height (> 36 μm for 1 °C min^{-1} samples). This can be explained by the fact that as the freezing rate is decreased, the profile becomes more and more like that of statically frozen samples. As we saw before, samples frozen entirely with static temperature gradients see progressively lower driving force for growth in the direction of the temperature gradient. This allows for enhanced growth along other crystallographically preferential directions: ex. normal to the basal planes of the growing ice crystals. The other observation that can be pulled from this figure is that by approximately 10 or 20 °C min^{-1}, λ and the macropore size no longer seems to decrease with increasing freezing rate.

It should also be noted that the "bottom" microstructural inset (Fig. 4.15) for the 1 °C min^{-1} sample appears to have a different morphology than other samples indicating that the freezing process has not reached steady-state at this height. Logically this is in agreement with previous knowledge of the morphological transition mechanism. The smaller the temperature gradient, the smaller the thermal drive for growth in the freezing-direction (essentially static profiles). Therefore, at this point in the growing process we still have a significant number of r-crystals remaining where in other freeze-casts made at faster rates we are obviously in the steady-state zone at this point in the growth process.

Using the knowledge gained from freeze-casting a variety of LSM-YSZ structures, the following processing map was created showing that we can achieve a broad range of microstructural control simply by altering the temperature profile during freeze-casting and the ratio of solids to water (Fig. 4.16).

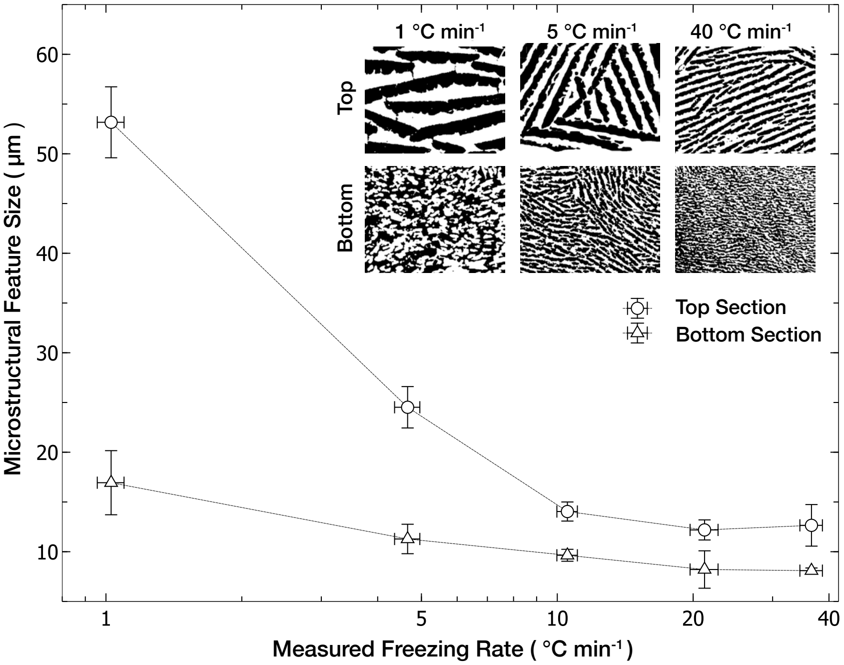

Figure 4.15: Measured average macropore size for 20 vol. % solids freeze-casts as a function of freezing rate at 2 mm (bottom) and 16 mm (top) along the freezing-direction (FD). The insets are thresholded microstructural cross-sections (transverse to the FD) taken from the top and bottom microstructures of samples frozen at 1, 5 and 40 °C min^{-1}

.

4.1.5 Slip-Cast LSM-YSZ Structures

To compare isotropically porous hierarchical structures with our anisotropic ceramics, aqueous LSM-YSZ mixtures were slip-cast with PMMA pore-formers of various sizes. In this case, the macropore size is controlled by the size of the pore-former and the ratio of PMMA to the ceramics controls the volume fraction of the macropore. The following data show pre- and post-sintering diameters of the macropores contained in the slip-cast ceramics (Fig. 4.17).

The overlayed bar chart indicates the relative shrinkage experienced by the macropores during sintering. On average, macropores shrunk between 18 - 20 % when sintered at 1200 °C.

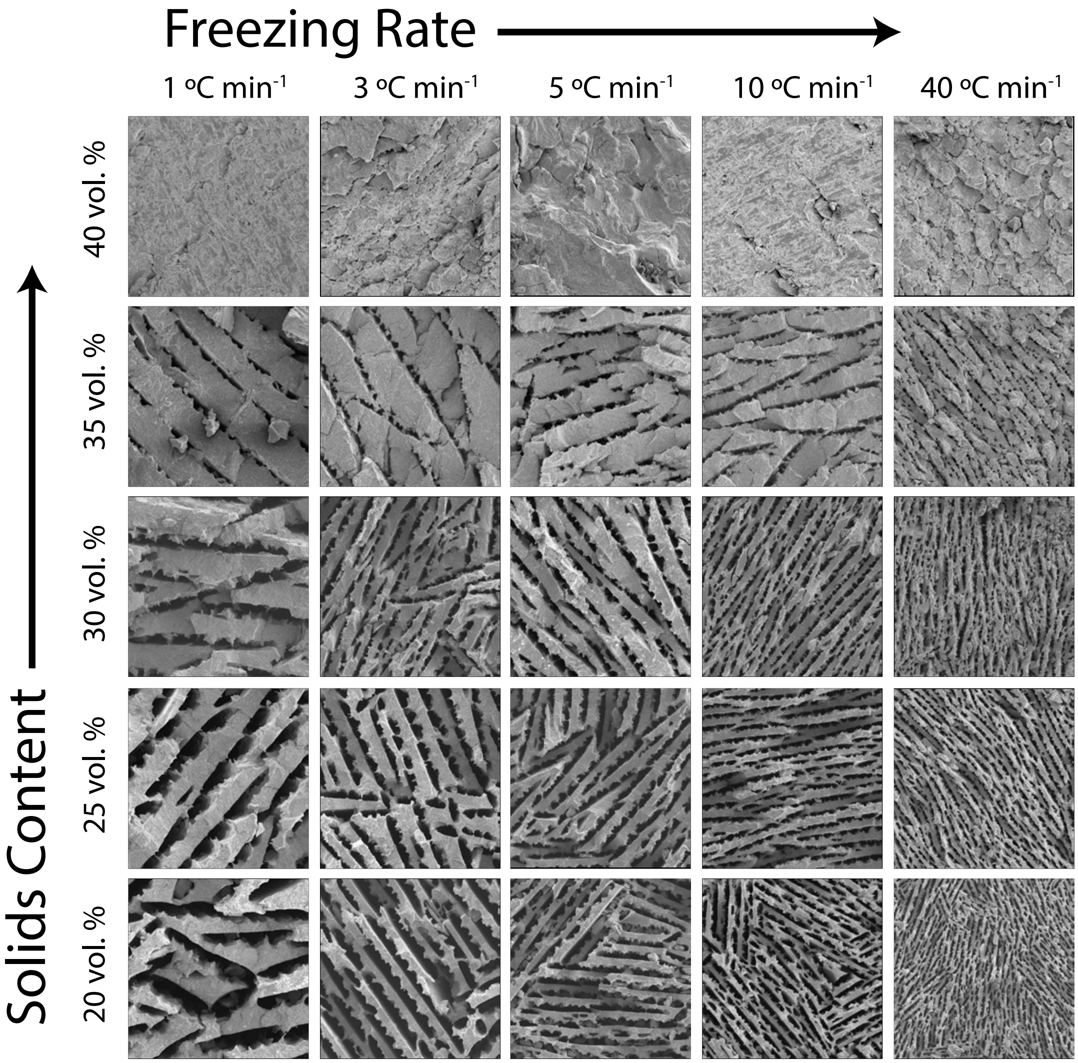

Figure 4.16: Processing map of LSM-YSZ freeze-casts. Each image is 435 x 435 μm. Samples were sintered to 1300 °C for easier sample preparation and imaging. All images were taken at a point approximately 7 mm along the freezing direction. Note that no 40 vol. % samples experienced templating, indicating that freeze-casting is not possible at this solid loading for this particular materials system.

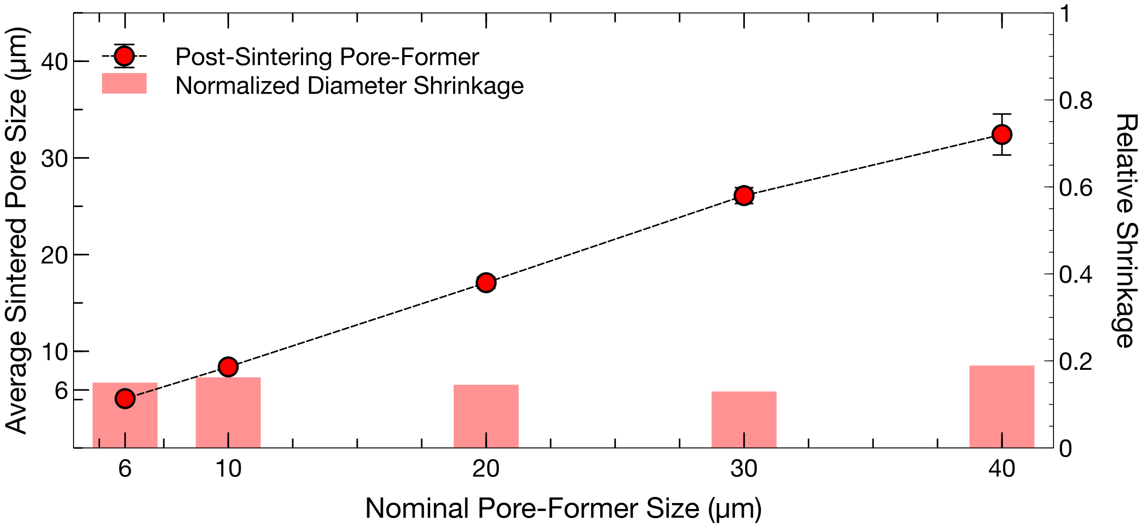

Figure 4.17: Post-sintering sizes of isotropic PMMA pore formers as function of their nominal pre-sintered size. Also shown (bar chart) is the relative shrinkage of the porogens after sintering.

4.2 Porosity and Sintering

The produced ceramics contain two levels of porosity which can be independently controlled. The macropores for the most part are determined either by freeze-cast processing or pore-former size in the case of isotropic, slip-cast ceramics. The micropores on the other hand are controlled by the extent of sintering. In the following section, the types of porosity are characterized and the effects of sintering on porosity and microstructure are explored.

4.2.1 Phase Connectivity, Triple Phase Boundaries (TPBs) and the Role of Sintering Temperature

Focused-ion beam (FIB) reconstructions of freeze-cast wall microstructures were performed on samples sintered to 1200 and 1300 °C (Fig. 4.18). These temperatures were chosen because they yielded samples with sufficient strength for handling while still retaining intrawall porosity.

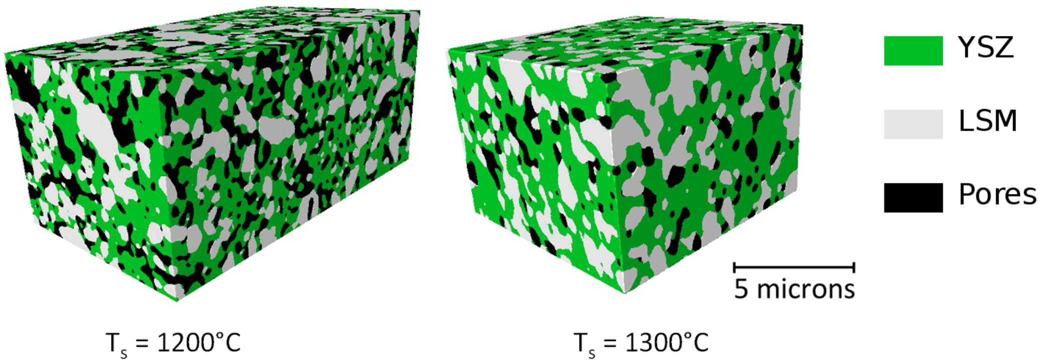

Figure 4.18: FIB reconstructions of samples sintered to 1200 and 1300 °C.

The two FIB reconstructions were fully characterized to see whether or not they could serve as good candidates for SOFC cathode material. To refresh, this means that each phase achieves as close to 100 % percolation as possible and that we have a high density of active TPBs. It was determined that all phases were nearly fully connected except for the pore phase in the sample sintered at 1300 °C, which showed a significant amount of unconnected and unknown connectivity volume (Fig. 4.19). This reduction in available, connected porosity would significantly hinder gas flow throughout the microstructure reducing SOFC performance. The FIB results provide further evidence that the method devised for dispersing and freeze-casting composite LSM-YSZ is sound.

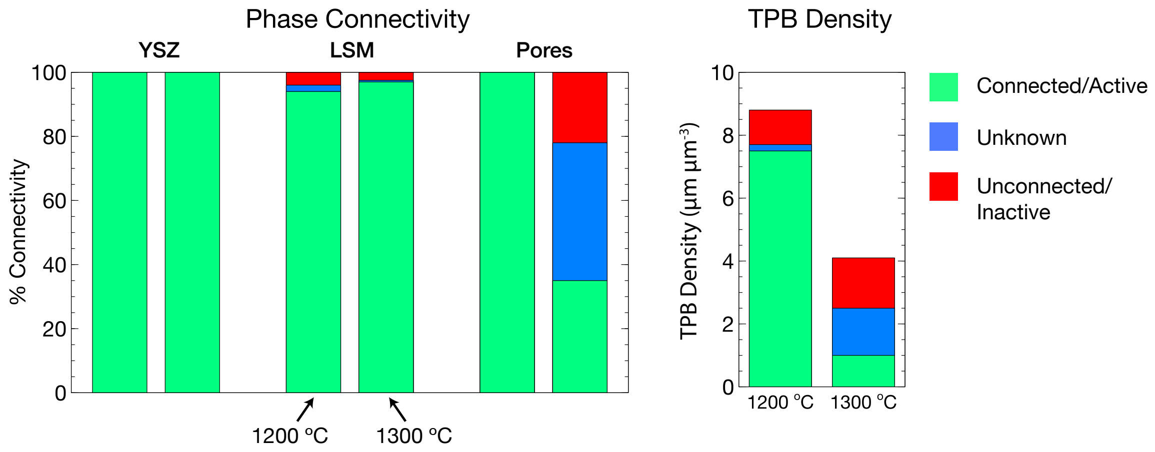

Figure 4.19: Effects of sintering temperature on phase connectivity and TPB density in LSM-YSZ freeze-cast samples.

Determination of electrochemical performance requires proper quantitative accounting of the TPBs. An algorithm was employed which determined where all TPBs were located. It then assigned a value of active, inactive or unknown to each TPB line. An active TPB is one where there are complete percolation paths from the TPB line for the electronic phase (LSM), the ionic phase (YSZ) and the porous phase to the proper edges of the reconstructed volume as defined in figure 3.15. The results, reported in figure 4.19, show that sintering to the higher temperature significantly decreases the total TPB density as well as the proportion of TPBs that are active. Figure 4.20 shows complete 3D breakdowns of each phase and TPB maps.

Once more looking at the FIB-SEM 3D reconstructions for both the 1200 °C and 1300 °C samples, we see that the high temperature sample exhibits a coarser microstructure than the one sintered at 1200 °C. In addition to the loss in connectivity of the pore phase, there is a significant loss in porous volume, 14.9 vol. % at 1300 °C compared with 25 vol. % at 1200 °C. To quantitatively analyze the coarsening of the microstructure at the higher sintering temperature, the size distribution of each phase at both temperatures was computed through image analysis[6] and is plotted in figure 4.21. These data confirm that the reconstructed volumes are good representative samples since the smallest dimensions of each reconstructed volume (7.4 and 7.2 µm) are 12 and 10 times larger, respectively, than the largest average particle size [176]. Secondly, it was observed that the average size of the LSM particles remains approximately the same when sintered at 1200 °C or 1300 °C

---

[6] Using the GeoDict software package.

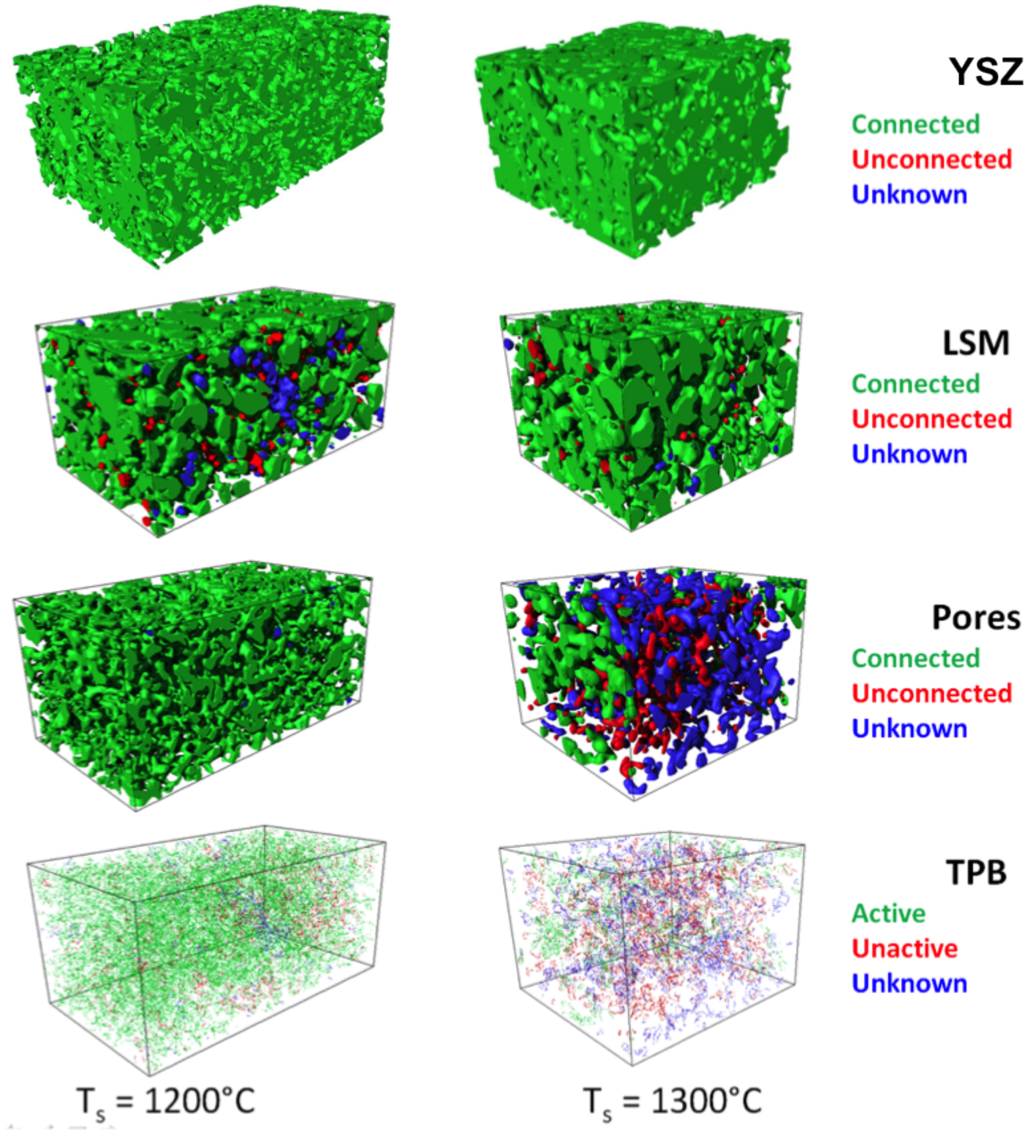

Figure 4.20: Freeze-cast samples sintered at 1200 and 1300 °C showing the connectivity of the three different phases as well as TPB density in LSM-YSZ freeze-casts.

(800 nm and 740 nm, respectively), whereas the average size of the YSZ particles grows from 300 nm to 550 nm.

Effect of Sintering on Gas Diffusivity within Walls

Using these same FIB microstructures, the tortuosity factors for YSZ, LSM and pore phases were found and are plotted in figure 4.22. The tortuosity was evaluated in the three Carte-

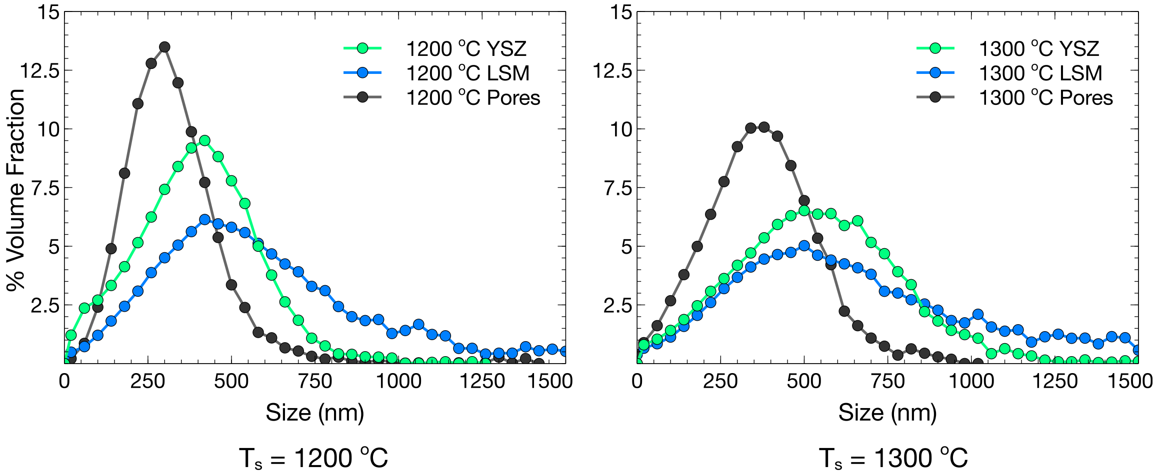

Figure 4.21: Size distribution of the three phases for (left) the low sintering temperature (1200 °C) and (right) the high sintering temperature (1300 °C).

sian directions (x, y, z) but it was found that there was essentially no difference in properties, spatially speaking, indicating that within the walls of the freeze-casts the structure is isotropic. The average tortuosity from the x, y and z-directions are shown in figure 4.22.

Generally speaking, tortuosity calculations show a decrease in tortuosity for both the ionic and electronic phases at the higher sintering temperature that can be attributed to coarsening of the structure. At 1300 °C the loss of porosity results in a phase with essentially zero percolation and therefore an infinite tortuosity factor (not shown). From this study as well as results from connectivity and TPB density studies, we conclude that 1200 °C is the optimal sintering temperature as far as functional properties are concerned for freeze-cast LSM-YSZ cathodes.

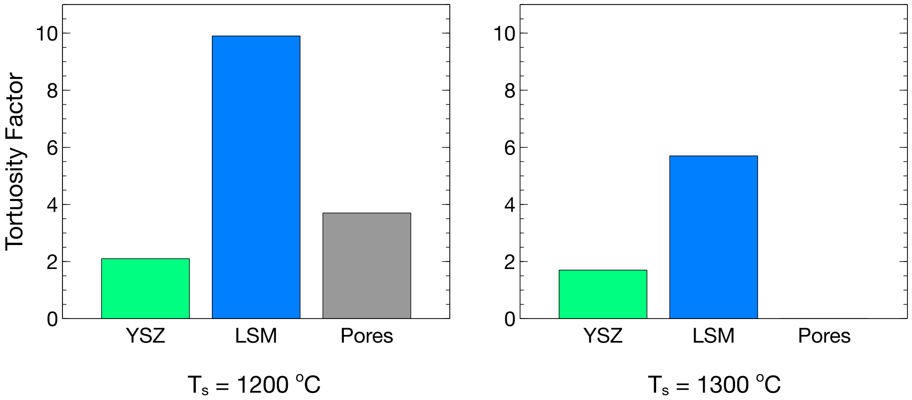

Figure 4.22: Tortuosity factors for the LSM, YSZ and pore phases at 1200 and 1300 °C.

4.2.2 Anisotropic Sintering Behavior

In their green-state, freeze-cast and slip-cast ceramics were fragile. They required some degree of sintering to not only provide strength but also to remove the organic binder and dispersant used during initial processing. The most commonly used sintering temperature throughout this thesis was 1200 °C since as shown previously, the resultant microstructure shows the most promise as an SOFC electrode. It was still prudent to test the full range of sintering temperatures to determine how the porous structure changed as a function of temperature. Physical measurements of samples before and after sintering showed that freeze-casts undergo anisotropic sintering behavior (Fig. 4.23). Optical dilatometry was then employed to track, in-situ, this phenomenon and give some insight into the sintering behavior of LSM-YSZ freeze-cast ceramics.

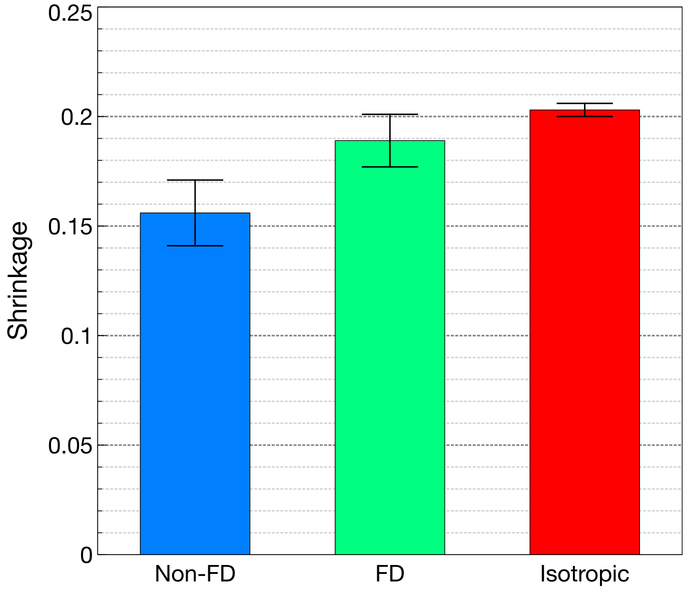

Figure 4.23: Sintering shrinkage from averaged physical measurements taken before and after sintering freeze-casts and slip-casts (isotropic) for sintering temperatures of 1400 °C in air. A minimum of 5 samples were utilized per treatment. FD = freezing direction.

In the freezing direction (FD), on average there was 3.4 % more shrinkage than in the non-freezing directions. Here we also see evidence that isotropic samples densify to a greater extent than freeze-cast samples for although they started with the same levels of green porosity these samples experience additional densification even when thermally treated in the same manner. This was the first indication that the microporous structure contained in slip-cast samples may differ from those made using freeze-casting. It is worth pointing that the variability in shrinkage for the isotropic samples is lower than for freeze-cast samples.

Interestingly enough, optical dilatometry showed rather mixed results when it came to deciphering the anisotropic behavior of freeze-casts. All samples were processed in the same way and testing was performed in as controlled a manner as possible yet there was still a good deal of spread and overlap when it came to deciphering the data. Although the trend does seem to indicate that samples reach higher levels of linear shrinkage in the FD, it would be difficult to definitively claim this from these data (Fig. 4.24). In my opinion, this is due to the rather insufficient tracking algorithms which were employed in the optical dilatometer software. The software was so unstable that we developed our own image analysis method to track the edges of our samples but in the process had to reduce the resolution of our images, severely limiting the precision of our measurements.

The optical dilatometer used for the study shown in (Fig. 4.24) was limited to a 1400 °C maximum. Using a separate optical dilatometer[7], we were able to get to 1500 °C but only under oxygen-free conditions. Freeze-casts were sintered in an argon atmosphere (reducing conditions) up to 1500 °C producing the following results (Fig. 4.25).

We see that by 1400 °C, we have achieved roughly the same relative linear change (Fig. 4.23) as those seen during air-sintering (0.15 and 0.20 for the non-FD and FD directions, respectively). Past this temperature, the gap between the two linear shrinkages widens even further as the linear change in the freezing direction pushes past 25 %, leading to 10 % greater linear densification in the freezing direction. The other interesting result from this study was that there was an obvious chemical change which took place at these temperatures and under reducing conditions (Fig. 4.26). It is unclear at what point this phase change took place and whether or not it had an effect on the densification behavior.

From our sintering studies of 40:60 vol. % LSM-YSZ we see that densification starts to occur at approximately 1000 °C and continues until full densification is achieved at approximately 1500 °C. The vast majority of densification occurs in the 1100 - 1300 °C range. This is right in the range that we are targeting for our hierarchical ceramics. Because sintering occurs so rapidly in this range, even small inhomogeneities in furnace temperature can lead to large discrepancies in shrinkage between specimens. This should be kept in mind when designing future studies. Changing furnaces or even furnace setups could potentially lead to dissimilarities in samples which are, at least to the experimenter, treated similarly.

---

[7] Located in the GPM2 lab in Grenoble, France

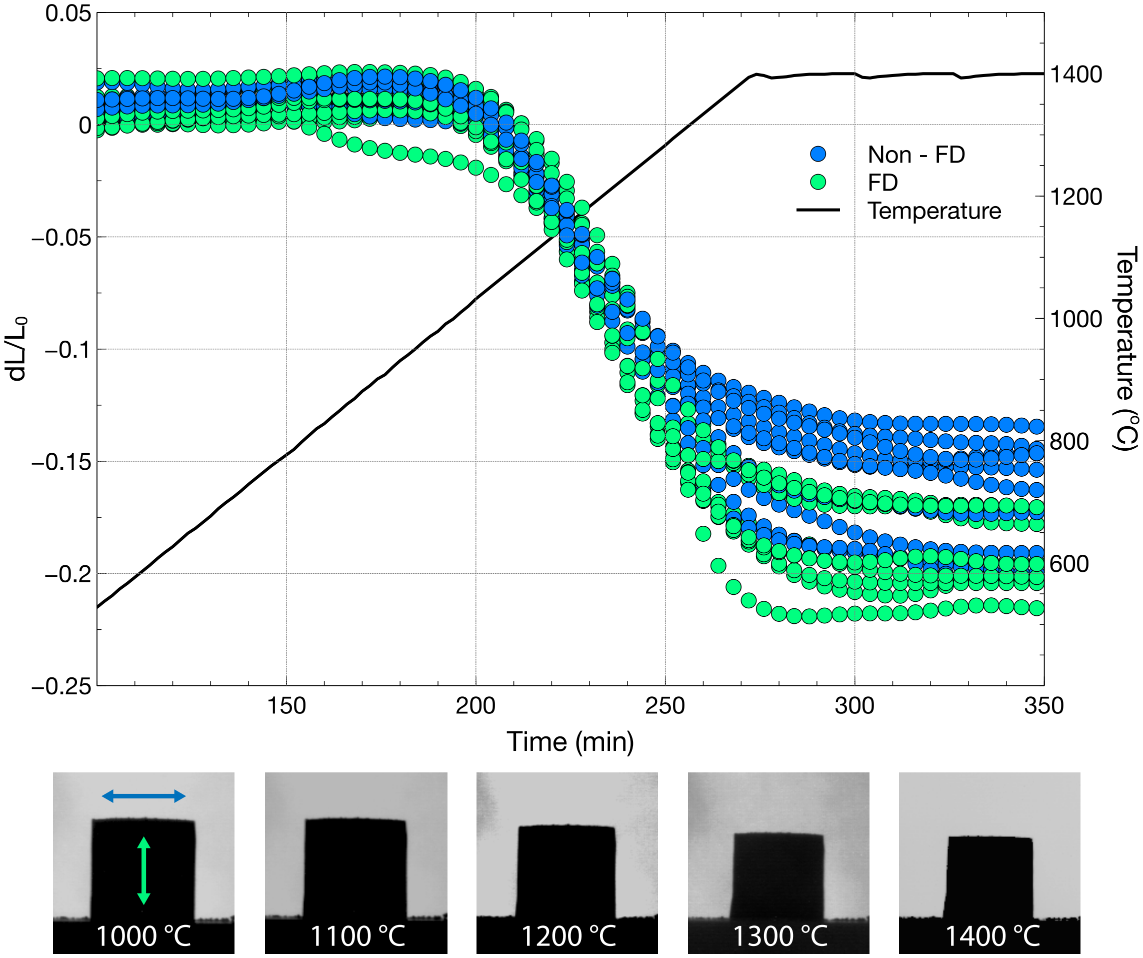

Figure 4.24: Multiple sintering profiles from samples oriented with their freezing-direction up. Still-frames from one of the sintered freeze-cast samples is included for reference.

4.2.3 Controlling Micropores and Macropores

Using a combination of FIB data, Archimedes data and optical microscopy, a processing chart was created specifically for freeze-cast samples made using 23 vol. % green-state solid loading (Fig. 4.27)[8]. If 23 vol. % solids is used, the sample will initially start with 77 vol. % total porosity, approximately 38 % of which consists of macropores the rest being micropores in the walls. As temperatures increase, the majority of porosity loss can be attributed to loss of microporosity. Although, the macropores do densify somewhat, even

---

[8] Although 23 vol. % solids loading was used, the trends seen here should be applicable to any other solid loading.

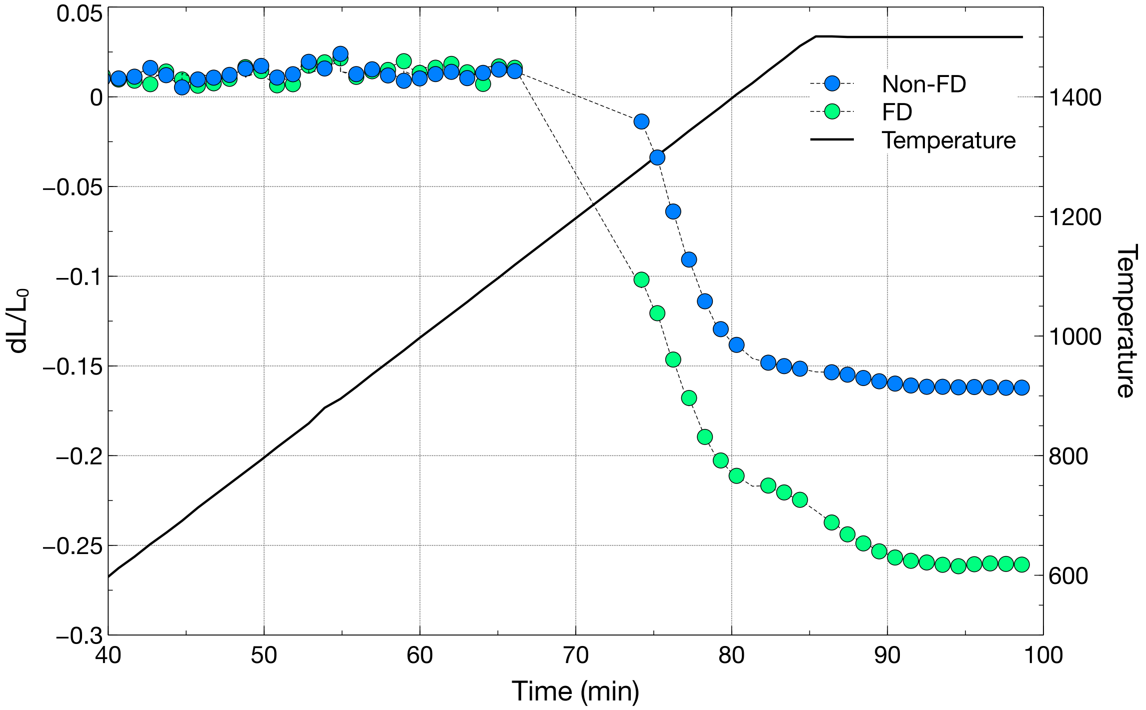

Figure 4.25: Optical dilatometry curves from freeze-cast LSM-YSZ sintered up to 1500 °C under argon.

Figure 4.26: Image of normally black LSM-YSZ freeze-cast after sintering under a reducing atmosphere to 1500 °C.

after sintering to 1500 °C, they remain for the most part unchanged in size and shape. As a result, their volume fraction decreases, on average, in proportion to the decrease in the sample volume.

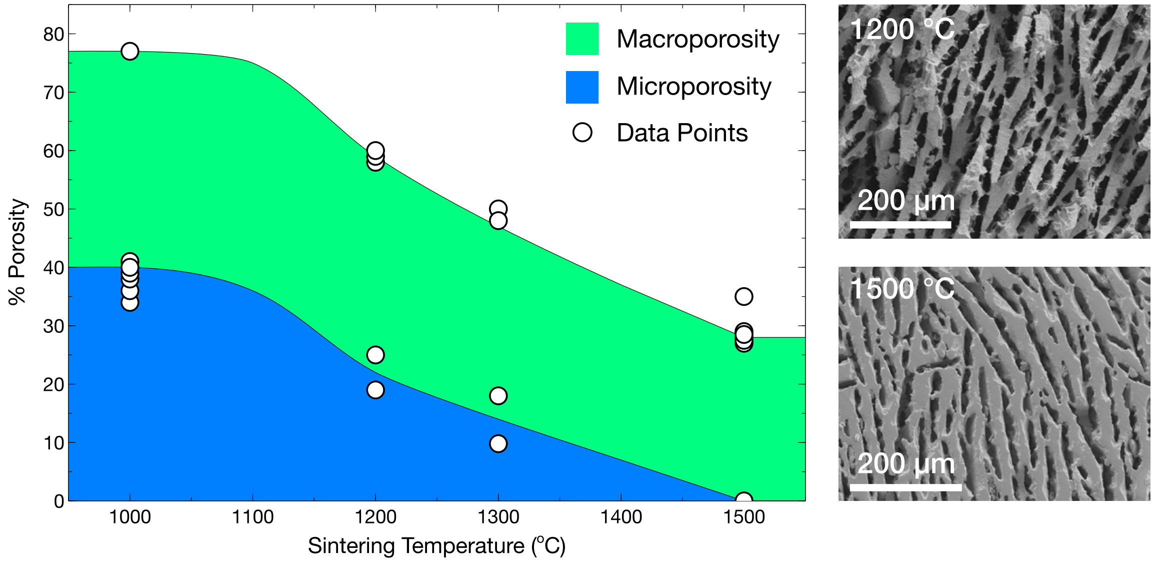

Figure 4.27: Effect of sintering temperature on micro/macro and total porosity for a 23 vol. % green-state solids LSM-YSZ freeze-cast. Images of 23 vol. % freeze-cast sintered to 1200 and 1500 °C showing that macropore size does not change drastically.

4.2.4 BET Adsorption Results

The idea of using BET adsorption to determine pore size distribution and surface area was highly attractive. Unfortunately, BET showed that we had <1 % porosity within the walls of our samples; as shown by FIB, we had at least 15 - 25 %. This discrepancy can be attributed to the pores simply being too large for BET measurement (>500 nm). This test was repeated multiple times to confirm the result.

4.3 Mechanical Response of Porous LSM-YSZ

4.3.1 Experimental Results

For this part of the project, our goal was to determine the effect, if any, that anisotropic pores had on mechanical properties. Freeze-cast and slip-cast samples were made with LSM-YSZ. The overall total porosity, average macropore size and microporous structure were kept the same (Table 3.7). As shown previously, 1200 °C was our optimal temperature so all ceramics were sintered to this level.

In the green state, all ceramics fabricated for mechanical testing (slip-cast and freeze-cast) contained either 70 or 80 vol. % porosity. Similar to the results shown in figure 4.23 however, we see that sintering produced distinct differences in macro and total porosity levels between samples made using the two processes (Fig. 4.28).

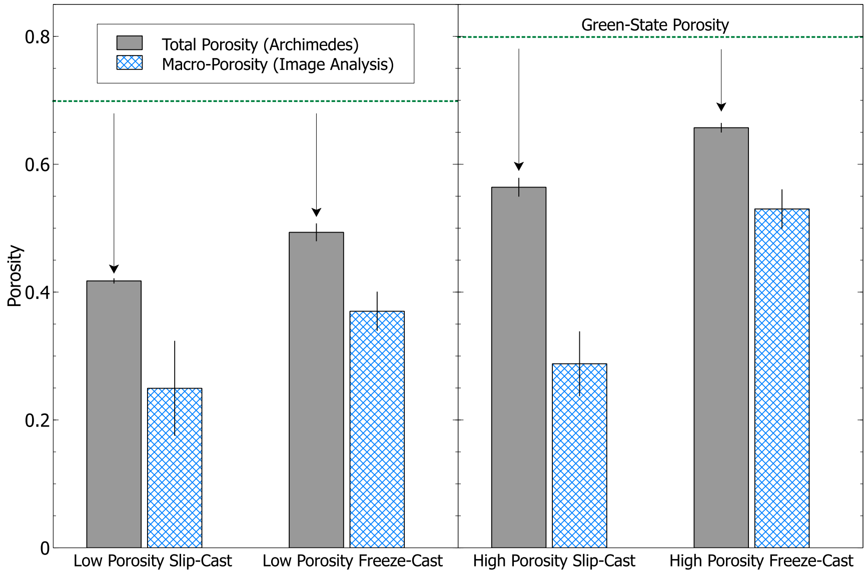

Figure 4.28: Total porosity and macroporosity for partially sintered slip-cast (isotropic) and freeze-cast (anisotropic) ceramics which initially had either 70 or 80 vol. % green-state porosity. The dotted green line indicates the initial level of green-state porosity. Note that slip-casts contain relatively less macroporosity than freeze-casts.

These discrepancies in porosity can likely be attributed to differences in packing efficiency caused by slip-casting versus freeze-casting [84]. Subsequent FIB was performed on slip-cast samples and showed that indeed they did contain less microporosity than freeze-cast samples sintered to the same degree, 14.3 vol. % versus 25 vol. % microporosity, respectively (Fig. 4.29).

During freeze-casting, ice crystals rapidly rearrange ceramic particles within the suspension without allowing sufficient time for the most efficient particle packing whereas slip-cast ceramics are given time to settle more efficiently allowing more uniform green state microporosity. The difference in microporosity values between slip-casts and freeze-casts is significant and likely does affect the mechanical properties. Even though the slip-casts were sintered to 1200 °C, they contained a volume of microporosity (14.3 vol. %) attained by freeze-casts sintered to 1300 °C (14.9 vol. %). It should also be pointed out that macroporosity accounts for a relatively higher level of the total porosity in freeze-casts than for

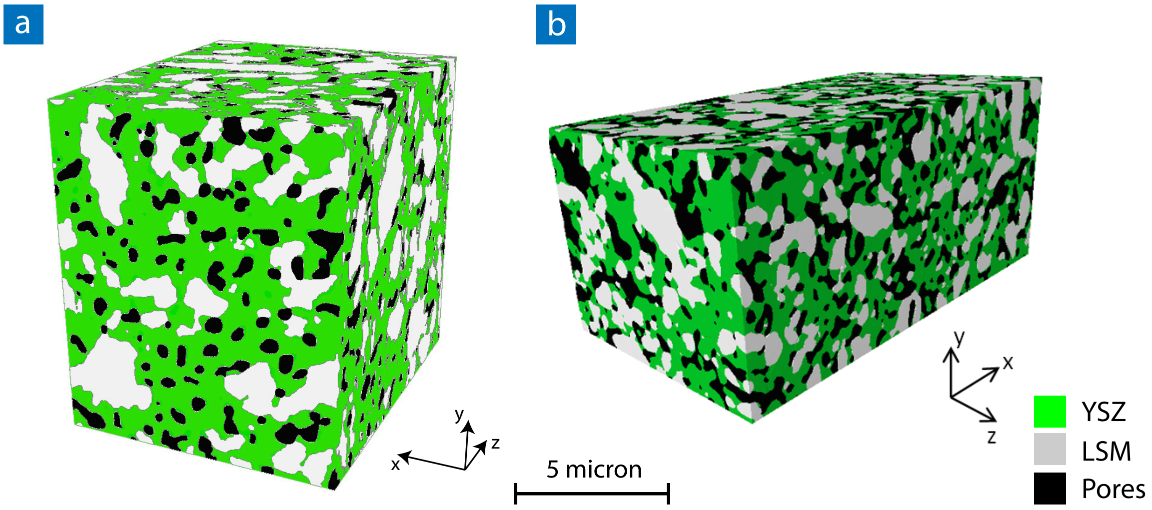

Figure 4.29: (a) FIB-tomography of slip-cast LSM-YSZ compared with (b) a freeze-cast sample sintered under the same conditions.

slip-casts. The additional densification which occurs in the microporous ceramic walls of slip-casts however does not account for the overall reduced macroporosity of the isotropic samples. Porosity not accounted for by the macropores can be attributed to the microporous walls.

Freeze-cast test specimens were prepared so as to only contain the SSZ regions. As shown previously however, macropore size increases as a function of freezing height, going from fine closer to where nucleation initiated (bottom) to coarser further along the freezing direction (top) (Fig. 4.15). Macroscopically there was also an apparent difference in behavior between the top and bottom of freeze-cast samples. When tested parallel to their freezing-direction, failure always initiated at the coarser top of the sample. For this reason, all subsequent microstructural datas are shown in reference to the top freeze-cast microstructure as this was the weakest section.

Comparing average macropore size of slip-casts and freeze-casts, we see good agreement between isotropic and anisotropic macropores for pore sizes in the 10 - 25 μm range (Fig. 4.30). Samples frozen at 1 °C min^{-1} achieved average post-sintered macropore sizes of 48 ± 4 μm and 53 ± 2 μm for the low and high porosity freeze-casts, respectively. There are no equivalent slip-cast samples made with pore-formers of this size.

It is interesting to note that at the higher freezing rates of 10, 20 and 40 °C min^{-1}, there was no difference in average macropore size between the two solid loadings indicating that for

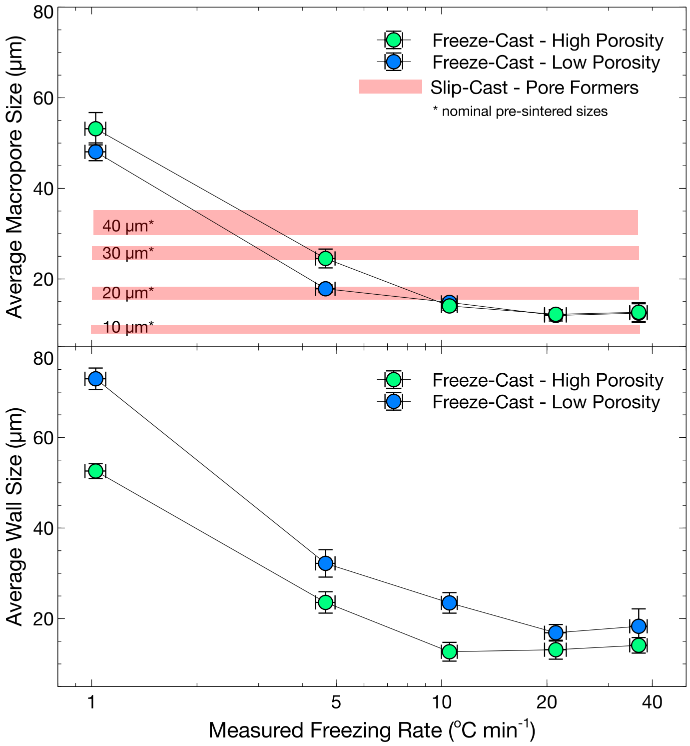

Figure 4.30: Average macropore (top) and wall size (bottom) for freeze-cast samples made using either the low or high porosity slurry. Isotropic macropore size and their standard deviations are shown as horizontal bars for the four pore sizes used.

this material system, once a rate of approximately 10 °C min^{-1} is reached, an equilibrium ice crystal size is attained which is more or less independent of initial ceramic loading [149]. Wall size however remains different between freeze-casts made using different ceramic loadings no matter the freezing rate. This ability to tune wall and pore size independently of one another could be further exploited for microstructural optimization [149].

Macropore Morphology and Mechanical Performance

Compressive mechanical properties were measured at room temperature with a constant strain rate of 0.01 mm s^{-1}. The freeze-cast samples were tested with applied stress along the freezing direction (parallel) and perpendicular to the freezing direction (transverse). The effect of macropore morphology was explored as a function of total porosity for samples with approximately the same macropore sizes. Stress-strain curves show clear differences between isotropic samples and both orientations (parallel and transverse) of freeze-casts (Fig. 4.31). The freeze-cast samples tested with the stress direction parallel to the freezing direction had the highest compressive strength and failed more gradually whereas isotropic samples typically experienced a sharp compressive peak followed by a catastrophic failure. Freeze-cast samples tested perpendicular to their freezing direction showed a long, extended crushing region before peak stress was achieved. Though not shown here, once a high enough strain was achieved ($\epsilon > 0.1$), the stresses measured from anisotropic samples tested in the transverse direction increased as the structure densified. Note that this is typical behavior for foam-like, cellular materials [136].

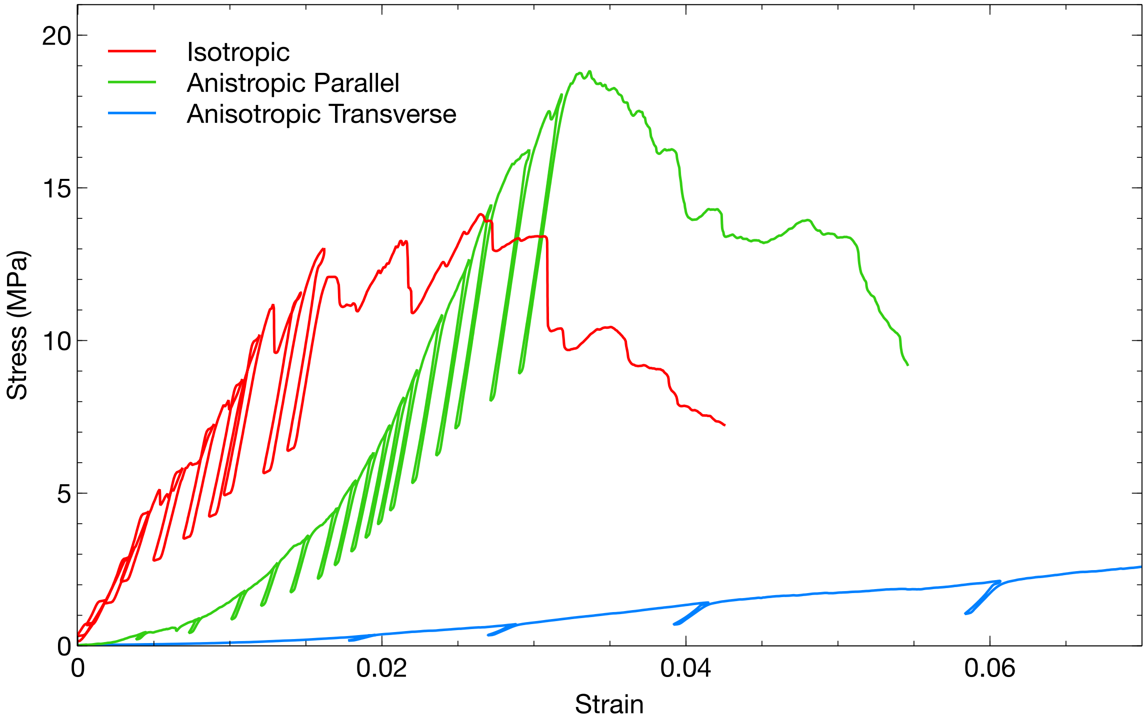

Figure 4.31: Representative stress-strain curves for isotropic, parallel and transverse samples showing the characteristic behavior of each under compression. The load-unload cycles are still included in the data.

The failure behavior of these samples is indicative of their general stress-strain behavior (Fig. 4.32). Parallel samples experience a kind of diffuse failure where nearly every portion of the sample contributes in some way to the failure. We can see a sort of "opening-up" or "mushroom-like" structure which formed as walls broke apart from one another and fanned out radially from the center. Note that, the bottom of the sample (close to where freezing initiated) remains relatively intact. Transverse samples immediately began failing as walls crushed on top of one another. In figure 4.32 (b) we also note that walls broke apart in sections, sliding upon a one another. This mechanism will be further discussed in subsequent sections. The isotropic samples experience a more localized rupture with fissures opening up along a path of least resistance.

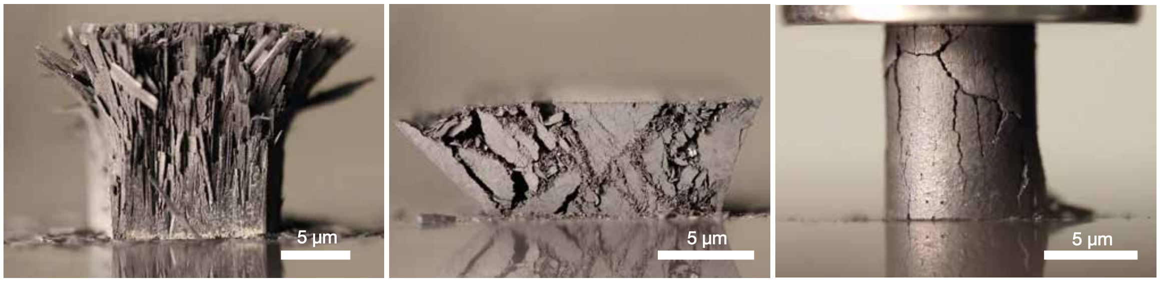

(a) Parallel **(b)** Transverse **(c)** Isotropic

Figure 4.32: Failure behavior of porous LSM-YSZ.

As discussed previously (see section 3.2.8), a load-unload method was utilized to measure stiffness in order to remove the effect of surface asperities and the slack in the load frame. To do this, the slope of the unload segment of each cycle was calculated. Looking at figure 4.31 it should be noted that these slopes (stiffness values) are not constant meaning that as the sample is deformed it actually becomes measurably stiffer. The measured stiffness is shown in figure 4.33. We found that as each sample was compressed, its stiffness values increased until failure. During testing, it was noted that as soon as any force was applied to the majority of samples that permanent, non-reversible damage was being done from the sounds that we heard coming from mechanical testing specimens. These were the sounds of individual walls and particles whose bonds were breaking; these failures occurred far before the ultimate compressive strength was reached. Locally, these pre-fractures caused the reorganization of the microstructure within both freeze-casts and slip-casts. This local reorganization densifies the structure producing the incrementally increasing stiffness as seen in figure 4.33.

Figure 4.34 shows the stiffness[9] and compressive strength for isotropic and anisotropic samples as a function of total porosity. The isotropic samples were made using 20 μm pore formers while the freeze-casts were frozen at 40 °C min^{-1} freezing rates, respectively producing average macropore sizes of 17 and 14 μm. As expected, there was a negative correlation for both stiffness and compressive strength with increasing porosity. Isotropically porous specimens had mechanical properties that fell in between those of the parallel and transverse orientation of the anisotropic samples. In fact, by comparing the mechanical properties of the high porosity isotropic samples (56.4 %) and high porosity parallel samples (65.7 %) it can be seen that similar mechanical performance was achieved with nearly

---

[9] Stiffness was used rather than elastic modulus because it is unclear whether or not these samples contain a reversible domain.

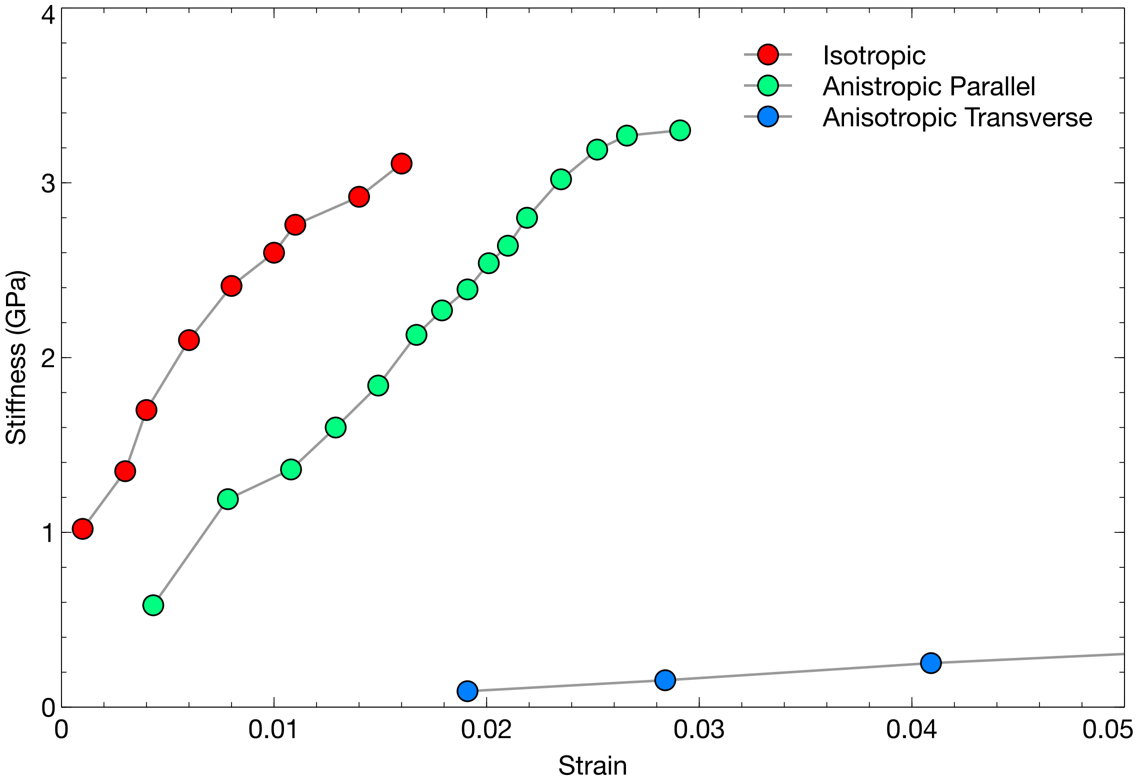

Figure 4.33: Evolution of stiffness as a function of strain.

10 % more porous volume. According to these observations, the nature of the macroporosity plays a significant role on mechanical performance. The same trends were seen when comparing isotropic and freeze-cast specimens with other macropore sizes. The rather large dispersion seen is also typical of porous ceramic materials. These results clearly show the potential to engineer mechanical properties for anisotropic materials.

It was also interesting to note that for all the differences in mechanical behavior between isotropic and anisotropic-parallel samples that their strain-at-rupture values were essentially the same ($\epsilon \sim 0.02$) (Fig. 4.35). Transverse samples on the other hand experienced rupture at $\epsilon \sim 0.07$. All macropore sizes were included in this plot and judging by the relatively small dispersion values, it seems as though macropore size plays little role in the ultimate strain-at-rupture value.

Role of Freezing Rate on Mechanical Properties

When results of the mechanical properties of freeze-casts were plotted as a function of freezing rate there were some obvious trends (Fig. 4.36). For samples made at 1 °C min^{-1}

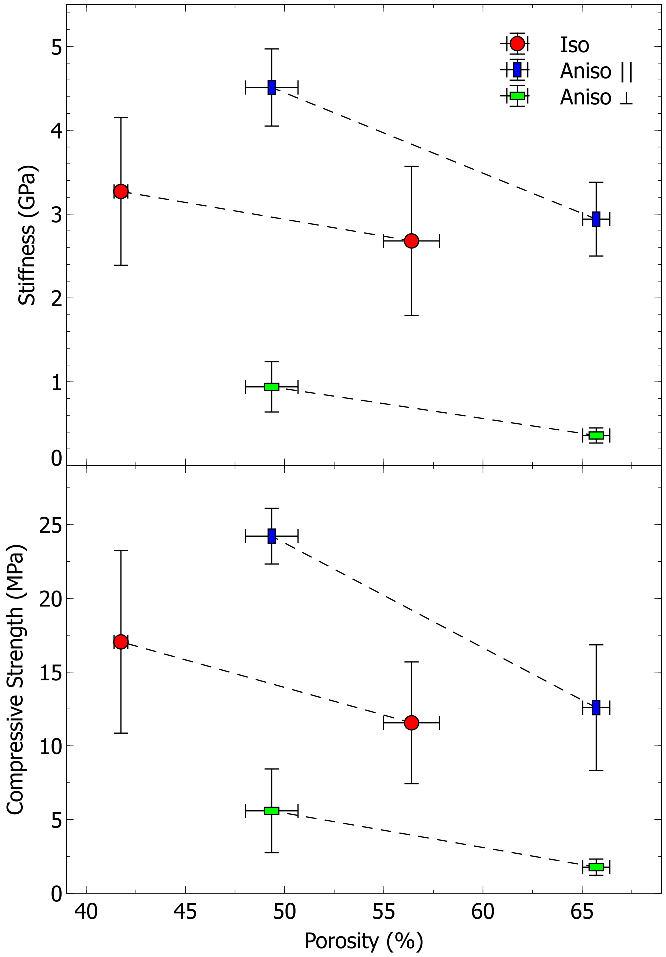

Figure 4.34: Effect of total porosity and macropore morphology on stiffness and compressive strength of slip-casts and freeze-casts. Only one macropore size combination is shown for clarity.

and tested in parallel, both stiffness and compressive strength were only slightly higher than equivalent samples tested perpendicular to their freezing direction. As the freezing rate was increased, mechanical performance of the parallel samples rose rapidly until it plateaued at a freezing rate of approximately 10 °C min^{-1}, the freezing rate past which little change in microstructural feature sizes were seen. Samples tested perpendicular to their freezing direction had values of stiffness and strength significantly lower than those tested in parallel and did not change significantly with increasing freezing rates.

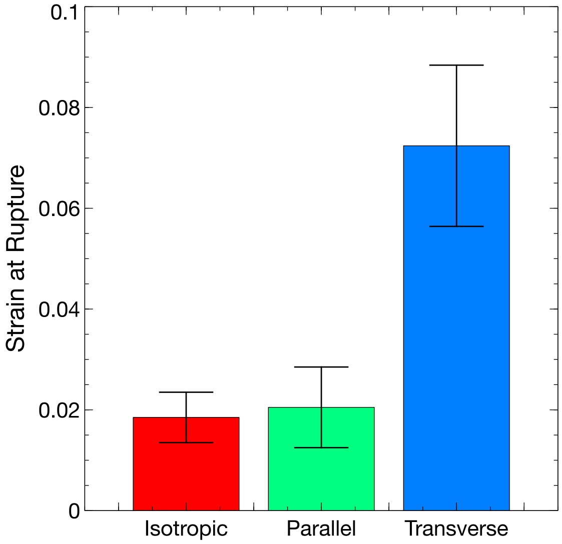

Figure 4.35: Strain at rupture. 72 measurements were performed for isotropic samples, 55 for parallel samples and 48 for transverse freeze-casts.

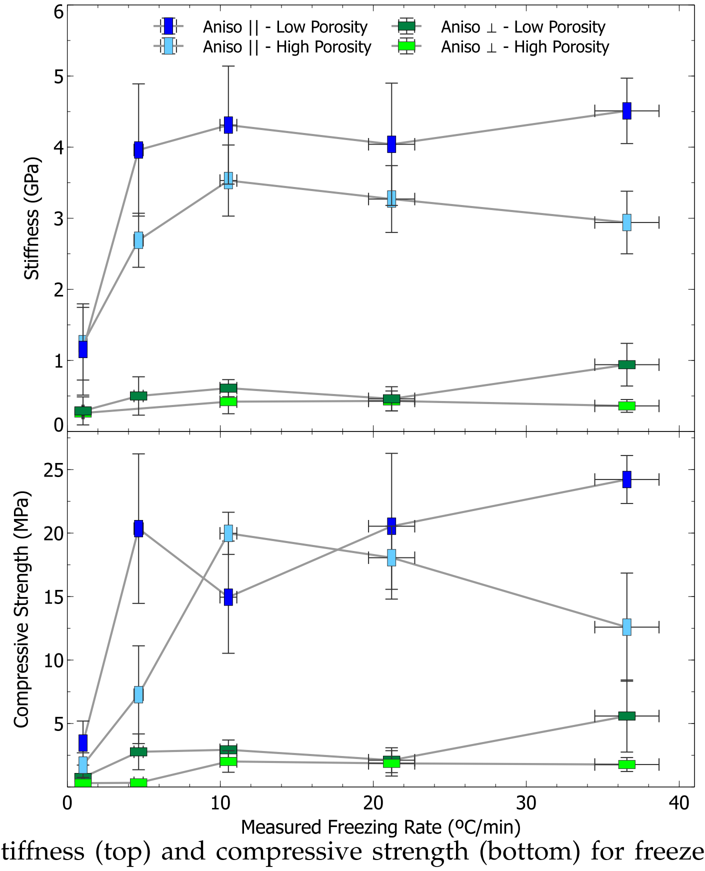

Figure 4.36: Stiffness (top) and compressive strength (bottom) for freeze-casts made at various freezing rates including both the high and low porosity samples.

4.3.2 Discrete-Element Simulations

Macroporous Structures: X-ray Tomography

In order to explain the observed mechanical properties, simulations were conducted on realistic microstructures. In total, six samples (four freeze-casts (**F: 1, 2, 3, 4**) and two slip-casts (**S: 1, 2**)) were reconstructed using X-ray tomography. These reconstructions are shown in figure 4.37.

Samples F1 and F2 were made using the same overall green-state porosity (80 vol. %) but different freezing profiles. Both F3 and F4 have a higher degree of solids content than either F1 or F2. At this higher solids content, the anisotropic macropores of the freeze-cast samples become seemingly less defined and there are fewer of them in a sample of the same volume. The two isotropic samples contained varying amounts of PMMA pore-formers with a pre-sintered nominal diameter of 20 μm. X-ray tomography images were insufficient to resolve the micropores within the walls. It was therefore assumed that the walls were composed of 25 vol. % micropores (derived from FIB of LSM-YSZ at 1200 °C)[10].

In table 4.2, two different post-sintering porosities are given for the six samples. The Archimedes porosity was experimentally determined prior to any processing, and the tomography porosity was calculated from image analysis of the reconstructions shown in figure 4.37 (macroporosity) plus the added microporosity contribution from FIB-tomography (25 vol. %). There is less than a 10 % difference between the Archimedes and tomographic values indicating that the reconstructions are valid representations at least of the total sample porosity.

Table 4.2: Six X-ray Synchrotron Samples Tested

Name	**Type**	**Freeze Rate °C min^{-1}**	**Green Porosity vol. %**	**Archimedes Porosity vol. %**	**Tomo Porosity vol. %**
F1	Freeze-cast	20	80	66	69
F2	Freeze-cast	40	80	66	69
F3	Freeze-cast	20	70	47	46
F4	Freeze-cast	40	70	47	44
S1	Slip-cast	N/A	80	57	61
S2	Slip-cast	N/A	70	42	44

---

[10] Note that microporosity data from freeze-casts were used for all structures including slip-casts which were subsequently shown to have a different microporous structure.

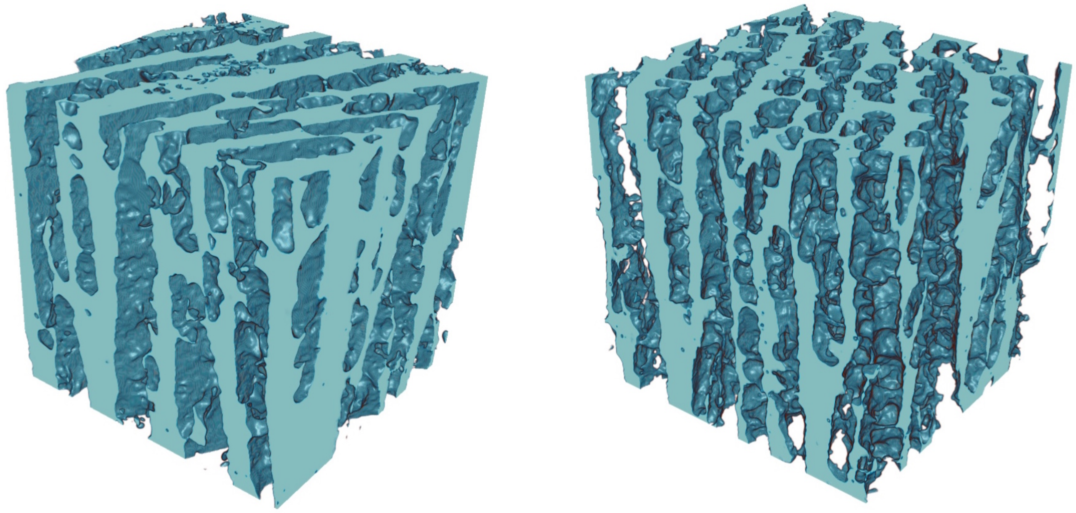

(a) F1 - 80 % Green Porosity, 20 °C min^{-1} **(b) F2** - 80 % Green Porosity, 40 °C min^{-1}

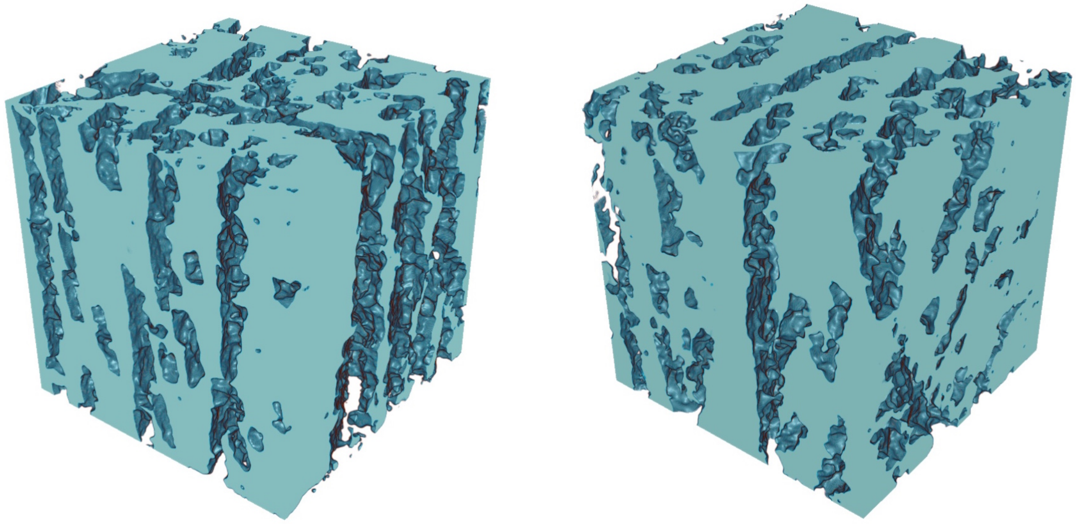

(c) F3 - 70 % Green Porosity, 20 °C min^{-1} **(d) F4** - 70 % Green Porosity, 40 °C min^{-1}

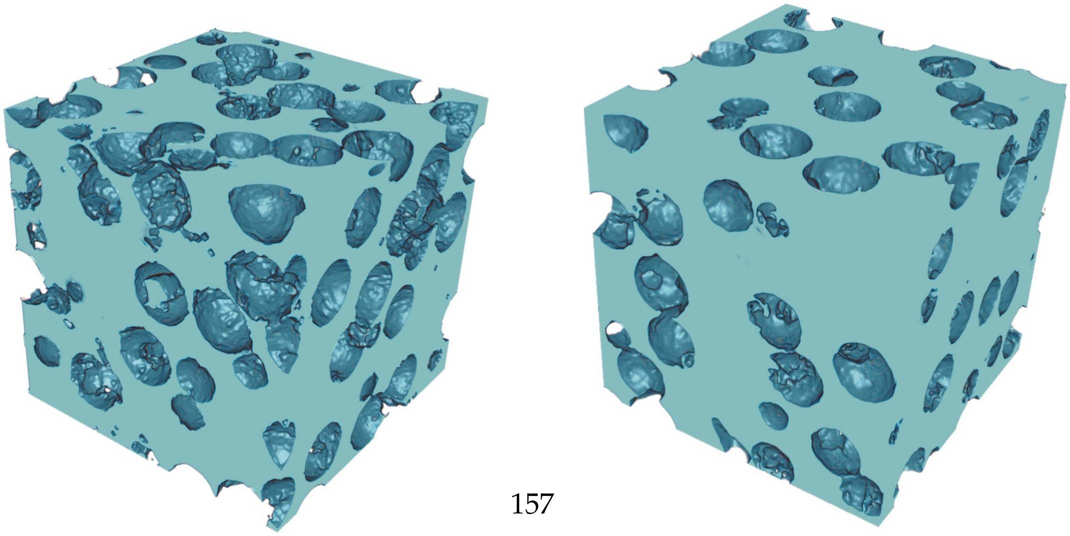

(e) S1 - 80 % Green Porosity **(f) S2** - 70 % Green Porosity

Figure 4.37: Reconstructed X-ray tomographies.

Simulated Mechanical Performance of LSM-YSZ ceramics

Approximately 4 million particles were used to create the initial DEM packing consisting of 40 vol. % LSM and 60 vol. % YSZ. An LSM particle size of 1 µm ± 5 % was used along with a YSZ particle size of 0.5 µm ± 5 %. The structure was numerically sintered until 25 vol. % porosity remained within the structure. As shown in section 3.3.1, the X-ray tomography images were then used to slice out swathes where there should be macropores.

After being built as DEM models, these structures were compressed in the three ordinal directions (x, y, z) to ascertain the effects of macropore anisotropy. We were curious as to how well the DEM microstructures could replicate (qualitatively and quantitatively) the behavior seen from experimental trials. Ideally, the isotropic, slip-cast samples should see roughly the same behavior in each direction. If this were not the case, that would mean that the slip-cast tomographies were not representative of isotropic structures. The freeze-cast samples should have at least two directions with distinctly different behavior.

Shown below are the stress-strain curves from numerically testing each of the six microstructures in the three directions[11]. The top and bottom rows of charts represent the high and low porosity structures, respectively (Fig. 4.38).

The curves show that between 0 - 0.001 strain, the stresses within all samples, no matter the direction, increase gradually. This behavior corresponds well with physical experiments where a sort of initial “ramp-up” was seen during the time when the compression platens were coming in contact with the bulk of the testing specimen. Unlike experimental results however, where we saw markedly different curve shapes for the three sample types, we see roughly the same general shape for all DEM curves. What differs is the ultimate stresses and stiffness.

Freeze-cast structures do show a difference in behavior between properties in the freezing direction and those in the transverse direction. What was perhaps unexpected was that there was a third direction, which we will call “Transverse-align”, whose properties range between those of the two other curves. This is particularly prominent in the F1 and F2 samples. The origins of this third curve can be pinpointed to the limited sample size tested. When studying real freeze-casts in the transverse direction we are actually looking at many different, randomly oriented colonies of pores. The sum totally of all these ran-

---

[11] It took over 70 days for parallel calculations on 8 nodes (Intel Xeon CPU) to run from start to failure for these 18 simulations.

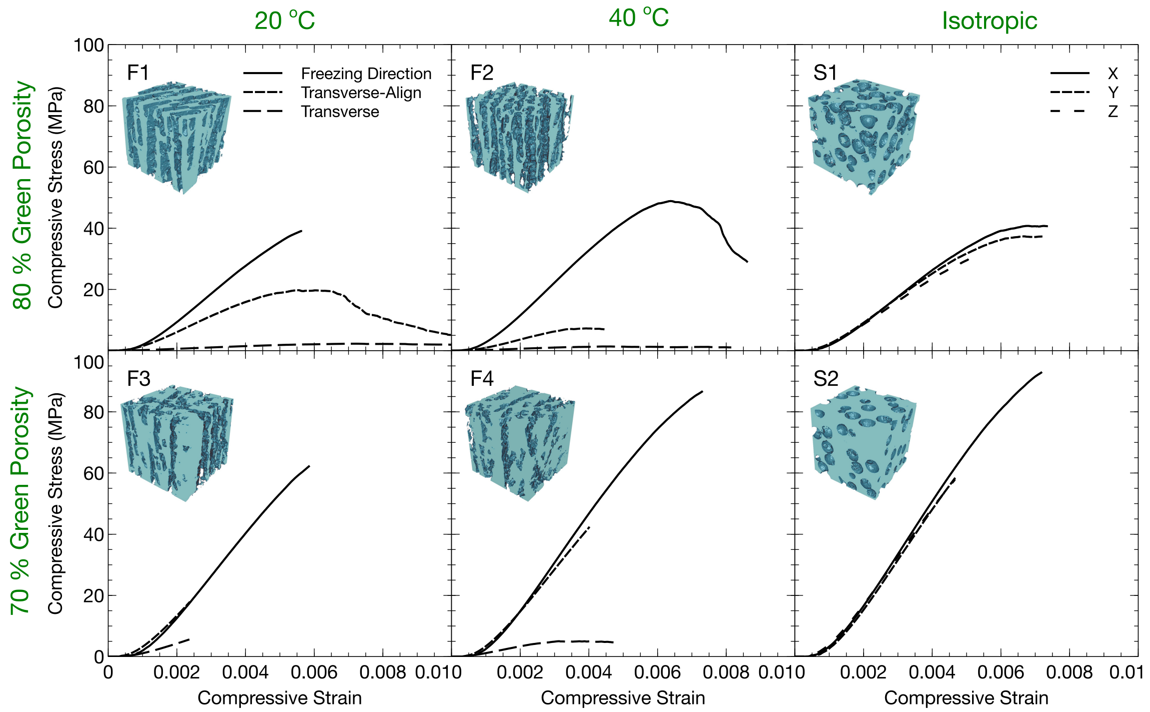

Figure 4.38: Stress-strain curves from simulated mechanical testing of the six reconstructed DEM samples.

domly oriented regions is isotropic behavior. The tomography samples allow us to probe the behavior of a few pores and walls but essentially only one "colony" of pores is being studied. For the reason, the behavior in the transverse direction is no longer isotropic. In the transverse-align direction, we are locally aligned with walls which parallel the macropores. If the structure is less porous (ex. F3 and F4), the transverse-align direction has uninterrupted walls and so the mechanical properties mirror those of the freezing direction.

As expected, the isotropic samples (S1 and S2) see essentially the same behavior in any of the ordinal directions. This helps to confirm that the developed samples were in fact representative of our original structures.

As a function of overall porosity, we found that our simulated structures follow a similar pattern as was seen for the experimental samples (Fig. 4.39). Performance decreases as porosity increases, and isotropically porous samples attain performance values straddling between those of the parallel and transverse freeze-casts. For these data, the isotropic values were found by averaging together the values from the x, y, and z-directions. The datapoints and error bars for the freeze-casts were calculated by averaging values from

F1 with F2 (high porosity) and F3 with F4 (low porosity). Each pair was made using the same solids loading and although the freezing rates differed, microstructurally they were equivalent so our combining their data seemed an appropriate assumption. In part, due to the long simulation time, the number of simulations were limited (one for each sample in one direction) and reproducibility was not investigated.

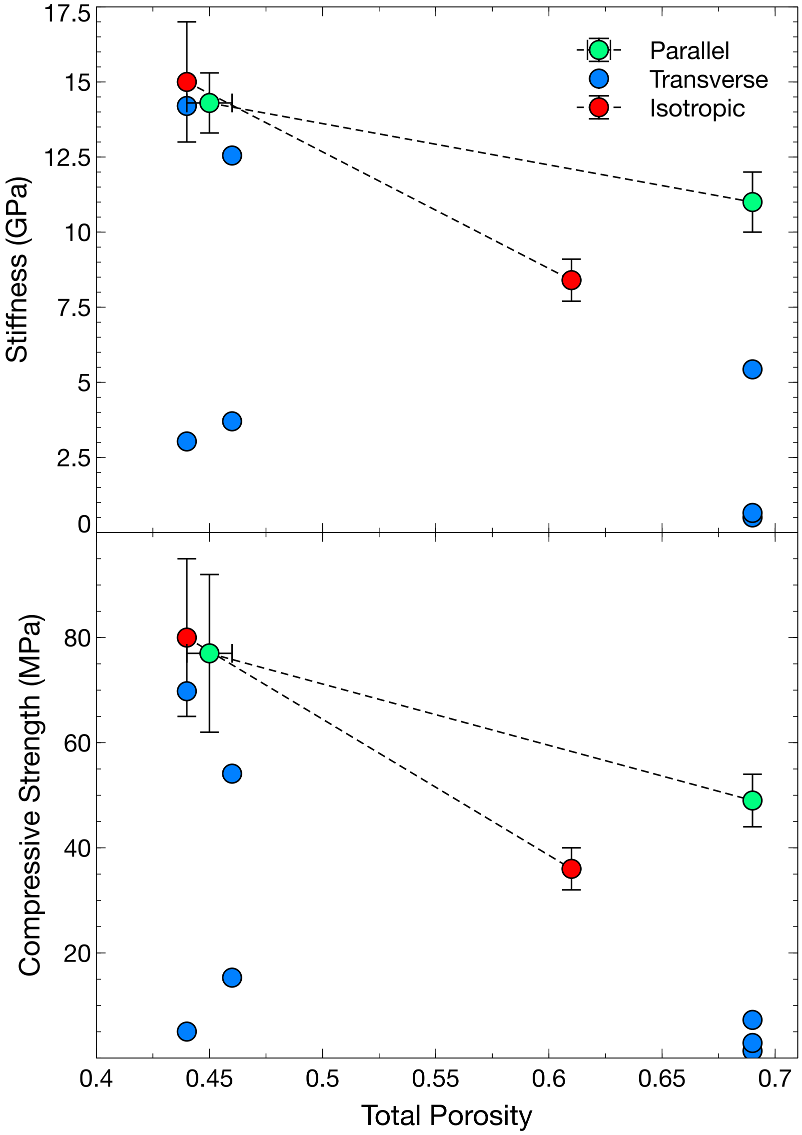

Figure 4.39: Simulated mechanical properties of tomography images as a function of porosity.

4.4 Half-Cells and Impedance Spectroscopy

Previous results have confirmed that our freeze-casts sintered at 1200 °C attain sufficient percolation of the LSM, YSZ, and pore phases. In addition, a favorable active TPB density of nearly 9 µm μm^{-3} was achieved at 1200 °C (see section 4.2.1). It was necessary to fabricate working half-cells to determine the effects of pore anisotropy on electrochemical performance. The problem that we consistently ran into however when fabricating half-cells was that if we wanted to maintain our hierarchical porosity, we couldn't sinter above 1200 °C which was the ideal sintering temperature we found for our freeze-cast LSM-YSZ cathode material. Not only that but we were interested only in the properties from the SSZ portion of our freeze-casts which were located in the center of our samples.

At first, using a pre-sintered pellet or tape of YSZ, we attached a thin slice of freeze-cast cathode using a YSZ slurry and then sintered it to 1200 °C. The slurry was able to attach the two layers together, but upon closer inspection, the attachment was only minimal (Fig. 4.40). The "thin" bond layer was nearly 500 µm thick and highly porous. It was difficult with samples made from this method to get any sort of electrochemical response from impedance spectroscopy.

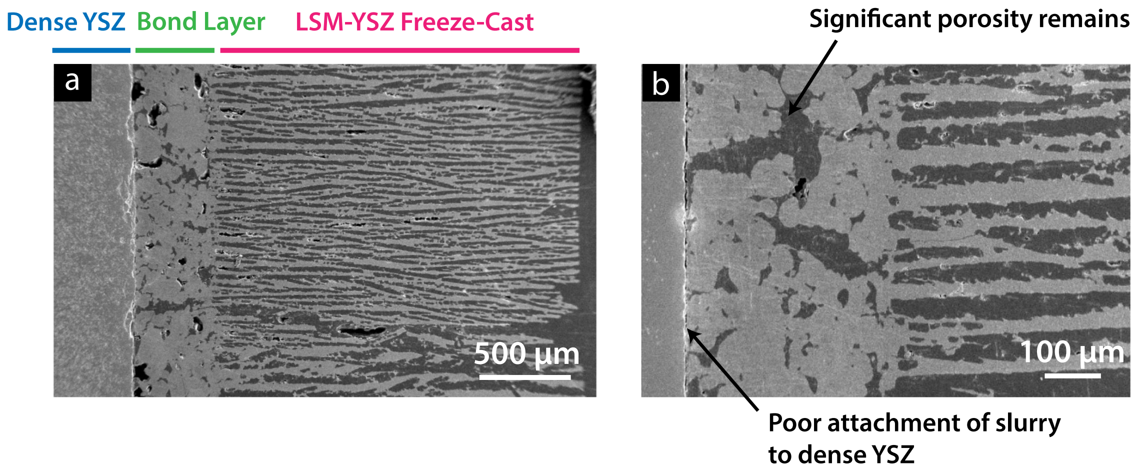

Figure 4.40: (a) Microstructure of a half-cell made using the "cut and attach" methodology showing (b) the highly porous bonding layer.

Using the "optimal" method of in-situ freezing the electrode and electrolyte (see section 3.1.6), a number of half-cells were fabricated. All half-cells were frozen using 10 °C min^{-1} temperature rates and homogeneous cooling. We were able to attain reasonably thin and flat half-cells where the electrode was securely attached to the electrolyte [Fig. 4.41 (a)].

The microstructure within the electrode was highly favorable. Macropores were aligned within the cathode portion, and the structure appeared isotropically dense where the YSZ-layer was placed.

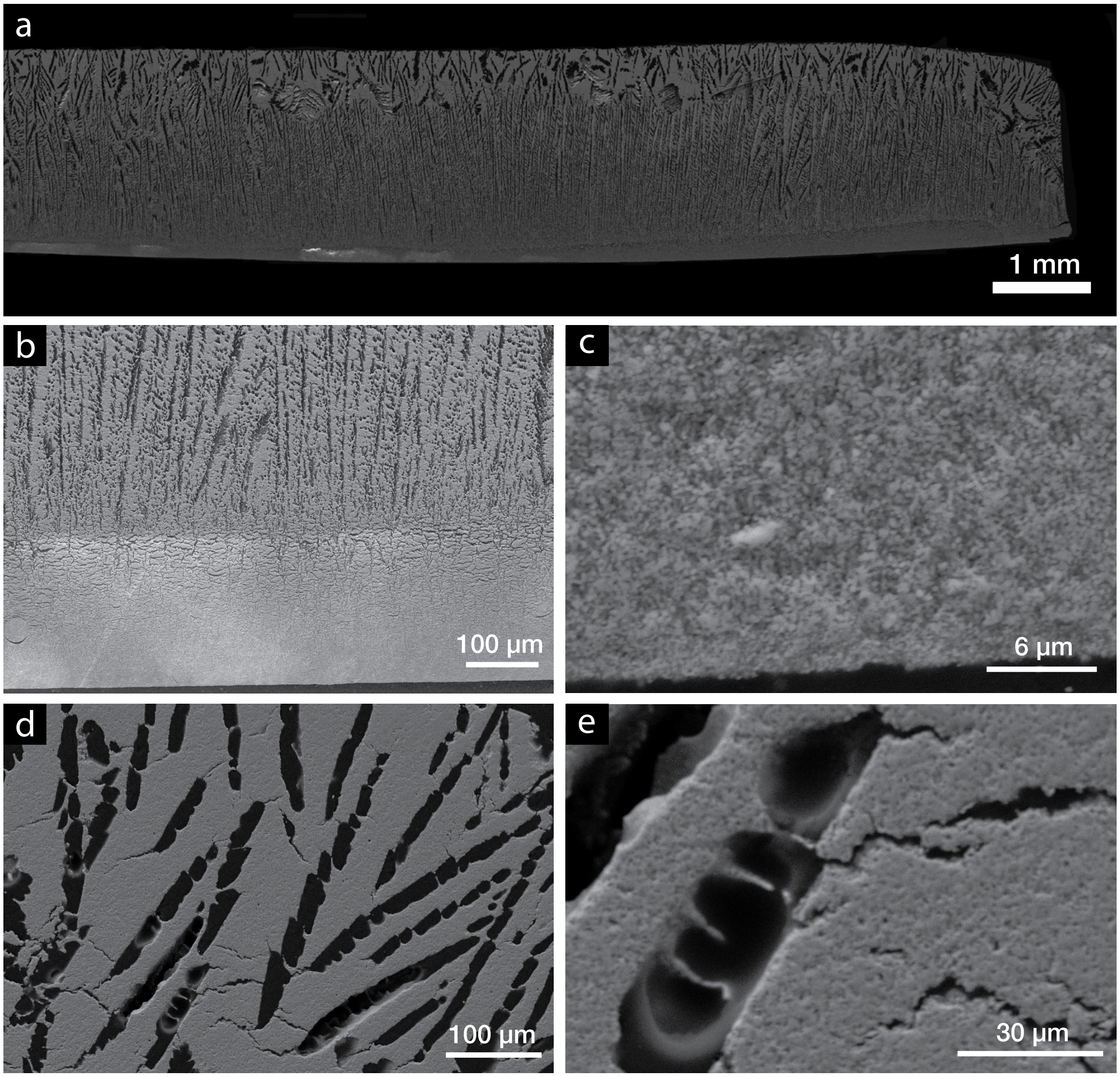

Figure 4.41: Micrographs from a half-cell made using the suggested method for producing freeze-cast button half-cells with bi-layer freeze-casting: (a) Half-cell cross-section with the freezing direction facing up (b) Electrolyte / Electrode bond (c) Residual porosity in the electrolyte (d) Cross-section transverse to the FD showing cracking through walls (e) Ceramic bridges between walls inside macropores.

Upon closer inspection however, a number of concerning microstructural features were discovered in these half-cells.

1. **Poor Adhesion** - many samples appeared to have imperfect adhesion between the electrode and electrolyte layers. Using EDS we were able to determine where, within the freeze-cast structure, the transition from YSZ electrolyte to LSM-YSZ cathode took place (Fig. 4.42). What we see is that the structure actually breaks before the transition to the LSM-YSZ cathode indicating that the bond itself is sufficiently strong. For another thing, we notice that the SSZ had started prior to the transition from electrolyte to electrode.

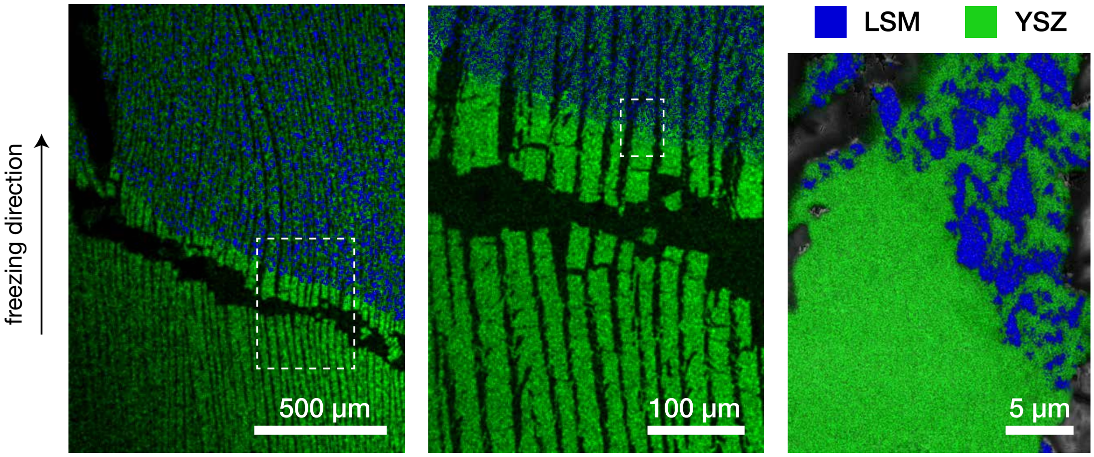

Figure 4.42: EDS imagery of a broken half-cell near the bond between the electrode and electrolyte layers.

2. **Residual Porosity** - it was observed that there was still residual porosity in the electrolyte layer. This was the case even though the electrolyte structure was frozen in the isotropic IZ and TZ zone and a high solid loading slurry was used. The question as to whether or not there was sufficient porosity for gas percolation from one side of the half-cell to the other (something to be avoided) was solved by placing a drop of water on the electrolyte side and eventually seeing collected moisture on the back of the cathode. These structures were certainly not gas-tight due to electrolyte porosity.

3. **Cracking** - many small fractures were seen propagating normal to the freezing direction between the ceramic lamellae. These were not localized to specific regions but appeared homogeneously distributed throughout the half-cell structures. It was thought that sintering of these thin structures may have been causing undue stress since the pure YSZ layer would sinter to a greater extent than the LSM-YSZ layer. The additional lateral contraction would generate stresses throughout the half-cell

which could have been released by cracking of the walls. This explanation however was proved wrong by imaging unsintered samples (Fig. 4.43) which showed the same lateral cracks permeating the structure. This would seem to indicate that the cracking either occurs during the freezing process itself or during sublimation of the ice crystals.

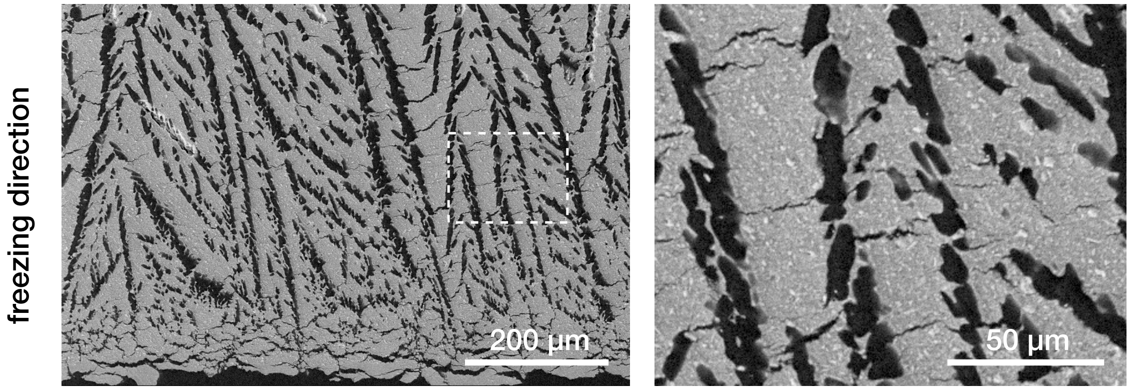

Figure 4.43: Unsintered half-cell showing lateral cracking.

4. **Morphological Transitions** - For many samples, there was also a morphological transition within the electrode layer where the microstructural feature size increased significantly. This phenomenon parallels what is seen with the bimodal alumina slurry (see section 4.1.2). In both cases we observe that at some point in the process conditions become such that an abrupt morphological change takes place.

We also explored the possibility of depositing an ESD layer of dense YSZ (see section 3.1.6) to create an airtight barrier at the electrolyte. SEM revealed that this was ineffectual. The samples were simply too porous (even after polishing) to allow for the deposition of a smooth dense layer of YSZ when only sintering to 1200 °C. ESD half-cells were not tested electrochemically due to a lack of time.

Even with these flaws, multiple half-cells like those shown in figure 4.41 were tested electrochemically. Only then did we uncover the greatest flaw in our method. Impedance setups are highly sensitive to their electrode configuration since they measure lines of current traveling through the samples. Since we were using a thin-electrolyte we utilized an electrode configuration wherein both the reference electrode and counter electrode are painted onto the bottom of the electrolyte (see figure 3.19). It turns out at least for the system that we were using, that the reference electrode had to be a platinum wire placed circumferentially around the cell, halfway down its thickness. Unfortunately, the results from testing the thin-electrolyte samples were unusable, they indicated that our half-cells were actually capacitive meaning that our results had no real physical basis from which we could extrapolate performance.

In order to use the proper electrode configuration, our half-cells had to be altered to have a thick electrolyte (> 1 mm). The structure which resulted is shown in figure 4.44.

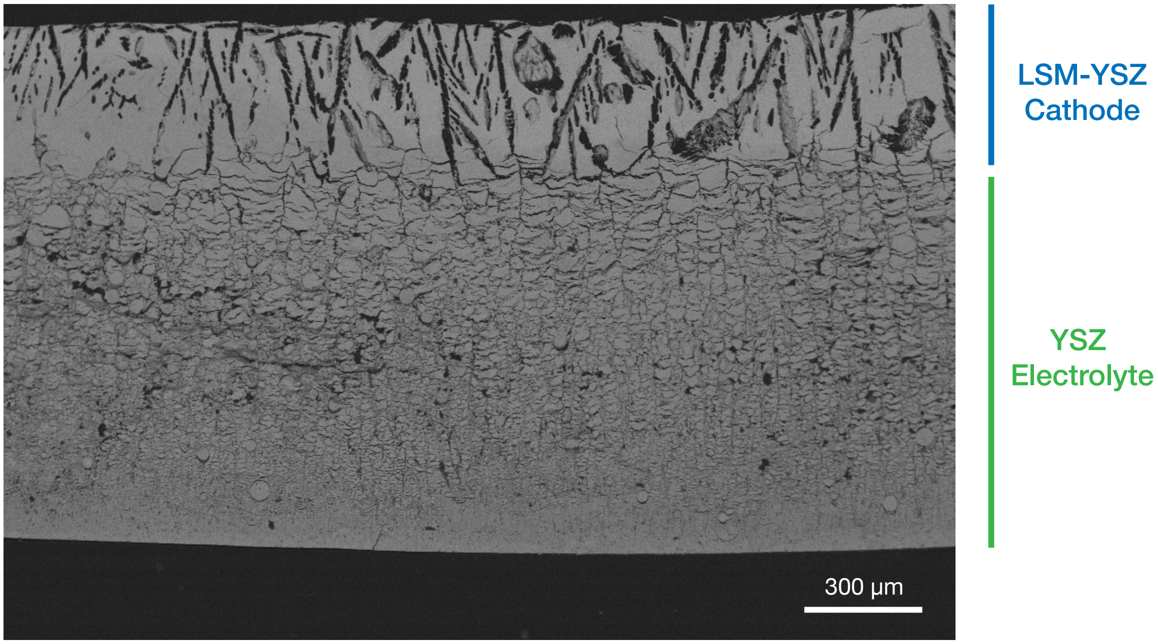

Figure 4.44: Half-cell made with a thick electrolyte and thin cathode.

The electrolyte microstructure was highly porous, with many voids and pores homogeneously distributed throughout. Interestingly enough, the more typical freeze-cast structure does not appear until the transition from electrolyte to electrode. It is possible that the electrolyte slurry was too concentrated for templating to occur. Within the electrode portion of the cell, the macropores are not well-aligned. Nevertheless, using this cell, we were able to attain working impedance spectra (Fig. 4.45).

The impedance is characterized by an enormous resistance in the high frequency range and a smaller electrochemical arc on the low frequency spectrum. The high frequency arc is so large that even at 100,000 Hz, the maximum frequency available for testing, we still cannot see the entire arc. The high frequency response can typically be attributed to the electrolyte and bond, and no doubt its size is related to the poor microstructure

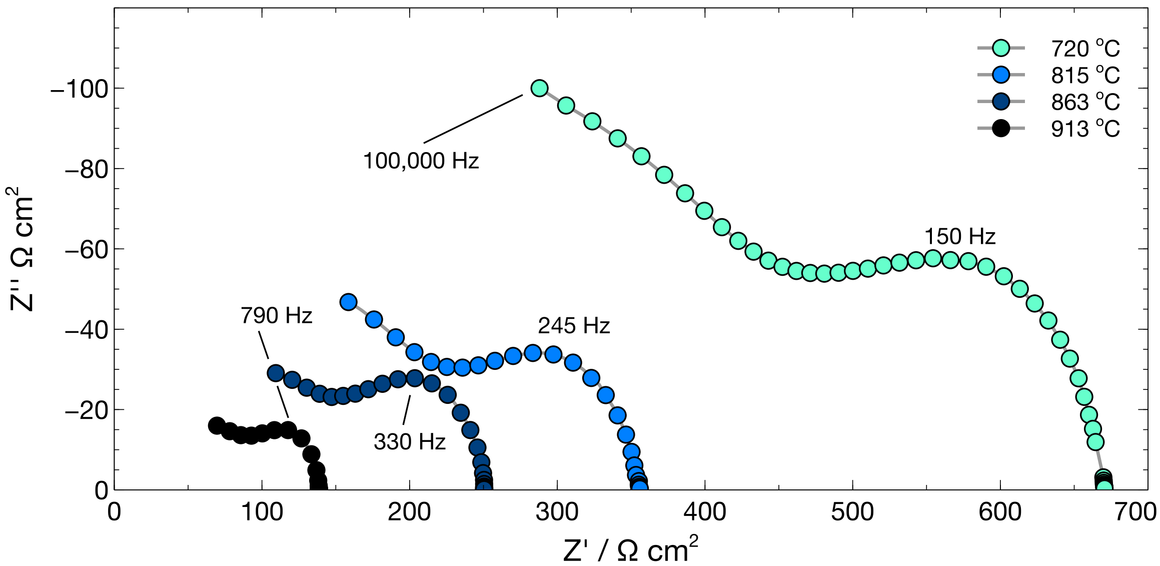

Figure 4.45: Impedance spectra (Nyquist Plot) of the structure seen in figure 4.44 at various temperatures.

seen in figure 4.44. It is difficult to comment at all on the performance of the anisotropic cathode (which is the goal of this study) since its response is thought to be overshadowed by the electrolyte arc. We do however see that impedance does decrease with temperature and that the apex frequency of the low frequency arc increases with temperature. This is typical behavior of a half-cell during electrochemical testing [177]. Comparing the total cell resistance (x-intercept) with LSM-YSZ half-cells made using traditional screen-printing methods sintered to 1180 °C [177], we find that our cell is nearly 400 times more resistive when tested at 900 °C. This is expected given the poor bonding and the amount of porosity contained within our half-cell.

4.4.1 Comparisons to Isotropically Porous Samples

Isotropically porous half-cells were made by laying down the same thick YSZ slurry used for freeze-casts, making sure to use approximately the same thickness as for freeze-cast cells. A cathode slurry containing 20 μm pore formers was then placed on top and the entire half was allowed to consolidate on top of a gypsum platen. The cell was thermally treated to 1200 °C to remove the organic pore formers and partially sinter the ceramic. The microstructure of this structure can be seen in figure 4.46. The results from impedance testing are presented in figure 4.47.

In this case, we see that we still have the same high-frequency response as was seen for

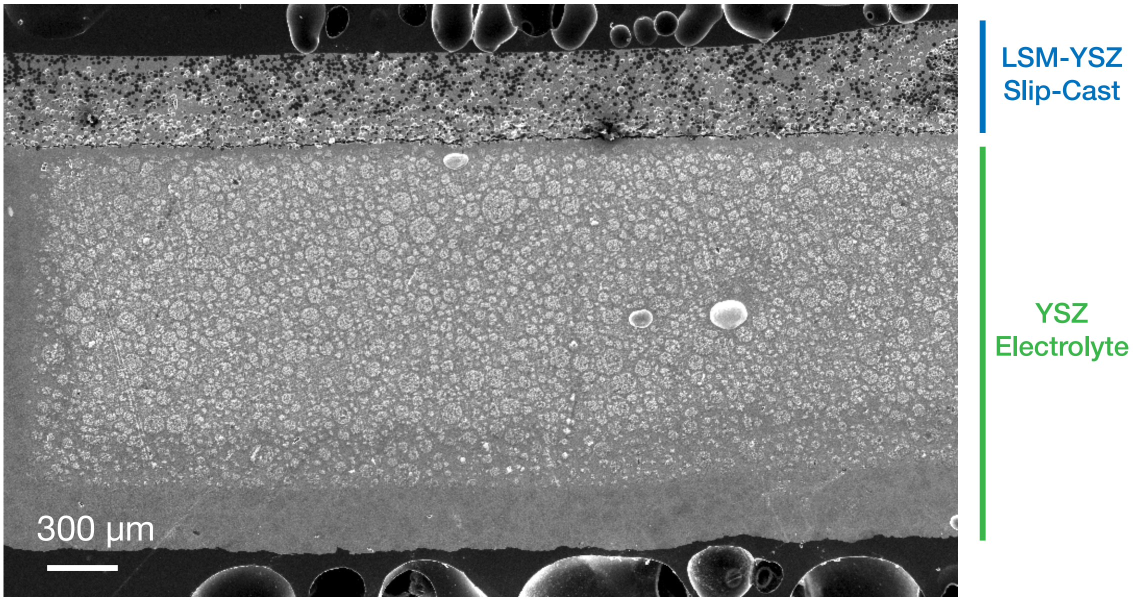

Figure 4.46: Slip-cast half cell microstructure used for comparison with freeze-cast structure.

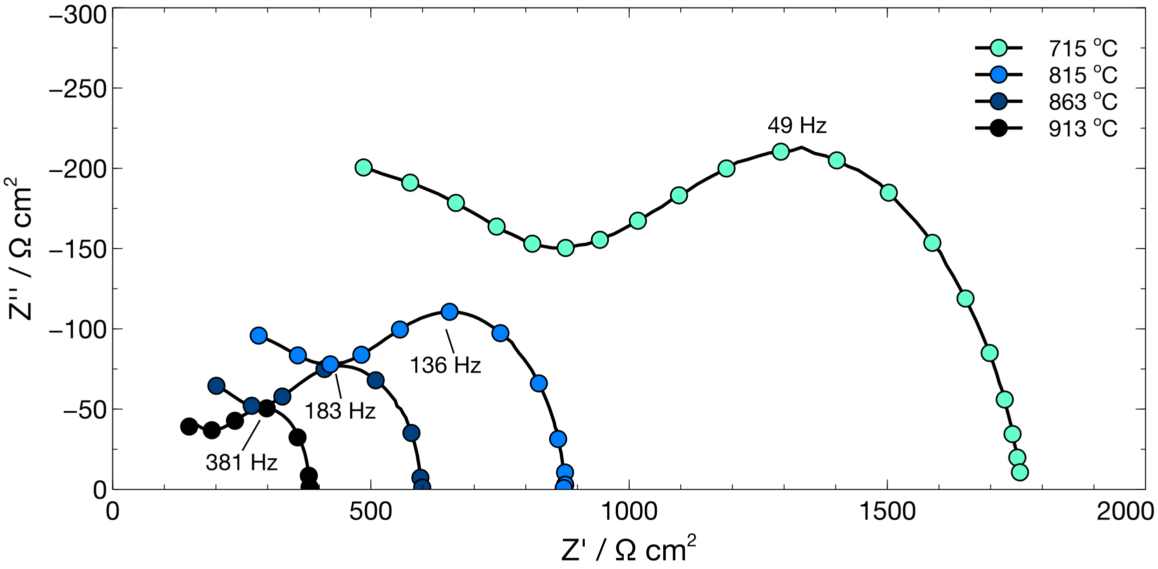

Figure 4.47: Impedance spectra of a slip-cast half-cell at various temperatures.

freeze-cast cells. Comparing the freeze-cast and slip-cast electrochemical performance, there is little that we can say about the microstructural contribution of the electrode portion of the cell since they are both overshadowed by the response from the electrolyte. Generally speaking, the slip-cast samples saw higher levels of total cell resistance at every tested temperature than the freeze-cast samples.

4.5 RedOx Behavior of NiO-YSZ Anodes

After sintering to 1200 °C, samples for reduction-oxidation cycling were cut out from the central SSZ regions of NiO-YSZ freeze-casts. These were shaped carefully into cuboidal specimens and then placed into a standard dilatometer.

The response of the dilatometer to the reduction-oxidation cycle is interesting (Fig. 4.48). It does seem as though the material is reducing in argon, since it is shrinking linearly. When air is reintroduced back into the system however, other than a small blip, it does not appear as though the sample responds to the change in gas. If anything, the response to oxygen should have been more obvious than the reduction because this material oxidizes so readily. We can postulate here then that under the rather impure Argon used, that the freeze-cast was not really reducing, but then there is the question as to why there is a seemingly permanent length change. In order to get more definitive results, the atmosphere within the dilatometer must be changed to something highly reducing such as a hydrogen/argon mixture. Then we can be sure that the NiO-YSZ anode is reducing.

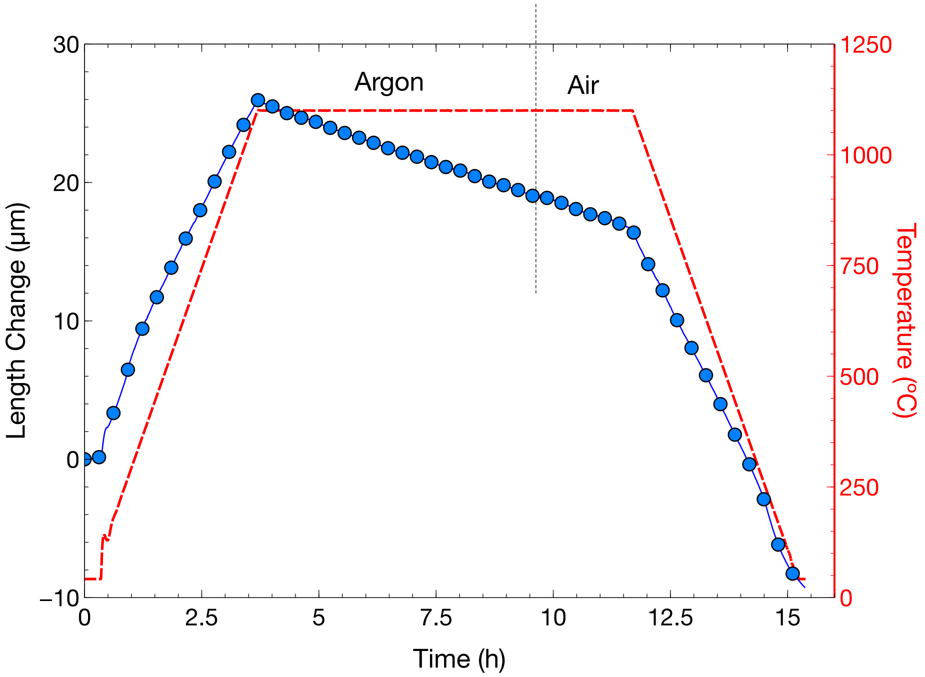

Figure 4.48: Dilatometer curve of a freeze-cast anode in an argon atmosphere. Measurements were taken in the freezing direction.

5

Discussion

Chapter Contents

5.1 Freeze-Casting the LSM-YSZ System

5.1.1 General Freeze-Casting Observations

Although a significant amount of energy was focused on studying systems specific to SOFCs, the overarching theme of this thesis was always to study the processing and characterization of anisotropic and/or hierarchical porosity composite ceramics. An additional focus was to develop simulation protocols that use realistic microstructures at the relevant length scales. Because of its flexibility and versatility, freeze-casting became our primary processing technique. But for all the flexibility that freeze-casting accords us, we found that there were still significant limitations when it comes to microstructural design. The range of macropore sizes that can be achieved is limited on both ends of the spectrum. Past a certain freezing velocity, no further changes will be seen in microstructure. In addition, without changing material system (ie. aqueous LSM-YSZ, alumina, zirconia, hydroxyapatite...) the shape of macropore does not change significantly. This can be both a good and bad thing depending on user requirements.

Seen multiple times from our results and the results of other authors [83, 116], freeze-cast lamellar size increases as a function of freezing height even when the solidification velocity is constant and the freezing front has progressed into the SSZ (Figs. 4.13 and 4.15) [83]. In truth, the term “Steady-State-Zone” is a bit of a misnomer. The system is metastable at best. As ice crystals grow through the suspension, releasing heat, they are at once pushing particles out of the way while the particles themselves move through Brownian motion [101]. The concentration of particles ahead of the freezing front is not fixed and with changes in concentration, the equilibrium freezing temperature of the suspension is altered producing side-branches, dendrites, and regions where certain ice crystals grow faster than others. At the same time, the competing forces of temperature-driven growth versus crystallographic preference tends to tilt ice crystals away from the direction of ΔT (see section 2.3.4). Over the course of freezing this leads to ice crystals intersecting one another. Two crystals merge into one and since now there aren’t two crystals competing for space, the one crystal can grow larger. Perhaps if perfectly straight crystals could be grown then constant solidification would lead to constant ice crystal size but this would require a control of the nucleation and freezing conditions that is currently beyond our grasp.

It is tempting to discount the change in microstructural size over height as insignificant seeing as how taken over the entire height of freezing, the change in microstructure is small[1]. Mechanical testing however showed that freeze-casts nearly always broke on the side furthest from the initiation of freezing, proving that this effect is clearly significant.

5.1.2 Freeze-Casting Empirical Relationships

As reported by Deville et al. [1, 86] microstructural wavelength is empirically dictated by a power-law:

---

[1] < 0.5 μm increase in macropore size per every 1 mm of freezing height for samples frozen at speeds greater than 10 °C min^{-1}

$$\lambda = Av^{-n} \tag{5.1}$$

where n represents the effect of solidification velocity (v) on microstructural wavelength (λ) and the prefactor (A) represents the contributions from the initial slurry, i.e. solid loading, viscosity, etc. By plotting average λ as a function of solidification velocity on a log scale (Fig. 5.1), we find that the experimentally derived average λ values for the LSM-YSZ system is also well approximated by this expression where A is 4034 and n is 1.5. The n-value derived from these experiments is larger than those found for alumina (n = 0.8 - 1.3) [86, 97] indicating that λ, for LSM-YSZ freeze-casts, shows a stronger dependence on solidification velocity which is actually advantageous for microstructural tailoring. The n-value has been shown to be dependent on particle size [86, 109] therefore, our large n-value could be partially attributed to the relatively large particle sizes ($d_{50\ LSM}$ = 0.8 µm, $d_{50\ YSZ}$ = 0.3 µm) being used. Using Eq. (5.1), average λ for freezing velocities in the proximity of those investigated here can be predicted, making this a powerful tool for tailored LSM-YSZ microstructures.

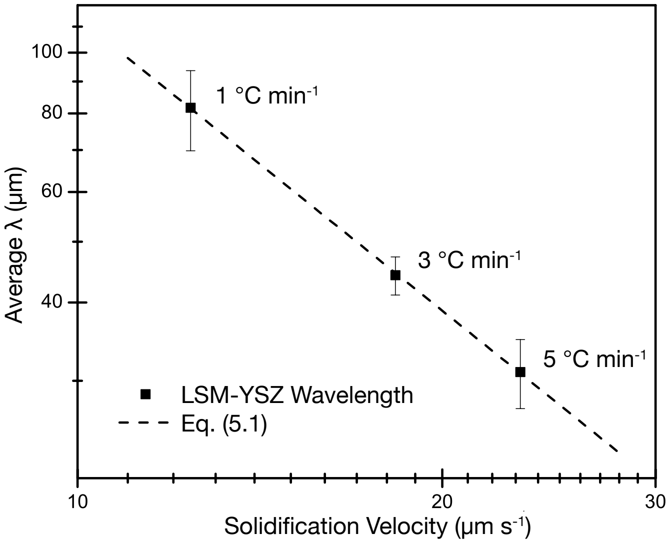

Figure 5.1: Average λ as a function of solidification velocity (for the 1 - 5 °C min^{-1} samples). Dispersant and solid loading are held constant at 2.0 wt. % and 23 vol. %, respectively. The data have been plotted on a log scale and fit with a power law (R-value > 0.99) to be used as a predictive relationship.

When solid loading is altered, both v and n remain constant; however, there is still a positive trend for average λ with solid loading [Fig. 4.14 (f)]. Using Eq. (5.1) with constant

ν and n, an expression for A with respect to solid loading was found and plotted in figure 5.2. It was determined that A can be approximated as a linear function where x is the solid loading fraction (vol. %) of the slurry. As both ν and n remained constant for this experiment, it is the change in A as a function of the solid loading that is responsible for the increase in average λ. To identify any specific changes on the microstructural level, the thickness of the ceramic walls and macropores were separated and individually plotted (Fig. 5.3).

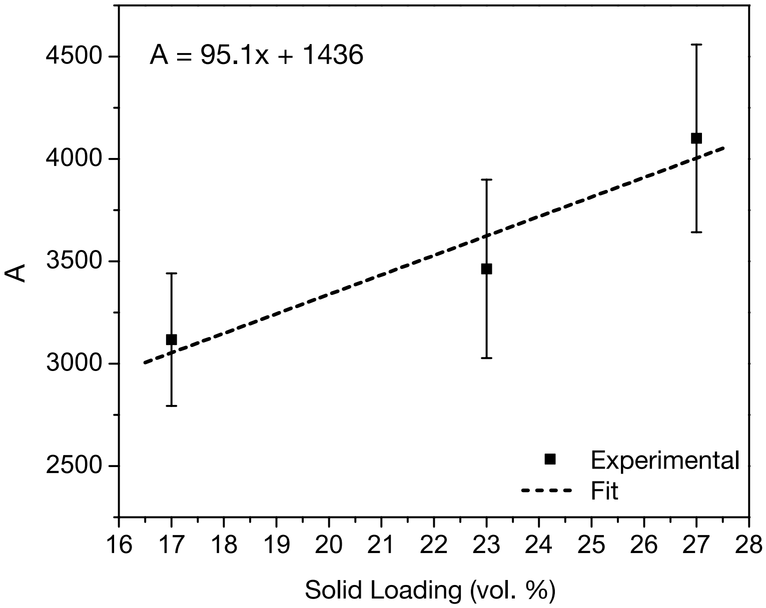

Figure 5.2: A as a function of solid loading. All data were taken at a freezing rate of 5 °C min^{-1}, and the values for ν and n were 23 µm s^{-1} and 1.5, respectively (R-value > 0.92).

It was found that the rate of ceramic wall growth does not equal the rate of macropore size decrease. For increasing solid contents, average wall size increased more than twice as fast as the decrease in average macropore size. It is this unequal wall-to-pore size change which accounts for the increasing average λ with solid loading [Fig. 4.14 (f) and Fig. 5.3].

Using the empirical relationship from Eq. (5.1), it can be seen that λ is exponentially dependent, and therefore highly sensitive, to changes in ν and only linearly dependent on the A-value. For a given set of experimental conditions, there will be an equilibrium solidification speed $\nu*$ and an equilibrium ice crystal. The size of this equilibrium crystal is predominantly related to $\nu*$, as the thickness of an ice crystal is directly proportional to the speed at which it freezes [86]. The thickness of the ceramic walls is a function of the space available between the growing ice crystals. Increasing the solid loading (Fig. 5.3) will re-

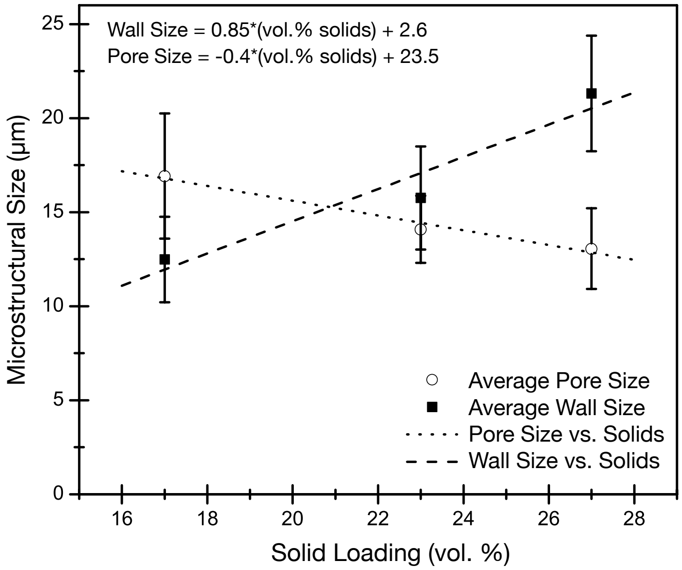

Figure 5.3: Plot of average microstructural size as a function of solid loading (vol. %) at 5 °C min^{-1}. Open circles represent macropores while black squares represent wall sizes. Using a linear trendline it was determined that the wall size (R-value > 0.93) increased faster than the macropore size decreased (R-value > 0.97).

sult in increased wall size to account for the increased solid fraction, however, because solidification velocity remains unchanged (Fig. 4.14 (c)), the ice crystals will be biased towards remaining their equilibrium size at $v*$. It is for this reason that average λ increases [Fig. 4.14 (f)] even though solidification velocity remained consistent [Fig. 4.14 (c)]. This allows for the ratio of wall-to-pore size to be tuned while holding pore size approximately constant (Fig. 5.3).

The suppressed effect of solid loading on macropore size is only the case for a limited range of solid loadings. At high solid loadings ($\geq$ 40 vol.%) particle-particle interactions begin to have a significant impact on the impinging freezing front [98, 120], additionally, particle redistribution becomes difficult and the ice crystals will engulf the ceramic particles rather than pushing them aside. The result is an isotropic, dense structure like those seen for the 40 vol. % samples in figure 4.16.

5.2 Derivation of Anisotropic Sintering Behavior

Freeze-cast LSM-YSZ underwent anisotropic densification during sintering. Samples shrunk to a greater extent (3 - 4 %) in their freezing-direction compared with their non-FD. The question as to why this occurs is dependent on the spatial arrangement of material and macropores contained within the freeze-cast.

Assume we have an idealized freeze-cast structure (only SSZ) with completely continuous walls running in the z-direction and lamellar pores which are randomly distributed in the x-y plane. If we assume that densification *within* the walls of the freeze-cast occurs isotropically at a given temperature, that is:

$$\varepsilon_{wall} = \varepsilon_{wall-z} = \varepsilon_{wall-xy} \tag{5.2}$$

then we can say that the normalized linear shrinkage in the z-direction (FD) is equal to the densification of the walls evaluated at some sintering temperature T_s:

$$\frac{\delta z}{z_o} = \varepsilon_{wall}\Big|_{T_s} = \varepsilon_z \tag{5.3}$$

In the x-y plane, the linear shrinkage can be described by two terms, the contribution from densification of the walls and that of shrinkage of the macropores.

$$\frac{\delta x}{x_o} = \frac{\delta x_{wall} + \delta x_{macropore}}{x_o} = \varepsilon_x \tag{5.4}$$

Of course, the macropores do not shrink of their own accord. There are small collections of particles which tie walls together across macropores. We hypothesize that it is the densification of these particulate bridges which drive the macropore shrinkage. Simultaneously, as the bridges traversing macropores are densifying, pulling walls towards one another, the walls of the freeze-cast densify towards the center of mass of each strut. These two strains oppose one another which explains why macropores do not seem to shrink a significant amount (Fig. 5.4). It also means that the strain across a macropore $\varepsilon_{macropore}$ will always be relatively less than the sintering strain experienced within a wall ε_{wall}. The relative shrinkage in the transverse direction can then be described with the following expression:

$$\frac{\delta x}{x_o} = \varepsilon_{wall} A_{wall} + \varepsilon_{macropore} A_{macropore} \tag{5.5}$$

where A_{wall} is the relative fraction of walls and $A_{macropore}$ is the relative fraction of macro-

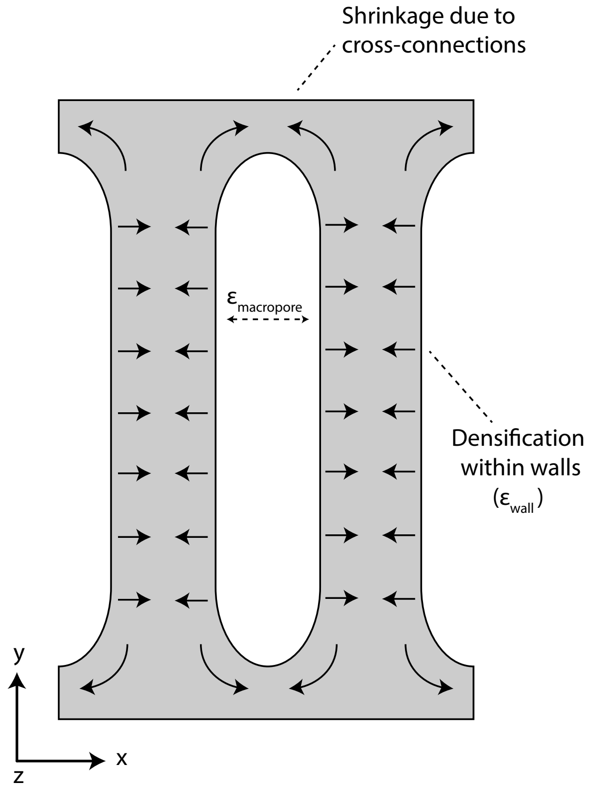

Figure 5.4: Idealized, schematic representation of the opposing shrinkages seen surrounding a freeze-cast macropore. Freezing-direction is out of the page.

pores $(1 - A_{wall})$, and because $\varepsilon_{wall} > \varepsilon_{macropore}$, the following will be true:

$$\overbrace{\frac{\delta z}{z_o} = \varepsilon_{wall}}^{\text{Parallel Shrinkage}} \quad > \quad \overbrace{\varepsilon_{wall} A_{wall} + \varepsilon_{macropore}(1 - A_{wall}) = \frac{\delta x}{x_o}}^{\text{Transverse Shrinkage}} \tag{5.6}$$

To test our explanation of the spatial orientation of macropores causing anisotropic densification, a packing of particles similar to what was used for mechanical testing was generated with 50 vol. % porosity. The freeze-cast structure was merged with this particle packing *before*[2] sintering took place so that we could see the effect of anisotropic macropores on the final shrinkage. The DEM structure was then sintered numerically to a density of 0.75 in the walls of the ceramic. This intrawall density is equivalent to that of an LSM-YSZ freeze-cast sintered to 1200 °C. Plotting the strain in the x, y and z-directions one can see that there is one direction that shrinks to a lesser extent ($\sim$ 3 %) than the other two (Fig.

---

[2] Simulated mechanical testing samples had their macropores removed after sintering took place.

5.5). As expected, this direction is normal to the freezing-direction (y).

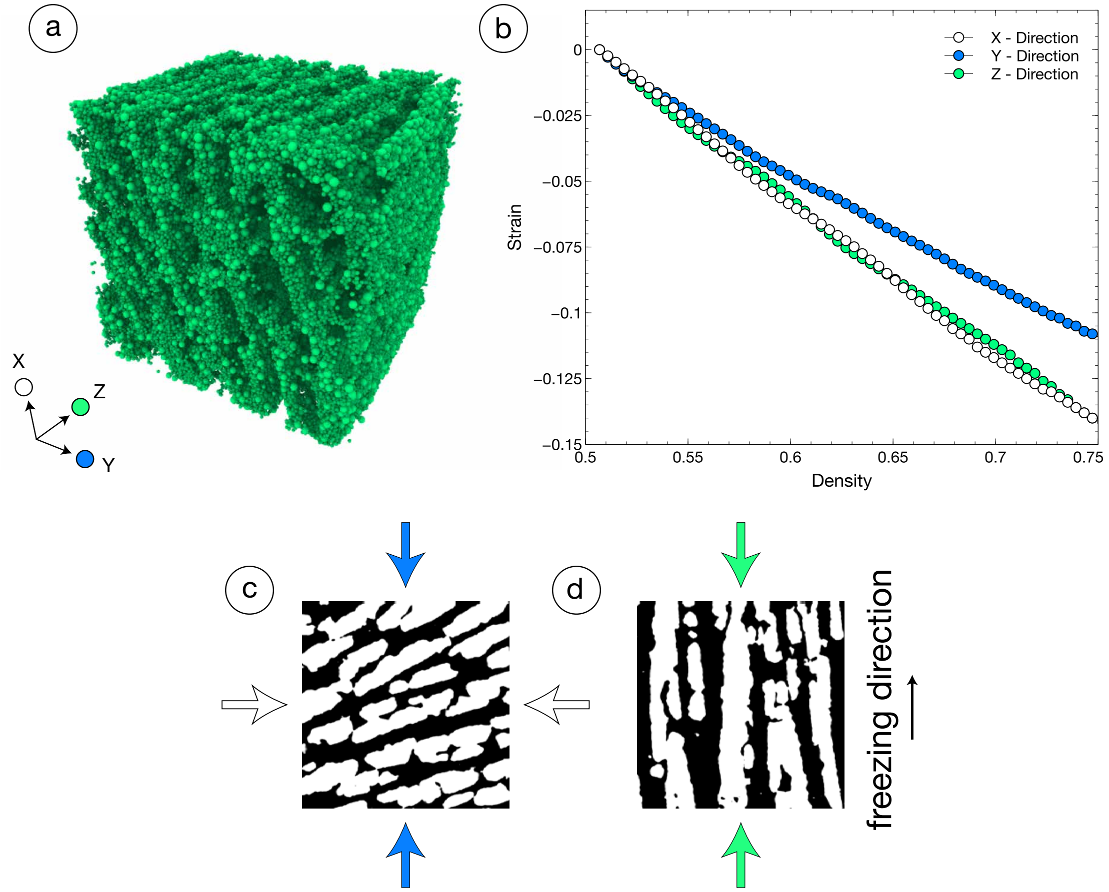

Figure 5.5: (a) Simulated sintering of a freeze-cast DEM structure showing (b) anisotropic shrinkage. Also shown are the (c) x-y and (d) z-y cross-sections to illustrate the macrostucture and relevant shrinkage. Macropores are shown in white.

Note, that the x-direction (Transverse - Align) sees equivalent strain values to the freezing direction (z), once again illustrating that within a colony of pores, the properties in the freezing-direction are similar to those in the Transverse - Align direction. As a comparison, the sintering strain experienced by a monolithic DEM packing of particles without macropores is plotted alongside strain values from the sintered freeze-cast (Fig. 5.6). We show here that the freeze-cast structure does have an unequivocal effect on sintering.

A good measure of how sintering proceeds is to examine the coordination number of particles in a structure after sintering. Areas which are more densely packed with particles must have densified more substantially than others. Looking at the discrete-element models in figure 5.7, one can see that the regions of highly coordinated particles run along the x and

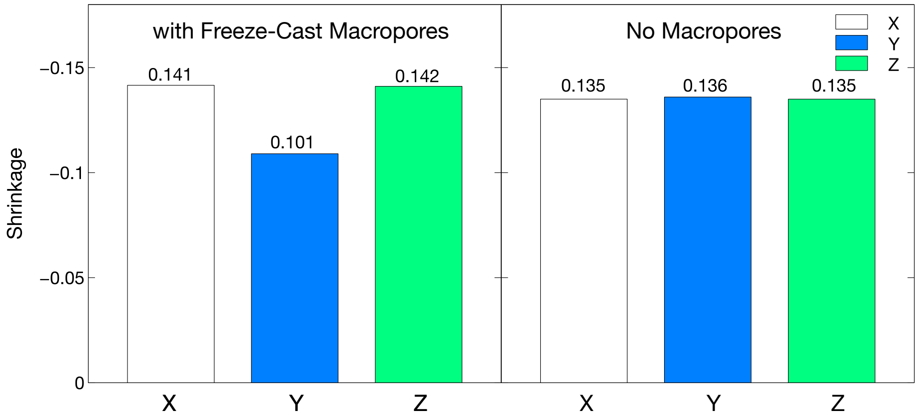

Figure 5.6: Shrinkage values in each direction at the final density of 0.75 for structures with and without macropores.

z-directions. These are both the directions where greater overall shrinkage values were seen. Comparatively, the y-direction is highly discontinuous, with only those previously mentioned small particulate bridges connecting walls. We also see that running along the free surfaces (macropores) of the structure, the coordination number is relatively lower than within the walls themselves. Areas of low coordination will sinter in the direction of particles with higher coordination.

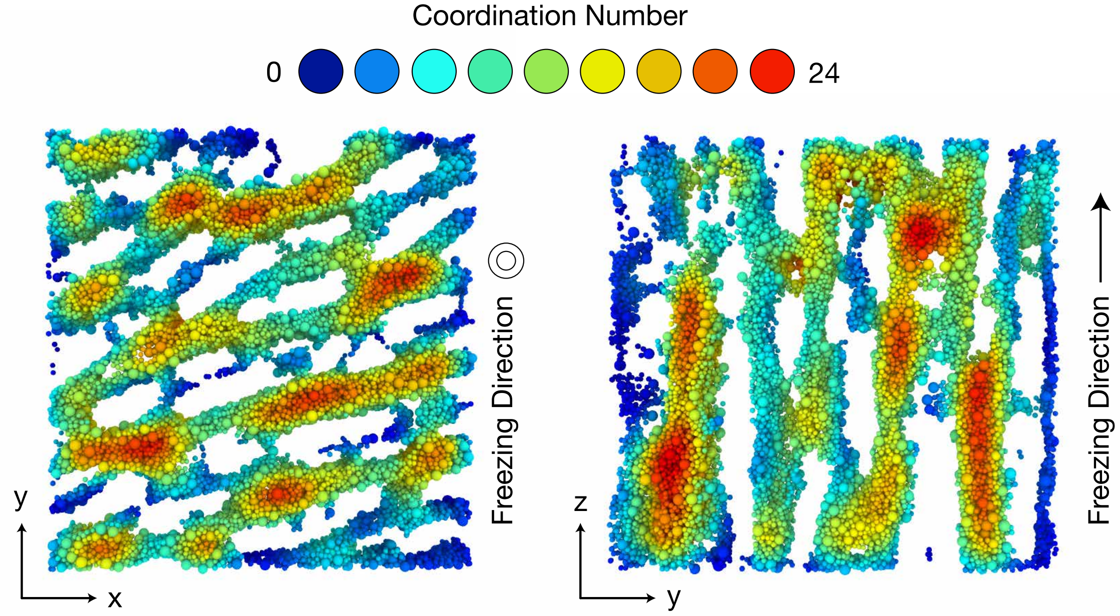

Figure 5.7: Coordination analysis of particles in a sintered DEM structure.

Sintering is a mass-transport phenomena, it is driven by the system's desire to reduce surface area and limited by mass diffusion. Particles which are well within the walls of a freeze-cast are surrounded in all directions by particles and so will sinter isotropically to reduce that energy term. Particles which find themselves running along the free surfaces of macropores however are only partially surrounded by other particles. Because of this they will sinter anisotropically and are driven towards attaining higher coordination numbers and in the process lowering their surface energy terms.

5.3 Role of Sintering on TPB Allocation in Freeze-Casts

The qualitative and quantitative analysis of the FIB tomography data show (see Fig. 4.18) that a high sintering temperature (1300 °C) decreases the freeze-cast microporosity from 25 vol.% (at 1200 °C) to 14.9 vol.% also leading to a significant degree of unconnected porosity (38 vol.% of the total micropore volume). It should be emphasized that unconnected porosity is undesirable since it will not contribute to enhancing electrochemical activity while at the same time decreasing mechanical integrity. The majority of the remaining connected porosity was found to be localized along the edges of the freeze-cast structure, adjacent to the large macropores. Additionally, it was determined that sintering to the higher temperature leads to an increase in grain size of the YSZ from 300 nm to 550 nm while preserving the size of the LSM grains. Overall, there was a decrease in the total TPB density as well as the active proportion of those TPBs. Densification reduced tortuosity by 40 % for the LSM phase while at the same time closing off gas percolation pathways resulting in a null tortuosity for the pore phase. The tortuosity of the YSZ phase decreases only slightly at the higher sintering temperature.

The significant growth of the YSZ grains will negatively affect the TPB length and nullify the TPB gain expected from using fine starting powders. Grain coarsening is, however, generally difficult to avoid during high temperature sintering. It is worth noting that Cronin et al. observed significant grain growth for both LSM and YSZ [178]. They used significantly smaller starting particles for LSM, which could explain why they observed grain growth for LSM while we do not.

The first direct consequence of the presence of unconnected porosity within freeze-casts sintered at 1300 °C is the decrease in the active portion of the TPBs, from nearly 100 % to 38 %. This comes in addition to a significant decrease in the total (active and inactive) TPB length (from 8.9 µm µm^{-3} to 4.1 µm µm^{-3}) due to YSZ particle coarsening and neck growth. We observed that the majority of active TPBs and connected porosity for the 1300 °C sample were localized on the sides of the ceramic lamella, within a thickness of approximately 2 µm from the wall-edges. It is no coincidence that this happens to be the region where there is still residual, connected open porosity. This seems to indicate that the presence of the aligned macropore channels allows for some active TPBs even with a microporosity value as low as 14.9 %.

While higher sintering temperatures result in reductions to TPB density and open porosity, the significant decrease in tortuosity also leads to increased conductivity for both the LSM and YSZ phases. While LSM conductivity is generally not a limiting factor for SOFC performance, due to the high intrinsic electronic conductivity of this material at operating temperatures, it is not the case for the low ionic conductivity of the YSZ phase that is primarily responsible for ohmic losses. Ohmic losses limit cell performance, and the TPB length taken alone is not necessarily the best indicator of electrochemical performance. An optimal microstructure results from a trade-off between activation and ohmic losses. For example, the maximum TPB length is obtained for a 50:50 LSM:YSZ ratio while the optimal ratio for cell performance is 40:60 when accounting for ohmic losses [41, 179].

Our analysis indicates that if our material system were to be used for a conventional isotropic composite LSM:YSZ cathode, the optimal sintering temperature would be approximately 1200 °C, which is in agreement with Cronin et al. [178]. Sintering at higher temperatures reduces performance because of the low activation due to unconnected porosity. However, the use of a lamellar, freeze-cast structure increases the active TPB density at low microporosity values thanks to the aligned gas channels. The optimal trade-off between activation and ohmic losses is therefore believed to shift toward higher sintering temperatures, which have the added benefit of strengthening the electrode. However, it is noted that the optimal sintering temperature may also depend on the average lamellar thickness. After sintering to 1300 °C a large amount of the active TPBs are found within the zone approximately 2 µm from the gas channels while the TPBs in the core of the lamella are inactive. Thus, reducing the lamellar size by utilizing faster freezing rates could reduce the inactive core region and increase the density of active TPBs within the cathode (Fig. 5.8). Using a thin lamellar structure, it is believed that sintering temperatures as high as 1300 °C could be used without compromising the density of TPBs in order to increase the ionic conductivity.

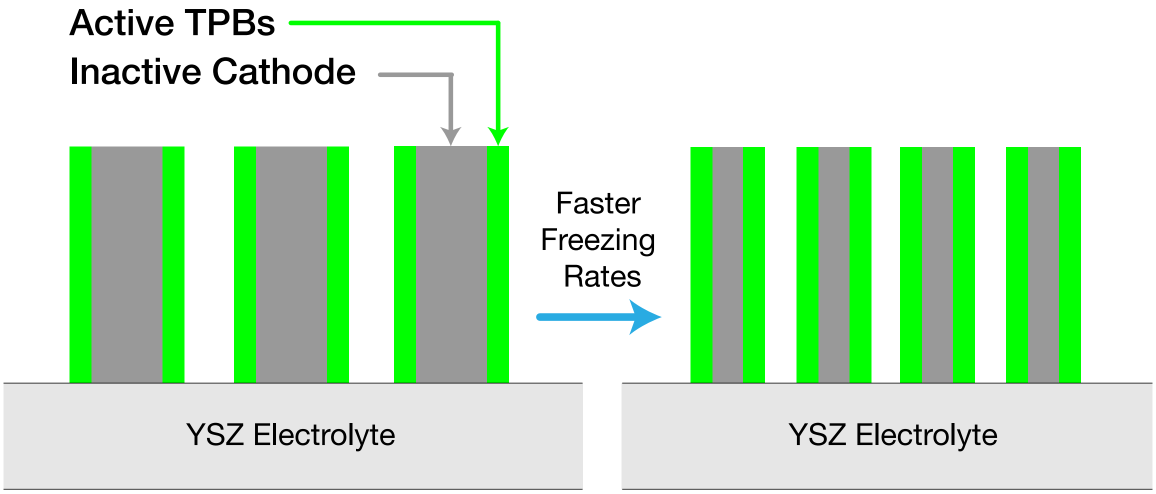

Figure 5.8: Potential electrode optimization scheme accounting for the active TPBs which localize along wall edges at samples sintered to higher temperatures.

5.4 Mechanical Behavior from Experiments and Simulations

For many of the studies reported herein, a significant amount of time and energy was spent preparing samples to certain specifications; typically a cuboidal specimen was removed from the center of each freeze-cast. Other groups test freeze-casts as-is, with their IZ and TZ regions still intact. This is a simpler method and allows for much faster data acquisition because the sample preparation is easily the most time-consuming aspect of testing freeze-casts. There is however the question as to whether or not it was worth it. We have a better idea of the structure which we are actually testing but in the process of sample preparation, it is inevitable that flaws are introduced into the samples. This was true even though a great deal of care was taken to ensure that the microstructures stayed as unadulterated as possible (infiltrating with low-viscosity resin before processing). There is no data available from other groups to compare with our material/processing combination.

During mechanical testing it was clear that there were different failure mechanisms at work for the different types of samples (isotropic and anisotropic) and for the different orientations of the anisotropic samples (parallel and transverse).

5.4.1 Failure of Freeze-Cast Samples: Parallel Orientation

Freeze-casts compressed in the direction parallel to their freezing direction showed that rather than the walls crushing vertically or sliding past one another, the walls preferentially split apart and spread out laterally in a mushroom-like structure [Fig. 4.32 (a)].

Although stress is primarily transferred vertically (z) through the structure, cross-members are required to provide rigidity in the x-y plane, normal to the walls of the porous ceramic. Other studies of freeze-cast mechanical properties have made similar observations [111, 115, 131]. The connectivity of walls transverse to the freezing direction aids in preventing walls from buckling and/or shearing past one another when tested in this direction. Comparisons between microstructural cross-sections from 1 °C min^{-1} and other faster freezing rate samples showed immediately apparent microstructural differences not only for feature scale but also for the morphology of connections between walls and pores (Fig. 5.9).

Freeze-casts contain domains, or colonies, of pores which are randomly oriented in the x-y plane [Fig. 5.9 (a, b)]. Within the domains however, macropores are aligned, creating an additional level of organization within the microstructure. This localized alignment provides strength transverse to the freezing direction. Where pore domains meet there are regions of disorder not unlike those seen along the grain boundaries of multi-crystalline materials. Fracture occurs preferentially along these domain boundaries. Notice in figure 5.9 (a, b) that the average size of the colonies is approximately the same, yet the number of macropores contained within the colonies for samples frozen at 1 °C min^{-1} is so small that each pore seemingly acts as its own randomly oriented domain. The resulting structure has a higher degree of disorder between pores (in the x-y plane). Additionally, these large macropores tend to intersect other macropores, creating regions where the walls themselves are unconnected to the greater microstructure [Fig. 5.9 (c, d)]. In fact, it was determined from 2D image analysis that between 17 and 35 % of the solid area is unconnected for 1 °C min^{-1} samples compared with other freezing rates, which averaged between 1 and 7 % unconnected solid area. Of course, from the 2D cross-sections, the connectivity of walls in three dimensions is unknown, however because of the highly directional nature of these structures it is reasonable to assume that unconnected walls remain unconnected for a significant distance along the freezing direction. These non-continuous portions of the wall structure will not contribute significantly to either strength or stiffness resulting in the poor performance of microstructures with this coarse porous morphology.

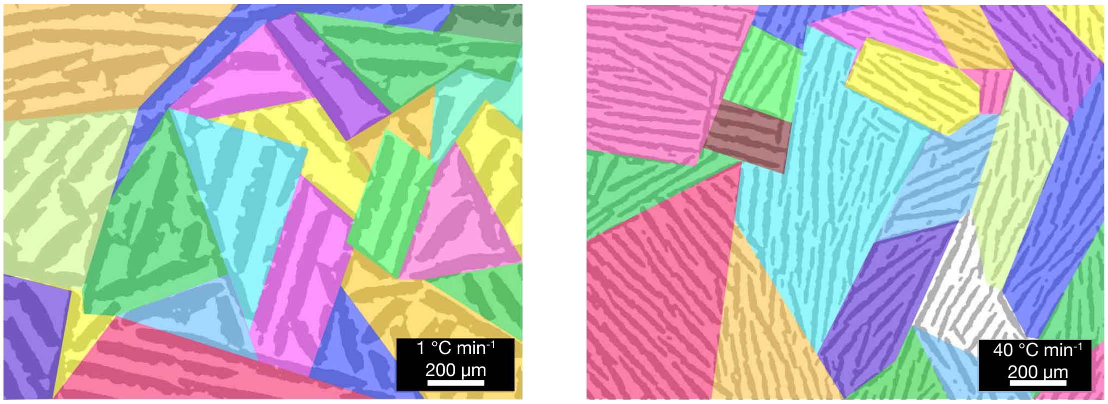

(a) Pore Colonies - 1 °C min^{-1} **(b)** Pore Colonies - 40 °C min^{-1}

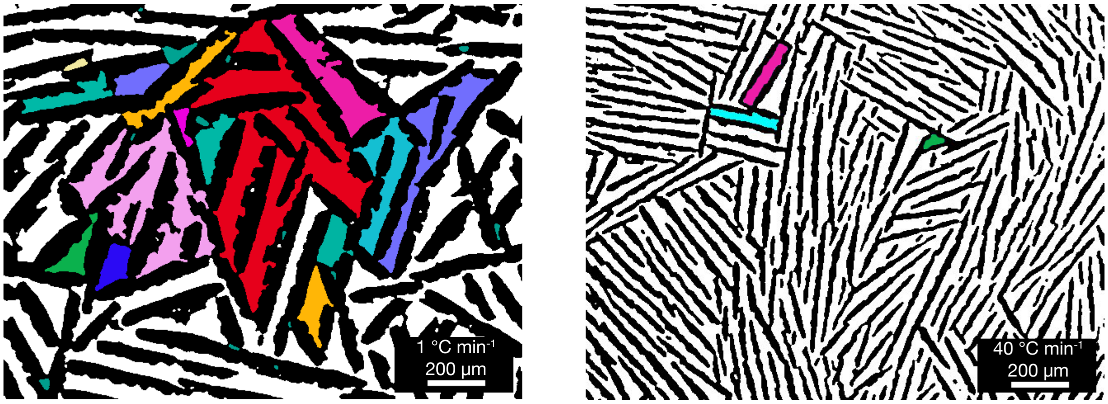

(c) Wall Connectivity - 1 °C min^{-1} **(d)** Wall Connectivity - 1 °C min^{-1}

Figure 5.9: Colorized cross-sections (x-y plane) at the same magnification from samples frozen at 1 °C min^{-1} and 40 °C min^{-1} showing (a, b) the relative size and location of macropore colonies and (c, d) the connectivity of walls within the same cross-sections. White represents walls which are connected to an edge, black represents macropores and each colored region represents a wall that is disconnected from the greater microstructure.

The highly discontinuous types of microstructures produced using slow freezing rates can be intimately tied to the nucleation conditions. For example, at 1 °C min^{-1}, there is little thermal drive for nucleation. As a result, only a few nuclei form and grow, and they do so spatially and crystallographically randomly from one another. In addition, given the weaker thermal drive for growth in the freezing direction, these crystals tend to grow transverse to their basal plane more so than ice crystals frozen at higher velocities. At some point, the growing crystals will intersect neighboring crystals. If this happens often enough, the resulting ceramic microstructure will contain regions of discontinuity in its x-y plane creating a freeze-cast structure with many discontinuities.

The role of microstructural connectivity also helps to explain the variation in failure behavior over the height of an individual freeze-cast. As can be seen from figure 4.32 (a), the "bottom" of the sample remains intact while the "top" has failed. Microstructural cross-sections from the "bottom" of the 1 °C min^{-1} freeze-casts show that they have a more continuous structure (averaging between 2 and 16 % disconnected solid area) which helps explains why these samples break more readily at their discontinuous "tops".

As mentioned previously, our tomographic-based DEM models sampled too small a volume to represent more than a single colony of pores. We were able however to create a 2D DEM packing from an SEM image containing multiple pore colonies. Using mirror symmetry in the z-direction, we compressed the structure seen in figure 5.10 in the y-direction.

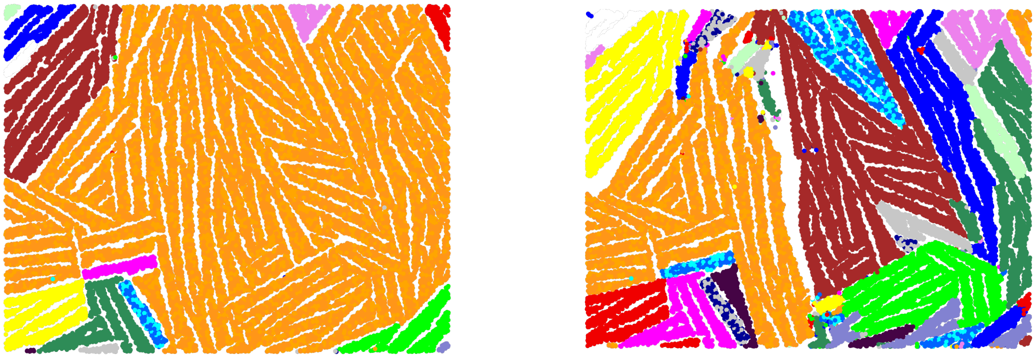

(a) Before **(b)** After

Figure 5.10: Simulated compression of 50 vol. % porous 2D-DEM structure frozen at 10 °C min^{-1} before and after testing showing the mechanical behavior of macropore colonies. y-direction is up, z-direction is out of the page.

This figure depicts connected solid area before and after mechanical compression for a freeze-cast with approximately 50 vol. % porosity, frozen at 10 °C min^{-1}. At first, [Fig. 5.10 (a)] we see that the majority of solid material is connected (orange). Contained within this orange block however are multiple pore colonies. After compression, [Fig. 5.10 (b)] it can be seen that the structure fractured along the boundaries between colonies while the organized walls within colonies experienced less damage.

5.4.2 Failure of Freeze-Cast Samples: Transverse Orientation

Unlike parallel samples where the bulk of the wall bears the load and the cross-members serve to provide rigidity, in the transverse orientation, it is the cross-members that actually take the brunt of the stress. The concept of transverse connectivity does not appear to be applicable to samples tested perpendicular to their freezing direction since there appears to be no significant effect of microstructure (other than relative porosity) on the performance of freeze-casts tested perpendicular to their freezing direction. It is believed that the lack of correlation between freezing rate and mechanical performance is due to the statistical nature of the porous structure in the x-y plane. Any benefits gained from having a structure with increased cross-connections between walls is nullified since the pore domains are randomly oriented in the direction of loading. This random orientation means that statistically it is likely that some pores and walls will be poorly oriented in relation to the applied stress.

When samples were loaded in the transverse direction, localized damage could immediately be seen long before peak stress was reached. During the loading sequence, individual walls broke (most likely at the boundaries between pore colonies) and then acted as a sort of dry lubricant for the remaining intact ceramic to slide along, releasing stress. A disconnected microstructure, such as those seen from samples frozen at 1 °C min^{-1}, does not have a significant effect on a freeze-cast tested in this direction because the disconnected walls would be compressed together immediately during the initial loading sequence. This is why freezing rate (i.e. macropore size) had no apparent effect on mechanical properties of samples tested in the transverse direction.

5.4.3 Failure of Isotropic Hierarchical Samples

In general, isotropic slip-cast samples tended to fail more catastrophically and unpredictably than the freeze-cast ones. This behavior is likely due to the dispersion of macropores throughout the isotropic samples. Slip-cast structures are prone to settling and agglomeration of PMMA spheres due to the long slip-casting process. Although complete pore coalescence was not observed, there did appear to be some regions with an increased concentration of isotropic macropores. These may have acted as stress concentrators resulting in catastrophic failure. The freeze-cast ceramics on the other hand showed more of a cellular material behavior [132] due to the regularity of its structure caused by the controlled templating of the microstructure by the freezing ice.

When freeze-cast samples were compressed, it was clear that individual particles were breaking free of the greater structure. This behavior however was not seen for slip-cast samples. As results from FIB reconstructions of slip-cast samples illustrates (see figure 4.29), the slip-casting process results in enhanced densification compared with structures produced by freeze-casting (even at the same temperature). This would indicate that the slip-cast microstructure has lost some of its particulate nature rendering it less able to release stresses by local particle rupture and rearrangement.

5.4.4 Modeling Mechanical Behavior

The differences in mechanical performance between isotropic and anisotropic samples is tied to the arrangement of their macropores (and hence solid volume) relative to the applied load (Fig. 5.11). Due to its directional templating, parallel samples have been optimized so that solid material is preferentially aligned in the direction of loading, meaning that nearly all the ceramic bulk is helping to carry and transfer load through the ceramic. Samples tested perpendicular to this direction (transverse), the volume of material taking load is minimized due to the orientation of the freeze-cast pores. In this configuration, much of the ceramic bulk is shielded from direct application of the load by the long macropores resulting in significant losses to mechanical performance. Isotropic samples had mechanical properties that fell in between those of parallel and transverse samples, which is in accordance with its non-optimized porous structure (Fig. 4.34).

This behavior is qualitatively well described using the minimum solid area MSA model, originally developed by Rice [180]. This non-empirically based model uses geometric factors rather than only total porosity to attempt to describe the behavior of porous materials (See section 2.5). Theoretically, according to the MSA method, mechanical performance will scale with the minimum geometric area actually under load (Eq. 5.7). Idealized representations of the MSA for our three different sample types is shown in figure 5.11. According to this model, the ratio of the modulus of the porous material (E_p) to that of the dense materials (E_0) should be equal to the MSA as given below.

$$MSA = \frac{E_p}{E_0} \tag{5.7}$$

As shown schematically in figure 5.11, Parallel samples will have the highest MSA and Transverse samples will have the lowest. This hierarchy should be (and is) reflected in mechanical performance. We found however that although MSA method can be used to describe the trends seen, it does a poor job of actually predicting the values of stiffness and strength (Fig. 5.12).

For samples tested parallel to their freezing direction, if we assume that pores are essen-

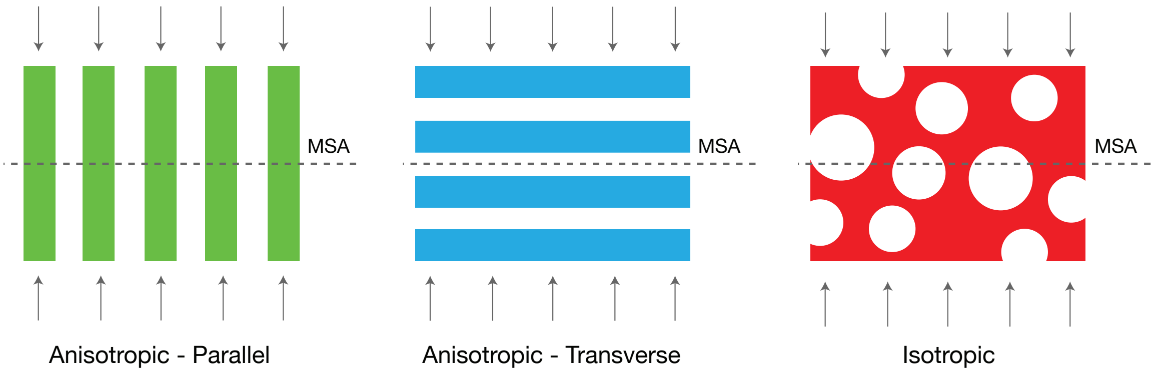

Figure 5.11: Schematic illustration of the MSA for our three sample types.

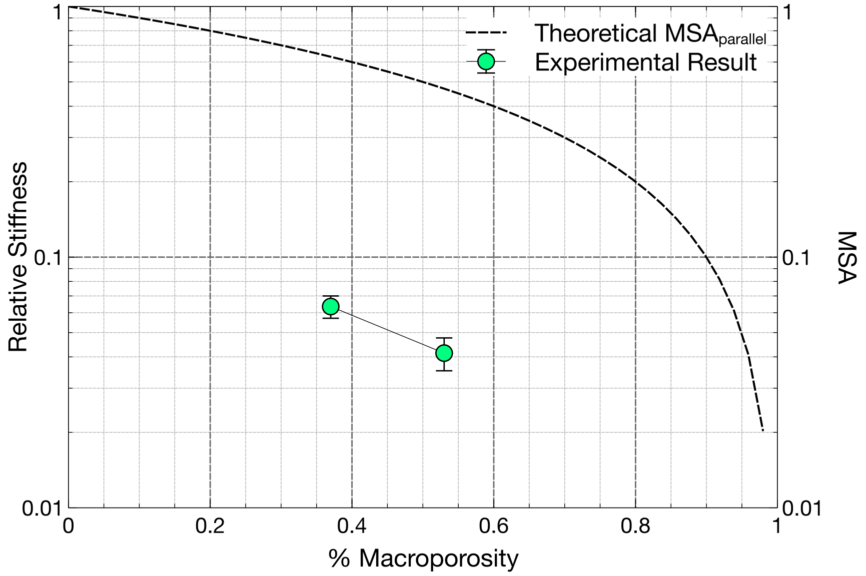

Figure 5.12: Plot of theoretical MSA for an ideal freeze-cast structure tested parallel to the freezing-direction with actual experimental data from testing multiple freeze-casts.

tially continuous in the freezing direction, the MSA should be the macroporosity of the sample which can be determined by visual inspection. The experimentally-derived values were normalized to 40:60 vol. % LSM-YSZ containing 25 vol. % micropores and no macropores (71 GPa) [171, 181]. According to the theoretical MSA curve, our experimental results are more than an order of magnitude lower than predicted (Fig. 5.12).

Within the literature, MSA models are typically verified on highly idealized samples with simple geometries such as packings of glass or alumina spheres [21, 133]. The fact that our structures are so complex and large compared to these representative structures was thought to account for why experimental values were so low. However, after application of MSA methodologies to DEM structures, we had to concede that the MSA model is unable to well describe the mechanical performance of freeze-cast structures.

Using our simulated mechanical structures we were able to exactly calculate the minimum solid area in each of the three directions for our DEM samples (Fig. 5.13). Like for our experimental evaluations we don't actually calculate the porosity within the walls but assume it is the isotropically distributed 25 vol. % that was seen with FIB tomography. From image analysis we can see oscillations in solid area which refer to the alternating macropores and walls within freeze-cast samples, then using DEM we can pinpoint where in the structure that bonds are breaking. If the MSA method were to accurately predict failure within our freeze-casts, then the majority of broken bonds should be localized near to the MSA. We found this not to be the case. Figure 5.13 shows that the majority of broken bonds are localized at the edges of the sample (this was a case for every DEM X-ray Tomo sample tested). Within the sample bulk interestingly enough, the majority of ruptured contacts were localized at the cross-section with the lowest porosity. This is the absolute opposite prediction from the MSA method.

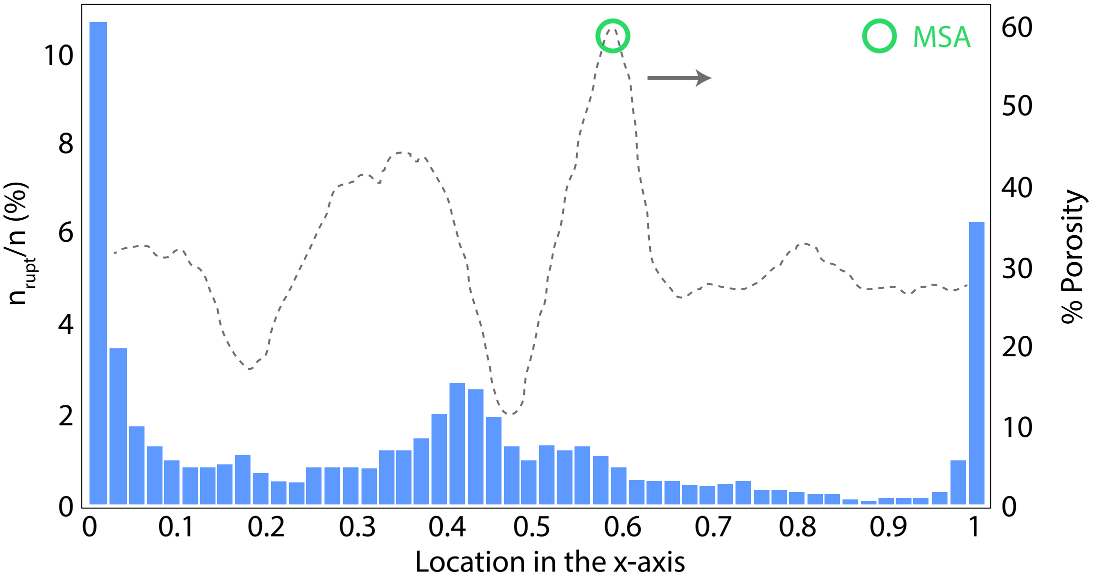

Figure 5.13: Location of ruptured contacts for a sample compressed in the x-direction (transverse) along with the superimposed percentage porosity showing where the MSA occurs for this sample.

Obviously, it would be beneficial to develop models to describe and predict the mechanical behavior of our freeze-cast ceramics but with only two different points describing porosity, we are unable to fit our data with any significant meaning. Producing more datapoints ranging across the porosity spectrum should be considered a priority in the future for developing reliable models.

5.4.5 Simulated Mechanical Properties

In general our DEM derived values for stiffness and compressive strength were about three times greater than the experimentally measured values. We can account for this in a number of ways. The DEM strength is only related to the strength of the bonds between particles, it does not take into account the strength of the particle itself, which may or may not contain flaws. The surface energy value that we used (1 J m^{-2}) was arbitrary because we were unable to find data within the literature for a composite of LSM-YSZ and physical determination of this value can be difficult. We are also only accounting for a tiny fraction (1 x 10 $^{-5}$ %) of the volume of our average experimental sample. There are certainly more flaws in the real samples whose properties will dominate the mechanical response. Given all these potential sources of misrepresentation however, we are still able to replicate the same trends, which is highly promising.

According to the number of broken bonds versus displacement, we found that only 1 % of all bonds needs to break in order to attain "failure" of transverse samples whereas approximately 5 - 8 % must break for the isotropic and parallel samples. From these numbers, we can see how much less actual material is involved in the transfer of stress for transverse samples.

5.5 On Freeze-Casting Half-Cells

Even though a plethora of methods were attempted to create a thin-half cell with a dense electrolyte and robust bond between electrode and electrolyte, none were successful. Initial attempts resulted in inadequate bonding between the electrode and electrolyte. Our in-situ freezing method appeared to produce adequate adhesion however the electrolyte portion of the cell still retained a significant amount of porosity. ESD was unable to cap the electrolyte, creating a fully dense layer because the macropores were too large and the surface was too rough. In the end, once we'd gotten a somewhat satisfactory half-cell (Fig. 4.41) it turned out that our impedance setup produced inconclusive results. A thick electrolyte was required so that the reference electrode could be placed circumferentially around the half-cell.

With all the changes that we had to implement in order to even produce a reasonable electrochemical response, the microstructure was so vastly altered from the freeze-cast samples that we had been testing throughout the thesis that it seems futile to try and compare performance. Especially when the impedance curves were so obviously dominated by the electrolyte response rather than that of the architectured cathode. Yet the fact remains that other groups were able to make and test working freeze-cast SOFC half-cells [8, 63, 65].

The groups that were able to fabricate working half-cells *all* utilized freeze-tape-casting methods. By tape-casting, these other groups were able to laminate multi-layer tapes with excellent adhesion between the porous electrodes and dense electrolyte. No group attempted to freeze-cast the LSM-YSZ system. NASA had an added novelty in their method in that they only freeze-tape-cast YSZ [65]. Their double-sided freeze-cast tape was laminated together and sintered sidestepping any issues deriving from the potential thermal expansion mismatch of composite electrodes. Post-sintering, the researchers infiltrated the active electode components (LSM and NiO) into the freeze-cast scaffold. Their impressive cell resistance of 0.166 Ω cm^{-2} indicates that alignment of walls around gas channels does enhance electrochemical performance. A question which must be asked however is whether or not the enhanced electrochemical efficiency is worth the additional processing, weight and material costs required by freeze-casting. State-of-the-art cathodes and anodes produced through screen-printing methods are typically between 10 - 100 μm in thickness [182]. Freeze-tape-cast macropores are typically on that same scale (10 - 100 μm) meaning that to get any effect from gas channelization will require a greater overall layer thickness; which is exactly what is seen from each and every freeze-tape-cast electrode [8, 63, 65]. Each of these freeze-cast layers is roughly 1 mm in thickness. The additional weight and cost must be taken into account for the system design.

Our work did result in some interesting observations for the relatively little-studied process of bi-layer freeze-casting. In a standard freeze-cast (such as those used for mechanical testing) the SSZ doesn't start till approximately 2 mm along the freezing direction. In the button half-cells with the thin electrolytes (Fig. 4.41), nearly the entire height has been templated with fairly well-aligned pores. A short experiment was run where in place of the bi-layer system (YSZ:LSM-YSZ), a single layer of LSM-YSZ was freeze-cast within the same half-cell molds. Although the same conditions were used as were used on the bi-layer half-cells, no significant templating took place. It can be surmised then that the thin layer of pure YSZ provided preferential nucleation conditions making the transition to the SSZ faster. This is an observation worth further investigation.

6

Summary and Conclusions

Processing and characterization techniques were developed for ceramics with hierarchical isotropic and anisotropic porous microstructures. The effects of anisotropic and hierarchical porosity on the properties of ceramic materials made for SOFCs were determined using both experimental and simulation methods. Samples were made using either freeze-casting or slip-casting followed by partial sintering. Both processing methods were studied extensively for the effect of processing parameters on the final porous microstructures. The simulations were conducted using discrete-element methods, taking advantage of the particulate nature of our ceramics by simulating their properties on appropriate length scales.

One pervasive limitation which was encountered was that there was no characterization technique which could be used to categorically describe our entire freeze-cast (or slip-cast) structure. We had at least four distinct levels of hierarchy and four different types of characterization techniques.

$$\underbrace{\text{Intrawall}}_{\text{FIB - Tomo}} \rightarrow \underbrace{\underbrace{\underbrace{\text{Macropores and Walls}}_{\text{X-ray Tomo}} \rightarrow \text{Pore Colonies}}_{\text{SEM}} \rightarrow \text{Macrostructure}}_{\text{Optical Imaging}} \tag{6.1}$$

6.1 Aqueous Dispersion of LSM-YSZ

Normal hetero-codispersion methods are ineffective at producing aqueous LSM-YSZ slurries, the iso-electric points of these two materials are too close together and because of their differing particle size and densities, they naturally segregate. By carefully controlling the dispersion conditions in an aqueous slurry, stable, workable composite LSM-YSZ suspensions were fabricated. There are three requirements for this to happen. First, YSZ must be fully dispersed prior to LSM. Second, the pH must range from 7 - 8, and third, the viscosity of the suspension should be high enough to prevent particle segregation while still being low enough to freeze-cast. We were able to produce stable suspensions from 17 - 40 vol. % solids using levels of dispersant ranging from 1.4 wt. % of the solids (at 17 vol. %) to 2.4 wt. % of the solids (at 40 vol. %). The resultant composites show good dispersion of the electronic and ionic conducting particles.

6.2 Freeze-Casting

Single-sided, homogenously cooled, freeze-casts frozen with linearly cooling rates were found to be ideal for promoting continuous aligned macropores with almost constant lamellar size.

Anisotropic, hierarchically porous microstructures with uniaxially aligned pores for SOFC cathodes were controllably fabricated by directionally freeze casting aqueous dispersions of LSM and YSZ powders. These are robust and display excellent control of porosity (52 - 66 ± 0.34 vol. %), and average λ (31 - 82 ± 6.3 µm). Average λ can be precisely controlled by controlling the freezing velocity and is well approximated by a simple power-law providing a method for the design and prediction of microstructures. In addition, the ratio of wall-to-pore size can be tuned using the solid loading.

Freezing rate was found to be the only significant factor affecting freezing velocity indicating that the freezing process is primarily a function of the freezing kinetics of the solvent and the thermal conditions of the system. Total and open porosity were found to be independent of microstructure and only affected by the initial solid loading of the slurry. Viscosity was found to have no significant effect on freezing velocity and only a minor although complex effect on microstructural characteristics, although its effect on dispersion of particles and creating workable slurries was significant.

The prefactor, A, in $\lambda = A\nu^{-n}$ is proportional to the microstructural wavelength, λ and was found to linearly depend on the solid loading. No significant change in microstructural feature size was reported for freezing rates higher than 10 °C min^{-1}.

6.3 Sintering and Microstructure

Sintering of freeze-cast structures resulted in significantly different relative levels of shrinkage in the freezing versus non-freezing directions. This can be explained by the fact that spatially, there is more void space in the non-freezing direction (macropores). The macropores themselves do not contribute significantly to the driving force for densification, meaning that all the shrinkage is a result of the walls densifying. All loss in porosity, during sintering, can be attributed to loss of micropore volume. Using the processing protocols developed in this research, we are able to independently control the microstructural wavelength, total porosity, and the relative amount of micro- and macroporosity.

FIB-SEM tomography shows that sintering to 1300 °C results in significant coarsening of the YSZ phase and decreased microporosity, but a negligible effect on the average grain size of the LSM phase. Additionally, the coarsened microstructure suffers from a loss in overall TPB density as well as a reduction in the activated proportion of those TPBs. Tortuosity calculations show that densification during sintering results in reductions in tortuosity for the solid phases (LSM and YSZ) but significant increases for the porous phase. However, the lamellar structure appears to localize active TPBs near the lamellar surfaces, indicating that the optimal sintering temperature depends on the lamella size and may be shifted higher as compared to a standard isotropic electrode microstructure.

6.4 Mechanical Properties

Experimental

Mechanical testing specimens with micropores and isotropic or anisotropic macropores were made using slip-casting and freeze-casting. Testing showed a clear effect on stiffness and strength based on the directionality of macropores within a sample for anisotropic samples. Isotropically porous ceramics maintained intermediate performance indicating a transition in mechanical properties with geometric rearrangement of void space. For anisotropic porous samples, by changing the orientation of pores from perpendicular to parallel to the applied stress, stiffness increased on average by 8.5 times and compressive strength increased an average of 6.9 times.

For freeze-cast structures, there was an effect of freezing rate on mechanical performance however, microstructural characterization and observation of failure gave further evidence that it was not the scale of the macroporous structure that affected mechanical properties but rather the overall connectivity of walls and the density of cross-connnections that limited the mechanical performance of freeze-casts parallel to their freezing direction. With too few cross-connections, walls broke individually resulting in poor mechanical properties, undermining any advantages gained from pore and wall alignment.

The inclusion of isotropic macropores resulted in brittle, catastrophic failures whereas freeze-cast structures were found to undergo extended fractures, helping to dissipate energy without catastrophically failing. The more regular structure and smaller average size of freeze-cast walls are believed to be responsible for this difference in behavior.

Additionally, it was found that there was no benefit gained, either microstructurally or mechanically, by freezing this particular material combination faster than 10 °C min^{-1}. Further gains in mechanical performance of freeze-casts could potentially be realized by optimizing the density of cross-connections normal to the freezing direction either through additives or templating.

Simulations

Results from simulated mechanical testing showed that we are able to qualitatively replicate the trends seen from experimental testing but the quantitative values are too high by a factor of about 3. This discrepancy can be attributed to the small sample sizes tested for simulated samples and the fact that our contact toughness values were assumed to be the same for all materials (Γ = 1 J m^{-2}).

6.5 Electrochemical Behavior

Even though FIB tomography showed promising results for our microstructure, our method for testing the impedance of our half-cells was inadequate. We were unable to produce any representative data for freeze-cast structures. Adhering freeze-casts to other layers proved to be a difficult task due to their high levels of porosity and surface roughness. Testing showed that we are able to freeze-cast multiple layers in-situ but the process still requires optimization to prevent cracking between the layers and reduce residual porosity within the electrolyte. This is especially true of freeze-casts whose different layers have differing solid loading and/or sintering rates, such as LSM-YSZ.

7

Future Perspectives

The work done throughout this thesis open up a number of interesting avenues in ceramic processing, characterization techniques and microstructural optimization. Although, we focused on the SOFC system, there is no reason that the techniques developed cannot be applied towards other systems like filters, bioscaffolds and catalysts, just to name a few.

Freeze-casting in particular was found to be a highly versatile process with a number of promising avenues of research. Our research shows that nucleation conditions can have a marked effect on the resultant microstructure. There are ways to control nucleation conditions which could be applied to the freeze-casting system. Templating the freezing surface for example could potentially be used to produce differing numbers and orientations of initial nucleates. It would be of interest investigate the effect of templated nuclei on the growth of freeze-casts as the solidification front moves through the suspension. Would there be relatively fewer r-crystals if nucleation was more facile? What effect would there be on the number and size of z-crystals?

Although researchers have shown time and again that λ is related to the freezing velocity (v) through a power law [83, 86, 149], there is at this point still only empirical data supporting this claim. It would be highly beneficial to the freeze-casting community if more comprehensive studies of freeze-casting fundamentals were undertaken to. For instance, what does the prefactor (A) and exponent (n) actually depend on?

More powerful models could be developed to describe mechanical properties if additional samples with differing levels of total porosity were tested. It would also be interesting to test the effect of sintering temperature, which alters the micro to macroporosity ratio, on mechanical properties. The experimental design shown in table 7.1 is my suggestion for a future mechanical testing DOE:

The largest differences in microstructure were observed for samples frozen between 1 and 5 °C min^{-1} but our low-speed freeze-caster is only able to produce one sample at a time.

Table 7.1: Comprehensive Potential Mechanical Testing Study

Factor	Experimental Parameter	Levels
1	Freezing Rate (°C min^{-1})	1, 3, 5, 10
2	Solids Content (vol. %)	20, 25, 30, 35
3	Sintering Temperature (°C)	1200, 1250, 1300

It would take an enormous amount of time to produce the number of samples needed to produce a statistically significant sample size for mechanical testing. A new freeze-caster should be built that can produce multiple samples simultaneously and with better thermal control than we currently have. There are a number of examples in the literature of researchers using refridgeration units attached to copper platens [72, 76]. These are able to attain precise, repeatable thermal profiles across a large surface area.

I would also be curious as to the effect on mechanical properties of only removing the IZ and TZ and not actually cutting cuboidal samples out of the center of each freeze-cast. This would speed up testing, and also reduce discrepencies from sample to sample since only one cut would be made (perpendicular to the freezing direction). This would also have the benefit of leaving the internal microstructure as intact as possible. Of course, if this were the case, the change in microstructural feature size from the bottom to the top of each sample would be accentuated potentially adding an additional layer of complexity to this already complex system.

Throughout our investigations, we strictly used aqueous suspensions for freeze-casting, there is no reason however that other solvents cannot be used. Camphene in particular has been well-studied as a solvent for freeze-casting. The macropores which derive from using such a solvent are highly branched and dendritic. It would be interesting to see the role that overall macropore shape has on freeze-cast properties.

If using freeze-cast structures for electrochemical cells still seems attractive, time should be invested in moving towards freeze-tape-casting. Freeze-tape-casts seen in the literature show highly favorable performance and structure. Also, altering the material system so that only YSZ is used as the freeze-cast scaffold followed by infiltration of the active components (as per [65]) reduces many of the issues which we encountered with our own half-cells.

As far as simulations are concerned, there are a number of ways in which our methods could be improved to better represent experimental data. Firstly, the sample sizes tested using X-ray Tomo were too small to fully represent the freeze-cast microstructure. By changing material systems to a less absorbent material (Al_2O_3), larger sample sizes could be obtained and studied. Of course if this were done, we would lose information about the effect that the LSM-YSZ material system has on the freeze-casting morphology. So, until higher power beamlines come online, using 2D-SEM images or large scale (low resolution) 3D-FIB images could be used to represent large sample volumes. Combined with DEM, simulations could be run for mechanical properties, electrochemical behavior as well as gas flow simulations and sintering experiments.

More broadly, the metrology within the field of porous ceramic characterization, and in particular as applied to the freeze-casting technique, must be addressed. Ideally when studying the properties of a material with a morphology altered from the standard, one wants to compare their results with similar materials found in literature. This was problematic for us however. As cited previously, researchers have discussed the detrimental lack of established characterization methods for porous ceramics [17]. This lack in established methodologies makes objective comparisons difficult to perform. With 4+ years of experience I can now say with confidence that this is in fact a serious handicap for researchers studying porous materials. Methods for describing microstructural features are often ill-defined and vary from paper to paper. Within the field of freeze-casting, researchers often utilize terminology such as: lamellar, columnar, dendritic or prismatic to describe subtly different morphologies. The methods used by researchers to calculate feature size (λ for example) are often vague. Until more standardized methods are introduced for quantitatively comparing one porous structure to another we are often comparing apples to oranges without even realizing it.

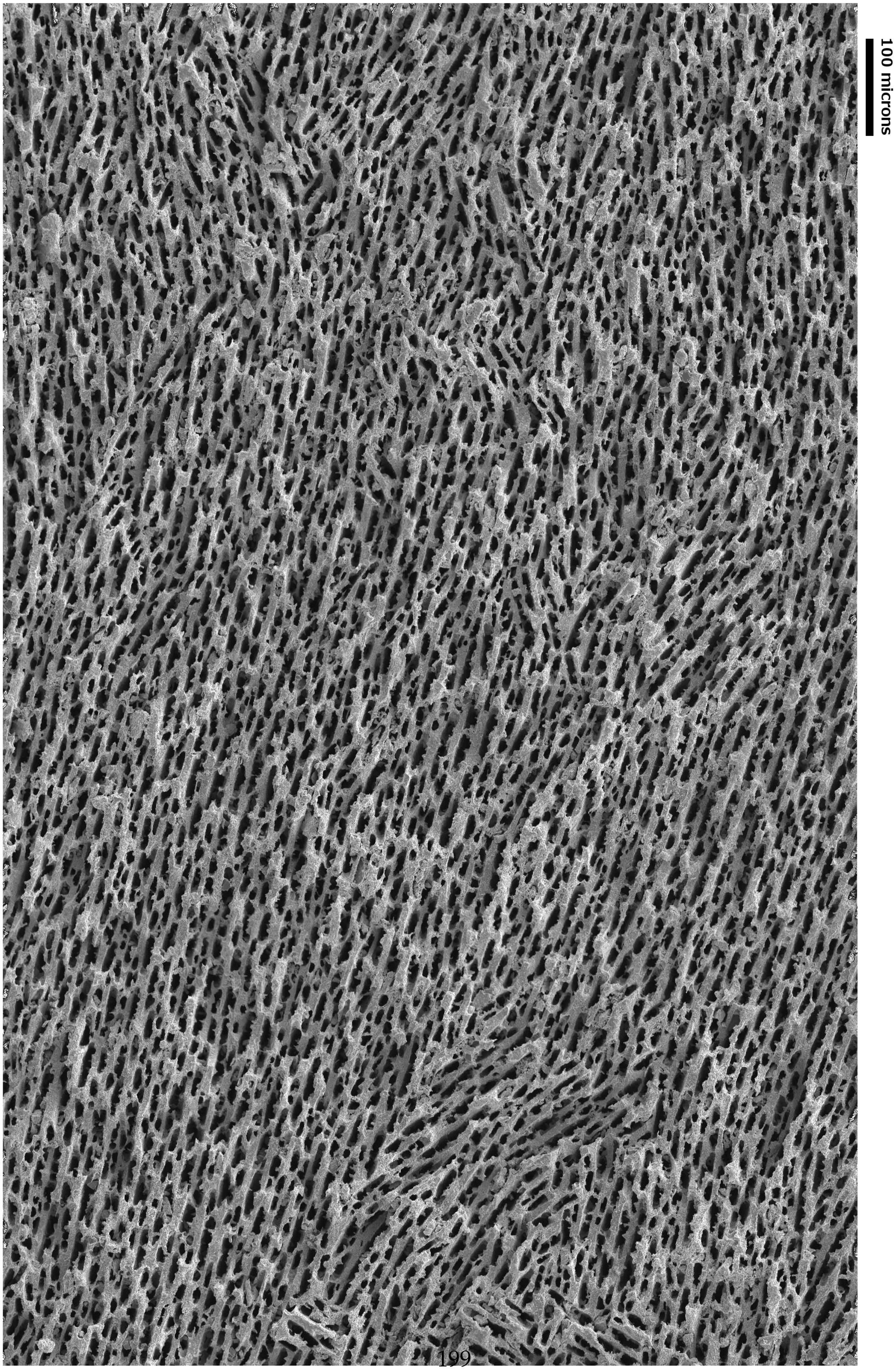
100 microns

References

[1] Sylvain Deville. Freeze-Casting of Porous Ceramics: A Review of Current Achievements and Issues. *Advanced Engineering Materials*, 10(3):155–169, March 2008.

[2] John M. Vohs and Raymond J. Gorte. High-Performance SOFC Cathodes Prepared by Infiltration. *Advanced Materials*, 21(9):943–956, March 2009.

[3] Sossina M Haile. Fuel cell materials and components: The Golden Jubilee Issue–Selected topics in Materials Science and Engineering: Past, Present and Future. *Acta Materialia*, 51(19):5981–6000, November 2003.

[4] F Tiezt, H.P. Buchkremer, and D Stoever. 10 years of materials research for solid oxide fuel cells at Forschungzentrum , Juelich.

[5] K. K. Phani and S. K. Niyogi. Young's modulus of porous brittle solids. *Journal of Materials Science*, 22:257–263, 1987.

[6] Brian D Flinn, Rajendra K Bordia, André Zimmerman, and Jurgen Rodel. Evolution of defect size and strength of porous alumina during sintering. *Journal of the European Ceramic Society*, 20:2561–2568, 2000.

[7] Fred F Lange. Densification of powder compacts: an unfinished story. *Journal of the European Ceramic Society*, 28:1509–1516, 2008.

[8] Yu Chen, Jacob Bunch, Tingshuai Li, Zhengping Mao, and Fanglin Chen. Novel functionally graded acicular electrode for solid oxide cells fabricated by the freeze-tape-casting process. *Journal of Power Sources*, 213:93–99, September 2012.

[9] Sylvain Deville, Eduardo Saiz, and Antoni P Tomsia. Freeze casting of hydroxyapatite scaffolds for bone tissue engineering. *Biomaterials*, 27(32):5480–9, November 2006.

[10] U. G. K. Wegst and M. F. Ashby. The mechanical efficiency of natural materials. *Philosophical Magazine*, 84(21):2167–2186, July 2004.

[11] Franziska Krauss Juillerat, Urs T. Gonzenbach, Pierre Elser, André R. Studart, and Ludwig J. Gauckler. Microstructural Control of Self-Setting Particle-Stabilized Ceramic Foams. *Journal of the American Ceramic Society*, 94(1):77–83, January 2011.

[12] S Singhal. Advances in solid oxide fuel cell technology. *Solid State Ionics*, 135(1-4): 305–313, November 2000.

[13] R. Mark Ormerod. Solid oxide fuel cells. *Chemical Society Reviews*, 32(1):17–28, December 2003.

[14] Frank Tietz, Andreas Mai, and Detlev Stöver. From powder properties to fuel cell performance – A holistic approach for SOFC cathode development. *Solid State Ionics*, 179(27-32):1509–1515, September 2008.

[15] Andre R. Studart, Urs T. Gonzenbach, Elena Tervoort, and Ludwig J. Gauckler. Processing Routes to Macroporous Ceramics: A Review. *Journal of the American Ceramic Society*, 89(6):1771–1789, June 2006.

[16] Paolo Colombo, Cekdar Vakifahmetoglu, and Stefano Costacurta. Fabrication of ceramic components with hierarchical porosity. *Journal of Materials Science*, 45(20): 5425–5455, June 2010.

[17] Roy Rice. *Porosity of Ceramics*. 1998.

[18] Rajendra K. Bordia. Competing Requirements for Electrochemical Performance, Mechanical Properties and Thermomechanical Stability in Porous Ceramics for Electrochemical Applications. In *Gordon Research Conference: Solid State Studies in Ceramics*, Mount Holyoke, MA, 2012.

[19] André Zimmerman, Mark Hoffman, Brian D Flinn, Rajendra K Bordia, Tze-jer Chuang, Edwin R Fuller Jr, and Jurgen Rodel. Fracture of Alumina with Controlled Pores. *Journal of the American Ceramic Society*, 57:2449–2457, 1998.

[20] Xigeng Miao and Dan Sun. Graded/Gradient Porous Biomaterials. *Materials*, 3(1): 26–47, December 2009.

[21] R W Rice. Evaluation and extension of physical property-porosity models based on minimum solid area. *Journal of Materials Science*, 31:102–118, 1996.

[22] K U O Kelly, A J Carr, and B A O Mccormack. Minimum solid area models applied to the prediction of Young' s modulus for cancellous bone. *Journal of Materials Science: Materials in Medicine*, 4:379–384, 2003.

[23] C T Herakovich and S C Baxter. Influence of pore geometry on the effective response of porous media. *Journal of Materials Science*, 4:1595–1609, 1999.

[24] Li-Hong He, Owen C Standard, Tiffany T Y Huang, Bruno a Latella, and Michael V Swain. Mechanical behaviour of porous hydroxyapatite. *Acta biomaterialia*, 4(3):577–86, May 2008.

[25] Candace K Chan, Hailin Peng, Gao Liu, Kevin McIlwrath, Xiao Feng Zhang, Robert A Huggins, and Yi Cui. High-performance lithium battery anodes using silicon nanowires. *Nature Immunology*, 3(1):31–35, 2008.

[26] Xiaoxing Liu, Christophe L. Martin, Gérard Delette, and Didier Bouvard. Elasticity and strength of partially sintered ceramics. *J. Mech. Phys. Solids*, 58(6):829–842, June 2010.

[27] Roy W Rice. *Porosity of Ceramics*. 1998.

[28] Roy W Rice and W R Grace Co. Evaluating Porosity Parameters for Porosity-Property Relations. *Journal of the American Ceramic Society*, 76:1801–1808, 1993.

[29] Rajendra K Bordia. NSF Materials World Network Proposal (Bordia) Project Summary. Technical report.

[30] Lifesaver: About Us, 2014. URL `http://www.lifesaversystems.com/about-us`.

[31] Peter Donachie and John Krahn. Report on Microbiological Tests Carried out for Lifesaver Systems. Technical report, 2007.

[32] Russ Jamison. Money-and-pain saving artificial bone implant created. Technical report, 2003. URL `https://itg.beckman.illinois.edu/technology_development/mandible_reconstruction/downloads/mandible-release-screen.pdf`.

[33] Damond Benningfield. Shuttle Tiles: Why the space shuttle can withstand reentry temperatures up to 2,300 degrees. *Air and Space Magazine*, May 2006. URL `http://www.airspacemag.com/how-things-work/shuttle-tiles-12580671/`.

[34] Aerogel.org. What is Aerogel?, 2012. URL `http://www.aerogel.org/`.

[35] Smithsonian. Fuel Cell Origins, 2004. URL `http://americanhistory.si.edu/fuelcells/origins/origins.htm`.

[36] Helge Kragh. *Confusion and Controversy : Nineteenth-Century Theories of the Voltaic Pile*. 1999.

[37] Marvin Warshay and Paul R Prokopius. The Fuel Cell in Space : Today, Tomorrow and Yesterday. *Journal of Power Sources*, 29:193–200, 1990.

[38] T Alleau. La pile SOFC (Solid Oxide Fuel Cell). *Association Francaise de l'Hydrogene*, pages 1–9, 2004. URL `http://www.afh2.org/uploads/memento/pdf/fiche_5_2_6.pdf`.

[39] Business Wire. Siemens Westinghouse's 100 kW SOFC System Passes 12,000 Hours. *EV World.com*, 2001.

[40] Fuel Cell Today. The Fuel Cell Industry Review 2013. *FuelCellToday*, 2013.

[41] L. C. R Schneider, C. L. Martin, Y. Bultel, D. Bouvard, E. Seibert, and E Siebert. Discrete modelling of the electrochemical performance of SOFC electrodes. *Electrochimica Acta*, 52(1):314–324, October 2006.

[42] Juan Carlos Ruiz-Morales, David Marrero-López, Juan Peña Martínez, Jesús Canales-Vázquez, Joan Josep Roa, Mercè Segarra, Stanislav N. Savvin, and Pedro Núñez. Performance of a novel type of electrolyte-supported solid oxide fuel cell with honeycomb structure. *Journal of Power Sources*, 195(2):516–521, January 2010.

[43] Eric S. Greene, Wilson K.S. Chiu, and Maria G. Medeiros. Mass transfer in graded microstructure solid oxide fuel cell electrodes. *Journal of Power Sources*, 161(1):225–231, October 2006.

[44] David L. Douglas and Herman a. Liebhafsky. FUEL CELLS: History, Operation, and Applications. *Physics Today*, 13(6):26, 1960.

[45] W.C Grove. On a Gaseous Voltaic Battery. *Journal of the Franklin Institute*, 35(4): 277–280, 1843.

[46] Svein Sunde. Monte Carlo Simulations of Polarization Resistance of Composite Electrodes for Solid Oxide Fuel Cells. *Journal of Electrochemical Society*, 143:1930–1939, 1996.

[47] Y. L. Liu, A Hagen, R Barfod, M Chen, H. J. Wang, F. W. Poulsen, and P. V. Hendriksen. Microstructural studies on degradation of interfaces beteen LSM-YSZ cathodes and YSZ electrolyte in SOFCs. *Solid State Ionics*, 180:1298–1304, 2009.

[48] S.P.S. Badwal. Zirconia-based solid electrolytes : microstructure , stability and ionic conductivity. *Solid State Ionics*, 52:23–32, 1992.

[49] Ho-Chieh Yu and Kuan-Zong Fung. Electrode properties of La(1-x)Sr(x)CuO(2.5-d) as new cathode materials for intermediate temperature SOFCs. *Electrochemical Society Proceedings*, 2003-07:591–596, 2003.

[50] H Yokokawa, H Tu, T Iwanschitz, and A Mai. Fundamental mechanisms limiting solid oxide fuel cell durability. *Journal of Power Sources*, 182:400–412, 2009.

[51] J. Molenda, K. Swierczek, and W. Zajac. Functional materials for the IT-SOFC. *Journal of Power Sources*, 173(2):657–670, November 2007.

[52] Antonin Faes, Aïcha Hessler-Wyser, Amédée Zryd, and Jan Van herle. A Review of RedOx Cycling of Solid Oxide Fuel Cells Anode. *Membranes*, 2(4):585–664, August 2012.

[53] B.C.H. Steele and A Heinzel. Materials for fuel-cell technologies. *Nature*, 414:345–352, 2001.

[54] M Cassidy, G Lindsay, and K Kendall. The reduction of nickel-zirconia cermet anodes and the effects on supported thin electrolytes. *Journal of Power Sources*, 61:189–192, 1996.

[55] N.M. Tikekar, T.J. Armstrong, and A.V. Virkar. Reduction and reoxidation kinetics of nickel-based SOFC anodes. *Journal of The Electrochemical Society*, 153:654–663, 2006.

[56] H Davarzani, M Marcoux, P Costeseque, and M Quintard. Experimental measurement of the effective diffusion and thermodiffusion coefficients for binary gas mixture in porous media. *Chemical Engineering Science*, 65(5092-5104), 2010.

[57] M. Ettler, H. Timmermann, J. Malzbender, A. Weber, and N.H. Menzler. Durability of Ni anodes during reoxidation cycles. *Journal of Power Sources*, 195(17):5452–5467, September 2010.

[58] D Rotureau. *Developpement de piles a combustible de type SOFC, conventionnelles et mono-chambres, en technologie planaire par serigraphie*. PhD thesis, Ecole Nationale Superieure des Mines de Saint-Etienne, 2005.

[59] Stephen W. Sofie. Fabrication of Functionally Graded and Aligned Porosity in Thin Ceramic Substrates With the Novel Freeze-Tape-Casting Process. *Journal of the American Ceramic Society*, 90(7):2024–2031, July 2007.

[60] Carolina Tallon and George V. Franks. Recent trends in shape forming from colloidal processing: A review. *Journal of the Ceramic Society of Japan*, 119(1387):147–160, 2011.

[61] F. Snijkers, A. de Wilde, S. Nullens, and J. Luyten. Aqueous tape casting of yttria stabilised zirconia using natural product binder. *Journal of the European Ceramic Society*, 24:1107–1110, 2004.

[62] Hirofumi Sumi, Toshiaki Yamaguchi, Koichi Hamamoto, Toshio Suzuki, and Yoshinobu Fujishiro. Effects of Anode Microstructure on Mechanical and Electrochemical Properties for Anode-Supported Microtubular Solid Oxide Fuel Cells. *Journal of the American Ceramic Society*, 96(11):3584–3588, 2013.

[63] Paul Gannon, Stephen Sofie, Max Deibert, Richard Smith, and Vladimir Gorokhovsky. Thin film YSZ coatings on functionally graded freeze cast NiO/YSZ SOFC anode supports. *Journal of Applied Electrochemistry*, 39(4):497–502, November 2008.

[64] J. C. Ruiz-Morales, D. Marrero-López, J. Canales-Vázquez, P. Núñez, and J. M. Domínguez-González. A Novel Approach to Engineer the Microstructure of Solid Oxide Fuel Cell materials. *Fuel Cells*, 11(1):144–149, February 2011.

[65] Thomas L Cable and Stephen W Sofie. A Symmetrical, Planar SOFC Design for NASA's High Specific Power Density Requirements. *Journal of Power Sources*, 174: 221–227, 2007.

[66] Ji-woong Moon, Hae-jin Hwang, Masanobu Awano, and Kunihiro Maeda. Preparation of NiO – YSZ tubular support with radially aligned pore channels. *Materials Letters*, 57:1428–1434, 2003.

[67] Keegan C. Wincewicz and Joyce S Cooper. Taxonomies of SOFC material and manufacturing alternatives. *Journal of Power Sources*, 140(2):280–296, February 2005.

[68] Anh T. Duong and Daniel R. Mumm. Microstructural Optimization by Tailoring Particle Sizes for LSM-YSZ Solid Oxide Fuel Cell Composite Cathodes. *Journal of the Electrochemical Society*, 159(1):B40–B53, 2012.

[69] Audrey Yoke Yee Ho, Lip Pin Yeo, Yee Cheong Lam, and Isabel Rodríguez. Fabrication and analysis of gecko-inspired hierarchical polymer nanosetae. *ACS nano*, 5(3): 1897–906, March 2011.

[70] Mark McGrouther. Thresher Shark, Alopias Vulpinus (Bonnaterre, 1788). *Austrailian Museum*, 2012. URL `http://australianmuseum.net.au/Thresher-Shark-Alopias-vulpinus-Bonnaterre-1788/`.

[71] Biomimicry Database and Matthijs. biomimicry - finding design inspiration in nature, 2010. URL `http://www.designboom.com/contemporary/biomimicry.html`.

[72] Florian Bouville, Eric Maire, and Sylvain Deville. Lightweight and stiff cellular ceramic structures by ice templating. *Journal of Materials Research*, 29(02):175–181, January 2014.

[73] Nathan Seppa. Highlights from annual meeting of infectious disease specialists. *Science News*, October 2013.

[74] Kiyoshi Araki and John W. Halloran. Porous Ceramic Bodies with Interconnected Pore Channels by a Novel Freeze Casting Technique. *Journal of the American Ceramic Society*, 88(5):1108–1114, May 2005.

[75] Kajal K Mallick, James Winnett, William van Grunsven, James Lapworth, and Gwendolen C Reilly. Three-dimensional porous bioscaffolds for bone tissue regeneration: fabrication via adaptive foam reticulation and freeze casting techniques, characterization, and cell study. *Journal of biomedical materials research. Part A*, 100(11):2948–59, November 2012.

[76] Ulrike G K Wegst, Matthew Schecter, Amalie E Donius, and Philipp M Hunger. Biomaterials by freeze casting. *Philosophical transactions. Series A, Mathematical, physical, and engineering sciences*, 368(1917):2099–121, April 2010.

[77] Weijiang Xue, Yong Huang, Zhipeng Xie, and Wei Liu. Al2O3 ceramics with well-oriented and hexagonally ordered pores: The formation of microstructures and the control of properties. *Journal of the European Ceramic Society*, 32:3151–3159, 2012.

[78] Serena A. Corr, Daniel P. Shoemaker, Eric S. Toberer, and Ram Seshadri. Spontaneously formed porous and composite materials. *Journal of Materials Chemistry*, 20 (8):1413–1422, 2010.

[79] Glenna L. Drisko, Andres Zelcer, Vittorio Luca, Rachel a. Caruso, and Galo J. De a. a. Soler-Illia. One-Pot Synthesis of Hierarchically Structured Ceramic Monoliths with Adjustable Porosity. *Chemistry of Materials*, 22(15):4379–4385, August 2010.

[80] Susmita Bose, Sahar Vahabzadeh, and Amit Bandyopadhyay. Bone tissue engineering using 3D printing. *Materials Today*, 16(12):496–504, December 2013.

[81] Mamoru Mizutani, Haruyuki Takase, Nobuyasu Adachi, Toshitaka Ota, Keiji Daimon, and Yasuo Hikichi. Porous ceramics prepared by mimicking silicified wood. *Science and Technology of Advanced Materials*, 6(1):76–83, January 2005.

[82] Sylvain Deville, Eduardo Saiz, Ravi K Nalla, and Antoni P Tomsia. Freezing as a path to build complex composites. *Science (New York, N.Y.)*, 311(5760):515–8, January 2006.

[83] Thomas Waschkies, Rainer Oberacker, and Michael J. Hoffmann. Control of Lamellae Spacing During Freeze Casting of Ceramics Using Double-Side Cooling as a Novel Processing Route. *Journal of the American Ceramic Society*, 92:S79–S84, January 2009.

[84] Sylvain Deville, Eric Maire, Audrey Lasalle, Agnès Bogner, Catherine Gauthier, Jérôme Leloup, and Christian Guizard. In Situ X-Ray Radiography and Tomography Observations of the Solidification of Aqueous Alumina Particle Suspensions-Part I: Initial Instants. *Journal of the American Ceramic Society*, 92(11):2489–2496, November 2009.

[85] M. Bettge, H. Niculescu, and P.J. Gielisse. Engineered porous ceramics using a directional freeze-drying process. *28th International Spring Seminar on Electronics Technology: Meeting the Challenges of Electronics Technology Progress*, pages 28–34, 2005.

[86] Sylvain Deville, Eduardo Saiz, and Antoni P. Tomsia. Ice-templated porous alumina structures. *Acta Materialia*, 55(6):1965–1974, April 2007.

[87] S. S. L. Peppin, J. a. W. Elliott, M. Grae Worster, Theoretical Physics, and Wilberforce Road. Solidification of colloidal suspensions. *Journal of Fluid Mechanics*, 554(-1):147–166, April 2006.

[88] A Lottermoser. Uber das Ausfrieren von Hydrosolen. Berichte der deutschen chemischen. *Gesellschaft*, 41:3976–3979, 1908.

[89] W.A. Maxwell, R.S. Gurnick, and A.C. Francisco. Preliminary Investigation of the "Freeze-Casting" Method for Forming Refractory Powders. *National Advisory Committee for Aeronautics*, pages 1–19, 1954.

[90] Takayuki Fukasawa, Motohide Ando, Tatsuki Ohji, and Shuzo Kanzaki. Synthesis of Porous Ceramics with Complex Pore Structure by Freeze-Dry Processing. *Journal of the American Ceramic Society*, 32(1):230–232, 2001.

[91] Sylvain Deville. Ice templating, freeze casting: Beyond materials processing. *Journal of Materials Research*, 28(17):2202–2219, May 2013.

[92] Jin-Woong Kim, Kohei Tazumi, Rika Okaji, and Masahiro Ohshima. Honeycomb Monolith-Structured Silica with Highly Ordered, Three-Dimensionally Interconnected Macroporous Walls. *Chemistry of Materials*, 21(15):3476–3478, 2009.

[93] G Wilde and J.H. Perepezko. Experimental study of particle incorporation during dendritic solidification. *Materials Science and Engineering: A*, 283(1-2):25–37, 2000.

[94] C Miller, D Lath, T Wang, and R Noort. Freeze Casting of High Strenght Composites for Dental Applications. In *Pan European Federation of the International Association for Dental Research*, 2008.

[95] Phuong T.N. Nguyen and Joachim Ulrich. Fast Dispersible Cocoa Tablets: A Case Study of Freeze-Casting Applied to Foods. *Chemical Engineering and Technology*, 37 (8):1376–1382, 2014.

[96] Valentina Naglieri, Hrishikesh a. Bale, Bernd Gludovatz, Antoni P. Tomsia, and Robert O. Ritchie. On the development of ice-templated silicon carbide scaffolds for nature-inspired structural materials. *Acta Materialia*, 61(18):6948–6957, October 2013.

[97] T. Waschkies, R. Oberacker, and M.J. Hoffmann. Investigation of structure formation during freeze-casting from very slow to very fast solidification velocities. *Acta Materialia*, 59(13):5135–5145, August 2011.

[98] Stephen S.L. Peppin, M. Grae Worster, and J.S. Wettlaufer. Morphological instability in freezing colloidal suspensions. *Proceedings of the Royal Society A: Mathematical, Physical and Engineering Sciences*, 463(2079):723–733, March 2007.

[99] S. Peppin, J. Wettlaufer, and M. Worster. Experimental Verification of Morphological Instability in Freezing Aqueous Colloidal Suspensions. *Physical Review Letters*, 100 (23):1–4, June 2008.

[100] Sylvain Deville, Eric Maire, Audrey Lasalle, Agnès Bogner, Catherine Gauthier, Jérôme Leloup, and Christian Guizard. In Situ X-Ray Radiography and Tomography Observations of the Solidification of Aqueous Alumina Particles Suspensions. Part II: Steady State. *Journal of the American Ceramic Society*, 92(11):2497–2503, November 2009.

[101] Sylvain Deville, Eric Maire, Guillaume Bernard-Granger, Audrey Lasalle, Agnès Bogner, Catherine Gauthier, Jérôme Leloup, and Christian Guizard. Metastable and unstable cellular solidification of colloidal suspensions. *Nature materials*, 8(12):966–72, December 2009.

[102] Andrea Bareggi, Eric Maire, Audrey Lasalle, and Sylvain Deville. Dynamics of the Freezing Front During the Solidification of a Colloidal Alumina Aqueous Suspension: In Situ X-Ray Radiography, Tomography, and Modeling. *Journal of the American Ceramic Society*, 94(10):3570–3578, October 2011.

[103] Young-Mi Soon, Kwan-Ha Shin, Young-Hag Koh, Jong-Hoon Lee, and Hyoun-Ee Kim. Compressive strength and processing of camphene-based freeze cast calcium phosphate scaffolds with aligned pores. *Materials Letters*, 63(17):1548–1550, July 2009.

[104] J Raymond, P Wilson, and L DeVries. Inhibition of growth of nonbasal planes in ice by fish antifreezes. *Proceedings of the National Academy of Sciences of the United States of America*, 86(3):881–5, March 1989.

[105] Audrey Lasalle, Christian Guizard, Jérôme Leloup, Sylvain Deville, Eric Maire, Agnès Bogner, Catherine Gauthier, Jérôme Adrien, and Loïc Courtois. Ice-Templating of Alumina Suspensions: Effect of Supercooling and Crystal Growth During the Initial Freezing Regime. *Journal of the American Ceramic Society*, 95(2):799–804, February 2012.

[106] Glenna L. Drisko, Andres Zelcer, Rachel A Caruso, and Galo Soler-Illia. One-pot synthesis of silica monoliths with hierarchically porous structure. *Microporous and Mesoporous Materials*, 148(1):137–144, January 2012.

[107] a. Sanson, P. Pinasco, and E. Roncari. Influence of pore formers on slurry composition and microstructure of tape cast supporting anodes for SOFCs. *Journal of the European Ceramic Society*, 28(6):1221–1226, January 2008.

[108] Ahmed a Eljaouhari, Rainer Müller, Matthias Kellermeier, Klaus Heckmann, and Werner Kunz. New anisotropic ceramic membranes from chemically fixed dissipative structures. *Langmuir : the ACS journal of surfaces and colloids*, 22(26):11353–9, December 2006.

[109] Sylvain Deville, Eric Maire, Audrey Lasalle, Agnes Bogner, Catherine Gauthier, Jérôme Leloup, and Christian Guizard. Influence of Particle Size on Ice Nucleation and Growth During the Ice-Templating Process. *Journal of the American Ceramic Society*, 93(9):2507–2510, April 2010.

[110] Jiecai Han, Changqing Hong, Xinghong Zhang, Jiancong Du, and Wei Zhang. Highly porous ZrO2 ceramics fabricated by a camphene-based freeze-casting route: Microstructure and properties. *Journal of the European Ceramic Society*, 30(1):53–60, January 2010.

[111] Etienne Munch, Eduardo Saiz, Antoni P. Tomsia, Sylvain Deville, and Munch. Architectural Control of Freeze-Cast Ceramics Through Additives and Templating. *Journal of the American Ceramic Society*, 92(7):1534–1539, July 2009.

[112] Yumin Zhang, Luyang Hu, and Jiecai Han. Preparation of a Dense/Porous BiLayered Ceramic by Applying an Electric Field During Freeze Casting. *Journal of the American Ceramic Society*, 92(8):1874–1876, August 2009.

[113] Sylvain Deville and Guillaume Bernard-Granger. Influence of surface tension, osmotic pressure and pores morphology on the densification of ice-templated ceramics. *Journal of the European Ceramic Society*, 31(6):983–987, June 2011.

[114] Yumin Zhang, Luyang Hu, Jiecai Han, and Zehui Jiang. Freeze casting of aqueous alumina slurries with glycerol for porous ceramics. *Ceramics International*, 36(2):617–621, March 2010.

[115] S. Farhangdoust, A. Zamanian, M. Yasaei, and M. Khorami. The effect of processing parameters and solid concentration on the mechanical and microstructural properties of freeze-casted macroporous hydroxyapatite scaffolds. *Materials Science and Engineering: C*, 33(1):453–460, January 2013.

[116] Annemarie Preiss, Bo Su, Simon Collins, and David Simpson. Tailored graded pore structure in zirconia toughened alumina ceramics using double-side cooling freeze casting. *Journal of the European Ceramic Society*, 32:1575–1583, January 2012.

[117] Sylvain Deville, Céline Viazzi, and Christian Guizard. Ice-structuring mechanism for zirconium acetate. *Langmuir : the ACS journal of surfaces and colloids*, 28(42):14892–8, October 2012.

[118] S. Deville, J. Adrien, E. Maire, M. Scheel, and M. Di Michiel. Time-lapse, three-dimensional in situ imaging of ice crystal growth in a colloidal silica suspension. *Acta Materialia*, 61(6):2077–2086, April 2013.

[119] Melissa Spannuth, S. G. J. Mochrie, S. S. L. Peppin, and J. S. Wettlaufer. Particle-scale structure in frozen colloidal suspensions from small-angle x-ray scattering. *Physical Review E*, 83(2):021402, February 2011.

[120] Audrey Lasalle, Christian Guizard, Eric Maire, and Sylvain Deville. Particles redistribution and structural defects development during ice templating. *Acta Materialia*, 2012.

[121] Amalie E. Donius, Andong Liu, Lars a. Berglund, and Ulrike G.K. Wegst. Superior Mechanical Performance of Highly Porous, Anisotropic Nanocellulose-Montmorillonite Aerogels Prepared by Freeze Casting. *Journal of the Mechanical Behavior of Biomedical Materials*, May 2014.

[122] Yasumasa Chino and David C. Dunand. Directionally freeze-cast titanium foam with aligned, elongated pores. *Acta Materialia*, 56(1):105–113, January 2008.

[123] Y.F. Tang, K. Zhao, J.Q. Wei, and Y.S. Qin. Fabrication of aligned lamellar porous alumina using directional solidification of aqueous slurries with an applied electrostatic field. *Journal of the European Ceramic Society*, 30(9):1963–1965, July 2010.

[124] Ping Wei, Stephen Sofie, Qi Zhang, and Anthony Petric. Metal Supported Solid Oxide Fuel Cell by Freeze Tape Casting. 35(1):379–383, 2011.

[125] David Jauffrès, Christophe L Martin, Aaron Lichtner, and Rajendra K Bordia. Simulation of the elastic properties of porous ceramics with realistic microstructure. *Modelling and Simulation in Materials Science and Engineering*, 20(4):045009, June 2012.

[126] Yuncheng Liang, Nidal Hilal, Paul Langston, and Victor Starov. Interaction forces between colloidal particles in liquid: theory and experiment. *Advances in colloid and interface science*, 134-135:151–66, October 2007.

[127] Malvern Instrumentation. Zeta Potential An Introduction in 30 Minutes. *Zetasizer Nanoseries Technical Note*, 2:1–6. URL `malvern.co.uk`.

[128] D.H. Napper. *Polymeric Stabilization of Colloidal Dispersions*. Academic Press, New York, 1983.

[129] James R. Wilson, J. Scott Cronin, Anh T. Duong, Sherri Rukes, Hsun-Yi Chen, Katsuyo Thornton, Daniel R. Mumm, and Scott Barnett. Effect of composition of (La0.8Sr0.2MnO3–Y2O3-stabilized ZrO2) cathodes: Correlating three-dimensional microstructure and polarization resistance. *Journal of Power Sources*, 195(7):1829–1840, April 2010.

[130] N. Vivet, S. Chupin, E. Estrade, A. Richard, S. Bonnamy, D. Rochais, and E. Bruneton. Effect of Ni content in SOFC Ni-YSZ cermets: A three-dimensional study by FIB-SEM tomography. *Journal of Power Sources*, 196(23):9989–9997, December 2011.

[131] Philipp M Hunger, Amalie E Donius, and Ulrike G K Wegst. Structure-property-processing correlations in freeze-cast composite scaffolds. *Acta biomaterialia*, 9(5): 6338–48, May 2013.

[132] S. Meille, M. Lombardi, J. Chevalier, and L. Montanaro. Mechanical properties of porous ceramics in compression: On the transition between elastic, brittle, and cellular behavior. *Journal of the European Ceramic Society*, 32(15):3959–3967, November 2012.

[133] J. A. Choren, S. M. Heinrich, and M. B. Silver-Thorn. Young's modulus and volume porosity relationships for additive manufacturing applications. *Journal of Materials Science*, 48(15):5103–5112, April 2013.

[134] J.M. Dewey. The elastic constants of materials loaded with non-rigid fillers. *Journal of Applied Physics*, 18:578–581, 1947.

[135] F. Pecqueux, F. Tancret, N. Payraudeau, and J.M. Bouler. Influence of microporosity and macroporosity on the mechanical properties of biphasic calcium phosphate bioceramics: Modelling and experiment. *Journal of the European Ceramic Society*, 30(4): 819–829, March 2010.

[136] L. J. Gibson and M. F. Ashby. *Cellular Solid Structure and Properties*. Cambridge University Press., 1997.

[137] R Ryshkewitch. Compression strength of porous sintered alumina and zirconia. *Journal of the American Ceramic Society*, 36(2):65–68, 1953.

[138] W Duckworth. Discussion of Ryshkewitch Paper. *Journal of the American Ceramic Society*, 36(2):68, 1953.

[139] F.P Knudsen. Dependence of mechanical strength of brittle polycrystalline specimens on porosity and grain size. *Journal of the American Ceramic Society*, 42(8):376–387, 1959.

[140] R.M Spriggs. Expression for the effect of porosity on elastic modulus of polycrystalline refractory materials, particularly aluminum oxide. *Journal of the American Ceramic Society*, 44(12):628–629, 1961.

[141] A. S Wagh, R. B Poeppel, and J. P Singh. Open pore description of mechanical properties of ceramics. *Journal of Materials Science*, 26:3862–3868, 1991.

[142] J.P Jernot, M Coster, and J.L Chermant. Model to describe the elastic modulus of sintered materials. *Physica Status Solidi*, 72, 1982.

[143] E Munch, M E Launey, D H Alsem, E Saiz, a P Tomsia, and R O Ritchie. Tough, bio-inspired hybrid materials. *Science (New York, N.Y.)*, 322(5907):1516–20, December 2008. ISSN 1095-9203. doi: 10.1126/science.1164865. URL `http://www.ncbi.nlm.nih.gov/pubmed/19056979`.

[144] Kyle N. Grew, Aldo a. Peracchio, Abhijit S. Joshi, John R. Izzo Jr., and Wilson K.S. Chiu. Characterization and analysis methods for the examination of the heterogeneous solid oxide fuel cell electrode microstructure. Part 1: Volumetric measurements of the heterogeneous structure. *Journal of Power Sources*, 195(24):7930–7942, December 2010.

[145] Geodict. Study of the percolation of LSM Evaluation of LSM size distribution fitting by log-normal law. pages 1–4.

[146] Christophe L. Martin, Didier Bouvard, and Gérard Delette. Discrete Element Simulations of the Compaction of Aggregated Ceramic Powders. *Journal of the American Ceramic Society*, 89(11):3379–3387, November 2006.

[147] Xiaoxing Liu, Christophe L. Martin, Gérard Delette, Jérome Laurencin, Didier Bouvard, and Thibaud Delahaye. Microstructure of porous composite electrodes generated by the discrete element method. *Journal of Power Sources*, 196(4):2046–2054, February 2011.

[148] Xiaoxing Liu, Christrophe L. Martin, Didier Bouvard, Stéphane Di Iorio, Jérome Laurencin, and Gérard Delette. Strength of Highly Porous Ceramic Electrodes. *Journal of the American Ceramic Society*, 94(10):3500–3508, October 2011.

[149] Aaron Z. Lichtner, David Jauffrès, Christophe L. Martin, and Rajendra K. Bordia. Processing of Hierarchical and Anisotropic Porosity LSM-YSZ Composites. *Journal of the American Ceramic Society*, 96:2745–2753, July 2013.

[150] D Bouvard and Robert M Mcmeeking. Deformation of Interparticle Necks by Diffusion-Controlled Creep. *Journal of the American Ceramic Society*, 79(3):666–672, 1996.

[151] F. Parhami and R.M. McMeeking. A network model for initial stage sintering. *Mechanics of Materials*, 27(2):111–124, February 1998.

[152] R.L Coble. Initial sintering of alumina and hematite. *Journal of the American Ceramic Society*, 41:55, 1958.

[153] Jerzy Rojek, Katarzyna Pietrzak, and Marcin Chmielewski. Discrete element simulation of powder sintering. *Computer Methods in Materials Science*, 11(1):68–73, 2011.

[154] George Jefferson, George K Haritos, and Robert M Mcmeeking. The elastic response of a cohesive aggregate – a discrete element model with coupled particle interaction. *Journal of the Mechanics and Physics of Solids*, 50:2539–2575, 2002.

[155] K Walton. The effective elastic moduli of a random packing of spheres. *Journal of Mechanical Physical Solids*, 35(2):213–226, 1987.

[156] A.N. Norris and D.L Johnson. Nonlinear elasticity of granular media. *Journal of Applied Mechanics*, 64(1):39–49, 1997.

[157] A Misra and C.S. Chang. Effective elastic moduli of heterogeneous granular solids. *International Journal of Solid Structures*, 30(18):2547–2566, 1993.

[158] David Jauffrès, Christophe L. Martin, Aaron Lichtner, and Rajendra K. Bordia. Simulation of the toughness of partially sintered ceramics with realistic microstructures. *Acta Materialia*, 60(12):4685–4694, July 2012.

[159] B Kenney and K Karan. Engineering of microstructure and design of a planar porous composite SOFC cathode: A numerical analysis. *Solid State Ionics*, 178(3-4):297–306, February 2007.

[160] Ali Abbaspour, Jing-li Luo, and K Nandakumar. Electrochimica Acta Three-dimensional random resistor-network model for solid oxide fuel cell composite electrodes. *Electrochimica Acta*, 55(12):3944–3950, 2010.

[161] Nicolas Bailly, Samuel Georges, and Elisabeth Djurado. Elaboration and electrical characterization of electrosprayed YSZ thin films for intermediate temperature-solid oxide fuel cells (IT-SOFC). *Solid State Ionics*, 222-223:1–7, August 2012.

[162] K Kleveland, M.-A Einarsud, C. S Schmidt, S Shamsili, S Faaland, K Wiik, and T Grande. Reactions between strontium-substituted lanthanum manganite and yttria-stabilized zirconia: Part II, diffusion couples. *Journal of the American Ceramic Society*, 82(3):729–734, 1999.

[163] N Li, M. K. Mahapatra, and P Singh. Sintering of porous strontium doped lanthanum manganite-yttria stabilized zirconia composite in controlled oxygen atmosphere at 1400 C. *Journal of Power Sources*, 221:57–63, 2013.

[164] V. Boulos, V. Fristot, D. Houzet, L. Salvo, and P. Lhuissier. Investigating performance variations of an optimized gpu-ported granulometry algorithm. In *Design and Architectures for Signal Processing (DASIP)*, pages 1–6, 2012.

[165] Julie Villanova, Peter Cloetens, Heikki Suhonen, Jerome Laurencin, Francois Usseglio-Viretta, Elisa Lay, Gerard Delette, Pierre Bleuet, David Jauffrès, Denis Roussel, Aaron Lichtner, and Christophe L. Martin. Multi-Scale 3D imaging of absorbing porous materials for solid oxide fuel cells. *Journal of Materials Science*, 49(16):5626–5634, 2014.

[166] Matthew L Fisher, Miroslav Colic, Masa P Rao, and Fred F Lange. Effect of Silica Nanoparticle Size on the Stability of Alumina / Silica Suspensions. *Journal of the American Ceramic Society*, 84(4):713–718, 2001.

[167] Geodict.com. ConductoDict Tutorial, 2013.

[168] James R Wilson, Worawarit Kobsiriphat, Roberto Mendoza, Hsun-Yi Chen, Jon M Hiller, Dean J Miller, Katsuyo Thornton, Peter W Voorhees, Stuart B Adler, and Scott a Barnett. Three-dimensional reconstruction of a solid-oxide fuel-cell anode. *Nature materials*, 5(7):541–4, July 2006.

[169] Jurgen Becker, Christian Wieser, Stephan Fell, and Konrad Steiner. A multi-scale approach to material modeling of fuel cell diffusion media. *Journal of Heat and Mass Transfer*, 54(7-8):1360–1368, 2011.

[170] Russell Goodall, Jean-François Despois, Ariane Marmottant, Luc Salvo, and Andreas Mortensen. The effect of preform processing on replicated aluminium foam structure and mechanical properties. *Scripta Materialia*, 54(12):2069–2073, June 2006.

[171] Sophie Giraud and Jérôme Canel. Young's modulus of some SOFCs materials as a function of temperature. *Journal of the European Ceramic Society*, 28(1):77–83, January 2008.

[172] C.W Kuo, Y.H Lee, K.Z Fung, and M.C Wang. Effect of Y2O3 addition on the phase transition and growht of YSZ nanocrystallites prepared by sol-gel process. *Journal of Non-Crystalline Solids*, 351(4):304–311, 2005.

[173] M Gaudon, C Laberty-Robert, and F Ansart. New chemical process for the preparation of fine powders and thin films of LSMx-YSZ composite oxides. *Solid State Sciences*, 5(10):1377–1383, 2003.

[174] M.B. Kakade, D. Das, and S. Ramanathan. Studies on slip casting behavior of lanthanum strontium manganite. *Ceramics International*, 37(6):1789–1793, August 2011.

[175] Amir Reza Hanifi, Mark Zazulak, Thomas H. Etsell, and Partha Sarkar. Effects of calcination and milling on surface properties, rheological behaviour and microstructure of 8 mol% yttria-stabilised zirconia (8 YSZ). *Powder Technology*, 231:35–43, November 2012.

[176] Jochen Joos, Moses Ender, Thomas Carraro, André Weber, and Ellen Ivers-Tiffée. Representative volume element size for accurate solid oxide fuel cell cathode reconstructions from focused ion beam tomography data. *Electrochimica Acta*, 3:268–276, May 2012.

[177] Jimmi Nielsen and Johan Hjelm. Impedance of SOFC electrodes: A review and a comprehensive case study on the impedance of LSM:YSZ cathodes. *Electrochimica Acta*, 115:31–45, January 2014.

[178] J. S. Cronin, Kullachate Muangnapoh, Zach Patterson, Kyle J. Yakal-Kremski, Vinayak P. Dravid, and Scott A. Barnett. Effect of Firing Temperature on LSM-YSZ Composite Cathodes: A Combined Three-Dimensional Microstructure and Impedance Spectroscopy Study. *Journal of The Electrochemical Society*, 159(4):B385, 2012.

[179] Benjamin Völker and Robert M. McMeeking. Impact of particle size ratio and volume fraction on effective material parameters and performance in solid oxide fuel cell electrodes. *Journal of Power Sources*, 215:199–215, October 2012.

[180] R. W. Rice. Extension of the Exponential Porosity Dependence of Strength and Elastic Moduli. *Journal of the American Ceramic Society*, 59(11):536–537, 1968.

[181] A Atkinson and A Selc. Mechanical behaviour of ceramic oxygen ion-conducting membranes. *Solid State Ionics*, 134:59–66, 2000.

[182] Ayhan Sarikaya, Vladimir Petrovsky, and Fatih Dogan. Effect of the anode microstructure on the enhanced performance of solid oxide fuel cells. *International Journal of Hydrogen Energy*, 37(15):11370–11377, August 2012.

Acronyms

AFC Alkaline Fuel Cell. 13, 14, 218

BET Brunauer-Emmett-Teller theory. 108, 147, 218

CE counter-electrode. 112, 218
CEA le Commissariat á l′ ènergie atomique. 4, 218

DEM discrete-element method. 2, 69–74, 76, 77, 114–116, 157, 158, 175–177, 183, 187, 188, 198, 218, 225
DI deionized water. 80, 82, 127, 218
DOE design-of-experiment. 132, 196, 218, 225
dp3D discrete-powder 3D. 69, 115, 218

EDS electron dispersive spectroscopy. 98, 99, 128, 131, 163, 218, 223
ESD Electro-Spray Deposition. 92, 93, 164, 188, 218
ESRF European Synchrotron Radiation Facility. 4, 100, 218

FD freezing-direction. 136, 143, 144, 162, 173, 174, 218
FEM finite-element method. 69, 218
FIB focused-ion beam tomography. 100, 102–105, 114, 139–141, 145, 147–149, 157, 178, 184, 187, 193, 194, 198, 218, 223

HAP hydroxyapatite. 80, 83, 96, 218

IEP iso-electric point. 60–62, 218
IR infra-red. 121–123, 218
IZ Initial Zone. 43, 68, 87, 94, 107, 108, 122, 124, 163, 180, 197, 218

LSM lanthanum strontium manganite. 20, 25–27, 70, 80–83, 88–92, 94, 96, 99, 100, 103–105, 108, 114–116, 119, 126–137, 139–144, 146, 147, 149, 151, 157, 161, 163, 166, 170, 171, 173, 175, 178, 179, 186, 188, 189, 191–193, 195, 198, 218, 221, 223, 225

MCFC Molten Carbonate Fuel Cell. 13, 14, 218
MSA minimum-solid-area. 9, 64–66, 185–187, 218, 224

NiO nickel oxide. 24, 27, 28, 55, 57, 80–83, 96, 114, 168, 189, 218, 225
NSF National Science Foundation. 4, 218
NTUF Nanotech User Facility. 4, 99, 218

PAFC Phosphoric Acid Fuel Cell. 13, 14, 218
PEG polyethylene glycol. 80–83, 218
PEMFC Polymer Electrolyte Membrane Fuel Cell. 13, 14, 218
PID proportional-integral-derivative. 84, 85, 218
PMMA Poly(methyl) methacrylate. 80–82, 84, 96, 108, 130, 136, 138, 157, 184, 218

RE reference-electrode. 112, 218

SEM scanning electron microscope. 30, 98, 99, 103, 105, 128, 131, 140, 164, 183, 193, 198, 218
SOFC Solid Oxide Fuel Cell. 3, 5, 11, 13–17, 19–24, 26–28, 30–35, 37, 55, 70, 74, 77, 78, 83, 91, 93, 105, 110, 112, 113, 125, 126, 139, 143, 169, 179, 189, 191, 196, 218
SSZ Steady-State Zone. 43, 44, 47, 48, 50, 53, 54, 68, 87, 91, 92, 94, 124, 149, 161, 163, 168, 170, 174, 189, 190, 218

TPB triple phase boundary. 21, 22, 25, 26, 28, 30, 37, 104–106, 139–142, 161, 178–180, 193, 218
TZ Transition Zone. 43, 45, 47, 68, 87, 94, 107, 108, 122, 124, 163, 180, 197, 218

WE working-electrode. 112, 218

X-ray Tomo X-Ray Synchrotron Radiation Tomography. 2, 102, 187, 197, 218
XRD X-ray diffraction. 96, 131, 218

YSZ yttria-stabilized zirconia. 20, 23–29, 34, 55, 57, 70, 80–83, 88–94, 96, 99, 100, 103–105, 108, 112, 114–116, 119, 126–137, 139–144, 146, 147, 149, 151, 157, 161–164, 166, 168, 170, 171, 173, 175, 178, 179, 186, 188–193, 195, 197, 198, 218, 223, 225

List of Figures

List of Tables